The Science Driving the 12 GeV Upgrade OF CEBAF

Jefferson Lab

February 2001

Jefferson Lab is managed and operated by the Southeastern Universities Research Association (SURA) for the U.S. Department of Energy.

Thomas Jefferson National Accelerator Facility
12000 Jefferson Avenue
Newport News
Virginia 23606
www.JLab.org
(757)-269-7100

Abstract

This White Paper presents the compelling scientific case for upgrading the Continuous Electron Beam Accelerator Facility (CEBAF) at Jefferson Lab to 12 GeV. Such a facility will make profound contributions to the study of nuclear matter. In particular, it will allow breakthrough programs to be launched in two key areas:

- *The experimental observation of the QCD flux tubes which cause confinement.* Theoretical conjectures, now confirmed by lattice QCD simulations, indicate that the most spectacular new prediction of QCD – quark confinement – occurs through the formation of a string-like “flux tube” between quarks. This conclusion (and proposed mechanisms of flux tube formation) can be tested by determining the spectrum of the gluonic excitations of mesons.
- *The measurement of the quark and gluon wavefunctions of the nuclear building blocks.* A vast improvement in our knowledge of the fundamental structure of the proton and neutron can be achieved. Not only can existing “deep inelastic scattering” cross sections be extended for the first time to cover the critical region where their basic three-quark structure dominates, but also measurements of new “deep exclusive scattering” cross sections will open the door to a new, more complete characterization of these wavefunctions by providing direct access to information on the correlations among the quarks.

In addition to opening up these qualitatively new areas of research, the Upgrade will:

- *Open important new research domains in key areas already under investigation.* These new research thrusts include:
  - Determining the dynamics underlying the quark-gluon wavefunctions through measurements of the high-momentum-transfer behavior of form factors.
  - Mapping out and understanding the transition from the hadronic to the quark-gluonic description of strongly interacting matter through the study of low-energy duality.
  - Searching for the onset of color transparency effects in the region where they are supposed to exist.
  - Determining the role of color polarization effects in the NN force by measuring the threshold ψN cross section.
  - Executing a unique and global study of short-range correlations in nuclei.
  - Examining the role of quark masses in determining hadron spectra by mapping out the currently obscure $s\bar{s}$ spectrum that straddles the boundary between the rigorously understood heavy-quark systems and the poorly understood light-quark world.

While focusing on science, this White Paper also summarizes reports on the required detector and accelerator upgrades so that it can serve as an overview of the entire plan for the 12 GeV project.

PREFACE

When the scientific case was made for the facility that became CEBAF, there was unanimous agreement on the importance of a continuous-beam electron accelerator but a great deal of discussion about the optimum beam energy. A subcommittee of NSAC (the Nuclear Science Advisory Committee of the U.S. Department of Energy and the National Science Foundation) chaired by Peter Barnes concluded [Ba82] that the accelerator's design energy should be 4 GeV, rather than the 2 GeV favored by some, because the higher energy would permit its experimental program "to study the largely unexplored transition between the nucleon-meson and the quark-gluon descriptions of nuclear systems". In anticipation of the future need to extend this experimental program to even higher momentum and energy transfers, the CEBAF accelerator was designed in the mid-1980s so that future extensions to energies of order 25 GeV would be straightforward.

As CEBAF's scientific program has progressed, the wisdom of these design choices has become increasingly clear. This White Paper outlines the scientific case for the upgrade of CEBAF to 12 GeV, and documents the accelerator and experimental equipment improvements necessary to carry out the scientific program. It is the result of lengthy discussions within the Jefferson Lab community that began as the 4 GeV program was just underway in the mid-1990s. In this preface we remind the reader of the main activities leading to this White Paper.

As CEBAF neared completion and its experimental program was about to begin, the CEBAF User Group began an examination of the physics accessible with an upgraded CEBAF energy. This decision led to the organization of a workshop held at Jefferson Lab from 14 to 16 April 1994. It was organized into four working groups centered around four main physics topics, by an organizing committee consisting of T. Barnes, R. Ent, B. Frois, R. Holt, R. Milner, P. Mulders, J. Napolitano, M. Petratos, and P. Stoler. Each working group was represented by one or two plenary speakers who were asked to summarize the outstanding physics issues that could be addressed by an upgrade, and by many shorter parallel contributions dealing with specific issues. Members of the organizing committee then summarized their presentations and their personal views on the physics case for an upgrade of CEBAF to higher energies. The result was the "yellow book" report, *CEBAF at Higher Energies*, edited by Paul Stoler for the CEBAF User Group and Nathan Isgur for Jefferson Lab, which marked the first step toward the goal of defining the physics program that would form the basis of an upgrade of CEBAF.

The compelling science which emerged from this workshop led to a study of the upgrade options by a laboratory strategic planning group, and to two "village meetings". These studies indicated that a cost-effective upgrade of CEBAF is possible. These conclusions were presented to

NSAC, which responded in the recommendations of its 1996 Long Range Plan that “the community looks forward to future increases in CEBAF’s energy and to the scientific opportunities that would bring”.

With this encouragement, the users held a second workshop from 15 to 18 June 1998. This workshop, organized by Steve Dytman, Howard Fenker, and Phil Roos, was structured to review the physics motivation for the Upgrade, but to focus on the specification of the equipment and instrumentation necessary for measurements at 12 GeV. It began with plenary sessions on physics, on the issues faced by Halls A, B, and C at 12 GeV, on the preliminary designs of a new Hall D for photoproduction, and on state-of-the-art detector and polarized-source developments. Next came parallel sessions organized by physics topic on photoproduction, high-Q^2 reactions, hadrons in the nuclear medium, and inclusive and semi-inclusive reactions. These were followed by parallel sessions organized by hall. More than 180 scientists participated in the workshop; their work is recorded in *Physics and Instrumentation with 6–12 GeV Beams*, edited by the three organizers. A remarkable feature of this workshop was the quick consensus reached on the set of detectors needed to exploit the vast new physics potential of the 12 GeV Upgrade within budgetary guidelines established by DOE.

Most recently, in anticipation of the imminent launching of the next NSAC Long Range Plan, the User Group organized a special January workshop devoted to delineating the 12 GeV program for the existing experimental halls. It commissioned five follow-on working groups to develop crisp scientific cases and identify key experiments or key experimental programs in five target areas focused on these halls. Following the January workshop, at their March 2000 meeting the User Group Board of Directors appointed a White Paper Steering Committee consisting of four members selected by the User Group and three members selected by Jefferson Lab. This is the group that has been responsible for editing the present document.

Prior to and in parallel with this effort, the new Hall D Collaboration produced a design for a new meson photoproduction facility designed to discover and investigate the properties of gluonic excitations. Their design underwent a rigorous review in December 1999 by a distinguished external committee; the collaboration emerged from the review having received high praise for both their physics goals and their experimental design.

In 2000 the users reviewed an early draft version of this White Paper at their annual June meeting, which was once again devoted to the Upgrade. At that meeting, key experiments were selected from the many ideas that emerged from the planning for the Upgrade. These experiments were developed in greater detail, for inclusion as part of the scientific case for the Upgrade, and presented to the Jefferson Lab Program Advisory Committee at a special meeting of that committee. The PAC commented on each proposal in a manner similar to their review of research proposals for the present accelerator. In summarizing their review, the PAC noted:

> *The laboratory and the user community have developed an impressive scientific case that demands this new capability. The Jefferson Lab Program Advisory Committee was charged by the laboratory to review this science, and to review the plans for the associated experimental equipment.*
>
> *The committee concludes that an outstanding scientific case has been identified which requires the unique capabilities of the JLab 12 GeV upgrade. The results of these experiments are likely to significantly change the way we think about nuclear physics and the strong (nonperturbative) limit of QCD. Two major new thrusts can produce definitive results: the experimental verification of the origin of quark confinement by QCD flux tubes as predicted by lattice gauge calculations, and the determination of the quark and gluon wave functions of the nuclear building blocks. The full technical capabilities of the upgrade are required for this progress. New research domains are also opened up that show great promise in leading existing research efforts to new levels of understanding.*
>
> *The proposed experimental equipment is well suited to addressing these new physics opportunities. The choices capitalize on the powerful existing equipment at the laboratory without compromising the physics goals.*
>
> *The Program Advisory Committee was excited by the research potential that the 12 GeV upgrade makes possible. The scope of the upgrade is very well matched to the problems we see driving the field for the next decade. The time has come to bring these opportunities to nuclear physics.*

This White Paper is based on these many workshops, their published proceedings and unpublished presentations, and on the published and unpublished work of many individuals on the physics opportunities that would open up with CEBAF at 12 GeV. A second, more detailed draft of this document was released in October 2000 to provide ample opportunity for community comment to be incorporated prior to the release of a third version in time for the NSAC Long Range Plan Town Meeting at Jefferson Lab in December 2000. Following discussions at that meeting and further comment from the user community, the present final version of the White Paper was published for presentation to the larger nuclear physics community as part of the Long Range Planning process.

The author list at the end of this document includes the names of all contributors to the effort known to us. Many of them commented extensively on the earlier drafts, resulting in a much-improved document. This White Paper would have been impossible without their intelligence, enthusiasm, time, and just plain hard work. We apologize to anyone whose contributions we have inadvertently failed to acknowledge. We also acknowledge extensive technical help in the production of this document from Mary Beth Stewart and Nilinga Liyanage.

The 12 GeV Upgrade White Paper Steering Committee:

Lawrence Cardman (cardman@jlab.org)
Rolf Ent (ent@jlab.org)
Nathan Isgur (isgur@jlab.org)
Jean-Marc Laget (laget@hep.saclay.cea.fr)
Christoph Leemann (leemann@jlab.org)
Curtis Meyer (cmeyer@ernest.phys.cmu.edu)
Zein-Eddine Meziani (meziani@vm.temple.edu)

Contents

1 EXECUTIVE SUMMARY

There has been a remarkably fruitful evolution of our picture of the behavior of strongly interacting matter during the almost two decades that have passed since the parameters of the Continuous Electron Beam Accelerator Facility (CEBAF) at Jefferson Lab were defined. These advances have revealed important new experimental questions best addressed by a CEBAF-class machine at higher energy. Fortunately, favorable technical developments coupled with foresight in the design of the facility make it feasible to triple CEBAF's beam energy from the original design value of 4 GeV to 12 GeV (corresponding to doubling the achieved energy of 6 GeV to 12 GeV) in a cost-effective manner: the Upgrade can be realized for about 15% of the cost of the initial facility. This Upgrade would enable the worldwide community using CEBAF to greatly expand its physics horizons.

Raising the energy of the accelerator to 12 GeV provides three general advantages:

1. It allows crossing the threshold above which the origins of quark confinement can be investigated. Specifically, 12 GeV will enable the production of certain "exotic" mesons, whose existence establishes that the origin of quark confinement is in the formation of QCD flux tubes and whose spectrum encodes information on the mechanism within QCD responsible for their formation. With 12 GeV one also crosses the threshold for charmed quark production.
2. It allows direct exploration of the quark-gluon structure of hadrons and nuclei. It is known that inclusive electron scattering at the high momentum and energy transfers available at 12 GeV is governed by elementary interactions with quarks and gluons. The original CEBAF energy was not fully adequate for study of this critical regime, while with continuous 12 GeV beams one can cleanly access the entire "valence quark region" and exploit the newly discovered Generalized Parton Distributions to access experimentally both the correlations in the quark wavefunctions and their transverse momentum distributions.
3. In addition to these qualitative changes in the physics reach of CEBAF, the 12 GeV Upgrade also allows important new thrusts in CEBAF's present research program, generally involving the extension of measurements to substantially higher momentum transfers (probing correspondingly smaller distance scales). We also note that most experiments that want to run at a presently accessible momentum transfer can do so more efficiently (*e.g.*, consuming less total beam time) at higher electron beam energy.

In the examples highlighted in this executive summary and in the more complete discussions of Chapter 2, these benefits of the energy upgrade will always be significant.

1.A Physics Overview

Chapter 2 provides a summary of the science motivation driving the 12 GeV Upgrade. The research program of the new facility dramatically extends and expands upon the major research themes (or "campaigns") that are driving our present program. These themes coincide with the broad directions of the field of nuclear physics as identified in two key documents: the 1996 Long Range Plan [NS96] of NSAC (the Nuclear Science Advisory Committee of the U.S. Department of Energy and the National Science Foundation) and the recent decadal survey [NA99] of the field by the National Research Council of the National Academy of Sciences. We identify these campaigns here to place our research program in this broader context. Each campaign corresponds to an outstanding question in nuclear physics that the laboratory's users address with a concerted program of experimental and theoretical work. The campaigns are:

On the Structure of the Nuclear Building Blocks:

> **Campaign 1: Testing the Origin of Quark Confinement** – experiments and theory aimed at examining the fundamentally new dynamics that underpins all of nuclear physics: the confinement of quarks.
>
> **Campaign 2: How Are the Nuclear Building Blocks Made from Quarks and Gluons?** – a program of measurements addressing this first question that must be answered in the quest to understand nuclear physics in terms of the fundamental theory of strongly interacting matter: quantum chromodynamics (QCD).
>
> **Campaign 3: Understanding the Origin of the Nucleon-Nucleon Force** – a broad program of experimental and theoretical work focused on moving beyond current phenomenological descriptions of the nucleon-nucleon force (for example, to determine its basic nature as a mixture of meson exchange, quark exchange, and color polarization effects).

On the Structure of Nuclei:

> **Campaign 4: Testing the Limits of the Meson/Nucleon Description of Nuclei** – a broad program of experiments taking advantage of the precision, spatial resolution, and interpretability of electromagnetic interactions to address long-standing issues in the classical nuclear physics of large nuclei.
>
> **Campaign 5: Probing the Limits of the "Standard Model" of Nuclear Physics** – the huge body of experimental and theoretical work now being carried out at Jefferson Lab and in the community at large focusing on few-body systems where directly interpretable experiments can be compared with exact calculations that are now feasible in the context of the "standard model" of nuclear physics.

The two "breakthrough" programs that have been identified as major motivations for the energy upgrade address key issues in Campaigns 1 and 2. The first, a program of *gluonic spectroscopy*, will provide data needed: i) to test experimentally our current understanding that quark confinement arises from the formation of QCD flux tubes; and ii) to explore the mechanism behind the formation of these flux tubes. The second program will explore the *complete quark and gluon wavefunctions* of the nucleons through measurements: i) of quark momentum distributions in the critical, but previously unreachable, valence quark region; and ii) of exclusive reactions that build on the framework of the newly discovered Generalized Parton Distributions. In addition to opening up these two qualitatively new areas of research, the Upgrade is also strongly driven by the fact that it will create important new research thrusts in key areas already under investigation with CEBAF's 6 GeV capability. In Sections 1.A.1, 1.A.2, and 1.A.3 we summarize these three key science drivers of the 12 GeV Upgrade. Section 1.B then completes the picture by summarizing the accelerator and experimental equipment upgrades required to accomplish these physics goals.

1.A.1 The Origin and Nature of Quark Confinement: Discovering and Studying the Exotic Mesons

The 12 GeV Upgrade will allow a breakthrough program to be launched in Campaign 1, "Testing the Origin of Quark Confinement".

In the early 1970s, evidence that the masses of strongly interacting particles increased without limit as their internal angular momentum increased led the theorist Yoichiro Nambu [Na70] to propose that the quarks inside these particles are "tied together" by strings. Numerical simulations of QCD ("lattice QCD") have demonstrated [Ba00] that Nambu's conjecture was essentially correct: in chromodynamics, a stringlike chromoelectric flux tube forms between distant static quarks, leading to their confinement with an energy proportional to the distance between them (see Figs. 1 and 2). The phenomenon of confinement is the most novel and spectacular prediction of QCD – unlike anything seen before. It is also the basic feature of QCD that drives all of nuclear physics, from the mass of the proton and other nuclear building blocks to the NN interaction.

The ideal experimental test of this new feature of QCD would be to study the flux tube directly by anchoring a quark and antiquark several fermis apart and examining the flux tube that forms between them. In such ideal circumstances one of the fingerprints of the gluonic flux tube would be its model-independent spectrum [Lu81] (see Fig. 3): its required two degenerate first excited states are the two longest-wavelength vibrational modes of this system, while their excitation energy is required to be π/r since both the mass and the tension of this "relativistic string" arise from the

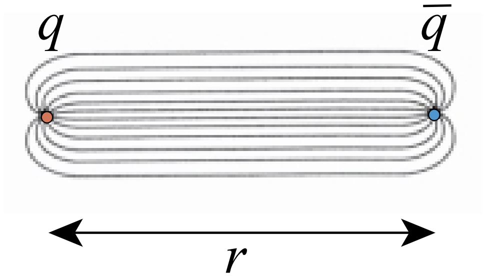

Figure 1: In QCD a confining flux tube forms between distant static charges. The Hall D program is designed to verify this fundamental new feature of chromodynamics.

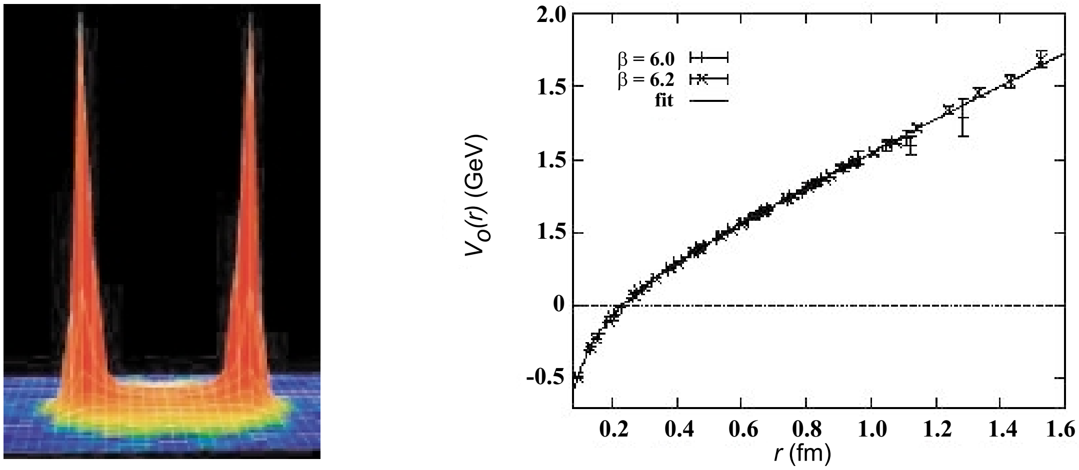

Figure 2: Lattice QCD has confirmed the existence of flux tubes between distant static charges for heavy quarks. In addition to the intense color fields in the immediate vicinity of each quark, one can see the formation [Ba00] along the line connecting the two quarks of a flux tube of constant thickness, leading to the linearly rising potential seen on the right [Ba97].

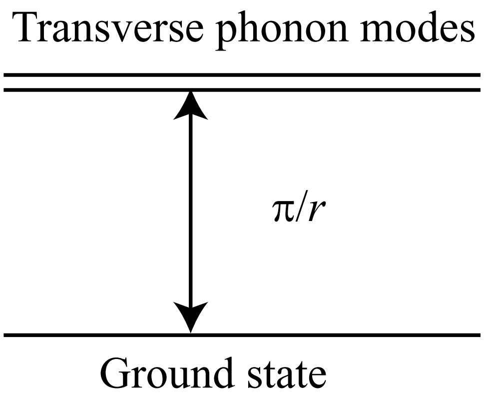

Figure 3: Model-independent spectrum of the glue (flux tube) of Fig. 1.

energy stored in its color force fields. Such a direct examination of the flux tube is of course not possible. In real life we have to be content with systems in which the quarks move. Fortunately, we know both from general principles [Is85] and from lattice QCD calculations [Mo97] that an approximation to the dynamics of the full system that ignores the impact of these two forms of motion on each other works quite well – at least down to quark masses of the order of 1 GeV.

To extend this firm understanding to yet lighter quarks, models are required [Is85], but the most important properties of this system are determined by the model-independent features described above. In particular, in a region around 2 GeV, a new form of hadronic matter must exist in which the gluonic degree of freedom of a quark-antiquark system is excited. The smoking gun characteristic of these new states is that the vibrational quantum numbers of the gluonic "string", when added to those of the quarks, can under certain circumstances produce a total angular momentum J, a total parity P, and a total charge conjugation symmetry C not allowed for ordinary $q\bar{q}$ states. These unusual J^{PC} combinations (such as 0^{+-}, 1^{-+}, and 2^{+-}) are called exotic, and the states are referred to as exotic hybrid mesons [Ba77]. Not only general considerations and flux tube models, but also first-principles lattice QCD calculations, require that these states have masses around 2 GeV; furthermore, they demonstrate that the levels and their orderings will provide experimental information on the mechanism that produces the flux tube.

On the experimental front, tantalizing evidence has appeared in recent years for both exotic hybrids and gluonic excitations with no quarks (glueballs). For the last two years a group of 90 physicists from 26 institutions in seven countries has been working on the design of the definitive experiment to map out the spectrum of these new states required by the confinement mechanism of QCD. Photon beams are expected to be particularly favorable for the production of the exotic hybrids [Is85]. The reason is that the photon sometimes behaves as a “virtual vector meson” with total quark spin $S = 1$. When the flux tube in this $S = 1$ system is excited, both ordinary and exotic J^{PC} are possible. In contrast, when the spins are antiparallel ($S = 0$), as in pion or kaon probes, the exotic combinations are not generated. (In the approximation that flux tube and quark dynamics separate, hybrid production would occur by pure flux tube excitation, and these selection rules would be strictly true. In practice, these two degrees of freedom interact with one another to produce corrections to the rules.) To date, most meson spectroscopy has been done with incident pion, kaon, or proton probes, so it is not surprising that the experimental evidence to date for flux tube excitation is tentative.

In contrast to hadron beams, high-flux photon beams of sufficient quality and energy to perform meson spectroscopy studies have not been available, so there are virtually no data on the photoproduction of mesons with masses in the 1.5 to 3 GeV region. Thus, experimenters have not been able to search for exotic hybrids precisely where they are expected to be found. The planned experiment will have a dramatic impact on this situation. Even if initial running is at only 10% of the planned photon fluxes of 10^8/s, the experiment will accumulate statistics during the first year of operation that will exceed the world’s supply of published meson data obtained by pion production by at least a factor of 10, and the existing photon production data set by at least a factor of 1000. With the planned detector (see Fig. 4), high statistics, and linearly polarized photons, it will be possible to map out the full spectrum of the decay modes of these gluonic excitations. This experiment is described in Section 4.E; a much more complete discussion of the physics driving the experiment is given in Section 2.A.

When the spectrum and decay modes of these gluonic excitations have been mapped out experimentally, we will have made a giant step forward in understanding one of the most important phenomena discovered in the twentieth century: quark confinement.

1.A.2 The Quark-Gluon Wavefunctions of the Nuclear Building Blocks

The 12 GeV Upgrade will also allow a breakthrough program to be launched in Campaign 2: “How Are the Nuclear Building Blocks Made from Quarks and Gluons?”

The classic program of deep inelastic scattering (DIS) experiments began with the Nobel Prize–winning work of Friedman, Kendall, and Taylor [Bl69] in the 1970s at SLAC. These measurements

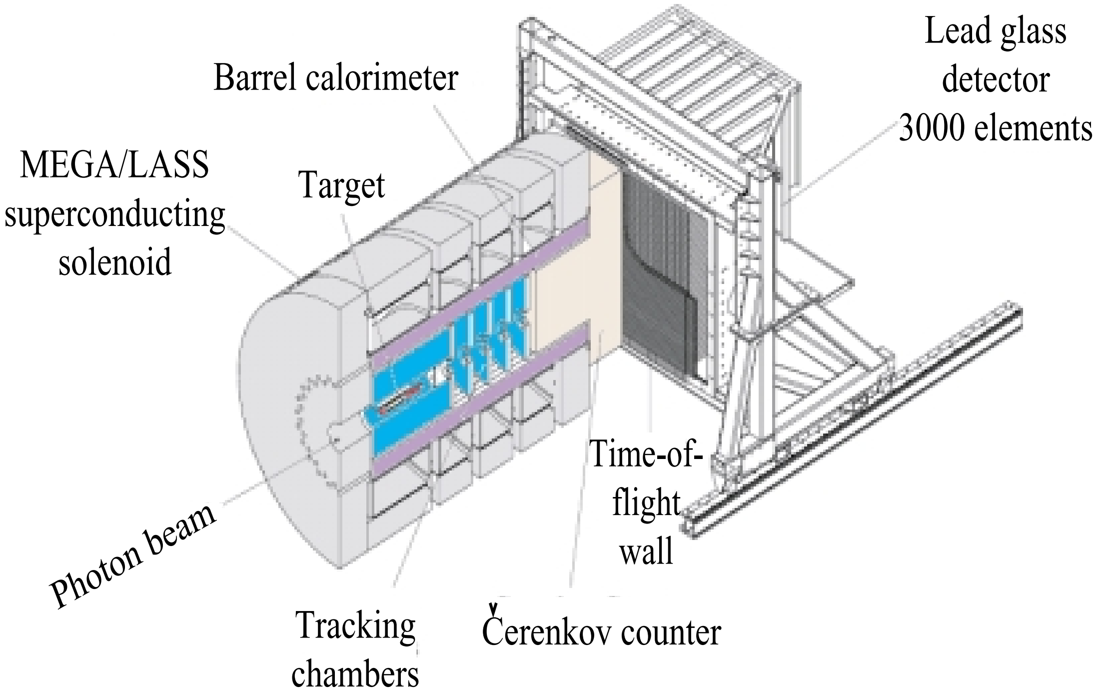

Figure 4: The conceptual design of the proposed detector to study the photoproduction of mesons in the mass region around 2 GeV.

led to the experimental confirmation of the existence of quarks and to precision tests of the fledgling theory of QCD, eventually confirming it as the fundamental theory governing all strongly interacting (*i.e.*, nuclear) matter.

Even though such experiments have been pursued vigorously for nearly 30 years, it is remarkable that there has never been an experimental facility that could measure the DIS cross sections throughout the kinematic regime where the three basic ("valence") quarks of the proton and neutron dominate the wavefunction. At modest values of the momentum transfer Q^2, the valence quarks play a substantial role in determining these cross sections over a large range of the kinematic variable x (which runs from 0 to 1 and is roughly interpretable as the fraction of the momentum of the initial nucleon state along the direction of the incident virtual photon that was carried by the struck quark). The contribution of the valence quarks peaks at $x \simeq 0.2$. However, if one is in the conventionally defined deep inelastic regime, the probability of finding a quark in the high-x "valence quark region" is small, and becomes smaller and smaller as $x \to 1$; moreover, with "pollution" from gluons and quark-antiquark pairs, it is only for $x > 0.5$ that the valence quarks dominate the $x \to 1$ wavefunction. The 12 GeV Upgrade will allow us to map out the quark distribution functions in this "clean" valence quark region with high precision. Such measurements will have a profound impact on our understanding of the structure of the proton and neutron.

Figure 5 shows one example of a measurement that can be done with the proposed Upgrade. (See Section 2.B.1 for details.) The neutron polarization asymmetry A_1^n is determined by the spin wavefunction of the quarks, and most dynamical models predict that in the limit where a single quark carries all of the nucleon's momentum ($x \to 1$), it will also carry all of the spin polarization (so, *e.g.* for the neutron, $A_1^n \to 1$ as $x \to 1$). Existing data on A_1^n end before reaching the region of valence quark dominance, and show no sign of making the predicted dramatic transition $A_1^n \to 1$. There are similar (if less dramatic) paucities of data on all other DIS observables in this region.

Even in unpolarized DIS, where the available data are best, there are unresolved issues. To extract the ratio of such a simple and basic a property as the relative probability of finding a d quark vs. a u quark at high x requires measurements on both the proton and neutron. However, high-x neutron information is difficult to disentangle from nuclear binding corrections. Figure 6 shows the precision with which this fundamental ratio (which is intimately related to the fact that the proton and neutron, and not the Δ, are the stable building blocks of nuclei) can be measured with the proposed Upgrade. (See Section 2.B.1 for details.) The planned experiment will exploit the mirror symmetry of $A = 3$ nuclei through simultaneous measurements of the inclusive structure functions for ^{3}H and ^{3}He. Regardless of the absolute value of the nuclear effects in the two measurements, their differences should be small, permitting the neutron-to-proton ratio (and thus the d/u ratio) to be extracted with precision.

While the historic DIS program will thus continue to be fruitful, it is intrinsically limited in what it can tell us about quark and gluon wavefunctions: structure functions are *probabilities*. Until recently, attempts to determine the quark and gluon *wavefunctions* of the nucleons have been hopelessly handicapped by the lack of a rigorous framework for making a connection between any experimental measurement and these wavefunctions. (For example, while intuitively related to the momentum wavefunction of the quarks, even the valence quark distribution functions are sensitive only to the square of the momentum wavefunction suitably averaged over momenta transverse to the virtual photon direction!) The discovery of Generalized Parton Distributions (GPD's) and their connection to certain totally exclusive cross sections has made it possible in principle to rigorously map out the complete nucleon wavefunctions themselves [Ji97, Ra96]. The GPD's are sensitive to the wavefunction at the *amplitude* level, instead of merely the probability level, and, in particular, explore quark-quark correlations. The 12 GeV Upgrade will provide the accelerator and detectors required to perform the difficult measurements that will allow the first comprehensive exploration of this new "Deep Exclusive Scattering" (DES) domain that is rigorously connected to the quark and gluon wavefunctions.

Standard techniques relate the total cross section for deep inelastic scattering to the imaginary part of the forward elastic scattering process $\gamma^* p \to \gamma^* p$, where p is a target particle (such as a proton). Of key importance is that in the deep inelastic scattering regime the elastic process is dominated by the diagram shown in Fig. 7, where pure electron-quark scattering *factorizes* from the probability for the quark to carry a fraction x of the target's momentum, depicted as the blob at the bottom of the diagram.

The new DES processes that lead to GPD's, and thence to quark and gluon wavefunctions, can be extracted *under appropriate kinematic conditions* from the generic cross sections shown in Fig. 8. Whereas the DIS process involved a γ^* in both the initial and the final state, for these new deep exclusive processes the final particle can be a $\gamma, \gamma^*, \pi, \eta, \rho, \omega, K$, etc. instead of just a γ^*. Furthermore, the initial and final targets can have different momenta (p can scatter to $p\,'$) and can even be of different types (i can scatter to f). If the final particle is a γ^*, forward scattering is possible, and in that case, assuming one is in the scaling region for these cross sections, the GPD's being studied would reduce to standard quark distribution functions. In every other case (once again assuming one is in the appropriate scaling region), these processes access a rich new body of information about the full wavefunction, including nonforward overlaps of their longitudinal parts and their transverse momentum structure.

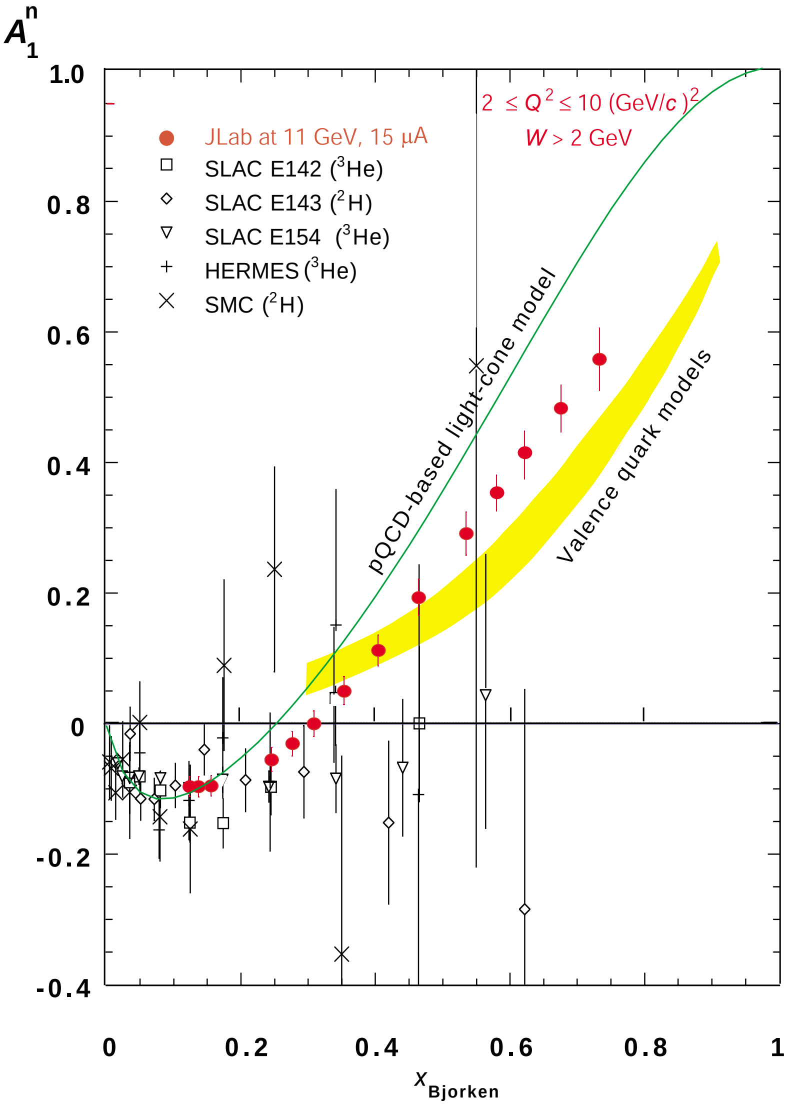

Figure 5: A projected measurement of the neutron polarization asymmetry A_1^n, determined by the spin structure of the valence quarks, made possible by the proposed 12 GeV Upgrade. The shaded band represents the range of predictions of valence quark models; the solid line is the prediction of a pQCD light-cone quark model.

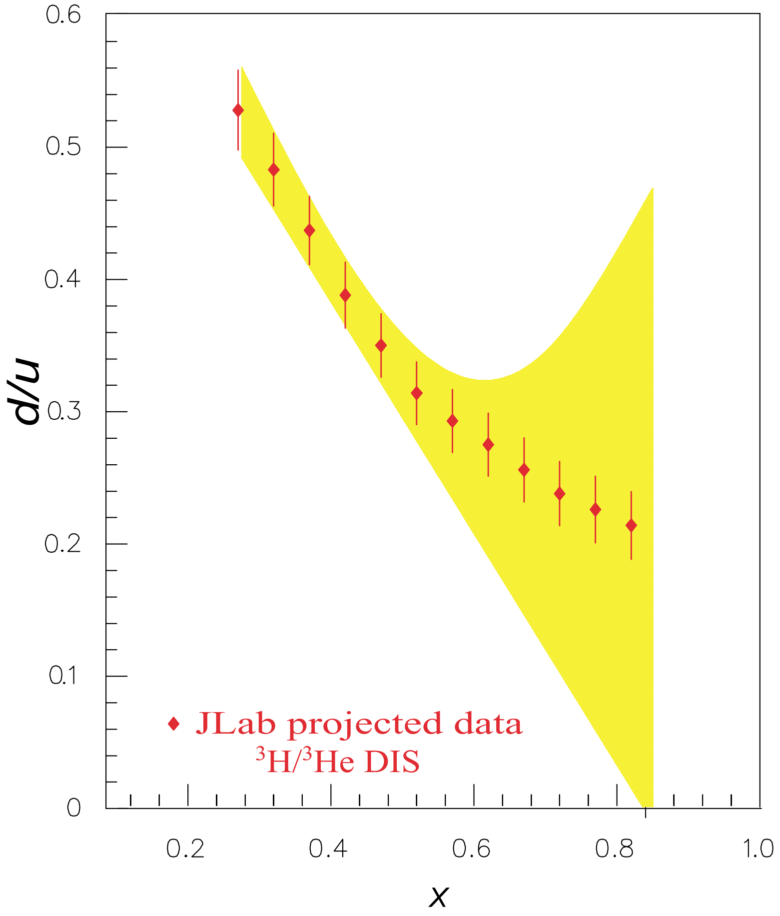

Figure 6: A projected measurement of the ratio of momentum distributions of valence d quarks to u quarks made possible by the proposed 12 GeV Upgrade. The shaded band represents the uncertainty in existing experiments due to nuclear Fermi motion.

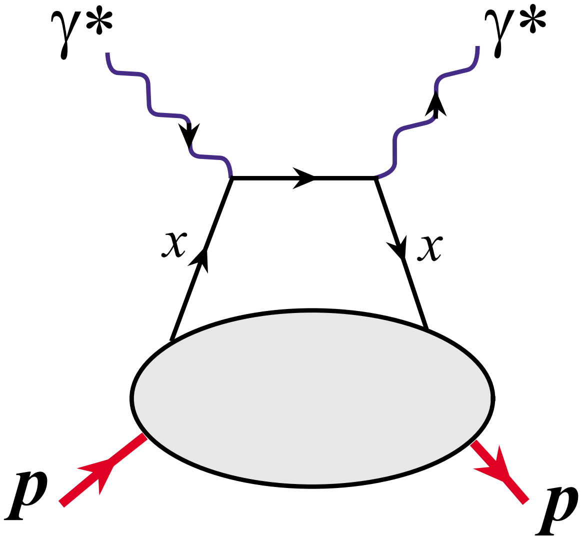

Figure 7: The asymptotically dominant contribution to deep inelastic scattering (DIS).

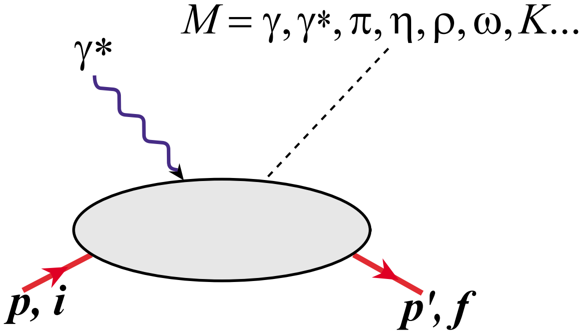

Figure 8: The special deep exclusive scattering (DES) processes that have been identified as providing a new window on the quark-gluon wavefunctions of the nuclear building blocks.

While theoretical guidance is available, the kinematic range over which measurements must be done for the above-mentioned DES scaling to apply must normally (as was the case historically for DIS) be determined experimentally. Moreover, as in DIS, there are two related but conceptually distinct requirements for being in the DES scaling regime so that Fig. 8 can be interpreted in terms of the GPD's and hence the quark-gluon wavefunctions. Wavefunctions are frame-dependent, and those probed in standard DIS and in the new DES processes are *not* those of the rest frame, but rather may be identified with those of a particle whose velocity is approaching the speed of light. Thus one condition for scaling is that the kinematic range of the measurements must bring one close enough to $\beta = 1$ that the wavefunction is close to its asymptotic form. The other condition is that the relevant underlying dynamical processes can be factorized into a "hard" pQCD scattering amplitude and a "soft" amplitude which arises from the wavefunctions.

In the DIS process of Fig. 7 on nucleons, we know that the conditions for scaling are achieved when $Q^2 > 1$ (GeV/c)^2 and the produced inelastic mass $W > 2$ GeV. We can understand these conditions intuitively. In this case we can expect that the "hot" quark between the two pointlike γ^* vertices (the upper line in the figure) will be effectively free from the remaining quarks (within the lower portion of Fig. 7) since these kinematic conditions localize the "hot" quark in space-time to the short-distance regime where asymptotic freedom applies. Moreover, our knowledge of the structure of the excited nucleon resonances strongly suggests that there is no scale greater than 1 GeV to interfere with the rapid evolution of the rest frame wavefunction to its $\beta \to 1$ form.

Similar factorization issues apply to DES. Consider first the $\gamma^* p \to Mp$ reaction with $M = \gamma$, *i.e.*, Deeply Virtual Compton Scattering (DVCS), which can actually proceed *via* a modified version of the Feynman diagram of Fig. 7 with the second γ^* replaced by a γ and with the imaginary part of the graph not taken. Since the two Feynman diagrams are the same, one may expect the two processes to have similar factorization and scaling properties. However, the cases of $\gamma^* p \to Mp$, where M is a meson, represent *terra incognita.* Figure 9 illustrates the essential features. For factorization, the kinematics of the experiment must force the struck quark to be effectively free, as before, but now, in addition, the kinematics must create the $q\bar{q}\,'$ meson by the pQCD process depicted. Note that by judicious choice of the meson and its production characteristics, the data probe complementary aspects of the hadron wavefunction, such as correlations among flavors and momenta of quarks, the transverse momentum distributions, and the role of the quarks' angular momentum and spin in building up the hadron's spin. (Note in addition that since Fig. 9 includes many time-orderings, it includes processes where a quark-antiquark pair is created by the hot photon *and* processes where a $q\bar{q}\,'$ pair in the target is knocked out. There are correspondingly two new types of wavefunctions being probed by these reactions.)

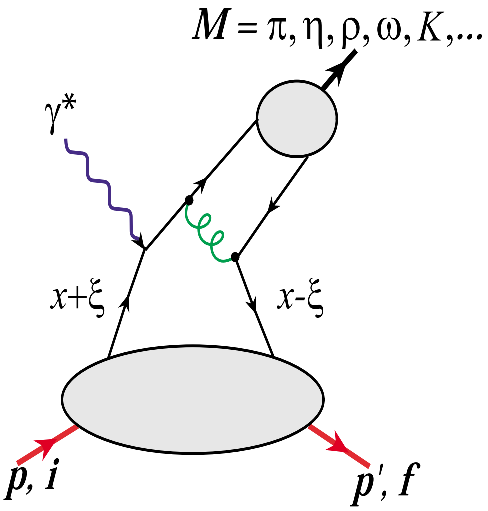

Figure 9: The asymptotically dominant diagram for DES with meson production in which a $q\bar{q}\,'$ pair is "forced" by the γ^* and a hard gluon exchange into the meson $M = \pi, \eta, \rho, \omega, K$, etc. These reactions are governed in their scaling regions by the new Generalized Parton Distributions (GPD's) which depend on three kinematic variables: $t = (p - p')^2$, $\xi = \frac{x_{Bj}}{2 - x_{Bj}}$, and x (defined in the figure).

Figure 10 shows two models for the GPD denoted $H(x, \xi, t)$ from which one can gain some insight into the richness of information available through the study of these new distributions. The figure is a three-dimensional representation at $t = 0$. $H(x, \xi, t)$ is modeled using the so-called double distribution of Radyushkin [Ra99], which parameterizes the usual parton distributions measured in inclusive scattering and parton correlations modeled via quark-antiquark (*i.e.* pion) distributions. In the right-hand surface the "D" term by Polyakov and Weiss [Po99] that represents two-pion contributions is included.

DIS experiments can measure the parton distribution only along the line at $\xi = 0$; $H(x, 0, t = 0)$ is the usual quark distribution for $x > 0$, and the antiquark distribution for $x < 0$. The ability of DES experiments to vary the "skewedness" parameter, ξ, provides access to the full surface and the ability to *measure* the correlations between the partons in the nucleon. ξ is given by the electron kinematics, and defines the fractional momentum difference between the initial- and final-state partons. For $\xi = 0$ the initial- and final-state partons have identical momenta, and for large ξ they carry very different fractions of the nucleon's momentum. At $\xi \to 1$, $H(x, \xi, t)$ takes on the characteristics of quark-antiquark (*i.e.*, meson) distribution amplitudes that are clearly visible in the figure. Additional information on quark-quark correlations can be obtained from mapping out the t-dependence of these surfaces.

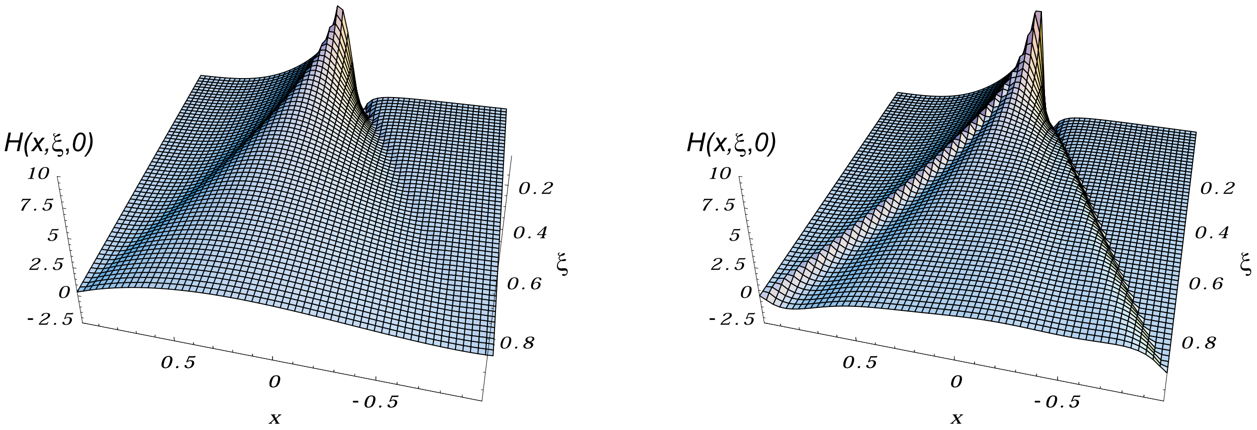

Figure 10: Two possible Generalized Parton Distributions [Vapc] that are consistent with available deep inelastic scattering data (*i.e.*, have identical values for $\xi = 0$) but contain very different quark-quark correlations (see text).

The 12 GeV Upgrade will allow these critical DES cross sections to be systematically measured in the relevant kinematic regions for the first time. In most cases a wide range of kinematic conditions can be achieved covering nearly an order of magnitude in the relevant variables beyond values at which DIS has exhibited scaling. One may therefore expect that the scaling properties of the cross sections can be determined experimentally.

There are thus reasons to be optimistic that either scaling will be achieved in these processes or that the scaling limits can be inferred by extrapolation from the behavior of the measured cross sections, so that the desired direct connection can be made with the wavefunction. Although this seems almost certain in the case of DVCS, as mentioned above, there are reasons to be cautious for other DES cross sections. For example, it is generally believed that the pion elastic form factor, which is asymptotically controlled by the upper part of the diagram of Fig. 9, is dominated by long-distance confinement-based physics for $Q^2 < 10$ (GeV/c)^2. We also recall that determining the GPD's will require not only factorization, but also that the new wavefunctions being probed have evolved to their asymptotic form. However, there is some evidence from the decay characteristics of highly excited mesons that the $q\bar{q}$ sea is produced with a very hard spectrum [Ge93], so that the $qqqq\bar{q}$ component of the nucleon wavefunction may evolve much more slowly than the qqq component to its $\beta \to 1$ limit.

In summary, it seems likely that the Upgrade to 12 GeV will access the required conditions for a DVCS program. Whether, in addition, 12 GeV will be sufficient to determine all of the GPD's described here, to get a first glimpse of them, or only to define how the scaling regime is approached, is a question that awaits experiment. At the least, the Upgrade will provide important information necessary to define the energies and luminosities of a future machine required to complete this vital task.

1.A.3 Other New Research Thrusts in the Major CEBAF Campaigns

The 12 GeV Upgrade will make a broad range of profound contributions to the study of nuclear matter beyond the two breakthrough programs described above. Many such examples of programs that the 12 GeV Upgrade will support are described in Chapter 2; they touch all of the research campaigns outlined above. Seven of them are highlighted here.

- *The pion form factor*

The high-Q^2 behavior of elastic and transition form factors probes the high-momentum components of the valence quark wavefunctions of the nuclear building blocks. Of particular interest in this regard is understanding when the dynamics of the valence quarks makes a transition from being dominated by the strong QCD [Cl95a] of confinement to perturbative QCD. This transition should occur first in the simplest systems; in particular, the pion elastic form factor seems the best hope for seeing this transition experimentally. Figure 11 shows how well the proposed 12 GeV Upgrade can explore this transition. Details of how such an experiment would be executed are described in Section 2.B.3.

- *Duality: the transition from a hadronic to a quark-gluon description of DIS*

At high enough energies, asymptotic freedom guarantees that the DIS cross section can be calculated based on nearly free electron-quark scattering as depicted in Fig. 7. However, confinement guarantees that the experimentally observed final-state particles are hadrons. Thus in the scaling region, the equality of these two sets of cross sections is simply the statement that the results associated with Fig. 7 are rigorously proved; *i.e.*, that QCD is the correct theory of the strong interactions. In contrast, as one proceeds to kinematic conditions that are below the Bjorken limit (*e.g.*, Q^2 well below 2 (GeV/c)^2), cross sections calculated assuming factorizing dynamics of the type depicted in Fig. 7 should be expected to fail to reproduce the hadronic cross sections, which when summed give *by definition* the true inclusive cross section. Low-energy quark-hadron duality suggests that hadronic cross sections, when averaged over an appropriate energy range, *nevertheless* coincide with the naïve leading twist quark-gluon calculations. Thus quark-hadron duality *at low energy* naturally examines the transition between strongly interacting matter and perturbative

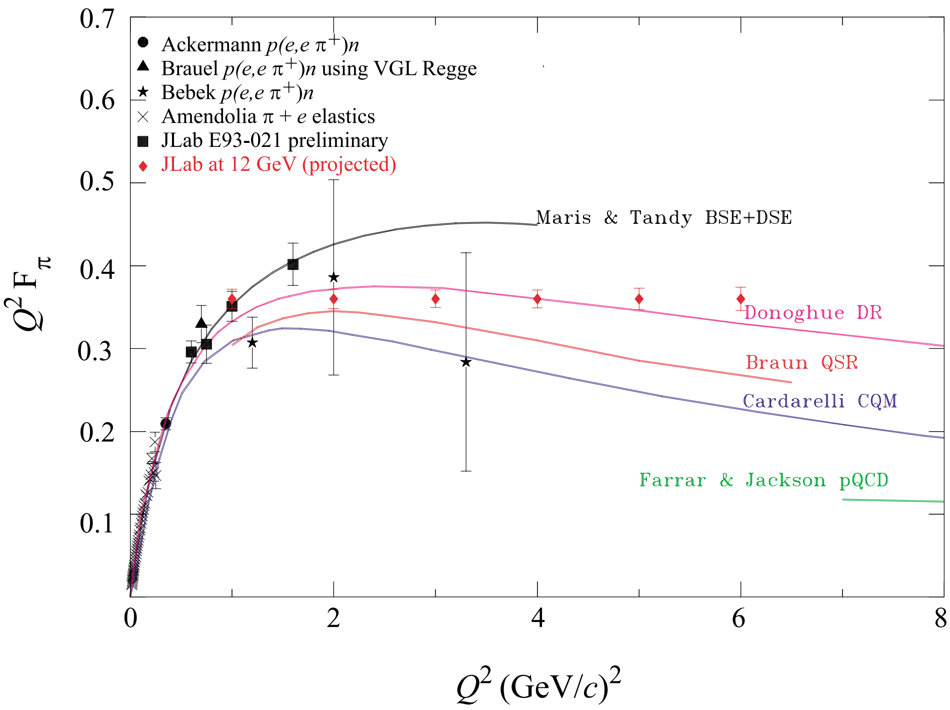

Figure 11: The projected measurements of the pion elastic form factor through the expected transition region from confinement-dominated dynamics to perturbative-dominated dynamics made possible by the proposed 12 GeV Upgrade. Systematic errors are estimated to be comparable to the statistical errors shown for the projected 12 GeV data. Also shown are a few of the dozens of model predictions, all characterized by being confinement-dominated below about 2 (GeV/c)^2 and making a transition to being perturbative-dominated with a value of $Q^2 F_\pi \simeq 0.1$ (GeV/c)^2 in the region of 10 (GeV/c)^2.

QCD. In the circumstances of the 12 GeV Upgrade, both Bjorken scaling and the approach to scaling must arise from very few channels. One may therefore expect that the underlying mechanisms of quark-hadron duality may be determined by utilizing the spin/flavor selectivity of 12 GeV electron scattering in both inclusive and exclusive reactions. The key issues addressed by this program are outlined in Section 2.B.4.

- *Color transparency: The nature of hadronic interactions can be investigated via tests of the prediction of "color transparency"*

Transparency is an unusual QCD effect predicted to have its most counterintuitive manifestation in $(e, e'p)$ at very high energy. Under the right conditions, three quarks, each of which would have interacted very strongly with nuclear matter, pass right through it. This can happen because bound states of three quarks must have zero net color charge by the "nonabelian" nature of charge and confinement in QCD, and they can also be arranged to have small color "dipole moments". While the nucleonic example is more exotic, and such measurements may very well succeed, there is evidence that the electroproduction of vector mesons (where the fact that a quark-antiquark pair has zero net color charge seems much more mundane) may provide a more practical setting for observing this phenomenon. Indeed, the evidence suggests that this reaction may show transparency at much lower Q^2 and ν than quasielastic proton scattering, and that it may have its most pronounced experimental signature in just the energy range of the CEBAF Upgrade. For details, see Section 2.C.2.

- *Learning about the* NN *force by the measurement of the threshold* ψN *cross section and by searching for* ψ*-nucleus bound states*

Threshold ψ photoproduction is a unique process since the small $c\bar{c}$ state will be produced by the interaction of its calculable small color dipole moment with a nucleon (in which it is presumed to *induce* a large, but uncalculable, color dipole moment). This simple color van der Waals–type force is a prototype for a possibly important component of the NN force. It is quite possible that this interaction is sufficiently strong that ψN or ψ-nucleus bound states exist; such relatively long-lived objects might be detected in subthreshold ψ production off nuclei. Based on the same picture, one could also look for ϕN states. Details are presented in Section 2.C.1.

- *Measuring short-range correlations in nuclei*

The higher-energy beams that will be available in Halls A, B, and C will support substantial extensions of CEBAF's current program measuring the high-momentum components of nuclear wavefunctions and investigating short-range nucleon-nucleon correlations. In the rare regions of strong nucleon-nucleon overlap that drive these correlations, instantaneous densities of the order of four times nuclear densities (comparable to those in a neutron star and close to those at which the zero temperature quark-gluon phase transition could occur) are expected. Figure 12 gives an example of a DIS measurement that can be made to study short-range correlations in nuclei. With the variety of measurements that can be made in the three halls, the Upgrade can be expected to fully answer this old question from nuclear many-body theory. See Section 2.D for details.

- *The spectroscopy of* $\mathrm{s\bar{s}}$ *mesons*

Figure 13 shows some of what we know about the spectra of $Q\bar{q}$ mesons for q a light quark and $Q = b, c, s$, and u or d. The rigorous results of Heavy Quark Effective Theory (HQET) should only be applicable for $Q = b, c$, but these data suggest that there is a remarkable similarity between the dynamics of "true" heavy-light systems and those where $Q = s$ or even $Q = u$ or d. It appears that the creation of the constituent quark mass through spontaneous chiral symmetry breaking is enough to boost any quark into the heavy-quark world, at least qualitatively. Figure 14 shows heavy quarkonia ($Q\bar{Q}$ systems) starting from the heaviest $b\bar{b}$ system to the lightest. Once again, even though there is no known rigorous explanation, there seems to be a great similarity between the spectra of the heavy quarkonia (which have a well-understood quark-model-like connection to QCD) and light-quark systems.

These interesting data showing possible relationships between heavy- and light-quark systems exist because nature has presented us with an interesting selection of quark masses. Historically the quarks have been divided into two groups based on their masses: the light-quark (u, d) world (or, by extension, the u, d, s world of SU(3)) and the heavy-quark world. It is ironic that in many critical areas we know much more (both experimentally and theoretically) about the heavy-quark world than we know about our own world. In this respect, these figures strongly suggest that it would be desirable to know much more about $s\bar{s}$ spectroscopy. Given that the photon is $s\bar{s}$ rich, a great deal of data will automatically be available from this sector as part of the planned Hall D program, creating the opportunity to correct this situation.

Mapping out the $s\bar{s}$ spectrum presents some challenges. Given that the intrinsic $s\bar{s}$ content of the proton is expected to be small, photon-initiated $s\bar{s}$ spectroscopy will strongly favor the production of diffractive-type $C = -1$ states. The exception will be channels where OZI-violating t-channel exchanges (like those of the $\eta - \eta'$ system) can occur. These effects will result in an uneven population of the spectrum. The very high data rates anticipated in Hall D should nevertheless lead to a data set of sufficient quality that the weakly excited states will still be identifiable. The possibilities for this program are presented in Section 2.A.6.

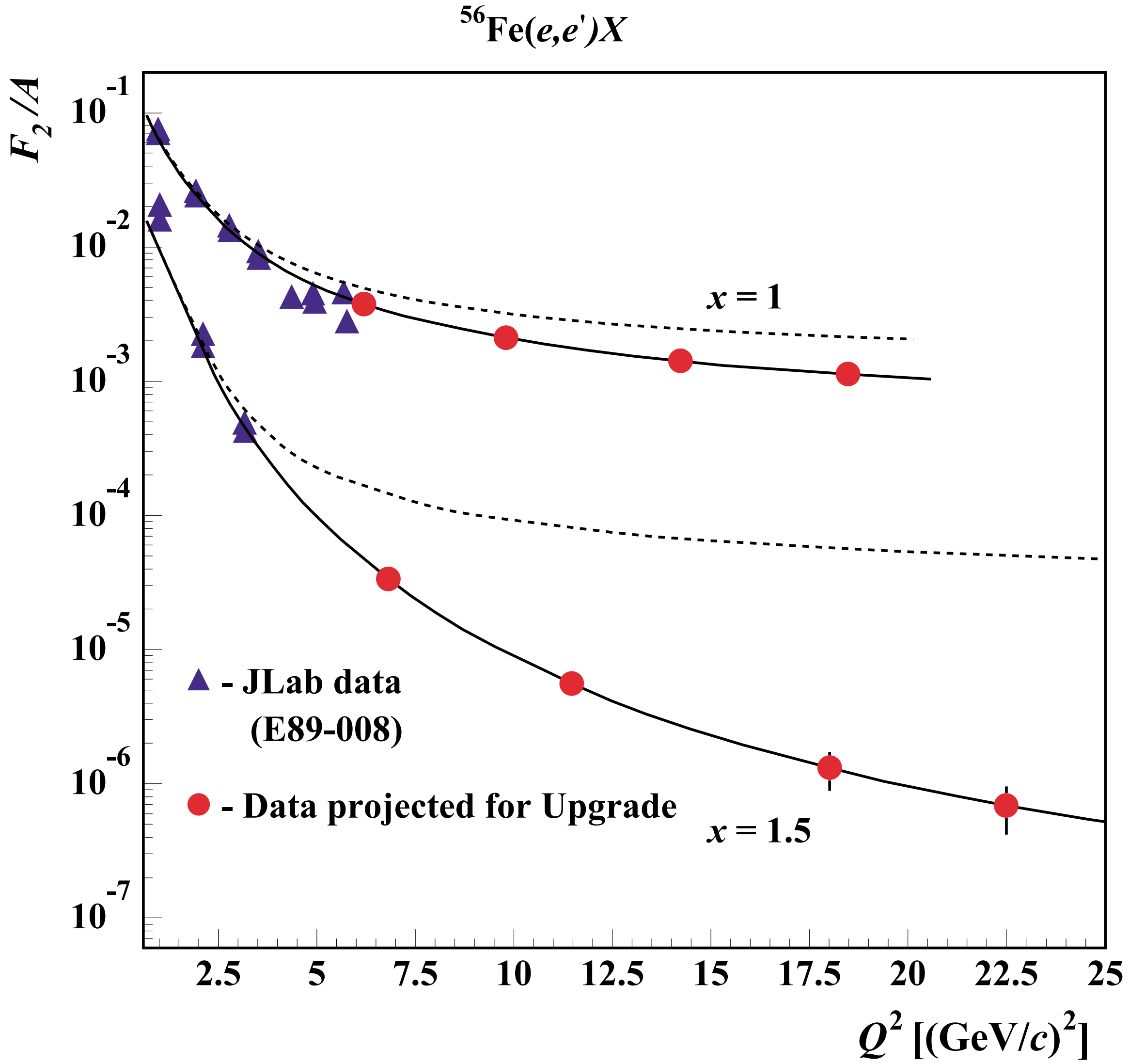

Figure 12: An example of the type of DIS measurement that can be made to study short-range correlations. The experiment is very sensitive to short-range correlations: solid lines are for two-body correlations only, while the dashed line shows the expected full effects of short-range correlations.

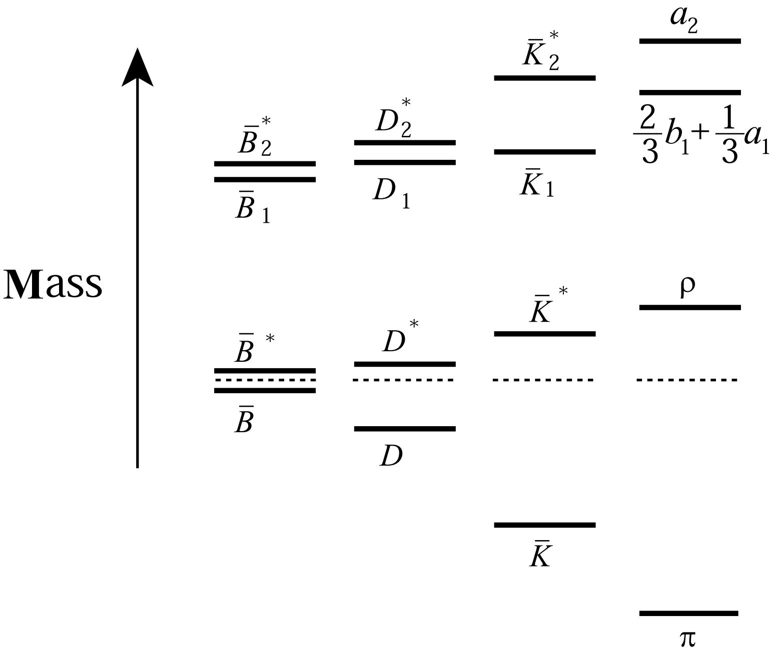

Figure 13: The relative splittings of the $Q\bar{d}$ states are shown to scale from the heaviest to the lightest with the center-of-gravity of the ground state multiplets aligned: $b\bar{d}$, $c\bar{d}$, $s\bar{d}$, and $u\bar{d}$. $\bar{B}^*$ and $\bar{B}$ are the $J^P = 1^-$ and 0^- "ground state" multiplet with light-degrees-of-freedom spin-parity $s_\ell^{\pi_\ell} = \frac{1}{2}^+$, while $\bar{B}_2^*$ and $\bar{B}_1$ with $J^P = 2^+$ and 1^+ are an excited heavy-quark spin multiplet with $s_\ell^{\pi_\ell} = \frac{3}{2}^+$ [Is91].

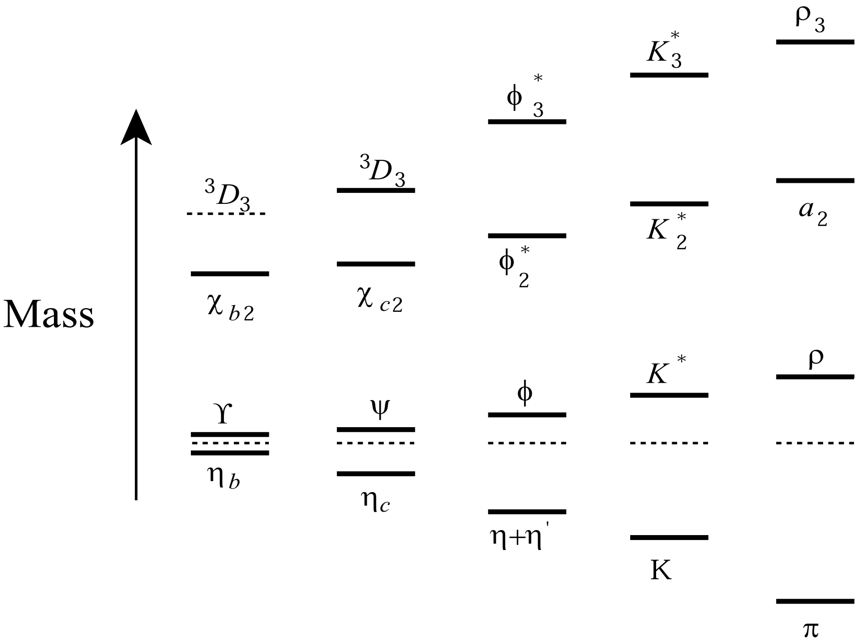

Figure 14: The $Q\bar{Q}$ states from the heaviest to the lightest: $b\bar{b}$, $c\bar{c}$, $s\bar{s}$, $s\bar{d}$, and $u\bar{d}$. Shown are the states in each sector with $J^{PC} = 0^-, 1^-, 2^+$, and 3^-; relative splittings are shown to scale with the center-of-gravity of the "ground states" 0^- and 1^- aligned.

- *Primakoff production of light pseudoscalar mesons*

The existence of the pseudoscalar Goldstone bosons due to spontaneous breaking of chiral symmetry and the profound roles played in QCD by the chiral anomalies responsible for their two-photon decays and for the η' mass are very basic phenomena of QCD. As a result, the system of three neutral pseudoscalar mesons, the π^0, η, and η', contains fundamental information about low-energy QCD, including certain critical low-energy parameters, the effects of SU(3)- and isospin-breaking by the u, d, and s quark masses, and the strengths of the two types of chiral anomalies. The 12 GeV Upgrade will in particular allow a new and in many respects unparalleled series of measurements of the radiative decay widths and transition form factors of these special mesons. In particular, the two-photon decay widths will provide the ultimate tests of the predictions of chiral perturbation theory for these chiral-anomaly-driven processes, and the $\gamma \to \gamma^*$ transition form factors at very small Q^2 will provide a model-independent extraction of the electromagnetic interaction radii of these mesons, answering fundamental questions about the relationship of these Goldstone bosons to QCD's other pseudoscalar mesons (recall Figures 13 and 14).

The Primakoff mechanism of electro- and photo-production of neutral mesons in the Coulomb field of a nucleus, described in Section 2.B.3, provides a powerful tool to measure these fundamental quantities. It is explained there how the 12 GeV Upgrade is required to reach much of the relatively high-mass η and η' part of this experimental program, while other properties can be studied as part of the current 6 GeV program.

1.B Upgrade Project Summary

While this White Paper is focused on a description of the science driving the 12 GeV Upgrade, in order to provide a complete overview, Chapter 3 gives a summary of the laboratory's plans for the accelerator, based on a 25 May 1999 internal JLab report, *Interim Point Design for the CEBAF 12 GeV Upgrade.* Chapter 4 outlines our plans for the new detector and detector upgrade projects necessary to carry out the program.

The key features of CEBAF that make the Upgrade so cost-effective are easily defined. By the summer of 1994, CEBAF had installed what was the world's largest superconducting radio-frequency (SRF) accelerator: an interconnected pair of antiparallel linacs, each comprising 20 cryomodules, with each cryomodule in turn containing eight SRF accelerating cavities. On average, these cavities exceed their design specifications by 50% in the two critical performance measures: accelerating gradient and Q. It is the success of this technology that has opened up the possibility of a relatively simple and inexpensive upgrade of CEBAF's top energy. This technological success would not be so readily multiplied if considerable foresight had not also been exercised in laying out the CEBAF tunnel "footprint", which was designed so that the magnetic arcs could accommodate an electron beam of up to 24 GeV. The latent accelerating power of the installed SRF cavities has already brought CEBAF to 6 GeV, 50% above its design energy, and recent successes in SRF development have led to the production of two cryomodules that are more than a factor of 2 more powerful than the original design. With expected further improvements in SRF technology, with the production of a new, compact cryomodule (that contains higher-performing seven-cell cavities but fits in the same space as the original cryomodules based on five-cell cavities), and with the use of space available in the linac tunnels to install ten new cryomodules, 12 GeV can be attained at a modest cost.

In fact, the accelerator portion of the Upgrade is straightforward. The basic elements can be seen in Fig. 15. The Upgrade utilizes the existing tunnel and does not change the basic layout of the accelerator. There are four main changes: additional acceleration in the linacs, stronger magnets for the recirculation, an upgraded cryoplant, and the addition of a tenth recirculation arc. The extra arc permits an additional "half pass" through the accelerator to reach the required 12 GeV beam energy, followed by beam transport to Hall D that will be added to support the meson spectroscopy initiative. Table 1 presents the key parameters of the upgraded accelerator.

Motivated by the science, the 12 GeV Upgrade derives its name from the fact that it will deliver a 12 GeV electron beam to the new end station, Hall D (where it will be used to produce 9 GeV polarized photons for the new gluonic and $s\bar{s}$ spectroscopies) while sending electrons of 2.2, 4.4, 6.6, 8.8, or 11.0 GeV to the existing Halls A, B, and C. Studies of the existing detectors have led to cost-effective plans for their upgrades. The increased physics power of the present halls comes from the qualitative jump in energy and momentum transfer that the Upgrade brings, and from the enhanced instrumentation capabilities planned for the detector complements in each of them. In describing the physics in Halls A, B, and C in what follows, we will often refer to an 11 GeV electron beam, to be precise about the maximum beam energy available in these halls, but we will use the phrase "12 GeV" to describe the overall energy Upgrade.

In Hall A, the Upgrade will add a large angular- and momentum-acceptance, moderate-resolution magnetic spectrometer (to be called the Medium-Acceptance Device, or MAD) together with a high-resolution electromagnetic calorimeter and a ^{3}H target. The spectrometer will provide a tool for high-luminosity, high-x studies of the properties of nucleons with an 11 GeV beam, and also be used for selected investigations of the GPD's, where high luminosity and good resolution

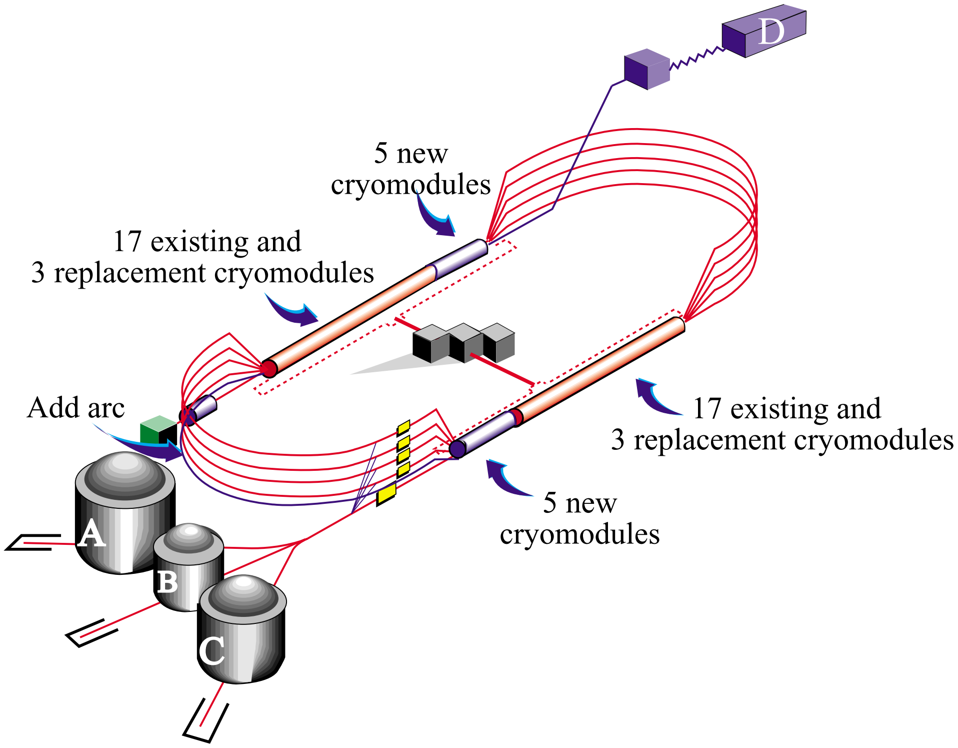

Figure 15: The configuration of the proposed 12 GeV CEBAF Upgrade.

Table 1: Selected key parameters of the CEBAF 12 GeV Upgrade

Parameter	Specification
Number of passes for Hall D	5.5 (add a tenth arc)
Max. energy to Hall D	12.1 GeV (for 9 GeV photons)
Number of passes for Halls A, B, C	5
Max. energy to Halls A, B, C	11.0 GeV
Max. energy gain per pass	2.2 GeV
Range of energy gain per pass	2:1
Duty factor	cw
Max. summed current to Halls A, C* (at full, 5-pass energy)	85 μA
Max. summed current to Halls B, D	5 μA
New cryomodules	10 (5 per linac)
Replacement cryomodules	6 (3 per linac)
Central Helium Liquifier upgrade	10.1 kW (from present 4.8 kW)

*Max. *total* beam power is 1 MW.

are needed. Details are provided in Section 4.B of this White Paper. In Hall B, the CEBAF Large Acceptance Spectrometer (CLAS), which was designed to study multiparticle, exclusive reactions with its combination of large acceptance and moderate momentum resolution, will be upgraded to optimize it for studying exclusive reactions (emphasizing the investigation of the GPD's) at high energy. Most importantly, the maximum luminosity will be upgraded from 10^{34} to 10^{35} cm^{-2} s^{-1}. The present toroidal magnet, time-of-flight counters, Čerenkov detectors, and shower counter will be retained, but the tracking system and other details of the central region of the detector will be changed to match the new physics goals. Details are provided in Section 4.C. In Hall C a new, high-momentum spectrometer (the SHMS, Super-High-Momentum Spectrometer) will be constructed to support high-luminosity experiments detecting reaction products with momenta up to the full 11 GeV beam energy. This feature is essential for studies such as the pion form factor, color transparency, duality, and high-Q^2 N^* form factors. The spectrometer will be usable at very small scattering angles. See Section 4.D for details. Finally, in Hall D, a tagged coherent bremsstrahlung beam and solenoidal detector will be constructed in support of a program of gluonic spectroscopy aimed at testing experimentally our current understanding that quark confinement arises from the formation of QCD flux tubes. This apparatus is described in detail in Section 4.E.

2 THE PHYSICS DRIVING THE UPGRADE OF CEBAF TO 12 GeV

This chapter describes in more detail the powerful physics case behind the push for doubling CEBAF's energy to 12 GeV. The material is organized in terms of the campaigns outlined in Section 1.A.

2.A Campaign 1: Testing the Origin of Quark Confinement

The goal of the Hall D project is the definitive and detailed measurement of the spectrum of exotic hybrid mesons. These first-ever manifestations of the gluonic degrees of freedom in the spectroscopy of hadrons will lead to an understanding of the most novel and spectacular prediction of QCD – confinement. The most fruitful place to search for these mesons is in the light-quark sector, and the optimal probe is the photon, which is expected to be far more effective in uncovering these states than beams of π or K mesons have been.

The power of the photon probe lies in its virtual $q\bar{q}$ structure: the quark spins are aligned as opposed to π or K mesons in which the quark spins are antiparallel. Unfortunately, almost all data on the spectroscopy of mesons below 3 GeV/c^2 come from π and K-induced reactions, central production in p-induced reactions, and $\bar{p}p$ annihilations. Tantalizing indications for gluonic excitations have emerged from these studies, but the evidence is far from solid, and the details needed for a full understanding are missing. The data in hand on the photoproduction of light mesons are sparse indeed, essentially nonexistent. Spectroscopy experiments rely on detecting complicated decays of produced mesons and on the full reconstruction of the reactions in which they are created. Large statistical samples are also required.

Up to now, photon beams of sufficient energy, flux, and other requisite beam characteristics could not be produced. The determination of quantum numbers of mesons is also greatly aided by using photon beams which are linearly polarized. The superb electron beam characteristics (small transverse emittance and energy spread) of the CEBAF accelerator make possible the employment of the coherent bremsstrahlung technique for producing photon beams with a high degree of linear polarization. Hybrid mesons, including those with exotic quantum numbers, are expected to lie in the range from 1.5 to 2.5 GeV/c^2. To reach these masses requires photons in the energy range from 8 to 9 GeV. This is based on the requirement that mesons are produced sufficiently above threshold that line shapes are not distorted. This band of photon energies also allows for a solenoid-only-based detector which, particularly for high-flux photon beams, is optimal in achieving 4π hermeticity.

With an electron beam energy of 12 GeV, photon fluxes of up to 10^8 photons/s with 50% linear polarization in the desired energy range are achievable. Even with initial fluxes of only 10^7 photons/s, the statistical sample collected after the first year of running will exceed those collected with incident hadron beams by at least an order of magnitude. With this sample size collected using a hermetic and well-understood detector, the application of the partial wave analysis (PWA) technique will be able to uncover the exotic states, even if they are produced with cross sections only a few percent of those for conventional mesons. Indeed, theoretical considerations [Af98, Is99b] lead us to believe that the exotic hybrids will be produced with cross sections which are nearly comparable to those of conventional mesons.

In what follows, we will expand on:

1. *The role of glue in QCD.* This will include a discussion of how the gluons form flux tubes, and how their excitations lead to mesons with the gluon degree of freedom excited, in particular exotic hybrids. This general picture is not restricted to a particular model but follows from the first principles of QCD.
2. *The current evidence for gluonic excitations.* The evidence comes from overpopulation of conventional nonets, and from possible glueball and exotic hybrid sightings in $\bar{p}p$ annihilations and π-induced interactions.
3. *Why the light-quark sector is the most fruitful venue for these searches.* We will compare this to searches in the charm or beauty quark sectors, or in e^+e^- annihilations.
4. *Why photons are expected to be particularly effective in producing exotic hybrids.* Its spin structure makes the photon a qualitatively different probe from π and K beams. In addition, there are meager data in hand on the photoproduction of light- quark mesons.
5. *The importance of the PWA technique in uncovering exotic mesons.* The PWA is a powerful analysis tool that has been successfully employed in experiments to uncover states which are not evident from a simple examination of mass spectra – "bump-hunting". The importance of a hermetic detector with excellent resolution and rate capability and sensitivity to a wide variety of decay modes will be explored.
6. *Why linear polarization of the photon beam is important for this search.* Linear polarization aids in determination of the J^{PC} quantum numbers, is essential in determining the production mechanism, and can be used as a filter for exotics once the production mechanism is isolated.

7. *Why the ideal photon energy range is from 8 to 9 GeV.* In order to reach the desired mass range we need to be far enough above threshold to avoid line-shape distortions. We also want to be high enough in energy to kinematically separate the production of baryon resonances from the production of meson resonances. This need for higher photon energies, however, has an upper limit because of additional considerations: the choice of a (simpler) solenoid-only-based detector limits the maximum energy, and the possibility of increased flux and linear polarization (both of which increase as the photon energy is decreased for a fixed available electron energy).

8. *The desired electron energy.* Having established the desired range of photon beam energies, an electron energy of 12 GeV provides sufficient flux and degree of linear polarization.

This then is the overview of the major physics thrust of the Hall D project. In addition to studying hybrid mesons, both with exotic as well as non-exotic quantum numbers, we will have the opportunity to study the $s\bar{s}$ sector as well. Little is known about $s\bar{s}$ mesons. Knowledge about this spectroscopy will allow us to connect from the light-quark (u and d) and the heavy-quark (c and b) sectors. Details are provided in Section 2.A.6 below.

The Hall D collaboration formed to carry out this physics currently consists of about 90 physicists from 27 institutions. The team also includes a contingent of theorists who are working closely with experimenters to focus the physics goals, to develop the analysis formalism and to ensure that the results uncovered by the experiment will be used to achieve the ultimate goal – understanding the confinement mechanism of QCD.

2.A.1 Spectroscopy of Gluonic Excitations

Flux tubes

Quantum chromodynamics (QCD) describes the interactions of quarks and gluons, and along with the electroweak theory they form the successful standard model of particle physics. At short distance scales, where perturbative techniques are applicable, QCD describes high-energy experimental phenomena both qualitatively and quantitatively. QCD is distinct from QED in that the force carriers of the former (gluons) carry color charge whereas for the latter the photons are electrically neutral. The gluonic degrees of freedom are experimentally evident at high momenta and manifested in the observation of gluon jets and the details of their production.

At large distance scales, the situation is far different. Here the successful calculational techniques of the perturbative regime cannot be used. We must rely on first-principles lattice QCD calculations or QCD-inspired models. On the experimental side there is little or no evidence of gluonic degrees of freedom as epitomized in the spectroscopy of hadrons. However, there are many indications that all this is about to change. Developments on the theoretical and experimental fronts give rise to optimism that these gluonic degrees of freedom will be observed, measured, and understood in detail. The prize in understanding these new manifestations of gluonic degrees of freedom (glueballs and hybrid mesons) is grand indeed: an understanding of the confinement mechanism of QCD. The phenomenon of confinement is the most novel and spectacular prediction of QCD – unlike anything seen before.

The development of the flux tube picture of confinement has a long history. It originally emerged in the 1970s when Yoichiro Nambu pointed out that the observation of a linear relationship between the spins of hadrons and the square of their masses could be explained as a consequence of the assumption that the quarks are tied to the ends of a relativistic string with constant mass per length. This assumption also leads to a linearly rising potential between static heavy quarks.

The confinement mechanism is related to the fact that gluons carry the color charge, and becomes evident when we realize that we cannot separate the quarks in a hadron from each other. The field lines of an electric dipole arrange themselves as shown in Fig. 16a. As we separate the two charges, the potential energy falls off like $1/r$ and the force like $1/r^2$. Consider now a quark and antiquark as shown in Fig. 16b. Because of the self-interaction of the gluons the field lines form flux tubes as we increase the separation between the quarks. If we compute the number of field lines intersecting an area perpendicular to the flux tube we notice that this number stays constant as we increase r, suggesting a constant force or linear potential. This leads to confinement since infinite energy is then required to separate the quarks. Recent lattice QCD calculations support the formation of flux tubes as shown in Fig. 17a where the action density (energy density) is plotted for a $q\bar{q}$ pair. The formation of the flux tube is evident. These lattice calculations also show that the potential for the $q\bar{q}$ pair is linear (Fig. 17b) for r greater than about 0.2 fm. Moreover, the energy levels observed for heavy quarkonium are in agreement with a linear potential. Today there is a wide consensus that the Nambu flux tube conjecture was correct and that QCD confines the quarks by flux tube formation.

Conventional mesons

The conventional mesons of the original quark model correspond to the flux tube being in its ground state. The conventional mesons made from the u, d, and s quarks are grouped in

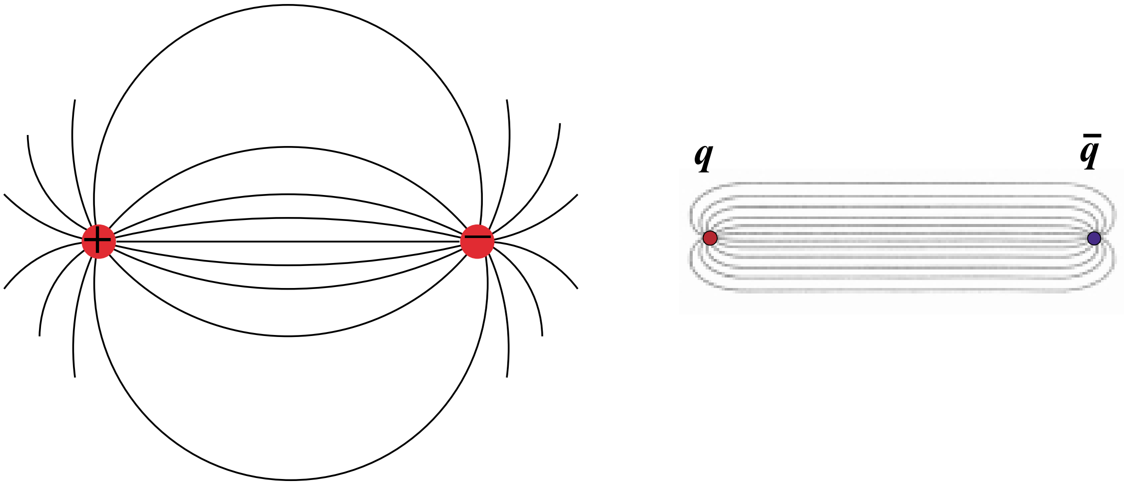

Figure 16: Comparing force field lines for QED and QCD. The field lines for an electric dipole (left); and the color field lines for a quark and antiquark (right).

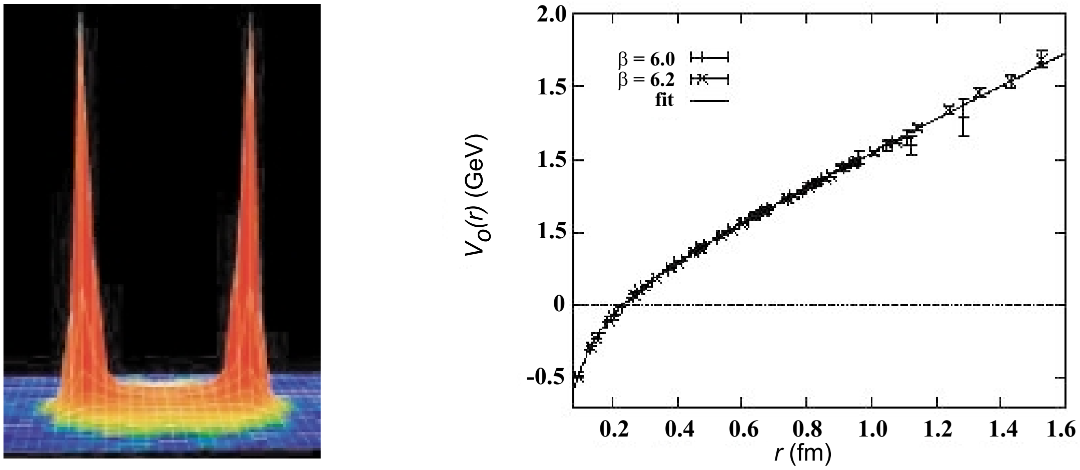

Figure 17: Evidence for flux tubes and linear potentials from lattice QCD. The action density (energy density) in the space surrounding a quark and antiquark (left) [Ba00]; and the inter-quark potential (right) [Ba97].

nonets, each characterized by a given J^{PC} determined by the relative orientation of the spins of the quarks and their orbital angular momentum. The rules for allowed values of J^{PC} follow from the requirements of a fermion-antifermion system: the quark spins can be parallel ($S = 1$) or antiparallel ($S = 0$) with relative orbital angular momentum (L), $\vec{J} = \vec{L} + \vec{S}$, $P = (-1)^{L+1}$ and $C = (-1)^{L+S}$. For these $q\bar{q}$ systems J^{PC} combinations of 0^{--}, 0^{+-}, 1^{-+}, 2^{+-}, ... are not allowed and are referred to as *exotic* quantum numbers. The range of masses of established conventional meson nonets and their radial excitations extend from the π mass up to about 2.5 GeV/c^2.

Mesons and gluonic excitations

Mesons can also be generated when the flux tube or string is *plucked* or excited. The two degenerate first excited states of the string are the two longest-wavelength vibrational modes of this system, and π/r is their excitation energy since both the mass and the tension of this "relativistic string" arise from the energy stored in its color force fields. (This low-lying gluonic spectrum is model-independent for $m \to \infty$.) The vibrational quantum numbers of the string, when added to those of the quarks, can produce mesons with exotic J^{PC} – *exotic hybrids* – hybrids because the mesons manifest both their quark and gluonic content. Because the gluons carry color charge it is also possible to form bound states of glue with no quarks present. Such mesons are called *glueballs.* Figure 18 shows a level diagram giving the range of masses for the conventional $q\bar{q}$ nonets and estimates of the masses of the lightest glueballs and hybrids, and thresholds for possible nearby associated molecular meson-meson bound states.

Focusing on light-quark exotic hybrids

The focus of the Hall D project is in the light-quark hybrid sector. The initial benchmark states will be the exotic hybrids, which cannot mix with $q\bar{q}$ and which therefore have a *smoking gun* signature. Although there is strong circumstantial evidence for glueballs, the possibility of mixing with $q\bar{q}$ complicates their discovery. Lattice QCD predictions about heavy-quark exotic hybrids are at least as reliable as for the light-quark hybrids but the experimental situation is far more problematic. The production cross sections are a few orders of magnitude lower. At the higher energies needed to produce these more massive states many other uninteresting processes can contribute to background. Also, these more massive states have many more decay channels available, decreasing the yield for any one particular mode to be studied. Finally, to unambiguously tag a charm or beauty hybrid one must identify detached vertices, further complicating the experimental setup. Another venue for exotic vector hybrids is production in e^+e^- collisions, but this production is suppressed by an angular momentum barrier (the excited flux tube carries $J = 1$).

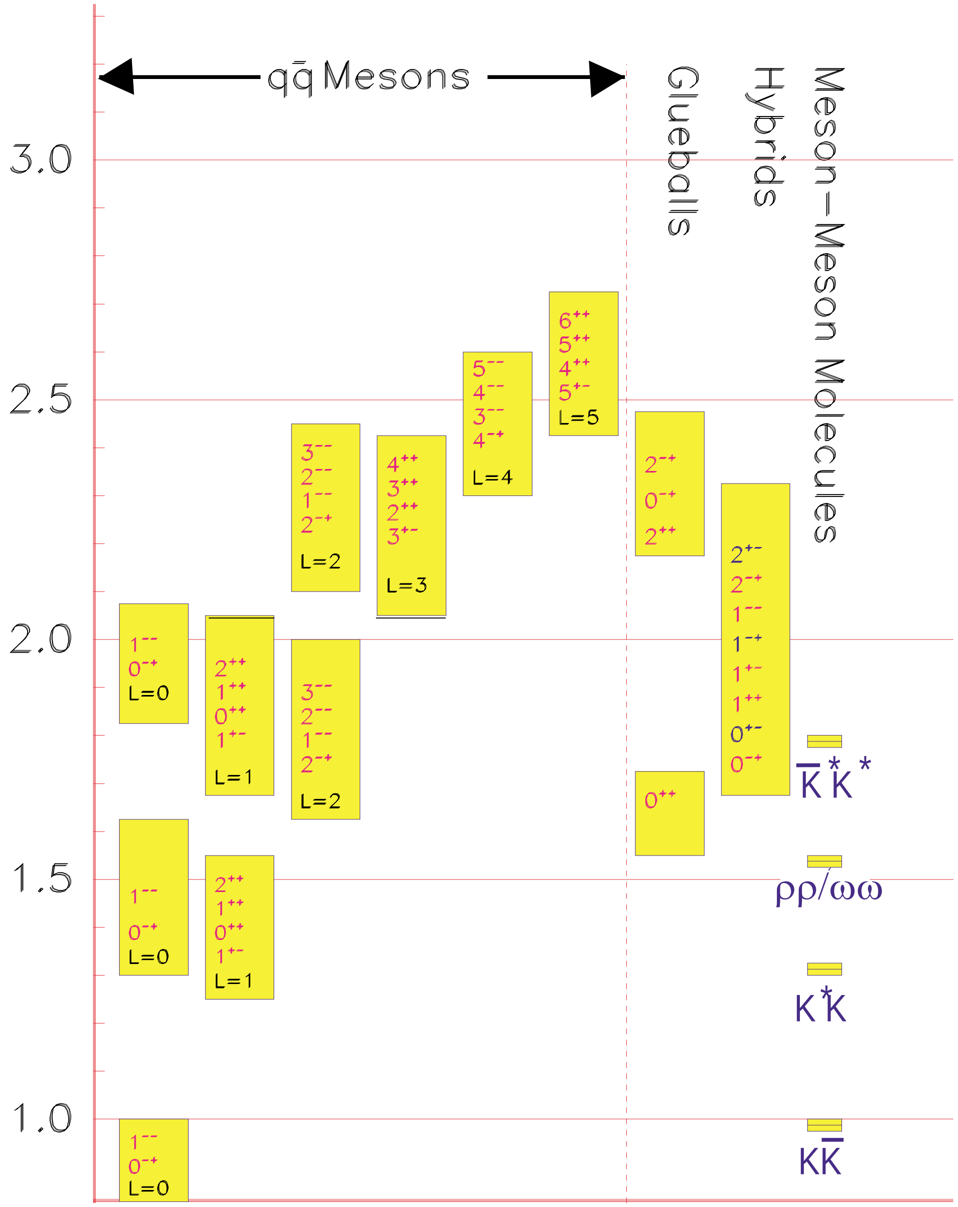

Figure 18: A level diagram showing conventional nonets and expected masses of glueballs, hybrids and molecular thresholds. The vertical axis is in units of GeV/c^2. For the $q\bar{q}$ boxes the L refers to the angular momentum between the quarks and each J^{PC} refers to a nonet of mesons.

From every point of view, photoproduction of light-quark hybrids is expected to be our best handle for providing the information we need to understand confinement.

Observation of gluonic excitations

Lattice QCD and flux tube model calculations are in agreement that the masses of light-quark hybrids range from 1.5 to 2.5 GeV/c^2 with the lightest exotic hybrid ($J^{PC} = 1^{-+}$) having a mass about 2 GeV/c^2 [Be97, Ju97]. After about 15 years of searching we have in hand two candidates for exotic hybrids. The first has a mass of 1.4 GeV/c^2 decaying into $\eta\pi^-$ [Th97, Ab98] – the evidence for this state is not without controversy. The second, perhaps a more firmly established state, is at 1.6 GeV/c^2 and decays into $\rho^0\pi^-$ [Ad98]. Both have the assignment: $J^{PC} = 1^{-+}$. These states were reported by the E852 collaboration which studied $\pi^- p$ interactions using the AGS at Brookhaven National Laboratory. Both states have also been independently confirmed. It is noteworthy that the two candidates have masses below the expectations from lattice QCD and the flux tube model for the lightest exotic hybrid [Ba95]. In addition, the decay modes observed are not those favored by the flux tube model. In this model, the exotic hybrid's favored decay mode is into $S + P$ where S indicates a conventional $q\bar{q}$ meson with $L = 0$ while P indicates a conventional $q\bar{q}$ meson with $L = 1$. This comes about from how the exotic hybrid gives up its spin to the decay daughters, and possibly explains why exotic hybrids have not yet been observed – the decay modes are complicated. A favored mode, for example, would be into $b_1\pi \to \omega 2\pi \to 5\pi$.

Lattice QCD calculations indicate that the lightest glueball is a scalar with a mass in the range from 1.5 to 1.7 GeV/c^2 [Mo97, Ba93, Se95, Ba97]. Indeed there is evidence from the Crystal Barrel experiment, which studied $\bar{p}p$ annihilations at CERN, that the $f_0(1500)$ is a leading candidate for a glueball [Am95, Am96]. There are, however, indications that this state is not a pure glueball but has some mixing with conventional $q\bar{q}$ [Cl00]. There are strong indications that the scalar meson sector contains one or more glueballs since there are several more states observed than can be accommodated in the simple $q\bar{q}$ model. However, the unique identification of a glueball is exacerbated by the possibility of mixing with $q\bar{q}$. Lattice QCD indicates a rich spectrum of glueballs, all with non-exotic quantum numbers, from 1.5 to 2.5 GeV/c^2. The lightest glueball with exotic quantum numbers is predicted to have $J^{PC} = 2^{+-}$ and to have a mass of 4 GeV/c^2 [Mo97].

This then is the tantalizing evidence in hand for gluonic excitations. In the case of the exotic hybrids, the range of masses of putative states observed is significantly lower than expectations, and the observed modes of decay are not those expected to be favored [Is85, Ba95]. Lattice QCD calculations are being refined, and significant progress on reducing the theoretical errors on masses and more information on decay modes is expected in the next five years as computational techniques improve and computer power keeps increasing. Flux tube model calculations are in hand for both masses and decay modes [Is85, Cl95, Ba95, Ca91]. Given the state of current observations, with their uncertainties and limitations, the flux tube model has not been ruled out. Clearly more data are needed. As will be shown below, photoproduction reactions are expected to be a rich source of hybrids – exotic and non-exotic. Once these states are discovered and mapped out, we will have the data needed to constrain our theoretical understanding of the details of confinement. Without more data, there will be little progress.

2.A.2 Photoproduction of Gluonic Excitations

The photon is expected to be particularly effective in producing a *smoking gun* signature for gluonic excitations: hybrids with exotic J^{PC}. In this regard, we will compare the effectiveness of the π or K as a probe with that of the photon. In the former case, the meson is a $q\bar{q}$ with spins anti-aligned ($S = 0$), and in the latter, the photon is a virtual $q\bar{q}$ with spins aligned ($S = 1$). In both cases, the relative orbital angular momentum is zero ($L = 0$) and the flux tube connecting the quarks is in its ground state. Exotic quantum numbers can also be produced by non-$q\bar{q}$ objects, such as meson-meson molecules, but these states are expected to have very different flavor systematics and production t-dependence than the J^{PC} exotics.

Consider what happens when the beam probe approaches a target proton and scatters. A possible outcome is a transfer of energy that excites the flux tube to its lowest excited state. Lattice QCD and flux tube models both indicate that the lowest excited flux tube has $J = 1$ [Be97, Is85, La97]. The flux tube, or string, can be spinning clockwise or counter-clockwise around the $q\bar{q}$ line leading to two degenerate states – degenerate since the energy should not depend on which way the flux tube is spinning. The states that are linear combinations of these two rotations are eigenstates of parity and charge conjugation leading to two possibilities for the excited flux tube: $J^{PC} = 1^{-+}$ or $J^{PC} = 1^{+-}$. Suppose we start with the $q\bar{q}$ in the $S = 0$ and $L = 0$ (or $J^{PC} = 0^{-+}$ – the π or K) configuration. Combining this with $J^{PC} = 1^{-+}$ or $J^{PC} = 1^{+-}$ of the excited flux tube results in hybrid mesons with $J^{PC} = 1^{++}$ or $J^{PC} = 1^{--}$. These are non-exotic. If, however, we start with $q\bar{q}$ in the $S = 1$ and $L = 0$ (or $J^{PC} = 1^{--}$ – the vector photon) configuration, the resulting hybrid can have $J^{PC} = [0, 1, 2]^{+-}$ for the flux tube with $J^{PC} = 1^{-+}$ and $J^{PC} = [0, 1, 2]^{-+}$ for the flux tube with $J^{PC} = 1^{+-}$. So we see that in the case of the vector probe, the resulting hybrids can have six possible J^{PC} of which half are exotic combinations whereas, for π or K probes, no exotic combinations are generated.

In the next section, we will discuss how the technique of PWA will be used to extract information about the spin and parity of produced states. In a photon beam this process is greatly aided by using photons that are linearly polarized. Linear polarization will be provided using the technique of tagged, coherent bremsstrahlung off a crystal radiator. The details of how this photon beam will be produced are discussed later in this White Paper (see Section 4.E.2).

2.A.3 Partial Wave Analysis and Photon Polarization

Kinematics

The technique used for identifying meson states (their masses, widths and J^{PC}) is partial wave analysis. Consider a specific exclusive process:

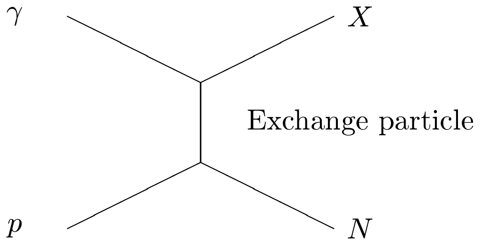

$$\gamma p \to X p$$

$$s = (p_\gamma + p_p)^2$$
$$t = (p_\gamma - p_X)^2$$

The center-of-mass energy squared, s, and the momentum-transfer-squared, t, between the incoming beam and outgoing X are defined in terms of the four-vectors of the particles as above. The behavior of the cross section with s and t depends on the production mechanism, which is usually described in terms of the particle or particles which can be exchanged as shown above. For example, if the exchange particle is a pomeron (diffractive process) the cross section is nearly constant in s. For meson-exchange processes, cross sections typically fall off as $1/s^2$. The dependence on t is typically exponential:

$$\frac{dN}{dt} \propto e^{-\alpha|t|}, \tag{1}$$

with $\alpha \simeq 6 - 8$ GeV^{-2}. For the process above, at high enough photon beam energy, E_γ, we can make the approximation $s \approx 2 \cdot E_\gamma^{m_X}$. For fixed s, and mass of X, m_X, there is a minimum value of $|t|$, or $|t|_{\mathrm{min}}$, needed to produce X. This $|t|_{\mathrm{min}}$ increases with increasing m_X for fixed E_γ, and decreases with increasing E_γ for fixed m_X. Coupled with the steep dependence implied in equation (1), the dependence of $|t|_{\mathrm{min}}$ on m_X will affect event yields. In addition, the line shape of a resonance can be distorted if the variation of $|t|_{\mathrm{min}}$ across the width of a resonance is too rapid.

Partial wave analysis goals

The goal of the PWA is to extract information about the line shape of a resonance with mass m_X and to determine the production mechanism and decay modes as well. This necessitates doing the PWA in fine enough bins in mass and $|t|$. Our criteria are to do the PWA in mass bins of 10 MeV/c^2, with roughly ten equally populated bins in $|t|$. With the statistical sample expected after one year of running with 10^7 photons/s, the statistical error in the central peak of an exotic meson for a given bin in $|t|$ will be of order 3%, assuming the exotic is produced with a 5% probability relative to conventional mesons.

It is important to stress here that the detector design focuses on hermeticity and resolution to ensure nearly uniform coverage with well-understood acceptance functions for various decay angles. Kinematic fitting will also be used to identify exclusive processes. The design focuses on the requirements of the PWA. The existence of well-established resonances will be used as benchmarks for the PWA. They also provide benchmarks for the phase variation of candidate exotic states. Furthermore, candidate exotics can appear with multiple decay modes which should give consistent results; *i.e.*, $b_1\pi$ and $f_1\eta$. In addition, the same decay mode, such as $\eta\pi$, should be observed in several channels where $\eta \rightarrow \pi^+\pi^-\pi^0$, $\eta \rightarrow 3\pi^0$, and $\eta \rightarrow 2\gamma$. Each of these modes leads to different acceptances and systematics, providing a powerful check on the PWA results.

This is all nicely illustrated by the PWA performed by the E852 collaboration, which reported the 1^{-+} $\rho^0\pi^-$ exotic state in the reaction $\pi^- p \rightarrow \pi^+\pi^-\pi^- p$ at a beam momentum of 18 GeV/c [Ad98]. In Fig. 19, the acceptance-corrected (average acceptance was 25%) distributions of the $\pi^+\pi^-\pi^-$ and $\pi^+\pi^-$ effective masses are shown. The positions of well-established meson states are shown, even though the $a_1(1260)$, for example, does not show up prominently. The PWA assumes a parent decaying into a $\pi\pi$ state and an unpaired π followed by the decay of the $\pi\pi$ state. The resulting decomposition into various waves is shown in Fig. 20. The decomposition now clearly shows the $\pi(1800)$ in the 0^{-+} wave, the $a_1(1260)$ in the 1^{++} wave, the $\pi_2(1670)$ in the 2^{-+} wave, and the $a_2(1320)$ in the 2^{++} wave. Evidence for the exotic 1^{-+} $\rho\pi$ is shown in Fig. 19c and d. Also shown in this figure is the effect of leakage of non-exotic waves. Finally in Fig. 20 a coupled fit to the wave intensities and phase difference between the 1^{-+} and 2^{-+} waves is shown.

We point out here that impressive as these data are, the statistics expected for Hall D will far exceed those of the E852 experiment, and the detector will be far better designed and understood since this project is focused on optimizing the design for this sort of analysis. A test partial wave fit using simulated data and the Hall D Monte Carlo is discussed within the context of the Hall D detector (Section 4E). The ability to do a good partial wave analysis is a critical part of the design

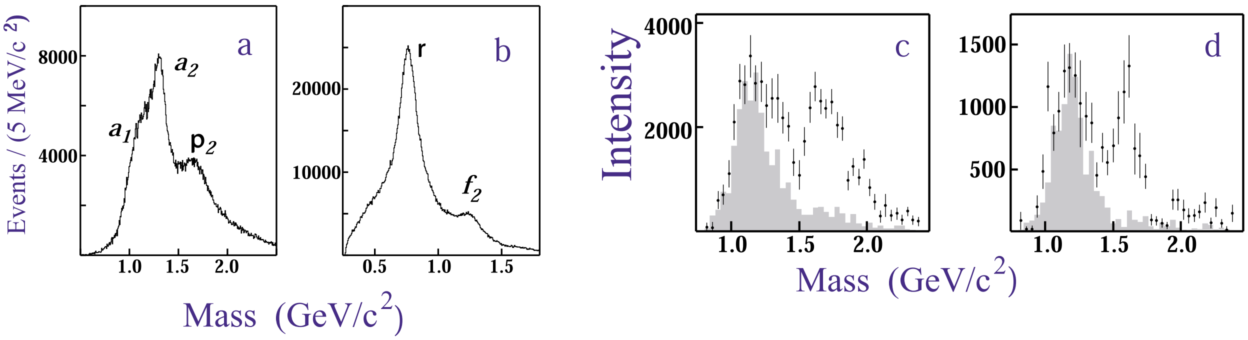

Figure 19: E852 results: acceptance corrected effective mass distributions for the $\pi^+\pi^-\pi^-$ combination (**a**) and the $\pi^+\pi^-$ combination (**b**) (two entries per event). (**c**) and (**d**) show the intensities for the waves corresponding to 1^{-+} into $\rho\pi$, where the two figures correspond to different naturalities of the exchanged particle. The shaded distributions are an estimate of leakage due to non-exotic waves.

of the Hall D detector. A discussion of the PWA technique for specific processes within the context of the Hall D detector is included in the discussion of the apparatus and its design criteria.

Linear and circular polarization

We start with a review of the relationship between linear and circular polarization. A right-handed, circularly polarized photon ($|R\rangle$) has $m = 1$ while for the complementary, left-handed $|L\rangle$ photon $m = -1$. These are related to the linear polarization states, $|x\rangle$ (in production plane) and $|y\rangle$ (perpendicular to production plane) by:

$$|x\rangle = \frac{1}{\sqrt{2}}\left(|R\rangle + |L\rangle\right) \tag{2}$$

$$|y\rangle = \frac{-i}{\sqrt{2}}\left(|R\rangle - |L\rangle\right) \tag{3}$$

We will use these relations in several straightforward cases to show how linear polarization:

1. can provide information on decays in lieu of statistics,
2. is essential in isolating production mechanisms, and
3. can be used as an exotics filter if the production mechanism is known.

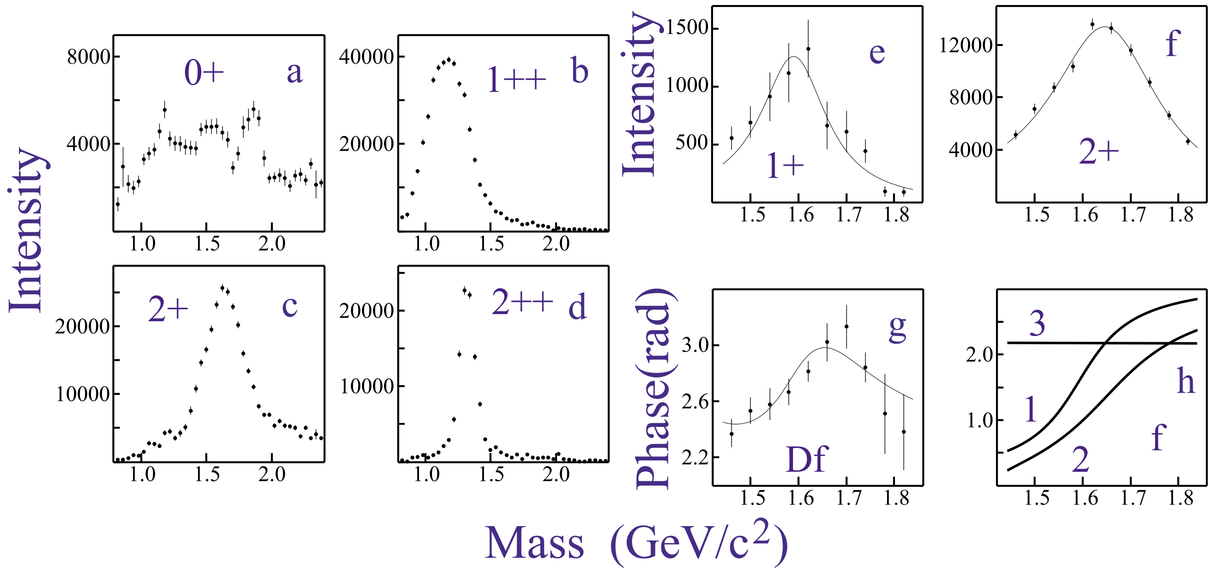

Figure 20: E852 results: the combined intensities for all fit waves. (**a**) is 0^{-+}; (**b**) is 1^{++}; (**c**) is 2^{-+}; and (**d**) is 2^{++}. Figures (**e**) and (**f**) show results for the intensities of a coupled mass-dependent Breit-Wigner fit of the 1^{-+} and 2^{-+} wave. (**g**) shows the phase difference between the two waves, and (**h**) shows the individual phases: 1 is the 1^{-+} wave, 2 is the 2^{-+} wave, and 3 is the background phase.

Linear polarization and statistics

To illustrate how linear polarization provides useful information in the PWA, consider the case of the photoproduction of a vector meson which subsequently decays into two pseudoscalar mesons. Possible examples are $\rho \to \pi\pi$ or $\phi \to K\bar{K}$. Suppose the production mechanism produces the vector meson with the same helicity as the incident photon (or s-channel helicity conservation). In the rest frame of the vector the two-pseudoscalar wavefunction is described by $Y_1^m(\theta, \phi) \propto \sin\theta e^{im\phi}$.

For circularly polarized photons (either $m = 1$ or $m = -1$) the square of this amplitude carries no ϕ information, while for in-plane photons there is a $\cos^2\phi$ dependence and out-of-plane a $\sin^2\phi$ dependence in the decay angular distribution since in these cases we have the sum or difference of Y_1^{+1} and Y_1^{-1} according to equations (2) and (3). Although not essential in determining spin, a gain of statistics is needed to recover a drop in the degree of linear polarization. Indeed our Monte Carlo simulation studies indicate that the increase in statistics necessary for a fixed accuracy in the analysis is proportional to the decrease in polarization.

Linear polarization and the production mechanism

This is best illustrated by considering a specific example. Suppose we produce a vector particle ($J^P = 1^-$) by the exchange of a scalar particle ($J^P = 0^+$, corresponding to natural parity exchange) or a pseudoscalar particle ($J^P = 0^-$, corresponding to unnatural parity exchange). We wish to determine whether the vector is produced by natural (amplitude A_N) or unnatural (amplitude A_U) parity exchange. In the center-of-mass of the produced vector particle, the momentum vectors of the beam photon and exchange particle are collinear. For circularly polarized photons, the m of the vector is the same as that of the photon. From parity conservation, the orbital angular momentum between the photon and exchange particle is $L = 0$ or $L = 2$ for natural parity exchange and $L = 1$ for unnatural parity exchange. So for circularly polarized photons, with $m = +1$, the total amplitude is $A_N + A_U$ whereas for $m = -1$, the total amplitude is $A_N - A_U$. This follows simply from the addition of angular momenta. Circularly polarized photons allow us to measure only the sum or difference of the two exchange amplitudes. If however, we have linearly polarized photons along the x-direction, we extract A_N using equation (2) and for polarization along the y-direction, we extract A_U using equation (3).

Linear polarization as an exotics filter

Using arguments similar to those above, it has been shown that linear polarization can be used as a tool to filter exotics. For example, a $\rho\pi$ system with $I = 1$ has $C = +$. Suppose that one can determine the naturality of the exchange particle by selecting data within a range of $|t|$. For a produced $C = +$ particle with spin 1 we can have natural parity ($J^{PC} = 1^{-+}$ – exotic) or unnatural parity ($J^{PC} = 1^{++}$ – non-exotic). In the case of natural parity exchange the in-plane polarization selects the $J^{PC} = 1^{-+}$ wave while out-of-plane polarization selects $J^{PC} = 1^{++}$. For unnatural parity exchange the reverse is true. Note that in this case we are specifying the naturality of the exchange and using linear polarization to select the naturality of the produced particle. In the previous section, we specified the naturality of the produced particle and used linear polarization to select the naturality of the exchanged particle.

2.A.4 The Optimal Photon and Electron Energies

What is the optimal photon beam energy to reach the Hall D physics goals? The goal of this experiment is to search for mesons in the mass range from 1 to 2.5 GeV/c^2. An incident photon energy of just under 8 GeV is sufficient to produce a meson of mass 3 GeV/c^2. We also want to produce mesons with sufficient yield. The yield is determined by the value of $|t|_{\text{min}}$ and the exponentially falling distribution in $|t|$, as discussed in the previous section. The relative yield for a slope parameter of $\alpha = 8$ (GeV/c)$^{-2}$ is shown in Fig. 21a. Another consideration is the ability to kinematically separate meson resonance production from baryon resonance production. As an example, we considered various reactions leading to a final state: $\pi^+\pi^-\pi^+n$. We enumerate the possibilities:

$$\gamma p \rightarrow X^+n \rightarrow \rho^0\pi^+n \rightarrow \pi^+\pi^-\pi^+n \tag{4}$$

$$\gamma p \rightarrow \rho^0\Delta^+ \rightarrow \rho^0\pi^+n \rightarrow \pi^+\pi^-\pi^+n \tag{5}$$

$$\gamma p \rightarrow \pi^+\Delta^{*0} \rightarrow \pi^+\pi^-\pi^+n \tag{6}$$

The first of these is the reaction of interest. We can reduce the other two by requiring that the effective mass of any πn or $\pi\pi n$ combination be outside the baryon resonance region (greater than 1.7 GeV/c^2 for this exercise). The fraction of events for which we are able to use kinematics to remove the offending reaction is shown in Fig. 21b as a function of beam momentum and for various m_X masses.

Whereas the considerations mentioned thus far favor higher photon beam energies, other considerations favor a lower photon beam energy. For the tagged and collimated coherent photon beam the variation in flux, for constant total hadronic rate in the detector, is plotted in Fig. 22a as a function of photon beam energy for three different values of electron energy. In Fig. 22b the degree

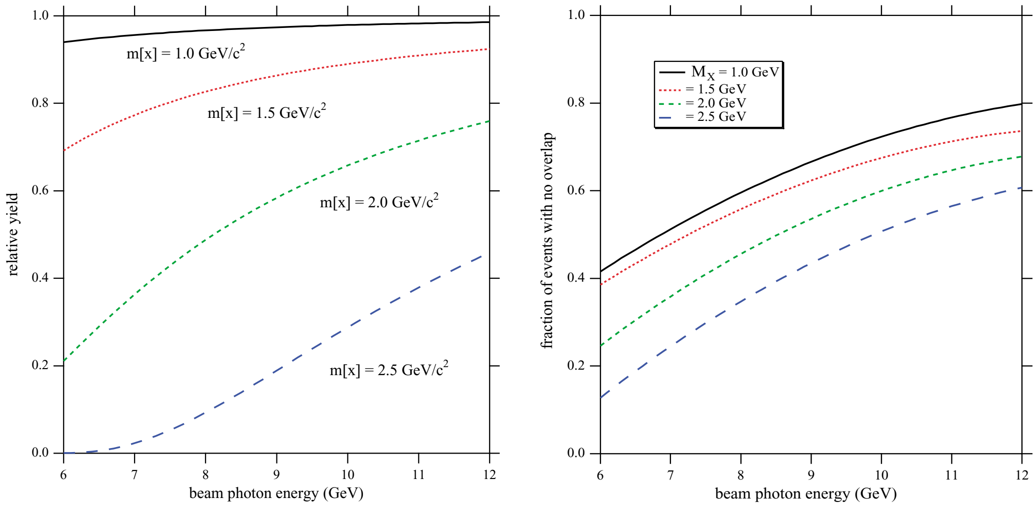

Figure 21: Various figures of merit to choose the optimal photon beam energy: (**a**) the relative meson yield as a function of photon beam energy for various meson masses (left); and (**b**) the fraction of events in which meson and baryon resonances are separated as a function of photon beam energy for various meson masses (right).

of linear polarization is plotted as a function of photon beam energy for three different values for the electron energy as well.

Finally, in Fig. 23 we plot an overall figure of merit that folds together the variation of beam flux and the degree of linear polarization with beam energy and with the effective yield (taking into account $|t|_{\text{min}}$ effects and the ability to kinematically separate meson resonances from baryon resonances).

From this and other considerations we conclude that the optimum photon beam energy is between 8 and 9 GeV. The other considerations include the facts that for beam energies significantly below 8 GeV the line shape for resonances at the upper end of our mass range of interest is severely distorted, and for beam energies above 9 GeV, the momentum resolution for charged particles from two-particle decays of mesons at the lower end of our meson mass range is degraded since the transverse momentum of the decay products is small.

Taking all of these considerations into account, we find a clear *sweet spot* for the photon beam energy – 8 to 9 GeV . Of equal importance is that it is clearly desirable to have an electron energy as close as possible to the maximum energy achievable with the proposed Upgrade. The plots of Fig. 22 show the price of dropping this electron energy in terms of flux and polarization.

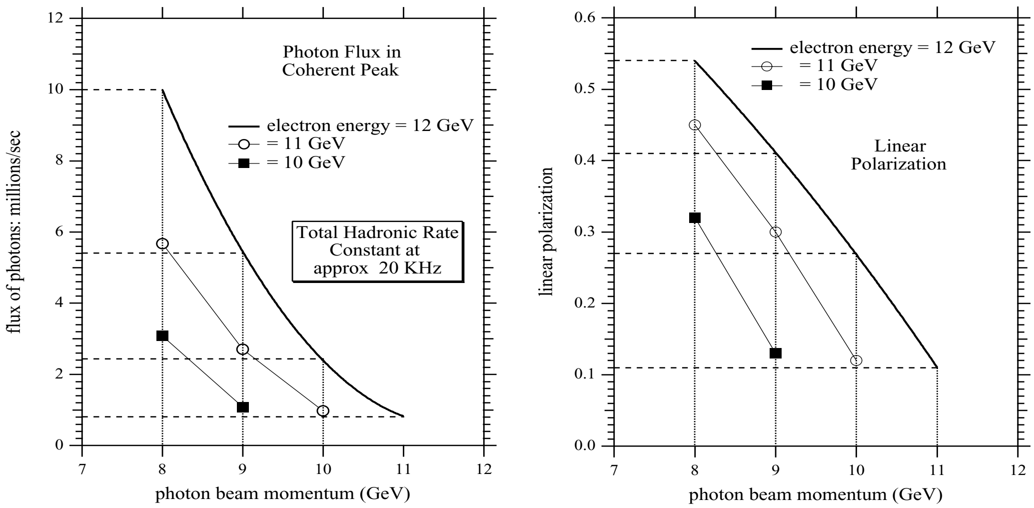

Figure 22: Photon beam flux and degree of linear polarization for various values of electron energy: (**a**) the flux dependence on photon beam energy (left); and (**b**) the degree of linear polarization dependence on photon beam energy (right).

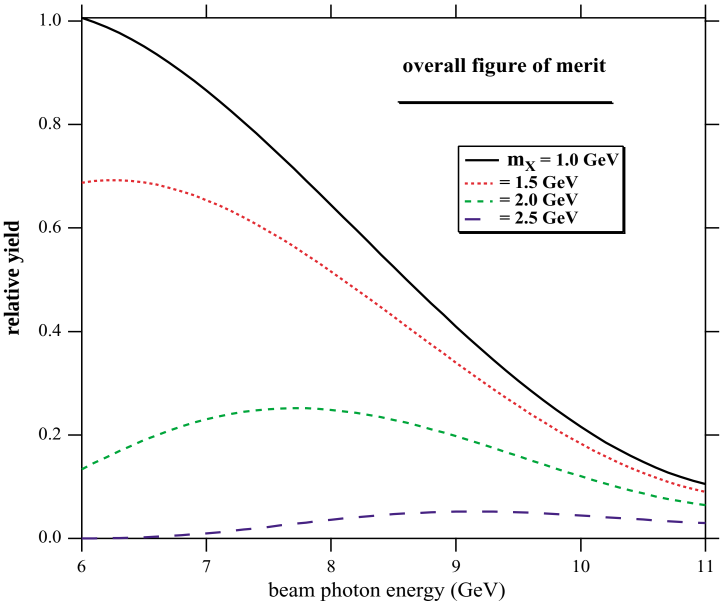

Figure 23: Figure of merit: relative meson yield as a function of photon beam energy for various meson masses and a fixed incident electron beam energy of 12 GeV.

2.A.5 External Review of the Hall D Project

The details of the civil construction, beam, detector, rates, and analysis will be presented in a later chapter of this White Paper. We point out here that a committee chaired by David Cassel (Cornell) and consisting of Frank Close (Rutherford Laboratory), John Domingo (Jefferson Lab), William Dunwoodie (SLAC), Donald Geesaman (Argonne), David Hitlin (Caltech), Martin Olsson (Wisconsin), and Glenn Young (Oak Ridge) reviewed the project plans in December 1999. The committee was asked to address three principal questions, whose answers were to be based on the answers to more detailed questions. The questions cover both the physics and the experimental technique [Ca00].

The physics motivation was described above and the technique, including the beam and detector, are discussed in greater detail in the discussion of Hall D. However, in order to provide some background to the review report summary below, we briefly point out the following about the beam and detector. The coherent bremsstrahlung technique involves passing a fine electron beam from the CEBAF accelerator though a wafer-thin diamond crystal: at special settings for the orientation of the crystal, the atoms of the crystal can be made to recoil together from the radiating electron, leading to the emission, at particular photon energies, of linearly polarized photons.

The use of a solenoidal spectrometer allows for the measurement of charged particles with excellent efficiency and momentum resolution while, at the same time, containing the shower of unwanted electron-positron pairs associated with the photon beam. One of the two largest components of the detector is the superconducting solenoid that was originally used in the LASS experiment at SLAC and later moved to LANL for the MEGA experiment. The other is the 3000-element lead glass detector originally built for the E852 experiment, which used the MPS at the Brookhaven AGS. Both components are available for use in Hall D, and their availability reduces the cost of the Hall D experimental apparatus by about $10M.

Review report summary

The questions posed to the review committee and their answers or conclusions were:

1. Evaluate the scientific opportunities presented by the Hall D project.

> *This collaboration proposes to explore systematically the light mesons (with masses up to about 2.5 GeV/c^2) with capabilities far beyond those of previous experiments. The copious spin and flavor initial states produced by photon beams will be an extremely*

useful tool in this endeavor. Thorough study of the masses, spins, parities, and charge conjugation states of these light mesons will require a complete partial wave analysis. This will provide a much deeper understanding of quark-antiquark states, and will as well permit a definitive search for mesons with exotic quantum numbers, particularly hybrid states and glueballs. This search is very high-priority physics, since the states involving excited glue, as well as quarkless glueball states, must exist if QCD is the correct theory of the strong interactions. JLab is unique in being able to provide the high-quality, low-emittance, cw photon beams that are required for this experiment. In addition, JLab and a significant segment of the JLab physics community are committed to this physics program. Together these provide a unique opportunity for exploring light meson states and making definitive searches for exotic states in this mass region.

2. Review the collaboration's approach to the realization of that facility.

The general design of the detector is technically sound. This is verified by a detailed comparison of the capabilities of the proposed Hall D detector with those of the successful LASS detector. This comparison leads to the conclusion that the proposed detector and beam combination will be able to realize the physics goals of the project. However, substantial effort must be invested to optimize the detector design and minimize the cost. The items requiring optimization that we have identified are described in detail in the report. These optimizations are part of the R&D required to prepare a conceptual design report (CDR) for the Hall D project. Preparation of a CDR with the associated work breakdown structure (WBS) and resource-loaded cost and schedule will require a project office at JLab with a project director and a well-structured organization designed to address the necessary R&D and optimization efforts.

3. Recommend R&D needed to optimize the facility design and to minimize the overall project cost.

The R&D item of greatest concern is ensuring that the magnet is still functional, particularly the fourth coil, which has not been used for at least 15 years. R&D should also include construction of prototypes to optimize detector design; to validate mechanical, electronic, and software choices; and to ensure the feasibility of the proposed coherent bremsstrahlung system.

The committee commented on the uniqueness of JLab for carrying out this search using the coherent bremsstrahlung beam:

> *JLab, with the energy upgrade, will be uniquely suited for providing such a beam. In particular, the excellent emittance of the JLab electron beam allows for strong collimation of the coherent bremsstrahlung radiation to enhance the polarization and ratio of tagged to untagged photons in the tagged photon beam. No other facility in the world will be able to provide a beam of this quality, with this combination of energy, duty factor, and emittance. If such a project were pursued at other existing high-energy facilities, either the data-taking rate would be dramatically reduced, compromising the physics goals, or a much more complicated detector would be required. We do not see any project at an existing accelerator complex (e.g., SLAC, CESR, DESY) which is likely to be able to compete with the Hall D initiative in this area.*

Since the report was issued in January 2000, the Hall D collaboration has started on an active R&D program to address issues of optimization and design. Work is underway in electronics, particle identification and tracking. The lead glass detector is now being moved from Brookhaven Lab to JLab.

Two areas of concern raised by the committee have now been addressed. An assessment team visited the Los Alamos National Laboratory (LANL) in March 2000 to examine the superconducting magnet and fourth coil. That team included the two engineers who originally designed, built, and tested the magnet for its use in the LASS spectrometer at SLAC and were also involved in the transfer of the magnet to LANL. The team found the magnet and fourth coil to be in excellent condition based on visual inspection, interviews with users and engineering and technical staff, and a review of written records. Another concern was the ability to obtain synthetic diamonds thin enough ($\approx$ 15 microns) to achieve the necessary collimation. Recently the group from the University of Glasgow has joined the Hall D collaboration. They have acquired sufficiently thin crystals and are making measurements of rocking curves with them.

In summary, the review committee recognized the uniqueness of an energy-upgraded CEBAF accelerator at JLab to carry out the *definitive searches* for the states required by QCD. The major concerns they raised have already been addressed. The program of R&D recommended for optimization and technology choices has started.

2.A.6 The Spectroscopy of $s\bar{s}$ Mesons

In order to carry out a complete search for exotic mesons, it will be necessary to understand the spectrum of normal mesons as well. They will both provide the references against which the exotic states will be observed, and mix with hybrids that have non–exotic quantum numbers. As such, understanding the normal meson spectrum will be a natural byproduct of the exotic searches in Hall D. Of particular interest with the normal mesons are the $s\bar{s}$ states, *strangeonium.*

The non-strange $n\bar{n}$ mesons (mesons built only from u and d) are fairly well established experimentally at lower masses, *albeit* with notable exceptions such as the scalar states. Taking 2.2 GeV/c^2 as a current frontier of light-meson spectroscopy, the quark model anticipates 44 $n\bar{n}$ states up to this mass. About half these mesons have been identified experimentally. Similarly we anticipate 22 kaonic J^{PC} levels ($n\bar{s}$ and $s\bar{n}$), and about two-thirds of these are known. In comparison the $s\bar{s}$ strangeonium states are a *terra incognita*: we consider only five $s\bar{s}$ states to be well established. These are the $\eta(547)$ and $\eta'(958)$ (counted as one $s\bar{s}$ state), $\phi(1019)$, $f_2'(1525)$, $\phi(1680)$, and the $\phi_3(1854)$. Other more controversial possibilities are $\eta(1295)/\eta(1440)$, $h_1'(1380)$, and $f_1(1420)$.

Photoproduction is an excellent technique for producing $s\bar{s}$ mesons, because the incident photon is, in effect, a vector-meson beam with a large ϕ-meson component. Much of the photon-hadron interaction takes place through vector dominance, in which the incident photon becomes a vector meson. The relative probability of interacting through the different light meson types is 9:1:2 for ρ°:ω:ϕ according to the quark model, and this relative coupling strength is approximately confirmed by the diffractive cross sections for vector-meson photoproduction. (There is an additional suppression of the $s\bar{s}$ cross section by about a factor of 2 that is not well understood.) Thus in photoproduction we have the opportunity to produce mesons with vector-meson beams of all diagonal light flavors $u\bar{u}$, $d\bar{d}$, and $s\bar{s}$, with a known relative luminosity between the flavors. At Hall D energies, and in the absence of a large $s\bar{s}$ component of the proton, diffractive photoproduction will presumably dominate the $s\bar{s}$ cross sections. Both of these produce exclusively $C = (-)$ states. The exception to this rule will be channels where t-channel exchanges of OZI-violating systems (like those of η-η') produce $s\bar{s}$ final states. Other mechanisms such as t-channel vector exchange can be expected to lead to photoproduction of $C = (+)$ $s\bar{s}$ states, albeit at a lower level. In contrast, hadronic production of $s\bar{s}$ states is suppressed because the initial hadrons provide, at most, one strange valence quark.

If these $s\bar{s}$ states were expected to be simple copies of the $n\bar{n}$ states, with the mass of each state simply shifted up by about 250 MeV/c^2, establishing the $s\bar{s}$ spectrum might be considered a mundane exercise. However, recent studies within the context of Heavy Quark Effective Theory have shown that while sometimes u, d, s behave like an $\mathrm{SU}(3)_{\mathrm{light}}$ multiplet (the Eightfold Way) and therefore do display such symmetry with respect to $n\bar{n}$ states, in other cases the s quark behaves like a heavy quark (s, c, b) and behaves like it is part of an $\mathrm{SU}(3)_{\mathrm{heavy}}$ symmetry. One dramatic example of this occurs for the $Q\bar{d}$ mesons with $Q = b, c, s$, where the two L=1 states with J=1 (namely the $^3\mathrm{P}_1$ and $^1\mathrm{P}_1$ states) are measured to have the heavy-quark mixing angle of about 35° for not only $b\bar{d}$ and $c\bar{d}$ as expected, but also for $s\bar{d}$. That the s quark might have such a schizophrenic character was pointed out long ago by Gell-Mann: a light quark is defined to be one with a mass $\ll \Lambda_{\mathrm{QCD}}$, while a heavy quark is one with a mass $\gg \Lambda_{\mathrm{QCD}}$. Since $m_s \simeq \Lambda_{\mathrm{QCD}}$, the s quark straddles the border between these two worlds. Exploring the similarity between the $\bar{s}s$ spectrum and the $Q\bar{Q}$ systems needs to be understood to bridge the gap between Heavy Quark Effective Theory and the light-quark world in which we live.

The $s\bar{s}$ sector has other interesting features. For example, some decay modes should be very clean. These include channels such as $\phi\eta$, $\phi\eta'$, and $\phi\phi$, which, according to the Zweig rule, should only arise from $s\bar{s}$ initial states. One may also study channels such as $\phi\pi$, which are *not* expected as decays of $q\bar{q}$ states. One might find evidence for molecular states or Zweig-rule violation in this channel. Observation of both the $n\bar{n}$ and $s\bar{s}$ partners of a flavor nonet would be useful for establishing the $q\bar{q}$ (and $q\bar{q}g$ hybrid) spectrum, since the relative photoproduction amplitudes can be estimated. This would distinguish a $q\bar{q}$ or hybrid flavor nonet from a meson-meson molecule or a glueball, as molecules and glueballs do not span nonets.

The discovery of the CERN glueball candidate has emphasized the puzzling behavior of $s\bar{s}$ systems [Ba93, Se95, We94, Am95, Am96]. The observed decays of the $f_0(1500)$ are far from the flavor-symmetric pattern of: $\pi\pi : KK : \eta\eta : \eta\eta' = 3 : 4 : 1 : 0$ (for branching fraction divided by phase space) that one would expect from a simple model of glueball decay, and instead strongly favor $\pi\pi$. This may be due to an intrinsic quark mass dependence of these couplings (as suggested by the LGT results of Weingarten *et al.* [We94]), or (as suggested by Close and Amsler [Am95]) it may be due to a large $n\bar{n} \leftrightarrow G \leftrightarrow s\bar{s}$ mixing similar to the $n\bar{n} \leftrightarrow s\bar{s}$ mixing in the $\eta - \eta'$ system. While all J^{PC} channels will provide important information regarding $n\bar{n} \leftrightarrow s\bar{s}$ mixing, the most likely *a priori* to show a significant effect are the radial pseudoscalars (perhaps the $\eta(1295)$ and the $\eta(1440)$) and the 2^{-+} pseudotensors. The 2^{-+} states are interesting because some models predict this to be one of the lighter glueball channels. In addition, there are η_2 states at about 1.65 and 1.87 GeV/c^2 (reported by Crystal Barrel [Ad96]), both of which couple strongly to modes forbidden to $s\bar{s}$ by the Zweig rule. Understanding the $s\bar{s}$ states and how they are mixed is likely to provide a significant constraint on our understanding of QCD.

2.B Campaign 2: How are the Nuclear Building Blocks Made from Quarks and Gluons?

This section describes the dramatic progress that can be achieved in our understanding of the fundamental structure of the nuclear building blocks. One glaring gap in our knowledge exists in the region of the three basic "valence" quarks that mainly contribute at large x_{Bj}. Section 2.B.1 highlights the substantial improvements that can be reached probing parton distributions at large x_{Bj} using the deep inelastic scattering process.[1] Such a process measures a diagonal matrix element (*i.e.*, initial and final state are the same) of QCD field operators. Recently, a generalization of these parton distributions encompassing the description of exclusive processes was developed. Section 2.B.2. describes the strategy needed to verify that one is in the domain where these generalized distributions can be accessed. In the most straightforward example, deeply virtual Compton scattering, one can gain supplementary information on partons in the intermediate and large x_{Bj} region. Here one accesses non-diagonal matrix elements of QCD field operators. Similarly, in this framework hadronic form factors access a non-diagonal matrix element of local QCD field operators. Thus, hadronic form factors are related to the same generalized parton distribution functions. As such, we highlight in Section 2.B.3 the substantial progress one can reach in hadronic form factor measurements.

Deep inelastic inclusive scattering shows that scaling at modest Q^2 and ν already arises from very few resonance channels. This duality reflects the transition from strongly interacting matter to a quark-gluon theory, and thus is of fundamental importance. If quantitatively understood, low-energy quark-hadron duality can be used to obtain precise constraints for parton distributions at even larger x_{Bj}. This is described in Section 2.B.4. Lastly, in semi-inclusive meson production the scattering and production mechanisms factorize at high energy. To what extent this factorization applies at lower energy is an open question. Confirmation of factorization at lower energies would open a rich semi-inclusive program, as discussed in Section 2.B.5, allowing an unprecedented spin/flavor decomposition of parton distributions.

---

[1] In this section x_{Bj} is used for "Bjorken-x", the deep inelastic scattering scaling variable (which ranges from $0 \rightarrow 1$) rather than the simpler notation, x, used in the executive summary. This has been done to avoid confusion with the variable x used in the Generalized Parton Distributions (GPD's) discussed in this section; for the GPD's, x denotes the generalized parton momentum distribution (which ranges from $-1 \rightarrow 1$ because it includes the antiquark distribution).

2.B.1 Valence Quark Momentum Distributions

One of the most fundamental properties of the nucleon is the structure of its valence quark distributions, since they are the irreducible kernel of each hadron. Sea quarks, which at very high Q^2 are largely generated in perturbative QCD through gluon bremsstrahlung and subsequent splitting into quark-antiquark pairs, at low Q^2 represent one source of the nonperturbative "meson cloud contributions" that act as "dressing" on the valence quarks. At higher x values these $q\bar{q}$ complications drop away, and the simple physics of the valence quark model is exposed [Is99].

Experimentally, most of the recent studies of nucleon structure have emphasized the small-x_{Bj} region populated mainly by sea quarks (x_{Bj} being the fraction of momentum of the nucleon carried by the quark), while the valence quark structure has for some time now been thought to be understood. Three decades of deep inelastic and other high-energy scattering experiments have provided a detailed map of the nucleon's quark distributions over a large range of kinematics with one major exception – the deep valence region, at very large x_{Bj} ($x_{Bj} \gtrsim 0.5$). In this region the valence structure of the nucleon can be probed most directly, since sea quark distributions, which must be subtracted from the measured cross sections to reveal the valence structure, are negligibly small beyond $x_{Bj} \sim 0.2 - 0.3$. It is both surprising and unfortunate that the large-x_{Bj} region has been so poorly explored experimentally.

This situation is clearly evident in the valence u and d quark distributions, which are usually obtained from measurements of the proton and neutron structure functions, F_2^p and F_2^n, respectively. At leading order these functions are defined as the charge-squared weighted sums of the quark and antiquark distributions of various flavors ($q = u, d, s, \ldots$):

$$F_2(x_{Bj}) \;=\; 2x_{Bj}F_1(x_{Bj}) \;=\; x_{Bj} \sum_q e_q^2 \left(q(x_{Bj}) + \bar{q}(x_{Bj})\right) \; . \qquad (7)$$

While the u quark distribution is relatively well constrained by the F_2^p data for $x_{Bj} < 0.8$, the absence of free neutron targets has left large uncertainties in the d quark distribution beyond $x_{Bj} \sim 0.5$ arising from incomplete understanding of the nuclear medium modifications in the deuteron, from which F_2^n is extracted. For instance, depending on whether one does or does not correct for Fermi motion and binding (off-shell) effects in the deuteron, the extracted $R^{np} \equiv F_2^n/F_2^p$ ratio can differ by $\sim 50\%$ already at $x_{Bj} \sim 0.75$ [Me96, Wh92] (see Fig. 24).

These large uncertainties have prevented answers to such basic questions as why the d quark distribution at large x_{Bj} appears to be smaller (or "softer") than that of the u, softer even than what would be expected from flavor symmetry. Furthermore, since the precise $x_{Bj} \to 1$ behavior of the d/u ratio is a critical test of the mechanism of spin-flavor symmetry breaking, the large errors on

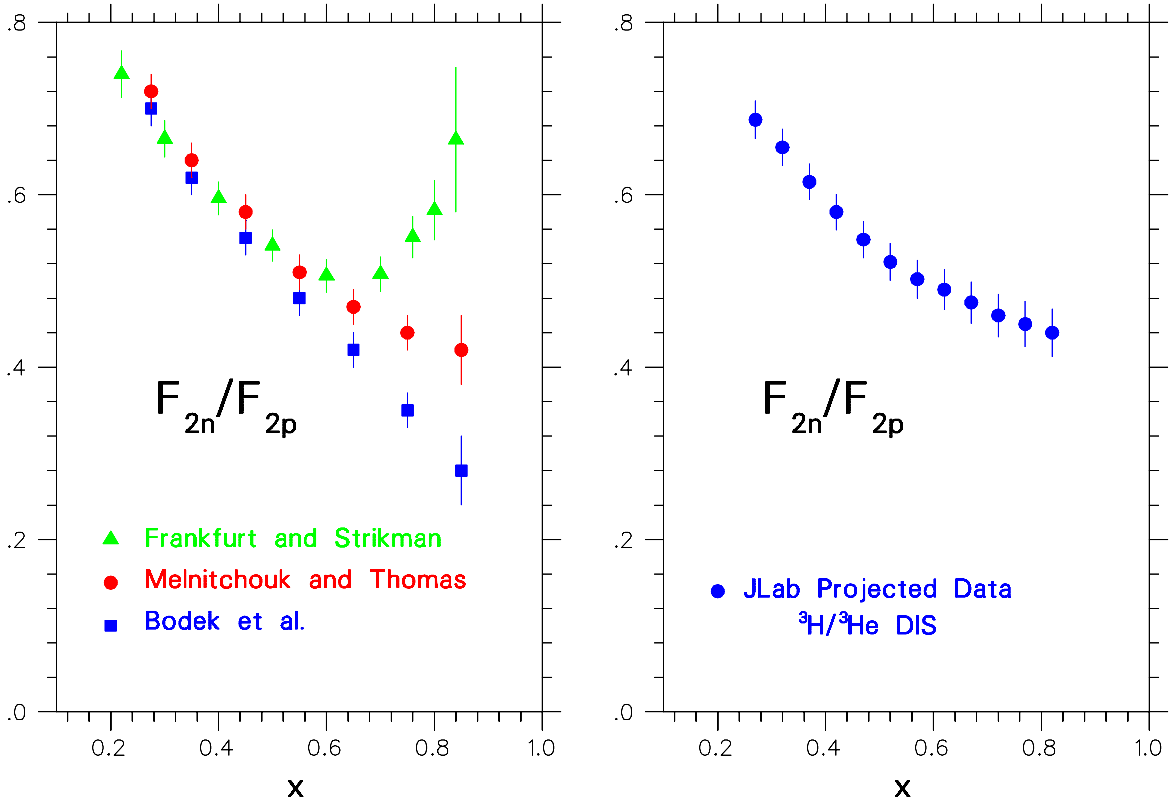

Figure 24: Ratio R^{np} of neutron to proton structure functions as a function of x_{Bj}, extracted from the SLAC data on the deep inelastic proton and deuteron structure functions. The left panel represents R^{np} extracted according to different prescriptions for treating nuclear effects in the deuteron: Fermi smearing only [Bo81, Wh92], Fermi motion and nuclear binding corrections [Me96], and assuming the nuclear EMC effect in the deuteron scales with nuclear density [Fr88]. The right panel shows the projected data with total (statistical, systematic, and model-dependent) errors for the proposed ^{3}H and ^{3}He JLab experiment.

the current data preclude any definitive conclusions about the fundamental nature of quark-gluon dynamics in the valence quark region. From another perspective, knowledge of quark distributions at large x_{Bj} is also essential for determining high-energy cross sections at collider energies, such as in searches for new physics beyond the standard model [Ku00], where structure information at $x_{Bj} \sim 0.6 - 0.8$ feeds down to lower x_{Bj} at higher values of Q^2 through perturbative Q^2 evolution.

The need for reliable large-x_{Bj} data is even more pressing for the spin-dependent quark distributions. Spin degrees of freedom allow access to information about the structure of hadrons not available through unpolarized processes. Spin-dependent quark distributions are usually extracted from measurements of the spin-polarization asymmetry, A_1, which is approximately given by the ratio of spin-dependent to spin-averaged structure functions:

$$A_1(x_{Bj}) \approx \frac{g_1(x_{Bj})}{F_1(x_{Bj})} , \tag{8}$$

where, to leading order,

$$g_1(x_{Bj}) = \sum_q e_q^2 \ (\Delta q(x_{Bj}) + \Delta \bar{q}(x_{Bj})) , \tag{9}$$

with Δq defined as the difference between quark distributions with spin aligned and anti-aligned with the spin of the nucleon, $\Delta q = q \uparrow - q \downarrow$. The first spin structure function experiments at CERN [As88] on the moment, or integral, of g_1, suggested that the total spin carried by quarks was very small, or even zero, prompting the so-called "proton spin-crisis". A decade of subsequent measurements of spin structure functions using proton, deuteron, and ^{3}He targets have determined the total quark spin much more accurately, with the current world average value being $\sim 30\%$ [La98a], which is still considerably less than the value expected from the most naïve quark model in which valence quarks carry all of the proton spin.

While the spin fractions carried by quarks and gluons (or generically, partons) are obtained by integrating the spin-dependent parton momentum distributions, the distributions themselves, as a function of the momentum fraction x_{Bj}, contain considerably more information about the quark-gluon dynamics than their integrals do. Furthermore, the spin-dependent distributions are generally even more sensitive than the spin-averaged ones to the quark-gluon dynamics responsible for spin-flavor symmetry breaking. Considerable progress has been made in measuring spin-dependent structure functions over the last decade, especially in the small x_{Bj} region. However, relatively little attention has been paid to the polarized structure functions in the pure valence region at large x_{Bj}. The lack of data in the valence region is particularly glaring in the case of the neutron, where there is no information at all on the polarization asymmetry A_1^n for $x_{Bj} \geq 0.4$. This is unfortunate, since there are rigorous QCD predictions for the behavior of A_1 as $x_{Bj} \to 1$ that have never been tested.

Theoretical predictions for large-x_{Bj} distributions

The simplest model of the proton, polarized in the $+z$ direction, has three quarks described by a wavefunction that is symmetric in spin and flavor [Cl73]:

$$\begin{aligned} |p\uparrow\rangle \quad = \quad & \frac{1}{\sqrt{2}}\,|u\uparrow(ud)_{S=0}\rangle \;+\; \frac{1}{\sqrt{18}}\,|u\uparrow(ud)_{S=1}\rangle \;-\; \frac{1}{3}\,|u\downarrow(ud)_{S=1}\rangle \\ & -\;\frac{1}{3}\,|d\uparrow(uu)_{S=1}\rangle \;-\; \frac{\sqrt{2}}{3}\,|d\downarrow(uu)_{S=1}\rangle\;, \end{aligned} \qquad (10)$$

where $q\uparrow\downarrow$ represents the active quark that undergoes the deep inelastic collision, and $(qq)_S$ denotes the two-quark configuration with spin S that is a spectator to the scattering. (The neutron wavefunction can be obtained by simply interchanging the u and d quarks in this expression.) On the basis of exact spin-flavor symmetry, which is described by the group SU(6), the $S=0$ and $S=1$ "di-quark" states contribute equally, giving rise to simple relations among the quark distributions, such as $u=2d$ and $\Delta u=-4\Delta d$, which in terms of the structure functions correspond to:

$$R^{np}\equiv F_2^n/F_2^p=\frac{2}{3};\quad A_1^p=5/9;\quad \text{and}\quad A_1^n=0. \qquad (11)$$

In nature the spin-flavor SU(6) symmetry is, of course, broken. It has been known for some time that the d quark distribution is softer than the u quark distribution, reflecting the fact that the neutron-to-proton ratio R^{np} (shown in Fig. 24) deviates strongly from the SU(6) expectation beyond $x_{Bj}\sim 0.4$. On the other hand, the data for the polarization asymmetries A_1^p and A_1^n (shown in Fig. 25) are so poor in the valence region that it is presently not possible to discern whether the SU(6) predictions are borne out for the spin-dependent distributions.

A number of models have been developed for quark distributions that incorporate mechanisms for the breaking of the SU(6) symmetry; some of these models can be linked directly to phenomena such as the hyperfine splitting of the baryon and meson mass spectra. Feynman and others [Fe72, Cl73, Ca75a] observed that there was a correlation between the nucleon and Δ mass difference and the suppression of R^{np} at large x_{Bj}. A quark hyperfine interaction, such as that due to one-gluon exchange, instantons or pion exchange (which can induce a higher energy for the $S=1$ spectator "di-quark" in Eq.(10)) will necessarily give rise to a larger mass for the Δ since the quark wavefunction for the Δ has all "di-quark" configurations with $S=1$. If the $S=0$ states are dominant at large x_{Bj}, Eq.(10) implies that the d quark distribution will be suppressed relative to that of the u in the valence quark region. This expectation has, in fact, been built into most phenomenological fits to the parton distribution data [Ei84, Di88, Ma94a, La95]. This mechanism also leads to specific predictions for the polarization asymmetries as $x_{Bj}\to 1$:

$$R^{np}\to\frac{1}{4};\quad A_1^p\to 1;\quad \text{and}\quad A_1^n\to 1\;. \qquad (12)$$

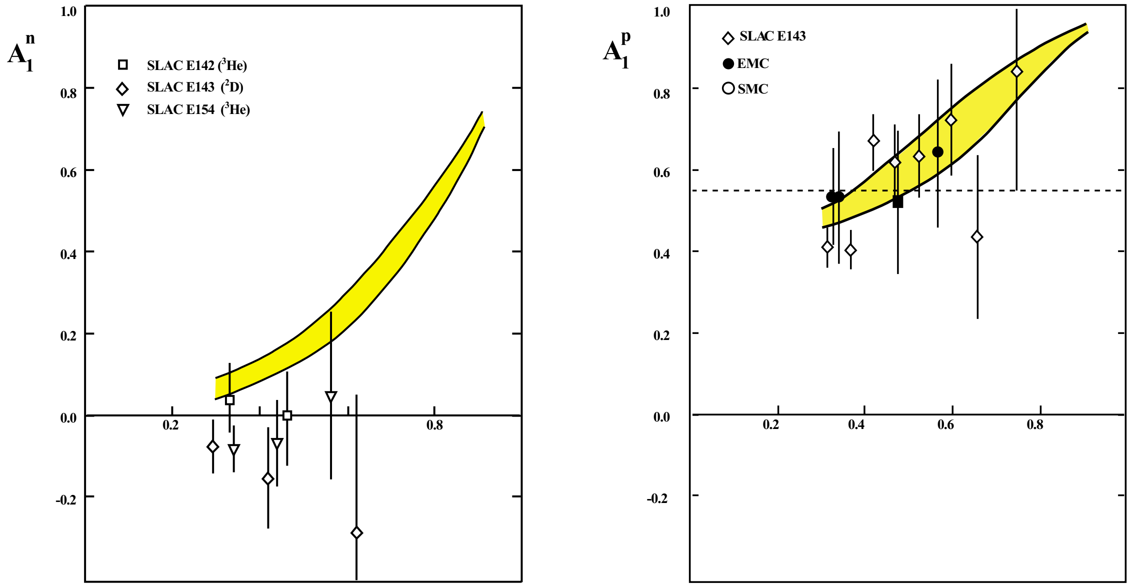

Figure 25: Sample of large-x_{Bj} data for A_1^n (left) and A_1^p (right). The predictions of SU(6) for $x_{Bj} \to 1$ are $A_1^n = 0$ and $A_1^p = 5/9$ (dashed line). The shaded bands are broken SU(6) valence quark model predictions versus x_{Bj} for A_1^n and A_1^p, as evaluated in Ref. [Is99].

More radical nonperturbative models of SU(6) breaking, such as those which include instantons as important degrees of freedom, predict dramatically different behavior for A_1^n as $x_{Bj} \to 1$; *i.e.*, that it goes to a low value close to zero [Ko97, Kopc].

Arguments based on perturbative QCD, on the other hand, predict that the dominant components of the proton valence wavefunction at large x_{Bj} are those associated with states in which the total "di-quark" spin projection, S_z, is zero [Fa75]. Consequently, scattering from a quark polarized in the opposite direction to the proton polarization is suppressed relative to the helicity-aligned configuration. From Eq.(10) this leads to the predictions in the $x_{Bj} \to 1$ limit:

$$R^{np} \to \frac{3}{7}; \quad A_1^p \to 1; \quad \text{and} \quad A_1^n \to 1 \; . \tag{13}$$

The novelty of these predictions, especially for A_1^p and A_1^n, is that they follow essentially directly from perturbative QCD in the limit of $Q^2 \to \infty$ and $x_{Bj} \to 1$. However, it is not clear *a priori* at which x_{Bj} and Q^2 the transition from the nonperturbative dynamics, embodied in the predictions (12), to perturbative QCD takes place, so experimental guidance on this issue is essential.

While the trend of the existing R^{np} data is consistent with models with broken SU(6) symmetry, they cannot discriminate between the competing mechanisms of SU(6) breaking (as evident from Fig. 24) because of uncertainties in the extraction procedure associated with nuclear corrections. For the asymmetries A_1^n and A_1^p, while we do not expect the SU(6) predictions to be accurate, the existing measurements at high x_{Bj} lack the precision to even distinguish any of the predictions from the naïve SU(6) result.

The ratio $R^{np} = F_2^n/F_2^p$ of the neutron and proton structure functions

If the nuclear EMC effect (the modification of the free nucleon structure function in the nuclear environment) in deuterium were known, one could apply nuclear smearing corrections directly to the deuterium data to obtain the free neutron F_2^n. However, the EMC effect in the deuteron requires knowledge of the free neutron structure function itself, so the argument becomes cyclic. The best way to reliably determine R^{np}, free of the large uncertainties associated with nuclear corrections at large x_{Bj}, is through simultaneous measurements of the inclusive ^{3}He and ^{3}H structure functions, maximally exploiting the mirror symmetry of $A = 3$ nuclei. Regardless of the absolute value of the nuclear EMC effect in ^{3}He or ^{3}H, the differences between the EMC effects in these nuclei will be small (on the scale of charge symmetry breaking in the nucleus).

In the absence of a Coulomb interaction, and in an isospin-symmetric world, the properties of a proton (neutron) bound in the ^{3}He nucleus would be identical to those of a neutron (proton) bound in the ^{3}H nucleus. If, in addition, the proton and neutron distributions in ^{3}He (and in ^{3}H) were identical, the neutron structure function could be extracted with no nuclear corrections, regardless of the size of the EMC effect in ^{3}He or ^{3}H separately.

In practice, ^{3}He and ^{3}H are of course not perfect mirror nuclei – their binding energies for instance differ by some 10% – and the proton and neutron distributions are not quite identical. However, the $A = 3$ system has been studied for many years, and modern realistic $A = 3$ wavefunctions are known to rather good accuracy. Using these wavefunctions, together with a nucleon spectral function, the difference in the EMC effects for the ^{3}He and ^{3}H nuclei has been calculated [Af00b, Pa00, Ci90, Uc88] to be less than 2% for $x_{Bj} < 0.85$. More importantly, the actual model dependence of this difference is less than 1% for all x_{Bj} values accessible experimentally with an 11 GeV beam.

By performing the tritium and helium measurements under identical conditions, the ratio of the deep inelastic cross sections for the two nuclei can be measured with 1% experimental uncertainty (SLAC Experiments E139 [Go94] and E140 [Da94, Ta96] have quoted 0.5% uncertainties for measurements of ratios of cross sections). Deep inelastic scattering with the proposed 11 GeV JLab electron beam can therefore provide precise measurements for the $F_2^{^3\mathrm{He}}/F_2^{^3\mathrm{H}}$ ratio, from which R^{np} can be extracted essentially free of nuclear corrections at the 1% level over the entire range $0.10 \leq x_{Bj} \leq 0.82$. In addition, it will for the first time enable the size of the EMC effect to be determined in $A = 3$ nuclei, which to date has been measured only for $A \geq 4$ nuclei. The key issue for this experiment will be the availability of a high-density tritium target, comparable with the previously used Saclay [Am94] and MIT-Bates [Be89] tritium targets. The quality of the projected data is highlighted in Fig. 24 and in Fig. 6 of the executive summary.

The neutron spin structure function A_1^n

While data on R^{np} and A_1^p give some indication of the large-x_{Bj} behavior of the valence quark distributions at $x_{Bj} \lesssim 0.5$, the experimental situation for the neutron A_1^n at large x_{Bj} is totally unclear. The statistical precision of the data available does not even allow a meaningful statement about the qualitative behavior of A_1^n for $x_{Bj} > 0.4$. The experiment proposed here, as outlined in the executive summary, will use the 11 GeV JLab electron beam to perform a precision measurement of A_1^n, utilizing the Hall A polarized ^{3}He target and the proposed MAD (Medium-Acceptance Device) spectrometer. Because the neutron in ^{3}He carries almost 90% of the nuclear spin, polarized ^{3}He is an ideal source of polarized neutrons [Fr90].

The experiment involves measurement of the polarization asymmetry, $A_1^{^3\mathrm{He}}$, defined as:

$$A_1^{^3\mathrm{He}}(x_{Bj}) \approx \frac{1}{D}\frac{d\sigma^{\uparrow\downarrow} - d\sigma^{\uparrow\uparrow}}{d\sigma^{\uparrow\downarrow} + d\sigma^{\uparrow\uparrow}} \ , \tag{14}$$

where $d\sigma^{\uparrow\uparrow}$ ($d\sigma^{\uparrow\downarrow}$) is the cross section for scattering polarized electrons from a polarized ^{3}He target with the beam and target helicities parallel (antiparallel) and D is a kinematic factor relating the virtual photon polarization to that of the electron. The neutron asymmetry A_1^n is extracted from $A_1^{^3\mathrm{He}}$ after correcting for residual nuclear effects in ^{3}He associated with Fermi motion and binding, using modern three-body wavefunctions [Wo89, Ci93a, Sc93], similar to those used in correcting for nuclear effects in $F_2^{^3\mathrm{He}}$ discussed in the previous section. Furthermore, because the asymmetry is a ratio of nuclear structure functions, the nuclear effects on A_1^n will be considerably smaller than those associated with absolute structure functions. In addition to the use of the polarized ^{3}He target, other polarized targets (ND_3 and NH_3)will be used for cross checks and for the investigation of the nuclear effects.

An example of the kinematics relevant for this experiment is given in Table 2. (Note that substantial improvements in the measurement of A_1^p at large x_{Bj}, or A_1^n at large x_{Bj} using polarized solid-state NH_3 and ND_3 targets, would also be possible with an 11 GeV cw beam). To illustrate the improvement of the projected results obtainable with JLab at 11 GeV compared with previously measured data from other facilities we introduce a figure of merit (FOM) = $D^2 \times \mathrm{Rate} \times f^2$, which allows a meaningful comparison between different laboratories. Here "Rate" takes into account the use of the proposed Medium-Acceptance Device spectrometer, and f is the dilution factor defined as the ratio of polarized nucleons to the total number of nucleons in the target. Table 2 shows the comparison between the relevant parameters at competitive existing laboratories at comparably large x_{Bj} and Q^2. Note that with increasing beam energy the depolarization factor decreases. The lowest beam energy, therefore, which guarantees access to the large-x_{Bj} region in the Bjorken limit is optimal. The anticipated data are shown in Fig. 26. JLab at 11 GeV would enable access to $x_{Bj} \lesssim 0.8$ at $W^2 \approx 4$ GeV.

Higher-twist effects and the g_2^n structure function

While the g_1 structure function has a simple interpretation in the quark-parton model in terms of quark helicity distributions and has been the focus of extensive experimental programs over the last decade, there have been few dedicated experimental studies of the g_2 structure function. The g_2 structure function is related to the transverse polarization of the nucleon, and although it does not have a simple quark-parton model interpretation, it contains important information about quark-gluon correlations within the nucleon.

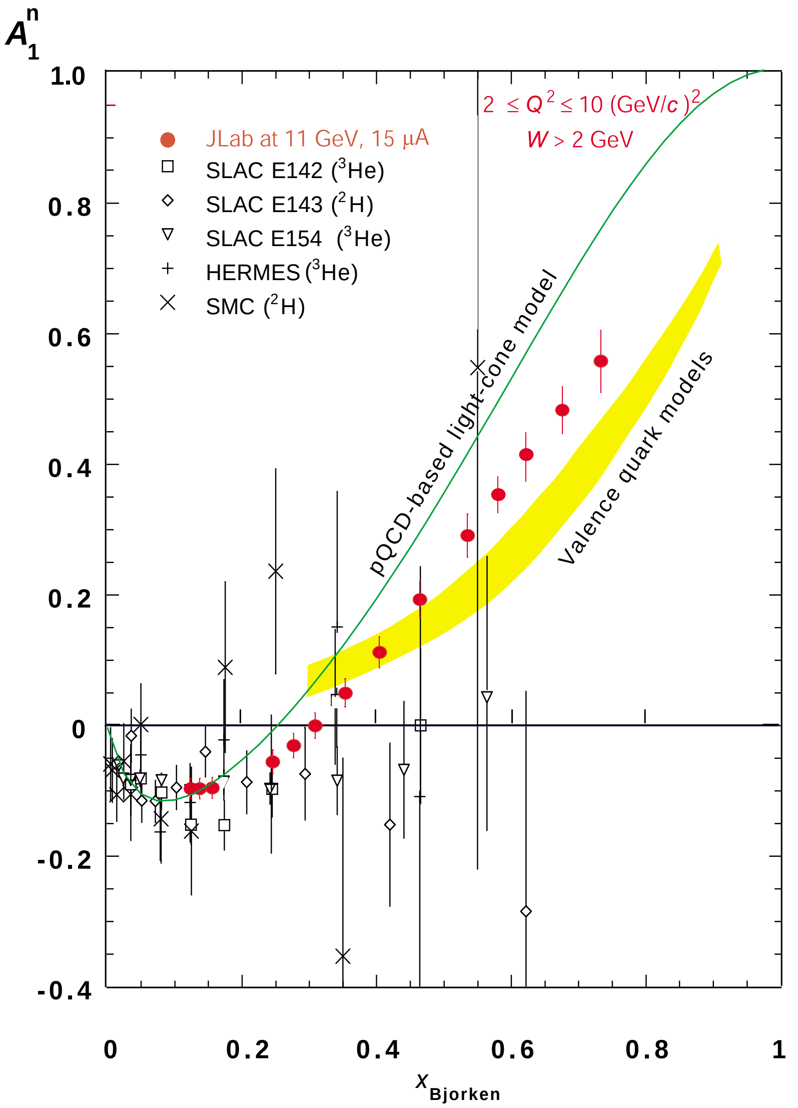

Figure 26: Simulated data for a measurement of A_1^n in the large Bjorken-x region, where it is determined by the spin structure of the valence quarks, made possible by the proposed 12 GeV Upgrade.

Table 2: Comparison of the figure of merit (FOM) for large x_{Bj} measurements of the A_1^n structure function at HERA, SLAC, and JLab.

Expt. name	E_i (GeV)	E' (GeV)	θ (deg.)	x_{Bj} bin	Q^2 $(\mathrm{GeV}/c)^2$	D	f	Rate (Hz)	FOM (10^{-4})
HERMES	35.0	17.0	5.2	0.60-0.70	9.1	0.22	0.3	0.05	2
SLAC E143	29.13	25.5	7.0	0.60-0.70	9.1	0.29	0.2	0.3	10
JLab	11.0	4.4	25	0.60-0.70	8.5	0.67	0.3	2.7	1000

In QCD the quark-gluon correlations are associated with so-called higher twist operators (where "twist" is defined as the difference between dimension and spin of an operator), which are suppressed by additional factors of $1/Q$ relative to the leading twist contribution (which is associated with free quark scattering). At large values of Q^2, QCD allows one to relate moments of spin structure functions to the matrix elements of operators of given twist. The simplest twist-3 matrix element that contains information on quark-gluon correlations is given by:

$$d_2(Q^2) \;=\; \int_0^1 dx_{Bj}\; x_{Bj}^2 \left[2g_1(x_{Bj},Q^2) + 3g_2(x_{Bj},Q^2)\right] \tag{15}$$

Note that because of the x_{Bj}^2 weighting in Eq.(15), d_2 is dominated by the large-x_{Bj} behavior of g_1 and g_2. The physical significance of d_2 is that it reflects the response of a quark to the polarization of the gluon color field in the nucleon, $d_2 = (2\chi_B + \chi_E)/3$, with χ_B (χ_E) the gluon-field polarizability in response to a color magnetic (electric) field $\vec{B}$ ($\vec{E}$) [St95].

Published data for g_2 were obtained from experiments E142-E155 at SLAC [Ab96] and the SMC experiment at CERN [Ad93]. The world's best data will soon be published from the recent E155x experiment at SLAC, which measured g_2 for proton and deuteron. Using preliminary results from this experiment [Bo00], values for g_2 for the neutron were extracted and are shown in Fig. 27. The curve labeled "g_2^{WW}" represents the leading twist contribution to g_2 [Wa77]. Using these data, a nonzero positive value for d_2^n has been extracted that is in disagreement with all of the theoretical calculations. However, in most cases, the disagreement is less than 1σ, and the size of the experimental error does not allow one to make a conclusive statement about the importance of higher-twist effects in the nucleon.

A 12 GeV JLab experiment will make a factor of 10 statistical improvement in the error on d_2^n, by taking advantage of the high-luminosity 11 GeV beam and the large-acceptance MAD spectrometer. Precision data for g_2 will be obtained in the range $0.15 \leq x_{Bj} \leq 0.8$, $W > 2$ GeV, for example at $Q^2 = 5$ $(\mathrm{GeV}/c)^2$, with special focus on the high-x_{Bj} region which dominates d_2. Projected uncertainties for such an experiment are indicated by the squares in Fig. 27.

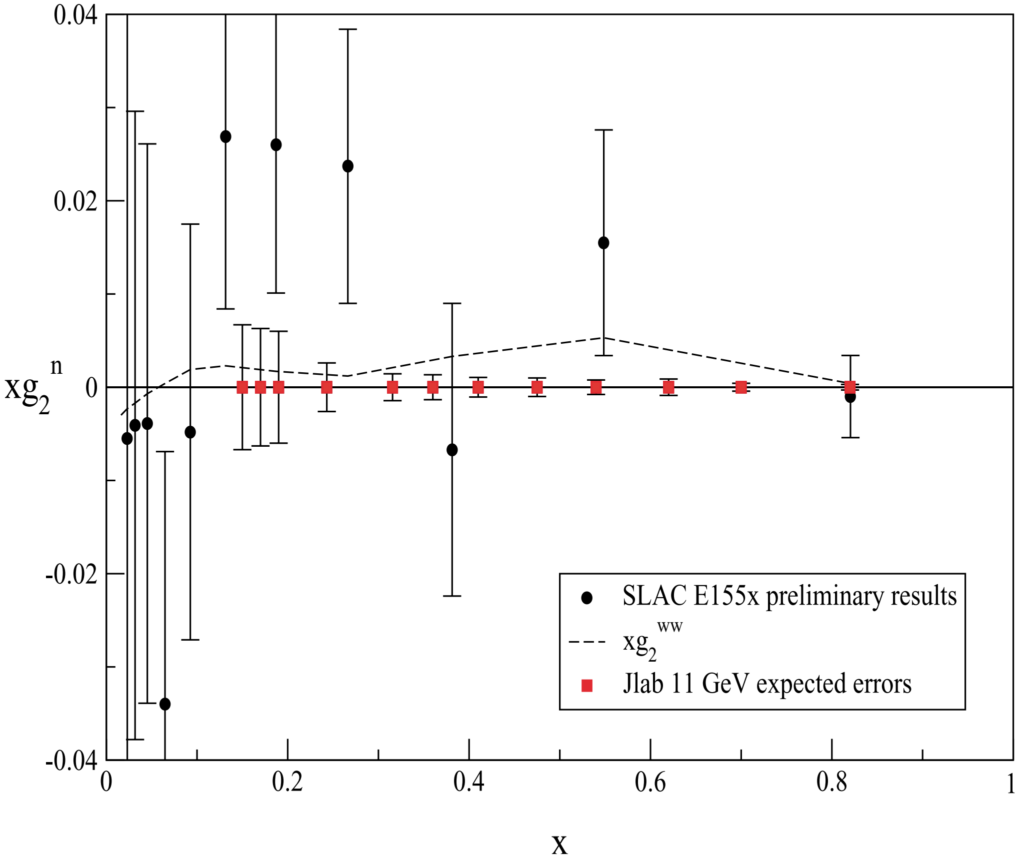

Figure 27: The preliminary results for the g_2^n spin structure function from SLAC experiment E155x. The dashed curve shows the Wandzura-Wilczek [Wa77] calculation of the leading twist contribution to g_2^n. The open squares are the expected uncertainties from an 11 GeV JLab measurement.

2.B.2 Deep Exclusive Scattering (DES) Cross Sections and Generalized Parton Distributions

Exclusive reactions allow us to determine new aspects of the nucleon structure which can be understood within the formalism of Generalized Parton Distributions. Inclusive measurements probe the longitudinal momentum distribution of quarks inside the nucleon. The exclusive measurements of photons and mesons probe the full nucleon wavefunction at the amplitude level and, for example, will shed light on the distribution of the transverse momentum of quarks, determine the contribution of the quark angular momentum to the spin of the proton, and measure quark-quark correlations through non-diagonal matrix elements.

The standard feature of applications of perturbative QCD to hard processes is the introduction of phenomenological functions describing nonperturbative long-distance dynamics. Thus, much of the internal structure of the nucleon, in the form of parton distribution functions, was revealed over the past three decades through the inclusive scattering of high-energy leptons on the nucleon in the Bjorken or "Deep Inelastic Scattering" (DIS) regime (Q^2 and ν large, with $x_{Bj} = Q^2/2M\nu$ finite). Simple theoretical interpretations of the experimental results and quantitative conclusions were reached in the framework of the parton model and QCD when summing over all possible hadronic final states. The parton distribution DIS functions inferred from DIS data are probabilities, and, for example, unpolarized (polarized) DIS revealed that the quarks carry about 50% (25%) of the nucleon's momentum (spin).

In contrast, in the asymptotic QCD regime one can extract information from exclusive processes on distribution amplitudes $\varphi(x)$ [Ch77, Fa79, Ra77, Ef80, Br79a, Br80]. For instance, $\varphi_{\pi^+}(x)$ gives the probability amplitude of finding a (positive) fast-moving pion in a quark-antiquark state $u\bar{d}$, with the longitudinal pion momentum p shared in fractions x and $1 - x$:

$$\varphi_{\pi^+}(x) \sim \Psi\{\pi^+(p) \to u(xp) + d((1-x)p)\} \ . \tag{16}$$

The two types of nonperturbative functions, parton distribution functions and distribution amplitudes (Fig. 28), provide complementary information about the hadronic structure. These latter functions are wavefunctions, not probabilities.

Recently the formalism of the Generalized Parton Distributions (GPD's) has been developed [Ji97, Ra96]. These hybrid functions generalize the features of the usual parton distribution functions, the hadron distribution amplitudes, and the electromagnetic form factors, and provide a unifying description for these fundamental quantities of hadronic structure. The GPD's contain a wealth of information about the transverse momentum and angular momentum carried by the

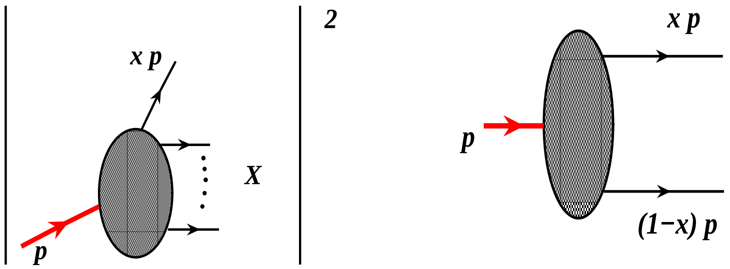

Figure 28: The parton distribution function (left) and the pion distribution amplitude (right).

quarks in the proton, and can be accessed through hard exclusive electroproduction of mesons and photons.

The GPD's $\tilde{H}^a(x,\xi;t)$, $\tilde{E}^a(x,\xi;t)$, $H^a(x,\xi;t)$, and $E^a(x,\xi;t)$, where $a = u, d, \ldots$ denotes the quark flavor, were called off-forward parton distributions when first introduced by X. Ji [Ji97]. [2] They correspond to a description (Figs. 29 and 30) in which the initial (h_i) and final (h_f) hadrons are treated in a symmetric way: the longitudinal momentum of the initial hadron is written as $p = (1+\xi)P$ and that of the final one as $p' = (1-\xi)P$. Here, the skewedness parameter ξ, or the longitudinal-momentum fraction of the transfer Δ, is related to x_{Bj} by

$$\xi = \frac{x_{Bj}}{2 - x_{Bj}} \tag{17}$$

and $P = (p+p')/2$ is the average momentum of the initial and final hadron.

The longitudinal momentum of the initial, struck, parton in Figs. 29 and 30 is written as $(x+\xi)P$ and that of the final parton as $(x-\xi)P$. Note that ξ varies between 0 and 1, and x, the momentum fraction of the struck quark in the quark loop, varies between -1 and 1. As such, x is not directly accessible experimentally. Lastly, $t = \Delta^2$ is the standard momentum transfer between the virtual photon and the final-state meson. Thus,

$$H^a(x,\xi;t) \sim \sum_X \Psi\{h_i(1+\xi) \to a(x+\xi) + \text{“}X\text{”}\} \times \Psi^*\{h_f(1-\xi) \to a(x-\xi) + \text{“}X\text{”}\}\ , \tag{18}$$

where “X” denotes all the intermediate states in the “soft” blob of Fig. 30. In the forward limit, when $p = p'$ [*i.e.*, $t = 0$ and $\xi = 0$], the GPD's H^a ($\tilde{H}^a$) collapse to the usual spin-independent

---

[2] A. Radyushkin [Ra96] introduced similar functions, which he called nonforward parton distributions (NFPD's; see also [Co97]). OFPD's and NFPD's can be treated as specific cases of skewed or generalized parton distributions.

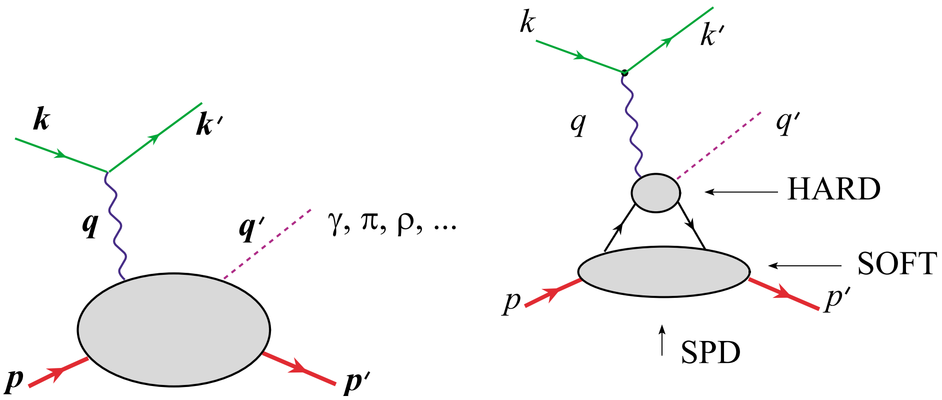

Figure 29: Hard electroproduction processes: the general structure (left); and perturbative QCD factorization (right).

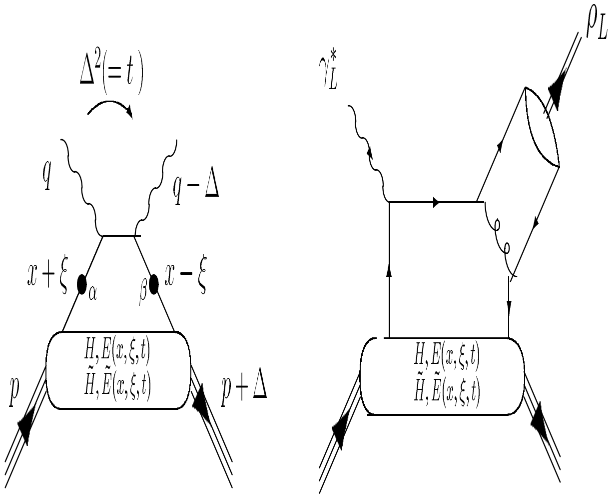

Figure 30: "Handbag" diagrams for DVCS (left) and meson production (right).

(spin-dependent) parton distribution functions measured in inclusive processes such as deep inelastic scattering. Furthermore, in a nonforward kinematics (a non-inclusive process), GPD's contain much richer information about the parton correlations. The latter can be nondiagonal in hadron/parton momenta and in hadron/parton spin, and can even correspond to different hadrons in the initial and final state (*e.g.*, one can consider matrix elements corresponding to $p \to n$, $N \to \Delta$, $N \to \Lambda$, etc. transitions).

The spin-independent (spin-dependent) GPD's H, E ($\tilde{H}, \tilde{E}$) provide detailed information about the nucleon structure: they are sensitive not only to probabilities but also to interference between different components of the nucleon wavefunction. The GPD's reflect the structure of the nucleon independent of the reaction that probes the nucleon. They can be accessed through the hard exclusive electroproduction of mesons ($\pi^{0,\pm}$, $\rho^{0,\pm}$, ω, ϕ,... ; see Fig. 30b) for which a QCD factorization proof has been given [Co97]. In this proof it was shown that factorization applies when the virtual photon is longitudinally polarized because, in this case, the end-point contributions to the meson wavefunction are power suppressed. It was also shown that the cross section for a transversely polarized photon is suppressed by $1/Q^2$ compared to a longitudinally polarized photon, so that asymptotically, only σ_L survives. Collins *et al.* [Co97] showed that leading-order pQCD also predicts that the vector-meson channels ($\rho_L^{0,\pm}$, ω_L, ϕ_L) are sensitive only to the unpolarized GPD's (H and E), whereas the pseudoscalar channels ($\pi^{0,\pm}$, $\eta, ...$) are sensitive only to the polarized GPD's ($\tilde{H}$ and $\tilde{E}$). In contrast, Deeply Virtual Compton Scattering (DVCS) depends on *both* the polarized and unpolarized GPD's. Therefore, by selecting specific mesons in the final state one selects the spin-dependent or spin-independent generalized parton distributions. Note that in this latter case, one can access polarized nucleon structure information without any polarization of external particles. To explore what can be done, real photon, vector meson, and charged pion channels will be discussed since they have relatively high cross sections. In a later section we will come back to measuring nucleon elastic form factors (corresponding to the $< x^0 >$ moment of the GPD's) nucleon transition form factors, and Real Compton Scattering (RCS) (measuring the $< x^{-1} >$ moment of the GPD's). Note that while the elastic form factors at large t become increasingly sensitive to high $x \to 1$, RCS is more sensitive to the medium x-region due to the $1/x$ weighting in the integral.

DVCS and hard meson electroproduction processes have the following features:

1. **Scaling.** DVCS and hard meson electroproduction processes depend on three invariants: the initial photon virtuality $q^2 = -Q^2$, the initial photon energy in the lab frame ν: $p \cdot q = m\nu$, and the invariant momentum transfer $t = (p - p')^2$. The nontrivial prediction of perturbative QCD is that for fixed t and sufficiently large Q^2 and pq, the hard exclusive electroproduction

amplitudes have a simple scaling structure $T(x_{Bj})/Q^N$, with a calculable integer power N (determined by dimensional analysis) and the function $T(x_{Bj})$ depending only on the Bjorken ratio $Q^2/2p \cdot q) \equiv x_{Bj}$. This prediction reflects the basic pointlike nature of the quarks and the fundamental short-distance properties of quantum chromodynamics such as asymptotic freedom.

2. **Exclusive-inclusive connection.** As already emphasized, another nontrivial prediction of QCD is that the generalized parton distributions $H(x, \xi; t)$ describing the amplitudes of purely exclusive processes like DVCS process $\gamma^* N \to \gamma N$ are directly related to the usual parton distribution functions describing the cross sections of inclusive processes like DIS process $\gamma^* N \to X$.

3. **Electroproduction–form factor connection.** Since the integrals of GPD's are related to hadronic form factors, the t-dependences of hard electroproduction amplitudes and elastic form factors are interconnected.

It is important to measure the Q^2-dependence of the nearly forward differential cross section at fixed x_{Bj}. It is still uncertain at which Q^2 value one will reach the scaling regime, where the leading-order pQCD domain applies fully for meson electroproduction. However, it is expected to be between 5 and 10 (GeV/c)^2, which is attainable with a 12 GeV beam. In any case, the way the asymptotic $1/Q^6$ behavior is approached is an important source of information on pre-asymptotic effects. "Soft" contributions are expected to drop as $1/Q^8$. An estimate of these pre-asymptotic effects in hard electroproduction reactions in the valence region is given in Ref. [Va99], where the effects of the intrinsic transverse momentum dependence of the quarks in the nucleon and in the meson are quantified. We may also note that reaching the fully asymptotic regime is not necessary as long as the corrections can be controlled by perturbative QCD methods. For example, if one is in a region of pre-asymptotic scaling a ratio of two production channels may lead to a nearly complete cancelation of "soft" contributions. Eides, Frankfurt, and Strikman [Ei99] point out that "It seems likely that a *precocious factorization* ... could be valid already at moderately high Q^2 [≥ 5 (GeV/c)^2], leading to *precocious scaling of the spin asymmetries and of the ratios of the cross sections* as a function of Q^2, and x_{Bj}".

The complete extraction of the GPD's presents an extensive program, not a single experiment, involving the measurement of a variety of channels and observables. As the GPD's also depend on the unmeasurable momentum fraction of the struck quark in the quark loop (see Fig. 30), a global analysis will be required to extract the GPD's definitively from a large set of measurements.

The goal is to simultaneously measure the Q^2, x_{Bj} and t-dependences of cross sections, beam asymmetries (for DVCS) and transverse polarized target asymmetries (for meson production). These observables involve the leading-order pQCD amplitudes, which are directly related to the GPD formalism. Toward this end, a large-acceptance spectrometer is highly desirable, as it will allow mapping the various dependences for all channels, simultaneously.

At JLab, one may begin to explore GPD's over a wide range of kinematics, for example $0.1 \lesssim x_{Bj} \lesssim 0.9$, $Q^2 > 2$ (GeV/c)^2, and -t <1.5 (GeV/c)^2. This program requires:

- high energy to reach the required high Q^2 at small x_{Bj},
- high luminosity to compensate for the typical fast drop of exclusive cross sections with Q^2 and hadronic center-of-mass system energy,
- good detector resolution to identify exclusive channels, and
- large acceptances for charged particle and neutral particle detection to measure various channels simultaneously, and over a large kinematic range, and to guarantee the exclusivity of the process.

JLab at 12 GeV, with the proposed CLAS detector upgrade, or, in specific cases, a high-luminosity spectrometer and calorimeter setup (DVCS) or two spectrometers (*e.g.*, hard charged pion electroproduction), will meet most of these requirements. Of course the beam energy will limit the kinematic range accessible, but given the rapid rate of cross section fall-off, this is not as serious a constraint as is commonly believed.

Deeply virtual Compton scattering

An important practical question is: what Q^2 is large enough to ensure the dominance of the lowest-twist handbag contribution? Guidance for DVCS can come from experimental data for the exclusive process $\gamma(q_1)\gamma^*(q_2) \to \pi^0$ studied on e^+e^- colliders. If one of the photons is highly virtual $q_1^2 = -Q^2$ while another is (almost) real $q_2^2 \sim 0$, the process is kinematically similar to DVCS. In the leading order of QCD, the $F_{\gamma\gamma^*\pi^0}(Q^2)$ transition form factor is given by a handbag diagram. The recent measurements by CLEO [Gr98] show that the pQCD prediction $F_{\gamma\gamma^*\pi^0}(Q^2) \sim 1/Q^2$ seems valid for $Q^2 \sim 2\,(\mathrm{GeV}/c)^2$ (see Fig. 31).

The $\gamma\gamma^*\pi^0$ vertex (for a virtual pion) can also be measured on a fixed-target machine, in which case it is just a part of the DVCS amplitude corresponding to the $\tilde{E}(x, \xi; t)$ generalized

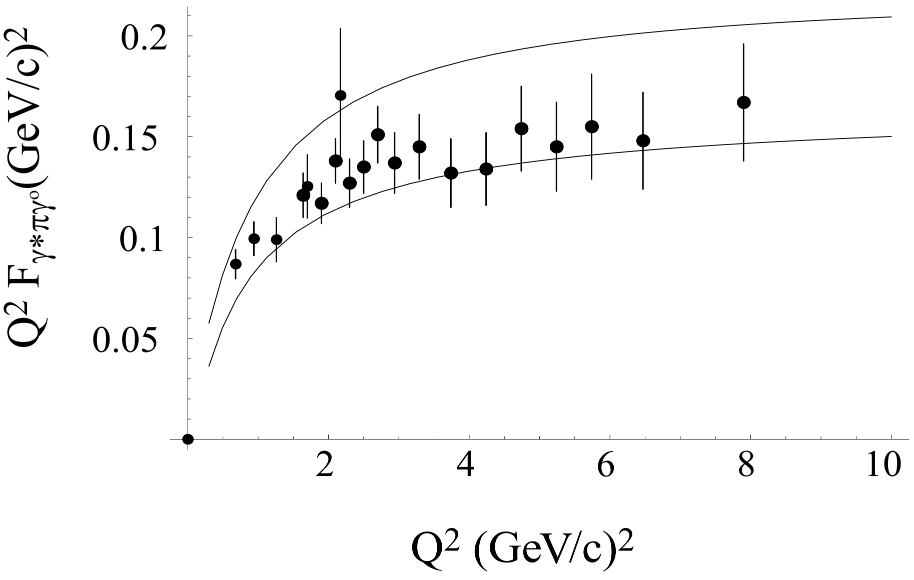

Figure 31: Comparison of experimental data on the $\gamma^*\gamma\pi^0$ form factor with quark transverse momentum power-corrected pQCD predictions using the asymptotic shape for the pion distribution amplitude (lower curve) and the Chernyak-Zhitnitsky model (upper curve).

parton distribution. Hence, CLEO data indicate that DVCS may be handbag-dominated for Q^2 as low as 2 (GeV/c)^2.

One complication with experimentally studying DVCS is the competing Bethe-Heitler (BH) process. Here higher energies are an advantage, since the relative strength of DVCS increases with increasing beam energy. One can either select kinematics where the DVCS contributions dominate the BH contributions, or, alternatively, measure an interference term between the BH and DVCS contributions, thus benefitting from the strong BH term.

Thus, DVCS contributions can be extracted in various ways:

- Direct measurements of the absolute DVCS amplitude in the region where the BH contribution is small and can be calculated.
- Extracting the imaginary part of the DVCS amplitude by measuring the single-spin asymmetry with longitudinally polarized beam.

Studies of all three processes are needed over a wide kinematic range for a complete understanding of GPD's. The first two can be achieved with the electron beams that will be available after the 12 GeV Upgrade, while the third requires use of positron beams. Note that the availability of JLab's highly polarized electron beam will especially allow unprecedented measurements of beam spin asymmetries, and the proposed upgraded CLAS detector in Hall B would be well suited to conduct these studies. Figure 32 shows the kinematic range in Q^2 and W accessible with CLAS for a beam energy of 11 GeV. Systematic studies in the range of Q^2 up to 6 (GeV/c)^2 and for x_{Bj} from 0.15 to 0.45 will be possible. Such a DVCS program would be complementary to a program with a high-momentum spectrometer detecting the scattered electron and the (upgraded) Hall A "RCS calorimeter" to detect the hard photon. In either case, one would measure the recoiling nucleon in coincidence to guarantee the full-exclusiveness of the reaction. This is important, as separating a single photon from π^o production becomes more problematic at higher beam energies.

For the upgraded CLAS (capable of running at a luminosity of $L = 10^{35}$ cm^{-2} s^{-1}), count rates are estimated using the cross sections calculated by [Gupc]. Figure 33 shows, as an example, the high-quality single-spin asymmetries one could obtain at $Q^2 = 3$ (GeV/c)^2, for a 500 hour run.

Hard meson electroproduction

The GPD's can also be measured in hard meson electroproduction processes. The leading-twist pQCD contribution in this case involves an additional one-gluon exchange, which means that the hard subprocess is suppressed by a factor of $\alpha_s/\pi \sim 1/10$ with respect to soft processes.

Calculating the one-gluon-exchange amplitude perturbatively, one obtains the hard contribution in the form of a product of two nonperturbative functions: the distribution amplitude $\phi(\tau)$ of the relevant meson [integrated with $1/\tau$] and a generalized parton distribution $H(x, \xi; t)$ (or $E, \tilde{H}, \tilde{E}$) integrated with $1/(x-\xi+i0)$ or $1/(x+\xi-i0)$, the same integrals as in DVCS. In distinction to the DVCS amplitude, which contains four GPD's $H(x, \xi; t)$, $E(x, \xi; t)$, $\tilde{H}(x, \xi; t)$ and $\tilde{E}(x, \xi; t)$, the nature of the produced meson "filters" the participating GPD's: vector-meson production is sensitive to $H(x, \xi; t)$ and $E(x, \xi; t)$, while the amplitude of the hard pion electroproduction is expressed in terms of $\tilde{H}(x, \xi; t)$ and $\tilde{E}(x, \xi; t)$ only.

As mentioned, $\tilde{H}(x, \xi; t)$ reduces to a spin-dependent parton distribution function in the forward limit. By taking advantage of this fact one can measure polarized parton distributions in this process without polarizing any participating particle. Note that polarization observables are expected to show precocious scaling already at $Q^2 = 3$ – 4 (GeV/c)^2.

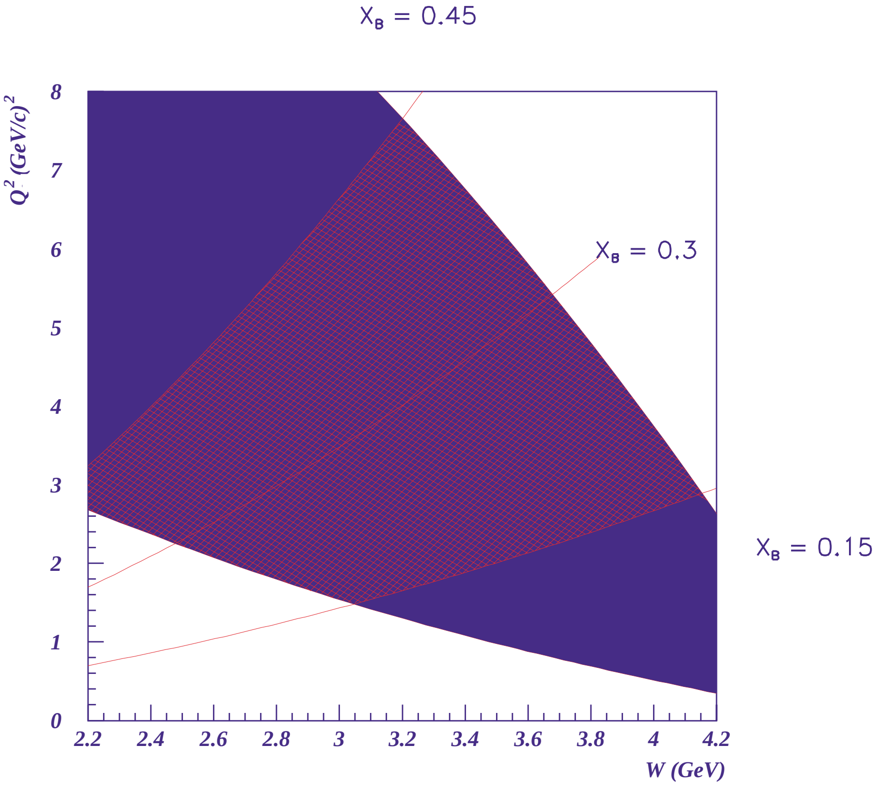

Figure 32: The accessible range of Q^2 and W at 11 GeV beam energy with the upgraded CLAS detector. The filled region is defined by detection of the scattered electron. The shaded region is the favorable kinematic range, accessible for DVCS measurements. The lines represent fixed values of x_{Bj}.

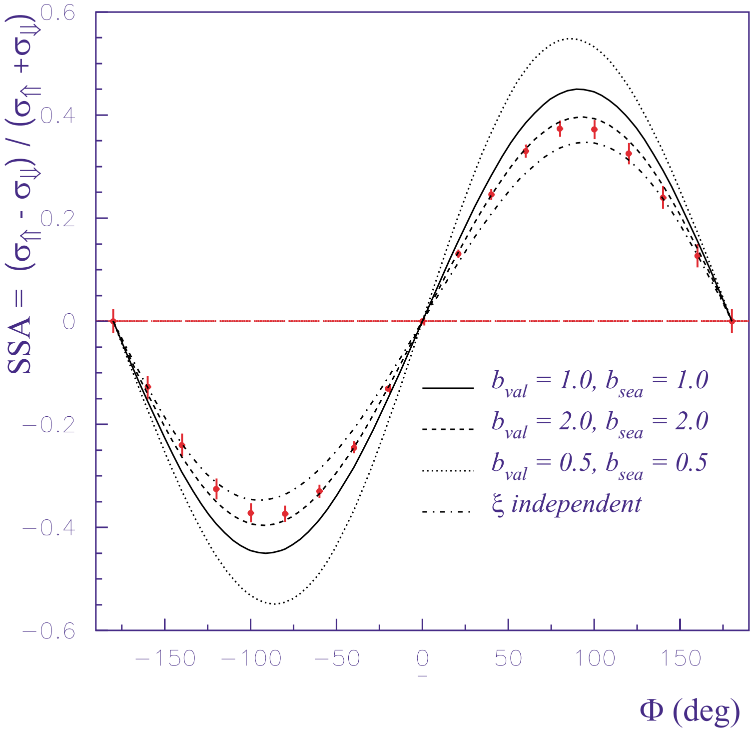

Figure 33: Single-spin asymmetry of the $ep \rightarrow ep\gamma$ reaction measured with a longitudinally polarized 11 GeV electron beam. Uncertainties correspond to a 500 hour run with CLAS operating at a luminosity of 10^{35} cm^{-2} sec^{-1}. Pseudo-data were integrated in the bins of $Q^2 = (3 \pm 0.1)$ (GeV/c)^2 and $W = (2.8 \pm 0.15)$ GeV and $-t = (0.3 \pm 0.1)$ (GeV/c)^2. The curves indicate various models of Generalized Parton Distributions, all of which are compatible with the known longitudinal parton momentum distributions.

The $ep \to e'\rho p$ channel We recall that an experimental program aiming to study the GPD's must begin by identifying the longitudinal part of the cross section for which the factorization theorem applies and the connection with the GPD formalism can be made. Longitudinal ρ^0_L's can be identified through the angular distribution of the vector-meson decay. Assuming s-channel helicity conservation, or SCHC, the desired cross section: $\gamma^*_L p \to p(\rho^0_L, ...)$ can be extracted by analyzing the angular distribution.[3]

The angular distribution of the decay products of the ρ reflects its polarization state. Assuming the outgoing electron and proton are detected, measurement of only one decay pion is sufficient to determine the decay angular distribution. The decay pion defines an angle, θ_{cm}, which is the polar angle relative to the direction opposite to the recoiling target in the ρ center-of-mass frame. The $\cos(\theta_{cm})$ distribution follows the form:

$$W\left(\cos(\theta_{cm})\right) = \frac{3}{4}\left\{1 - r^{04}_{00} + (3r^{04}_{00} - 1)\cos^2(\theta_{cm})\right\}. \tag{19}$$

The matrix element r^{04}_{00} depends on Q^2 and W, and is linked to the longitudinal polarization state of the ρ. For example, r^{04}_{00}=1 (0) corresponds to pure longitudinal (transverse) polarization of the ρ, respectively, and, in terms of angular distribution, to $\frac{3}{2}\cos^2\theta_{cm}$ ($\frac{3}{4}\sin^2\theta_{cm}$), respectively. Assuming SCHC, one often links the ρ polarization to the virtual photon polarization, and defines:

$$R = \frac{\sigma_L}{\sigma_T} = \frac{1}{\epsilon}\frac{r^{04}_{00}}{1 - r^{04}_{00}}. \tag{20}$$

The link is obvious: as r^{04}_{00} represents the longitudinal degree of polarization, $1 - r^{04}_{00}$ represents the transverse degree of polarization, and the factor $1/\epsilon$ accounts for the degree of longitudinal polarization of the virtual photons.

R has been measured in many experiments. It is displayed in Fig. 34 as a function of Q^2, though for a mixture of W values. (The HERMES collaboration recently reported a slight dependence on W, for $W > 4$ GeV [Ac00].) The observed increase of R with Q^2 means that longitudinal ρ's are dominant at large Q^2. However, there are no data in the region of interest for this study ($Q^2 \approx 3$ (GeV/c)^2 and $2 < W < 3$ GeV).

To estimate the accuracy we will be able to achieve for a measurement of R, events were

---

[3] The SCHC hypothesis can actually be tested by considering the interference response functions R_{TT} and R_{TL}, which are accessible with a large-acceptance detector such as CLAS.

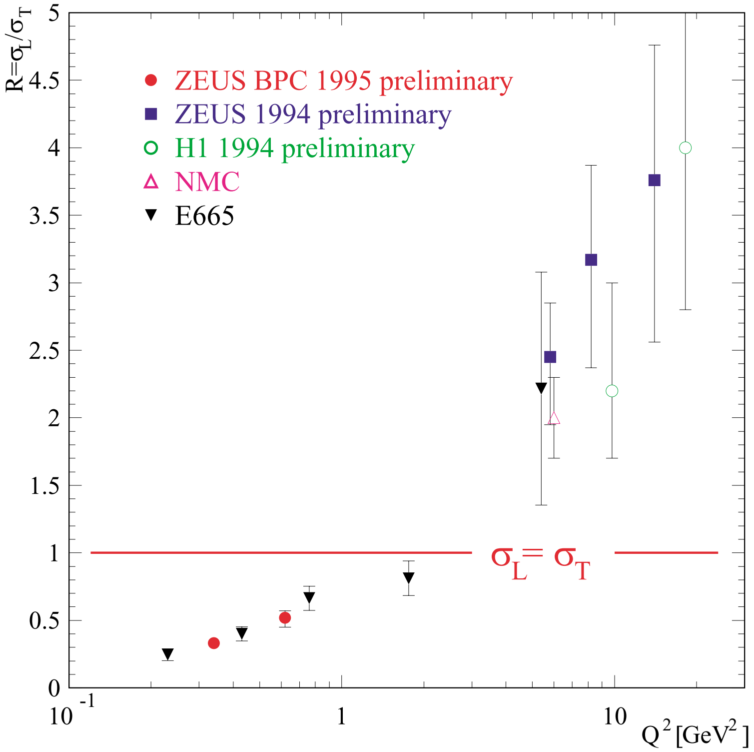

Figure 34: World data for $R = \sigma_L/\sigma_T$ as a function of Q^2 (assuming SCHC) [Cr97].

generated with the ratio R using the relationship:

$$R = \xi^2 \frac{Q^2}{M_\rho^2} \tag{21}$$

This formula is based on the Vector Meson Dominance (VMD) approach [Sa69], and describes the data of Fig. 34 at intermediate Q^2 [≈ 3 (GeV/c)^2] with a value $\xi^2 = 0.3$.

The θ_{cm} angular distribution of the decay π^+ has been simulated for different Q^2 bins, taking the acceptance of the upgraded CLAS into account. We assumed a luminosity of 10^{35} cm^{-2} s^{-1}, a beam energy of 11 GeV, and a 400 hour run time. Bin sizes of $0.3 < x_{Bj} < 0.4$, $-0.2 < -t < 0.4$ (GeV/c)^2, and $\Delta Q^2 = 1$ (GeV/c)^2 were assumed. The ratio R=σ_L/σ_T has been extracted from the simulated θ_{cm} distribution as described above. Figure 35 shows the separated cross sections for ρ electroproduction, with the anticipated statistical uncertainties. If it is found that the trend of the current data is confirmed with high precision at the upgraded CEBAF machine, corrections for σ_T maybe applied to σ_{tot} without performing an L/T separation. In this case the data can be extended to even higher Q^2.

Hard pion electroproduction The L/T separation for pions obviously can be accomplished using the Rosenbluth technique. In order to separate σ_T and σ_L, it is necessary to vary the virtual photon polarization parameter ϵ, which can only be done, keeping x_{Bj} and Q^2 fixed, by varying the beam energy (Rosenbluth separation). In the following, we will assume 6, 8, and 11 GeV incident beams. For the identification of the reaction, it is sufficient to detect the scattered electron and the charged pion, the neutron being reconstructed by the missing-mass technique.

Figure 36 shows the anticipated data; separated cross sections can be obtained up to $Q^2 \approx 6$ (GeV/c)^2. Obviously, the unseparated cross-section estimates reach a higher Q^2 value as one does not require a range in ϵ for L/T separation. For the case of Hall B, the maximum Q^2 attainable would be ≈ 8 (GeV/c)^2. In principle, Halls A and/or C could extend these Q^2 ranges utilizing their high-luminosity capabilities. For example, using the HMS-SHMS combination in Hall C (the existing High-Momentum Spectrometer and the planned Super-High-Momentum Spectrometer), one could do precise measurements of $R = \sigma_L/\sigma_T$ in $H(e, e'K^+)\Lambda$ electroproduction up to Q^2 of 10 (GeV/c)^2.

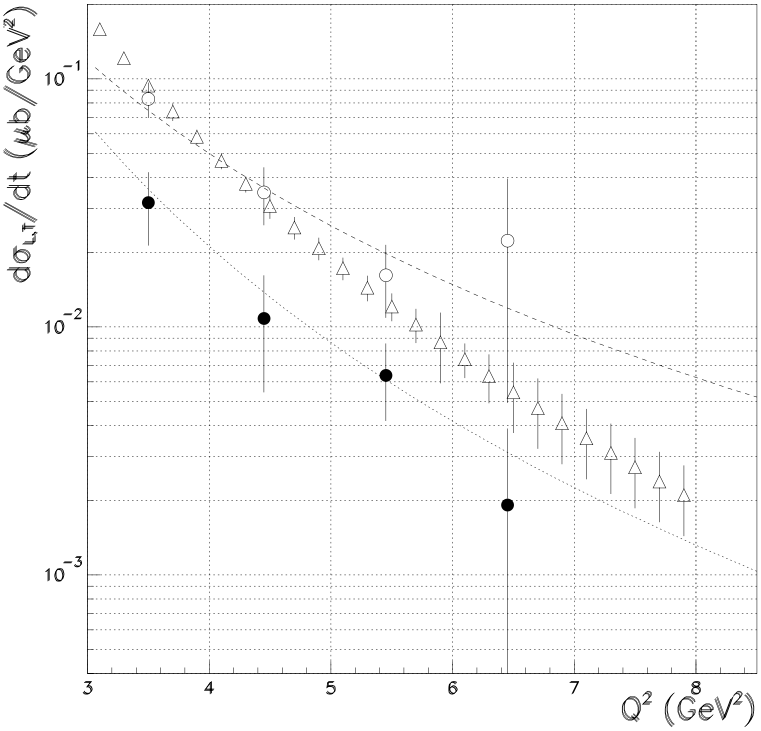

Figure 35: Simulation of the L/T separated cross section $d\sigma/dt$ for ρ electroproduction with an 11 GeV electron beam. Open triangles are the total (unseparated) cross section ($\sigma_{\text{tot}} = \sigma_T + \epsilon\sigma_L$). Full circles are σ_T, decreasing like $1/Q^8$ (dotted line). Empty circles are σ_L, decreasing like $1/Q^6$ (dashed line).

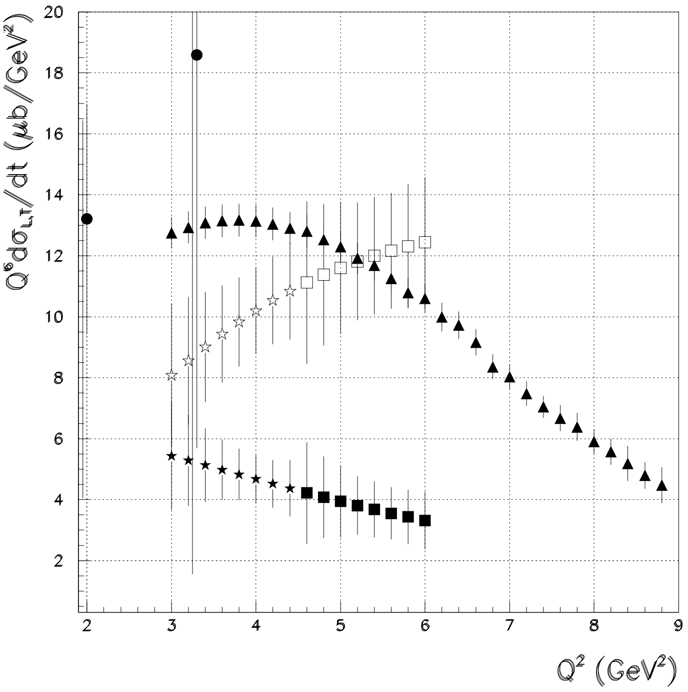

Figure 36: Separated and unseparated differential cross section $d\sigma/dt$ (multiplied by Q^6) for $ep \to \pi^+ n$ as a function of Q^2. Circles are the existing data points of Bebek *et al.* [Be78]. Open (filled) stars and squares correspond to projected σ_L (σ_T) data. Projected data at lower Q^2 use a 6 GeV-11 GeV beam energy combination, data at higher Q^2 an 8 GeV-11 GeV beam energy combination. The solid triangles are the unseparated differential cross sections. Bins of $x_{Bj} = 0.4 - 0.5$, and $-t = 0.2-0.4$ (GeV/c)^2 are used. An upgraded CLAS acceptance and a luminosity of 10^{35} cm^{-2}s^{-1}, and 1600 hours of beam time have been assumed.

2.B.3 Form Factors

Hadron form factors are fundamental quantities in nuclear physics. They are the most basic observables which reflect the composite nature of the hadrons. Indeed, the first indication that the nucleon is a composite object came from measurements of the proton form factors in elastic electron-proton scattering [Ho55].

Nucleon elastic and transition form factors

Measurements of nucleon elastic and transition form factors have become very interesting in recent years due to the development of a variety of precise, new measurement techniques. At small Q^2, below 1 (GeV/c)^2, precise measurements of the neutron charge form factor show values statistically significantly different from 0; the neutron magnetic form factor remains controversial due to disagreements between precise experiments in excess of their stated uncertainties. Next to this, few precise measurements exist beyond $Q^2 = 1$ (GeV/c)^2. For the proton, recent JLab polarization measurements [Jo00] have shown that the electric form factor falls much faster than the magnetic form factor. Lastly, the $E2/M1$ ratio for the $N \to \Delta$ transition has remained near 0 over the entire range of momentum transfer explored [up to $Q^2 = 4$ (GeV/c)^2] [Fr98a], whereas the perturbative QCD expectation for this ratio is unity.

JLab at 12 GeV would provide the opportunity to measure many important form factors precisely: the proton electric and magnetic form factor, the neutron magnetic form factor, the $N \to \Delta$ and $N \to S_{11}$ transition form factors, and Real Compton Scattering (RCS) up to momentum transfers of $Q^2 = -t = 10 - 15$ (GeV/c)^2. Precise measurements above a few (GeV/c)^2 are available only for the proton magnetic form factor. (We have listed RCS within the GPD framework, as it is the $< x^{-1} >$ moment of the $H(x, \xi, t)$ GPD, whereas the Dirac form factor $F_1(Q^2)$ is the $< x^0 >$ moment of the same GPD.) Baryon resonance structure generalizes the elastic nucleon structure studies, providing a bridge between the elastic and deep inelastic regimes. The Δ resonance is especially significant for its role in hadron structure [Th84], and for the qualitatively different Q^2-dependence of its form factor from the elastic and other resonant form factors [St93]. Moreover, the contribution of the $N \to \Delta$ transition to polarization asymmetry is known to be large and negative at low Q^2, while the same asymmetry is positive at large Q^2. Understanding this transition, and the related nontrivial Q^2-dependence of the evolution of the Gerasimov-Drell-Hearn integral at intermediate Q^2, requires a precise determination of the $N \to \Delta$ transition form factor over a large range in Q^2. The S_{11} may be considered the negative parity partner of the nucleon: in the limit of exact chiral symmetry the masses of the nucleon and the S_{11} would be degenerate, so the properties of the S_{11} form factor reveal fundamental aspects of dynamical chiral symmetry breaking in QCD.

Understanding the transition from low to high Q^2 is vital for other reasons as well. Form factors in the transition region are very sensitive to mechanisms of spin-flavor symmetry breaking, some of which can not be described in principle within perturbation theory. A classic example is the electric form factor of the neutron, which is identically 0 in a simple valence quark picture. A nonzero value for the neutron form factor can only be understood in terms of nonperturbative mechanisms such as the hyperfine interaction between quarks [Is81] or in terms of a pion cloud [Th84]. Similarly, in the purely asymptotic picture the proton electric form factor is identically 0 in a simple valence quark picture, and a non-vanishing form factor again requires a nonperturbative wavefunction.

To summarize, the nucleon elastic form factors (G_M^n, G_E^p, and G_M^p), the nucleon transition form factors (*e.g.*, the $N \to \Delta$ and $N \to S_{11}$), and wide-angle Real Compton Scattering can be measured precisely out to large Q^2. As examples we highlight: (i) a measurement of the $D(e,e'n)/D(e,e'p)$ ratio in CLAS to extract $G_M^n(Q^2)$ (Fig. 37); (ii) the expected behavior of the ratio of $E2/M1$ in the $N \to \Delta$ transition, a ratio that can be precisely measured up to $Q^2 \approx 15$ (GeV/c)^2 with the Hall C HMS-SHMS spectrometer combination (Fig. 39); and (iii) a projected measurement of the RCS vector form factor $R_V(t)$ in Hall A using the (upgraded) RCS calorimeter and the MAD spectrometer (Fig. 38). Each of these measurements would take of order one month of 12 GeV beam time.

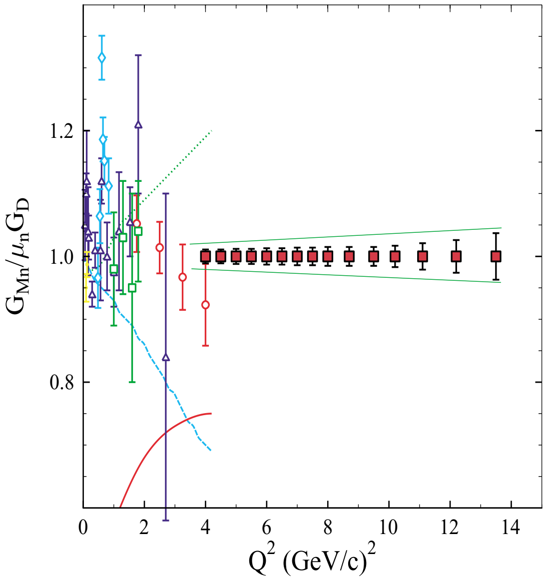

Figure 37: Projected statistical and systematic uncertainties versus Q^2 for the proposed measurements of $G_M^n(Q^2)$, contrasted with previous data.

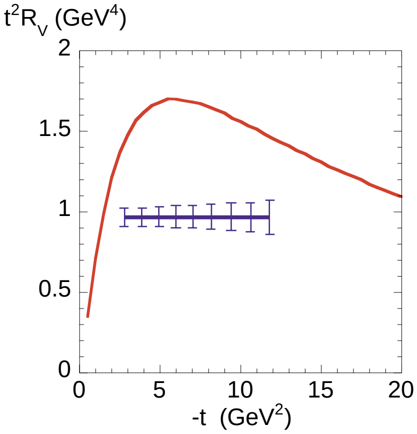

Figure 38: The RCS vector form factor $R_V(t)$, multiplied with t^2, versus t. The projected uncertainties attainable with a 12 GeV JLab are shown. The theoretical form factor is due to a calculation of Radyushkin [Ra98a].

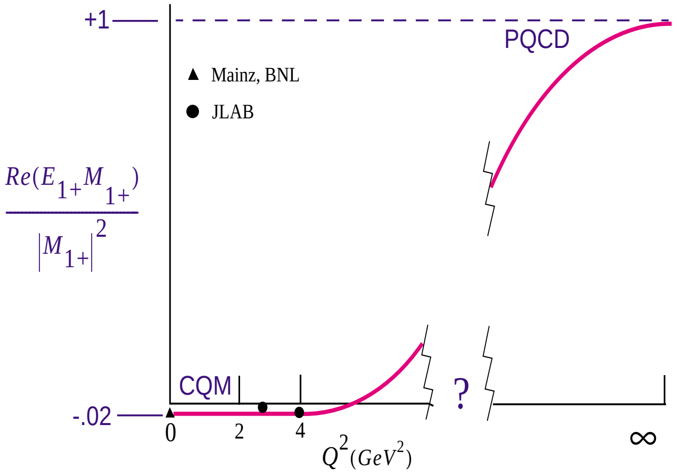

Figure 39: $Re(E_{1+}^* M_{1+})/|M_{1+}|^2$ for excitation of the $\Delta(1232)$ as a function of Q^2. The datum at $Q^2 = 0$ is the result of experiments at Mainz and BNL. The data points at $Q^2 = 2.8$ and 4.0 $(\mathrm{GeV}/c)^2$ are the JLab results. The unmodified $SU(6)$ value is 0, while the pQCD prediction is +1. The curve is a suggestion of what may be expected. The break in the abscissa indicates our lack of knowledge about where in Q^2 the transition to hard processes occurs. JLab at 12 GeV would provide precise measurements up to $Q^2 \approx 15$ $(\mathrm{GeV}/c)^2$.

The pion form factor

The π^+ electric form factor is a topic of fundamental importance to our understanding of hadronic structure. It is well known [Ch77, Fa79, Ra77, Ef80, Br79a] that the asymptotic behavior is rigorously calculable in perturbative QCD (pQCD), and takes the form

$$F_\pi \to \frac{8\pi\alpha_s f_\pi^2}{Q^2} \tag{22}$$

at high Q^2, where $f_\pi = 133$ MeV is the π^+ axial-vector decay constant.

The theoretical prediction for F_π at experimentally accessible Q^2 values is less certain, as soft scattering contributions must be taken into account explicitly. For example, in Ref. [Ja93] it was found that the inclusion of both Sudakov corrections and the transverse momenta of the quarks leads to values too small with respect to the data, thus leaving room for an important role of other, soft, contributions. A recent study [Br00a] based on a light-cone sum rule calculation found that the nonperturbative hard contributions of higher twist strongly cancel the soft components, even at relatively modest Q^2. Other models [Ja90, Ti92, It92] obtain good agreement with the experimental data over a broad region of Q^2 by incorporating a confining potential (which dominates at low Q^2) and a QCD-based interaction (which dominates at high Q^2) that takes the form of a one-gluon exchange potential or dynamic chiral symmetry breaking. Finally, Bethe-Salpeter plus Schwinger-Dyson equations were used in Ref. [Ma00] to determine the pion form factor. In this case, the model's parameters were adjusted to reproduce m_π, f_π, and $< \bar{q}q >$, and then the predicted F_π is found to be in reasonable agreement with the existing data. Reliable experimental data at intermediate Q^2 are clearly needed to delineate the role of hard versus soft contributions and aid the further development of these models.

Unfortunately, our experimental knowledge of F_π is poor. Many of the experimental difficulties in extracting the pion form factor are well understood. One must obtain high-quality $p(e, e'\pi^+)n$ data, in which the contribution of the pion pole diagram is optimized by measuring the π^+ in parallel kinematics at the smallest possible $|t|$ and performing an L/T separation. The complications of the proton target are taken into account by using a model, such as that of Ref. [Va98]. The value of $F_\pi(Q^2)$ is obtained via a fit of the σ_L model to the data. This procedure renders experimental values of $F_\pi(Q^2)$ with far smaller systematic uncertainties than the previous Chew-Low extrapolations. The high-quality, continuous electron beam of CEBAF is essential for these measurements. In 1997, E93-021 obtained data up to $Q^2 = 1.6$ (GeV/c)^2 in Hall C [Vo00], and expects to extend these measurements to $Q^2 = 2.6$ (GeV/c)^2 in 2002. As can be seen from Fig. 40, 2.6 GeV^2/c^2 will not be a high enough Q^2 value to determine the soft-to-hard transition definitively. Given its importance, measuring $F_\pi(Q^2)$ well at the highest possible Q^2 is warranted.

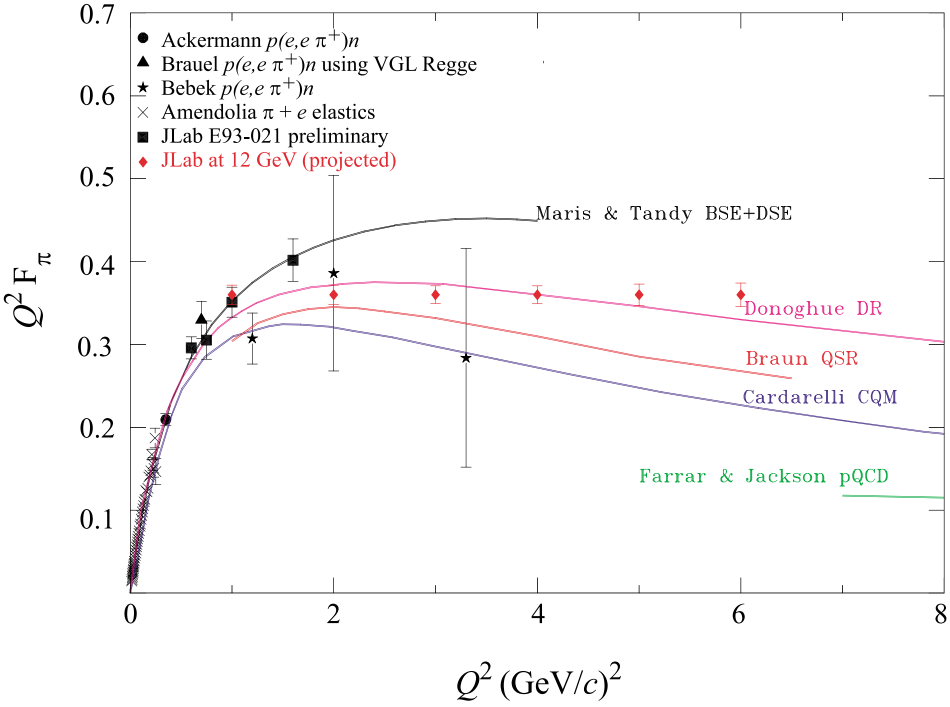

Figure 40: The measurements of the pion elastic form factor through the expected transition region from confinement-dominated dynamics to perturbative-dominated dynamics made possible by the proposed 12 GeV Upgrade. Systematic errors are estimated to be comparable to the statistical errors shown for the projected 12 GeV data. Also shown are a few of the dozens of model predictions, all characterized by being confinement-dominated below about 2 (GeV/c)^2 and making a transition to being perturbative-dominated with a value of $Q^2F_\pi \simeq 0.1$ (GeV/c)^2 in the region of 10 (GeV/c)^2.

The 12 GeV Upgrade will allow one to obtain data at a higher value of the invariant energy W, resulting in lower values of $|t|$, thus enhancing the t-pole part of the cross section and the L/T ratio. Also the models used to extract the pion form factor from data on the proton are believed to be more reliable at higher values of W.

Since the pion will be emitted at rather small angles with the beam, the proposed SHMS spectrometer is essential for this measurement because of its 5.5° forward angle capability, combined with its good angular resolution (to control systematic errors in the L/T separation) and sufficient missing-mass resolution to cleanly separate $p(e, e'\pi^+)n$ events from $p(e, e'\pi^+)N\pi$. Figure 40 shows the expected error bars that could be obtained with the SHMS+HMS combination and an 11 GeV beam after 100 days of running time. It is clear that the CEBAF Upgrade would allow a significant advance in the understanding of the pion form factor.

Primakoff photo- and electro-production

One can exploit the high-energy electro- and photo-production of pseudoscalar mesons in the Coulomb field of a nucleus, the Primakoff effect, to study the two-photon decay widths, $\Gamma_{\gamma\gamma}$, and the transition form factors, $F_{\gamma\gamma^* P}$, where P represents the π°, η, and η' pseudoscalar mesons.

In the chiral limit, the classical QCD Lagrangian,

$$\mathcal{L}_{\rm QCD} = \sum_{i=u,d,s} \bar{\psi}_i (i\not{\partial} - g\not{A} - m_i)\psi_i - \frac{1}{4} G^a_{\mu\nu} G^{\mu\nu}_a , \tag{23}$$

is invariant under both chiral $SU_L(3) \times SU_R(3)$-flavor and axial $U_A(1)$ transformations. The chiral $SU_L(3) \times SU_R(3)$ symmetry is also a symmetry of the full quantum field theory, but is spontaneously broken to $SU(3)$ in the ground state. As a result, there are eight massless Goldstone bosons corresponding to the eight spontaneously broken degrees of freedom in the symmetry transformations: the octet pseudoscalar mesons (π°, η, K, etc.). In reality, these Goldstone mesons are not massless because the quark masses are nonzero (albeit small), thus breaking the symmetry explicitly.

Unlike chiral $SU_L(3) \times SU_R(3)$, the axial $U_A(1)$ is not a symmetry of the full quantum theory because of the chiral anomaly [Be69]:

$$\partial_\mu j^\mu_A = \frac{N_F \alpha_s}{8\pi} \varepsilon^{\mu\nu\lambda\sigma} G^a_{\mu\nu} G_{a\lambda\sigma} \tag{24}$$

and the existence of topologically distinct QCD vacua that make the right-hand side of Eq. 24 nonzero. (Here $N_F = 3$ is the number of flavors appearing in the axial current, and G is the gluon field.) The existence of such “Θ-vacua”, which lead to the strong CP problem, and the mechanisms by which topological transitions occur (instantons or confinement-driven vacuum fluctuations) remain one of the most profound issues in QCD. Moreover, the nature of the η' as an "almost Goldstone boson", which gets its mass from vacuum gluonic interactions, stands as one of the most interesting questions in hadron dynamics.

There is a second type of $U_A(1)$ anomaly that involves the coupling of the quarks to the photon fields. This leads to similar non-vanishing divergences:

$$\partial_\mu j^\mu_{A3} = \frac{N_c \alpha_{em}}{3\pi} \epsilon^{\mu\nu\rho\sigma} F_{\mu\nu} F_{\rho\sigma}$$

$$\partial_\mu j^\mu_{A8} = \frac{N_c}{\sqrt{3}} \frac{\alpha_{em}}{3\pi} \epsilon^{\mu\nu\rho\sigma} F_{\mu\nu} F_{\rho\sigma} \tag{25}$$

where the F's are the electromagnetic fields and N_c is the number of colors in QCD. This anomaly is directly responsible for the decay of the π°, η, and η' mesons into photon pairs, leading to a rigorous prediction in the chiral limit.

In the real world the current quark masses are non-vanishing, and have values of order $m_u \sim$ 5 MeV, $m_d \sim 10$ MeV, and $m_s \sim 150$ MeV. These masses make the π° and the η massive, and shift the mass of the η' due to explicit breaking of chiral symmetry, while SU(3) and isospin breaking induce mixing among the three mesons. The mixing is expressed in terms of three mixing angles. Writing on the left the eigenstates of the chiral limit, we have:

$$\pi^\circ_8 = \pi^\circ - \epsilon\eta - \epsilon'\eta'$$

$$\eta_8 = (\eta + \epsilon\pi^\circ)\cos\theta + (\eta' + \epsilon'\pi^\circ)\sin\theta$$

$$\eta_\circ = -(\eta + \epsilon\pi^\circ)\sin\theta + (\eta' + \epsilon'\pi^\circ)\cos\theta. \tag{26}$$

The mixing angle, ϵ, is predicted in ChPT to be approximately -0.55°. There are no rigorous predictions for the other two angles. In the large N_c limit they become: $\epsilon' \sim -0.25^\circ$ and $\theta \sim -22^\circ$, but the size of deviations from this limit is unknown. The 12 GeV Upgrade will allow significantly improved measurements of some of the parameters of this fundamental system of QCD.

Figure 41 (left) shows a Monte Carlo simulation of the expected angular distribution of $\eta \to \gamma\gamma$ events on ^{12}C, where the resolution and geometrical acceptance of the anticipated PRIMEX hybrid calorimeter were taken into account. A target thickness of 2×10^{19} carbon atoms/cm^2 was assumed, a beam current of 5 μA, and 30 days of data-taking. The simulation yields 72,500 $\eta \to \gamma\gamma$ events and a 0.7% statistical uncertainty on the width. The estimated systematic uncertainty is of order 2%. The uncertainty in the η–η' mixing angle from the combined measurements, $\pi^\circ \to \gamma\gamma$, $\eta \to \gamma\gamma$,

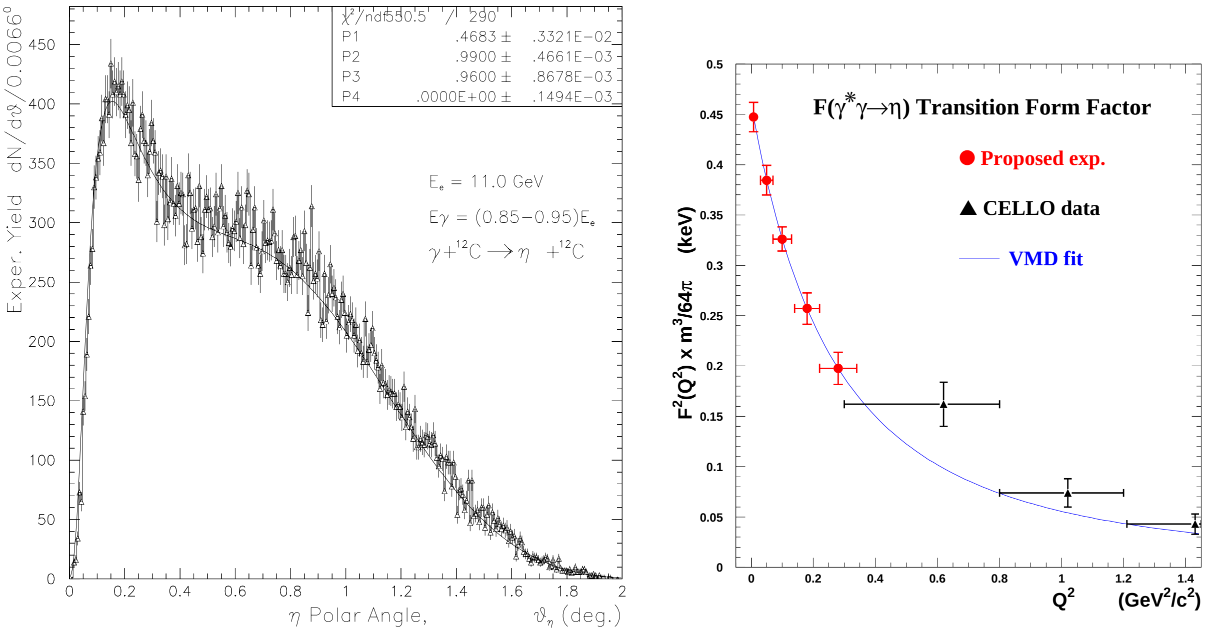

Figure 41: Left: Monte Carlo simulation of experimentally measured angular distribution of $\eta\gamma\gamma$ events on ^{12}C. Right: Projected uncertainties for a measurement of the η transition form factor.

and $\eta' \to \gamma\gamma$, would amount to $\sim 2\%$, to be compared with the present knowledge of this mixing angle of $\sim 8\%$.

In addition, using Primakoff electroproduction it is possible to gain access to the transition form factors $F_{\gamma\gamma^* P}$ for one off-shell photon. So far, the transition form factors have been determined in collider experiments [Be91], where $Q^2 \geq 0.6$ (GeV/c)^2, except for the recent form factor for the η' measured by the L3 collaboration [Ac98a] where Q^2 is as low as 0.05 (GeV/c)^2 but with a large error on Q^2. Measurements of the π°, η, and η' transition form factors at very low Q^2 [$\sim$ 0.001–0.5 (GeV/c)^2] will also enable the extraction of the slope of the transition form factor, and determine the size of the meson's electromagnetic interaction radius model-independently.

An example of an 11 GeV measurement of the η transition form factor is given in Fig. 41 (right). Such a determination of the slope of the π° and η form factors would allow one to uniquely fix an $\mathcal{O}(p^6)$ low-energy constant in the effective chiral Lagrangian [Bi88, Mo95]. With a measurement of the η' form factor slope, one could also have a clear test of how well the U(3) flavor symmetry implied by the large N_c limit holds. In this limit, the same $\mathcal{O}(p^6)$ low-energy constant should determine all slopes.

2.B.4 Low-Energy Quark-Hadron Duality

Understanding the structure and interaction of hadrons in terms of the quark and gluon degrees of freedom of QCD is one of the greatest unsolved problems of the standard model. While at present we can only rarely describe the physics of hadrons directly from QCD, we know that in principle it should just be a matter of convenience in choosing to describe a process in terms of quark-gluon or hadronic degrees of freedom. This fact is referred to as *quark-hadron duality*, and means that one can use either set of complete basis states to describe physical phenomena. At high energies, where the interactions between quarks and gluons become weak and quarks can be considered asymptotically free, an efficient description of phenomena is possible in terms of quarks; at low energies, where the effects of confinement make strongly coupled QCD highly nonperturbative, it is more efficient to work in terms of collective degrees of freedom, the physical mesons and baryons.

The duality between the quark and hadron descriptions reflects the relationship between confinement and asymptotic freedom, and is intimately related to the nature of the transition from nonperturbative to perturbative QCD. Achieving a better understanding of this transition was one of the main motivations for building Jefferson Lab.

Although the duality between quark and hadron descriptions is, in principle, formally exact, how this reveals itself specifically in different physical processes and under different kinematic conditions is the key to understanding the consequences of QCD for hadronic structure. The phenomenon of duality is quite general in nature and can be studied in a variety of processes, such as $e^+e^- \to$ hadrons, or semi-leptonic decays of heavy quarks [Vo88]. For the latter, one does not even need to invoke an averaging process – the results in terms of quark and hadronic variables are identical in the limit of infinitely heavy quarks [Is91]. One of the more intriguing examples, observed some 30 years ago, is in inclusive deep inelastic electron-nucleon scattering.

In studying deep inelastic scattering in the resonance region and the onset of scaling behavior, Bloom and Gilman [Bl70] found that the inclusive F_2 structure function at low W generally follows a global scaling curve that describes high-W data; the resonance structure function averages to this curve. Furthermore, the equivalence of the averaged resonance and scaling structure functions appears to hold for each resonance, over restricted regions in W, so that the resonance-scaling duality also holds locally. More recently, high-precision data on the F_2 structure function from Jefferson Lab [Ni00] have confirmed the earlier observations, demonstrating that duality works remarkably well for each of the low-lying resonances, including the ground state, to rather low values of Q^2 [~ 0.5 (GeV/c)^2]. This one-to-one correspondence is unlikely to generalize [Je00].

Bloom-Gilman duality can be thought of as a "truncated" version of duality, in the sense that one can apparently describe the physical process with a limited set of quark states, as in perturbative QCD calculations, or in terms of a few resonances which average to the quark result. Understanding duality therefore gives insight into the relationship between inclusive (deep inelastic scattering) and exclusive (resonance production) processes.

Bloom-Gilman duality can be formulated in the operator product expansion (OPE) language of QCD moments of structure functions, in which contributions are organized according to powers of $1/Q^2$ [Ru75]. The leading terms are associated with free quark scattering, and are responsible for the scaling of the structure function. The $1/Q^2$ terms involve interactions between quarks and gluons and hence reflect elements of confinement dynamics. The weak Q^2-dependence of the low moments of F_2 can be interpreted within the OPE as indicating that the non-leading, $1/Q^2$-suppressed, interaction terms do not play a major role even at low Q^2 [≈ 1 (GeV/c)^2].

On the other hand, while the OPE formalism allows us to organize hadronic observables in terms of an asymptotic expansion, it does not tell us *a priori* why certain matrix elements are small or cancel. This can only be addressed via numerical solutions of QCD or experiment. Since the details of quark–hadron duality are expected to be process-dependent [Je00], there is no reason to expect the accuracy to which it holds and the kinematic regime where it applies to be similar for different observables. In fact, there could be qualitative differences between the workings of duality in spin-dependent structure functions and spin-averaged ones, or for different hadrons – protons compared with neutrons, for instance. Data available relevant to these issues are inadequate: there are some data on the F_2 structure functions of the proton and deuteron [Ni00, Ni00a]; the data on the g_1 and g_2 structure functions (which correspond to cross-section differences) are either of poor quality or in kinematics not relevant to duality considerations; and there are essentially no data on the longitudinal-to-transverse structure function ratio, R. It is vital for our understanding of duality and its practical exploitation that the spin and flavor dependence of duality be established empirically.

An important consequence of duality is that the strict distinction between the resonance and deep inelastic regions is quite artificial – both regions are intimately related, and properly averaged resonance data can help us understand the deep inelastic region. For example, at $Q^2 = 1$ (GeV/c)^2 about 70% of the total cross section comes from the resonance region, $W < W_{\text{res}} = 2$ GeV. However, because of duality the resonances and the deep inelastic continuum conspire to produce only about a 10% correction to the lowest moment of the scaling F_2 structure function at the same Q^2 [Ji95a]. The resonances should therefore be viewed as an integral part of the deep inelastic scaling structure functions.

It is standard procedure in global analyses [Ma98, La95] of deep inelastic scattering to omit from the database the entire resonance region below $W = 2$ GeV. Including the vast quantity of data that has been excluded would not only improve the statistics significantly, but also decrease the uncertainties that arise from extrapolations into the regions excluded by the W cuts. This is especially pertinent for structure functions at large x_{Bj}, where for finite Q^2 one is always limited by the kinematics to $x_{Bj} < x_{Bj,\mathrm{res}} = Q^2/(W_{\mathrm{res}}^2 - M_N^2 + Q^2)$. In extending data to very large x_{Bj} at a finite Q^2 one always encounters the resonance region. A revolutionary application of duality, if one understands the workings of the resonance–deep inelastic interplay, would allow access to the region of very high x_{Bj}, which has not been possible in any other experiment.

The region of $x_{Bj} \approx 1$ is an important testing ground for mechanisms of spin-flavor symmetry breaking in valence quark distributions of the nucleon [Cl79, Me96, Is99]. With nuclear targets it would permit a measurement of the nuclear medium modification of the nucleon structure function (nuclear EMC effect) [Ge95] at large x_{Bj}, where the deviation from unity of the ratio of nuclear to nucleon structure functions is largest and the sensitivity to different nuclear structure models greatest.

Another largely unexplored domain with potentially broad applications is the production of mesons (M) in semi-inclusive electron scattering, $eN \to e'MX$. At high energy the scattering and production mechanisms factorize: the cross section at leading order in QCD becomes a simple product of the structure function, which gives the probability of finding a quark in the nucleon, and a quark $\to$ meson fragmentation function, or the probability that the quark hadronizes into the meson M. The usefulness of semi-inclusive production lies in its ability to identify individual quark species in the nucleon by tagging specific mesons in the final state, so that both the flavor and spin of quarks and antiquarks can be uniquely determined.

The extent to which factorization applies at lower energy is an open question, and the signatures of duality in the resonance region of semi-inclusive scattering need to be investigated. It is imperative therefore that both of these questions be answered experimentally. It is worth stressing that confirmation of factorization and truncated duality would open the way to an enormously rich semi-inclusive program, allowing unprecedented spin and flavor decomposition of quark distributions. Such a program is discussed briefly below.

CEBAF at 12 GeV would provide a unique opportunity to shed light on all the issues associated with Bloom-Gilman duality. Several examples are discussed in greater detail in the following.

Recent results

Substantial progress has been made over the past twenty years both theoretically in understanding QCD and experimentally in determining the scaling behavior of the F_2 structure function. By combining these data with new, precision, resonance data from Jefferson Lab [Ni00], it has been possible to revisit quark-hadron duality more quantitatively, addressing the recent theoretical interest in the topic (see, for example, [Ji95a, Be95, We96, Ri98, Co98, Ca95a, An96a]). Parameterizations of deep inelastic data were found to equal (within 10%) an average of the resonance region F_2 spectra at disparate kinematics (see Fig. 42). This echoes the original Bloom and Gilman observation of duality. The above results – namely that duality seems to be holding and the resonances average to the perturbative scaling curve – indicate that higher twist contributions to the lower F_2 moments are small or cancelling on average, even in the low-Q^2 regime where they should be largest due to their $1/Q^2$ behavior. Higher twists can be viewed in this light as deviations from duality.

Although the dynamical origin of local duality is not understood, it seems intricately intertwined with the behavior between the $Q^2 \to 0$ limit, where only elastic scattering contributes to the moments, and $Q^2 > 5$ (GeV/c)^2, where deep inelastic scattering already dominates the lower moments [Ar00]. In the region $0.2 < Q^2 < 5$ (GeV/c)^2 the nucleon resonances contribute to a substantial part of the moments, and, on average, seem to be indistinguishable from deep inelastic scattering at $Q^2 > 1$ (GeV/c)^2. This is consistent with the findings of Bloom and Gilman, as shown quantitatively in Ref. [Ni00] for the second moment. In the $Q^2 < 1$ (GeV/c)^2 transition region, the contribution of the coherent elastic peak to the second moment dies out, whereas the nucleon resonances already show the onset of their duality behavior, in that they tend to oscillate [already at $Q^2 \approx 0.2$ (GeV/c)^2] around a single smooth curve, resembling neutrino/antineutrino xF_3 data or a valence-like sensitivity only [Ni00a]. Furthermore, the nucleon resonances shuffle their strength around such that, at $Q^2 \approx 1$ (GeV/c)^2, they have, if properly averaged, reached the same behavior as a function of x_{Bj} and Q^2 as one would expect from deep inelastic data.

Thus, the world's data on F_2 are reasonably well described down to $Q^2 \sim 1$ (GeV/c)^2 by models obtained by fits to deep inelastic scattering. This includes the nucleon resonance data, which average to a similar scaling curve due to local duality. Local duality seems to describe the transition from the elastic contribution only, at $Q^2 = 0$, through the excitations of the nucleon resonances, into the scaling region.

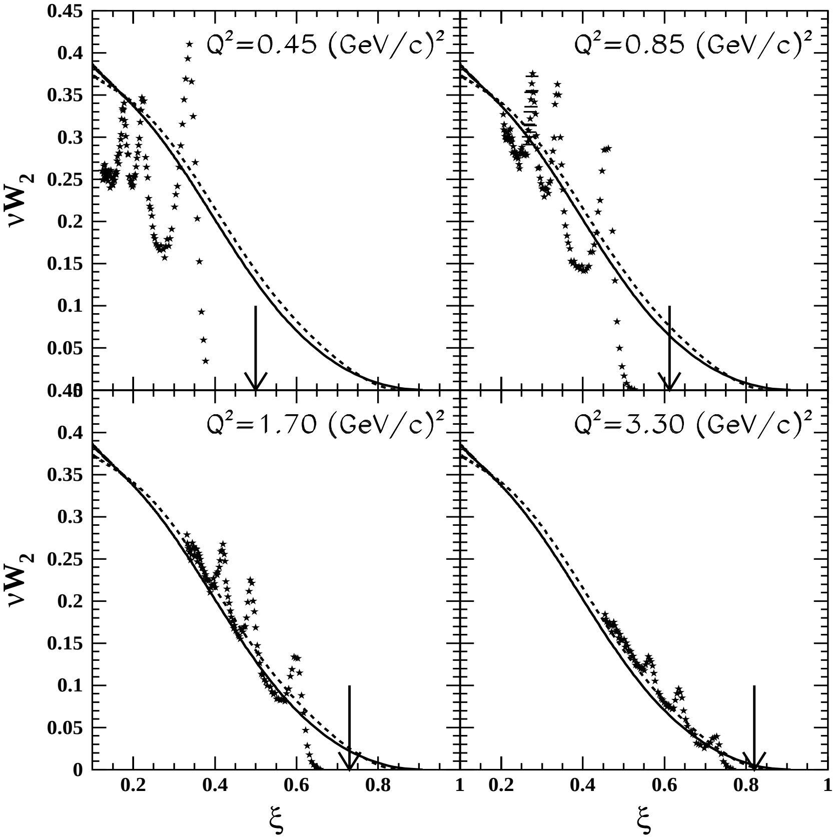

Figure 42: Sample hydrogen νW_2 structure function spectra obtained at $Q^2 = 0.45, 0.85, 1.70$, and 3.30 (GeV/c)^2 and plotted as a function of the Nachtmann scaling variable ξ. Arrows indicate elastic kinematics. The solid [dashed] line represents the NMC fit of deep inelastic structure function data at $Q^2 = 10$ (GeV/c)^2 [$Q^2 = 5$ (GeV/c)^2].

Duality in unpolarized structure functions

While duality has been studied extensively for the F_2 structure function at Jefferson Lab, and approved proposals exist to continue this work at lower Q^2 values, duality remains essentially untested for the F_L (or F_1) structure functions. The reason for this is that no relevant data exist; no separated measurements exist at x_{Bj} values $\gtrsim 0.5$ below $Q^2 \approx 10$ (GeV/c)^2.

There are predictions [Ca95a] and some scant experimental evidence [En00] that the longitudinal structure function exhibits duality. In contradiction, there are data and models [Wh92, Ta96] that hint that higher twist effects may be quite large in the longitudinal structure function at low Q^2 values. Unfortunately, no measurements are available to sort out this controversy.

The necessary measurements require separation of the longitudinal and transverse components of the cross section, traditionally accomplished by linear fits to data at fixed (x_{Bj},Q^2) values but differing virtual-photon polarization ϵ, requiring a wide range in beam energies and spectrometer angles. An 11 GeV CEBAF is the perfect machine for carrying out these measurements. The longitudinal structure function can be measured precisely in the range $0.1 < Q^2 < 10$ (GeV/c)^2, fully covering both the large x_{Bj} regime and the nucleon resonance region.

Evolution of the parton distribution functions at large x_{Bj}

Parton distribution functions (PDFs) are determined experimentally from the cross sections for a number of hard processes by using a procedure referred to as *global fitting* [Ma98, La95, Gl98]. A fully quantitative description of the proton structure in terms of PDFs relies, however, on our ability to unravel the Q^2-dependence of the data in detail. In particular it is important to obtain more quantitative information on the boundary or "transition" regions of x_{Bj} and Q^2 where perturbative QCD (pQCD) evolution regulated by the Q^2-evolution [Gr75] equations can no longer be expected to describe the main mechanism responsible for the Q^2-dependence of the data, and nonperturbative contributions become important. In pQCD analyses performed to date, higher-twist terms have been extracted from DIS data by applying a cut in the kinematics at $W^2 \geq 10$ GeV^2 [Vi92, Al00]. In Refs. [Ni99, Li00] it was shown, however, that only a relatively small higher-twist contribution, consistent with the one obtained in Ref. [Vi92, Al00], is necessary in order to describe the entire set of F_2 structure function data, including the low-W^2 region which is dominated by nucleon resonances; this is consistent with the applicability of duality. Detailed analyses of large x_{Bj} evolution would be possible with an 11 GeV beam at JLab. Given a better constraint on the Q^2-dependence in this kinematic region, one could, as mentioned also in Section 2.B.1, derive parameterizations for the PDFs at large x_{Bj} directly from the data without necessarily resorting to theoretical inputs [*e.g.*, $F_2 \approx (1 - x_{Bj})^a$ with $a \approx 3$].

Duality in spin-structure functions

Deep inelastic scattering experiments in a long series dating back to the late seventies [Al76, Ba83, As89, An93, Ab98b, Ad94a, Ab97, Ab99a, Du91, Ar97] have studied the spin structure functions. The proposed 11 GeV JLab beam energy opens up opportunities for additional studies of the spin structure in the region of the resonances, particularly in connection with the question of polarized parton-hadron duality.

What is required for new, detailed studies of duality, similar to those already performed for the F_2 structure function, are additional spin-structure function data in the resonance region. To obtain higher-order moments to utilize in an OPE analysis, data at large x_{Bj} are imperative. A large body of resonance region data is also required in order to determine whether the g_1, g_2 data oscillate around a global curve, and whether this curve corresponds at moderate Q^2 values to the curve obtained from deep inelastic scattering. The questions of whether the polarized structure functions will exhibit local duality and/or valence-like sensitivity are completely unresolved.

The main advantages of a high-energy beam are that it opens up a wide range of kinematic coverage at large x_{Bj} and the resonance region for duality studies and that it provides the ability to reach larger values of Q^2 at smaller scattering angles than at low energy, with the attendant larger cross sections. Studies of possible 11 GeV measurements of the spin asymmetry $A_1^{p,n}$, assuming duality to hold, indicate a dramatic increase in x_{Bj} range afforded by utilizing duality-averaging. The 11 GeV beam energy will provide a good cross check of the lower x_{Bj} region, and allow extension of these measurements up to $x_{Bj} \sim 0.9$, using either solid-state polarized hydrogen and deuterium targets or high-pressure gaseous ^{3}He targets in conjunction with either the spectrometers in Halls A and C or the upgraded CLAS in Hall B.

Duality and pions at high transverse momenta

While the phenomenon of duality in inclusive scattering is well established, duality in the related case of meson photo- and electro-production has not been tested experimentally. First we concentrate on reactions where the pion exits with transverse momentum large enough that it is directly produced at short range and exits the reaction in kinematic isolation from other reaction products [Br99]. Direct pion production is calculable within pQCD by virtue of the pion's large transverse momentum: the cross section for hard pion photoproduction can be written as a kinematic factor times a scaling function [Af00], where the latter is a function that, in general, depends on several variables but in the limit of large t and large m_X depends only on the variable x_{Bj} (up to logarithmic corrections).

A goal here is to see what happens at smaller recoiling mass m_X, particularly in the resonance region. The scaling curve will become bumpy at low m_X, and one may ask whether the resonances, averaged over their own widths, reproduce the established scaling curve, and whether the resonance peak-to-background ratio remains constant for a given resonance as $|t|$ increases.

One needs, of course, to have a scaling region where m_X is large and direct pion production is dominant. One problem when the energy or transverse momentum is not high is a background coming from soft processes, which can be estimated assuming vector-meson dominance (VMD). One can reduce the VMD background by having the photon off shell. For a 12 GeV incoming beam, preliminary estimates based on earlier work [Af00a] indicate that with photons space-like by 1 $(\mathrm{GeV}/c)^2$ there is a significant scaling region with m_X between 2 and 3 $(\mathrm{GeV}/c)^2$ and with direct pion production dominating both the fragmentation and VMD processes. There is also a resonance region with m_X between 1 and 2 $(\mathrm{GeV}/c)^2$. Thus, an 11 GeV beam at CEBAF would clearly allow this category of semi-inclusive duality experiments to be performed.

Fragmentation duality

Related to the above case is semi-inclusive deep inelastic scattering in parallel kinematics. Here a parton exits the initial reaction, and then, at some distance later, fragments into a jet of hadrons, one of which is the observed pion. This is in contrast to the process described above, where, at large transverse momentum, short-range direct production dominates. Here again duality would manifest itself with an observed scaling in the meson plus resonance final state.

Assuming one is in a kinematic region that mimics single-quark scattering, the question here (in analogy with the inclusive scattering case) is whether the remaining part of the process can be described in terms of a process where the struck quark hadronizes into the detected meson. As mentioned above, such a factorization approach is strictly valid at asymptotic energies only, as at low energies there may not be clear separation of the target and current fragmentation regions [Sl88, Fr94a]. However, similar to the inclusive case (where the nucleon resonances average at low energies to the scaling curve), the nucleon resonances remaining in the final state after the production of a fast meson may average to the fragmentation function. Where the usual Bloom-Gilman duality involves comparison of a structure function over some range in Bjorken x_{Bj} at low W^2 (and hence low Q^2) with that structure function over the same range in x_{Bj} but at high W^2

(and Q^2), we may find a similar behavior in terms of the fragmentation functions $D_i^h(z, Q^2)$ in the case of semi-inclusive meson electroproduction. The variable $z = E_h/\nu$, where ν is the electron energy loss. (For orientation, in the limit of $z \rightarrow 1$, one approaches the exclusive limit.) Given the (x_{Bj}, Q^2)-dependent part, we can look for a truncated duality behavior in the (z, Q^2)-dependent part.

In practice, we will extract the meson yield dN^m/dz over a range of z at several values of x_{Bj} and Q^2. This allows the comparison of dN^m/dz in the resonance region to that in the deep inelastic regime, which we obtain from the quark model or from parameterizations of data. Sparse information from both older Cornell data and recent JLab data strongly suggests that 6–11 GeV will provide the right kinematic region to study the onset of the duality phenomenon in meson electroproduction [Be75, En00a].

Here the combination of two high-momentum spectrometers reaching the smallest angles possible (the HMS-SHMS combination) is of prime importance. This will enable us to verify meson duality, and, if also quantified, access fragmentation functions and parton distributions (through a flavor decomposition) in hitherto inaccessible regions.

2.B.5 Low-Energy Fragmentation Functions

The production of mesons (M) in semi-inclusive electron scattering, $eN \rightarrow e'MX$, yields insights into the quark structure of the nucleon that are unavailable in inclusive measurements. As mentioned in Section 2.B.4, at asymptotic energy the scattering and production mechanisms factorize into a parton distribution function and a quark → meson fragmentation function. The extent to which factorization applies at lower energy is an open question. Nonetheless, confirmation of factorization (or truncated duality) at lower energies would open the way to an enormously rich semi-inclusive program, allowing unprecedented spin and flavor decomposition of quark distributions. By measuring deep inelastic π^+ and π^- yields from hydrogen and deuterium targets, the HERMES experiment demonstrated sensitivity to the light-quark-sea flavor asymmetry comparable to the Fermilab E866 Drell-Yan measurement at much higher Q^2 and ν. There is, additionally, some preliminary experimental indication that factorization seems to hold at lower than asymptotic energies, provided one makes an additional cut in z [Ac98, En00a]. With the high luminosity available at Jefferson Lab, a high-precision separation of the x_{Bj} and z-dependence of meson production cross sections becomes possible, allowing tests of factorization at low (Q^2, ν). Figure 43 shows the quality of the data we might obtain at two fixed values of z, as a function of x_{Bj}, to probe the assumption of factorization. Additionally, one can carry out more complete tests of independent

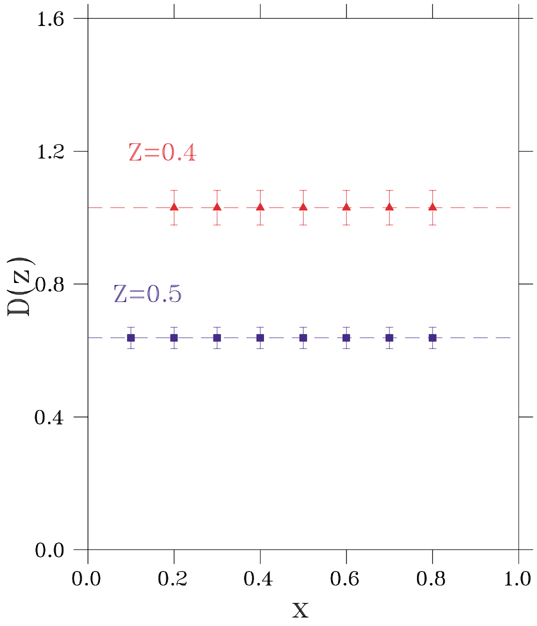

Figure 43: The projected mean fragmentation function as a function of x_{Bj} for two bins in z. The uncertainties represent statistics only for a two-day measurement for each bin of z.

fragmentation [Ch99] in which the asymmetry of the total charged-pion yield is compared to the proton-neutron difference ratio of polarized and unpolarized deep inelastic structure functions.

To exhibit the importance of understanding the onset of factorization, we highlight two examples in Fig. 44: (i) a measurement of semi-inclusive pion asymmetries using polarized proton and deuterium targets in CLAS, to extract the ratio of the polarized to unpolarized valence down-parton distribution function, adding complementary information to the measurement of A_1^n described before; and (ii) a projected extraction of the flavor asymmetry of the light-quark sea from semi-inclusive deep inelastic scattering, assuming factorization (or, less strictly, fragmentation duality) works for $Q^2 > 2$ (GeV/c)^2 and $z > 0.3$. The latter measurement could be carried out either in Hall A or Hall C in less than one month of beam time. Please note that only statistical uncertainties are shown. Systematic uncertainties due to nuclear corrections are expected to be a substantial contribution to the flavor asymmetry for $x_{Bj} \geq 0.3$. With an 11 GeV JLab beam energy one could easily extend these measurements to other mesons, such as charged kaons, and to other nuclei, to investigate the nuclear dependence of semi-inclusive meson production.

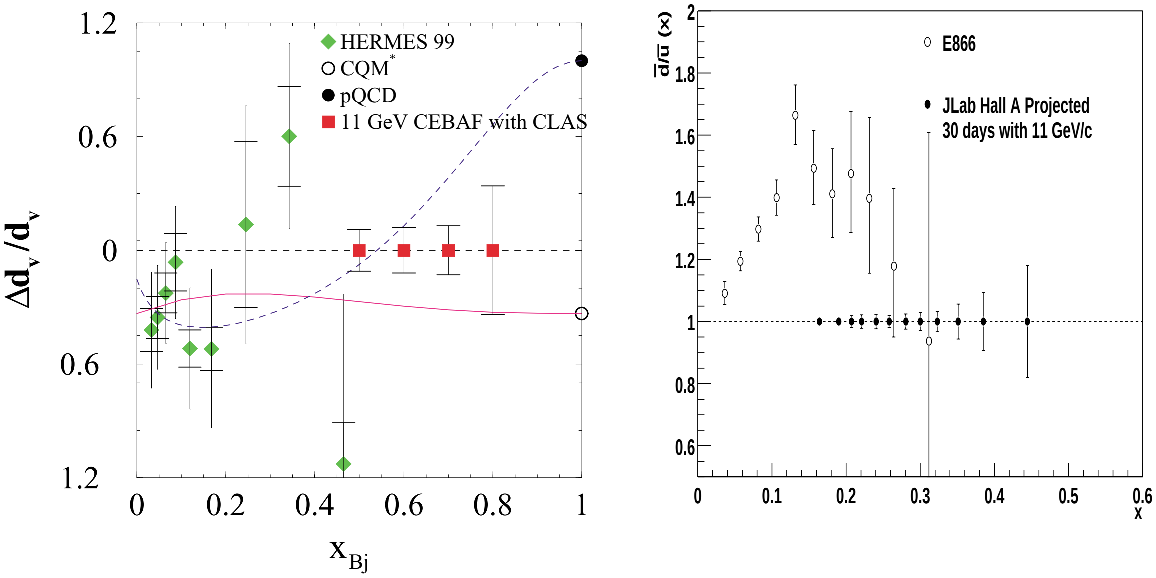

Figure 44: Examples of low-energy fragmentation. *Left*: The ratio of polarized to unpolarized valence down parton distribution functions. The solid squares represent the predicted accuracy (dominated by systematics for $x_{Bj} < 0.8$) for an 80 day measurement in Hall B. The solid curve uses wavefunctions from a constituent quark model. The dashed curve uses pQCD-constrained fits to the world data set. *Right*: The projected precision of $\bar{d}/\bar{u}$ extractions (right) assuming either fragmentation duality or factorization work with strict Q^2 and z cuts, and an 11 GeV JLab beam energy. The experiment would take one month of beam time, either in Hall A (shown here) or Hall C. The published measurements of E866 [Ha98] are shown for comparison. Only statistical uncertainties are shown.

2.C Campaign 3: Understanding the Origin of the *NN* Force

At large distances ($\gtrsim$1.5 fm), the origin of nuclear forces is well understood. Meson exchange and, in particular, pion exchange provide us with a coherent and powerful framework that has been confirmed elegantly by the observation of meson-exchange currents: the electromagnetic probe couples to (and reveals) the charged mesons when they travel between two hadrons.

In contrast, the mechanism controlling the NN interaction for short distances could be very different, and remains to be identified. Some of the simplest possibilities include (see Fig. 45): that the three quarks in each proton interact only by gluon exchange, that one quark is exchanged between each nucleon, and that a quark "Z"-graph exchange occurs (this would include the known, long-range meson-exchange force between nucleons). In some of these cases the nucleons and the hadrons lose their identity, and direct interactions between their constituents become relevant. When two quarks in different hadrons come close enough (within the gluon correlation length), they exchange gluons which have no time to recombine into a pomeron. Alternately, the quarks may be interchanged between the two hadrons without having time to recombine into a meson. Experiments are needed to guide the development of models that describe this nonperturbative sector of QCD.

Experiments addressing the origin of the short-distance behavior of the nuclear force are already an important part of the CEBAF research program at 6 GeV. Examples include:

- The study of meson photoproduction and of photodisintegration of few nucleon systems at large angles is sensitive to quark-interchange mechanisms.
- The study of strangeness photo- and electro-production takes advantage of the creation and the propagation of the strange quark in nuclear matter. Since it is not a normal building block of matter, the strange quark acts as an impurity whose motion traces the nature of the flow of energy and momentum transfer between hadrons.
- The study of the creation and the propagation of color dipoles of small transverse size gives access to multi-gluon exchange mechanisms that may lead to van der Waals forces between overall color singlets. This issue is being addressed through ϕ meson photoproduction at large momentum transfer and through attempts to observe color transparency at moderate Q^2.

While these studies will continue to be pursued using 11 and 12 GeV beams from CEBAF, the increased energy and duty factor open two important new opportunities: the study of charm photoproduction near threshold, and the comprehensive study of color transparency.

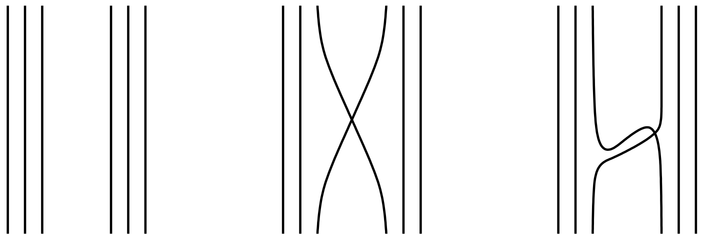

Figure 45: Three of the simplest interactions between two nucleons: pure gluon exchange, quark exchange, and meson exchange.

2.C.1 J/ψ Photoproduction near Threshold

The threshold production of charmonium and open charm production open up a new window into QCD dynamics; in particular, these reactions are sensitive to multiquark, gluonic, and so-called "hidden color" correlations in nucleons and nuclei[4]. In contrast to diffractive charm production at high energy, which tests the behavior of the gluon structure functions at small x, charm production near threshold tests the structure of the target near $x = 1$ and its short-range behavior.

This difference results from the kinematics of the reaction products. For J/ψ production off the nucleon, the threshold energy is $E_\gamma = 8.20$ GeV, and because of the large mass of the charmed quark [$m_c \approx 1.5$ (GeV/c)^2] the $c\bar{c}$ fluctuation of the photon travels over a short coherence length $l_c \cong 2E_\gamma/4m_c^2 = 0.36$ fm (see Fig. 46). The large mass of the charmed quark also imposes a small transverse size $r_\perp \sim 1/m_c = 0.13$ fm on this fluctuation. The minimum value allowed for the momentum transfer is large [$-t_{\rm min} \sim 1.7$ (GeV/c)^2 at threshold, and ~ 0.6 (GeV/c)^2 at $E_\gamma = 10$ GeV]. Thus charm production near threshold implies a small impact parameter ($b \sim 1/m_c \sim 0.2$ fm). All five valence quarks (the two heavy charm quarks in the probe and the three light quarks in the target) must be in the same small interaction volume. As a consequence, all the quarks must be involved in the reaction mechanism. For nucleon targets, this implies that three-gluon exchange may dominate two-gluon and one-gluon exchange, and open the way for the study of correlations between valence quarks.

Relying on the short-distance behavior of hadronic matter [Ho97, Br92], Brodsky *et al.* [Br01] showed that the charm production cross section can be cast in a simple form using general properties of perturbative QCD. For two-gluon exchange, the cross section of the $\gamma p \to J/\psi p$ reaction takes

---

[4] The "hidden color" language must be used with caution. With color treated as a quark label, a multiquark system can be expanded with fixed clusters in a color basis or in a basis where only color singlet clusters are used. These two bases are equivalent.

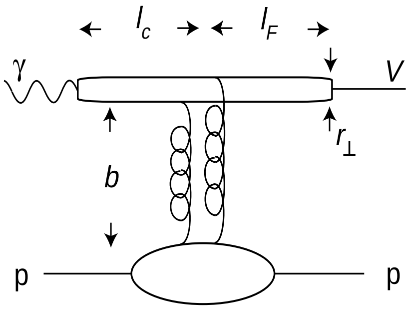

Figure 46: The characteristic time scales in J/ψ production on the proton.

the form:

$$\frac{d\sigma}{dt} = \mathcal{N}_{2g}\frac{1}{16\pi}\frac{(1-x)^2}{R^2\mathcal{M}^2}F_1^2\left(\frac{t}{4}\right) \tag{27}$$

while for three-gluon exchange it takes the form:

$$\frac{d\sigma}{dt} = \mathcal{N}_{3g}\frac{1}{16\pi}\frac{(1-x)^0}{R^4\mathcal{M}^4}F_1^2\left(\frac{t}{9}\right) \tag{28}$$

where $x \approx (2m\mathcal{M}+\mathcal{M}^2)/(s-m^2)$ and $\mathcal{M}$ is the mass of the $c\bar{c}$ pair. The relative weight of the two- and three-gluon exchange terms is controlled by the probability $1/R^2\mathcal{M}^2$ that two quarks in the proton (of radius $R \sim 1$ fm) are found within a transverse distance $1/\mathcal{M}$ (see [Br79]). $F_1(t)$ is the isoscalar proton form factor. This argument takes into account the fact that the momentum transfer is shared between two or three valence quarks in the proton. This implies that the t distribution for the three-gluon exchange cross section is flatter than the t distribution for the two-gluon exchange cross section. The upper limit of the normalization coefficient, $\mathcal{N}$, was estimated by assuming that each channel saturates the experimental cross section measured at Stanford [Ca75] and Cornell [Gi75] around $E_\gamma = 12$ GeV. As depicted in Fig. 47, this conjecture is consistent with the limited data that are available [Ca75, Gi75, An77]. Clearly 12 GeV beams from an upgraded CEBAF will allow a more comprehensive determination of the J/ψ photoproduction cross section between threshold and 12 GeV.

On few-body targets each exchanged gluon may couple to a colored quark cluster and reveal the hidden color part of the nuclear wavefunction, a domain of short-range nuclear physics where nucleons lose their identity. It is striking that in $\gamma d \to J/\psi pn$ the $|B_8\overline{B_8}\rangle$ hidden color state of the deuteron couples naturally by two gluons to the $J/\psi pn$ final state [La94] (see Fig. 48). Such a contribution may dominate subthreshold production, since the high momentum of the nucleon suppresses quasifree mechanisms. The threshold for J/ψ production on deuterium is ~ 5.65 GeV, while on heavy nuclei the threshold is simply the J/ψ mass, 3.1 GeV.

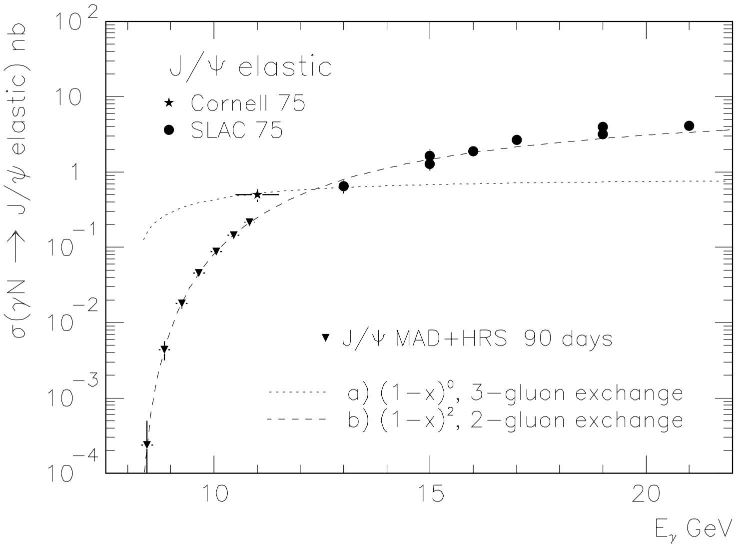

Figure 47: The variation of the cross sections of J/ψ photoproduction near threshold for two- and three-gluon exchange mechanisms. The inverted triangles show the expected accuracy at CEBAF with 11 GeV beam.

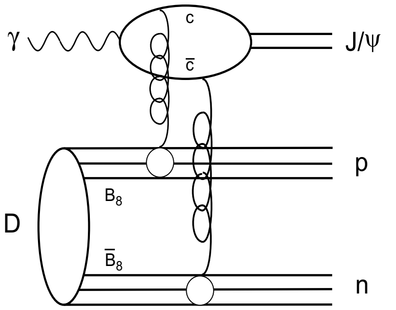

Figure 48: The simplest diagram to reveal hidden color state in deuterium [La94].

Table 3: The values of nuclear transparencies for ψ propagation, calculated in the model used by the SLAC measurement [An77b], for three values of $\sigma_{\psi N}$. The last column presents the expected statistical error, $\delta\sigma_{\psi N}$ for a $\sigma_{\psi N}$ measurement at CEBAF using 11 GeV beam, assuming a statistical error of 3% for the yields on every target.

	A						
	9	12	27	63	108	207	$\delta\sigma(\sigma_{\psi N})$, mb
T for $\sigma_{\psi N}$=1.0 mb	0.982	0.980	0.974	0.963	0.952	0.929	0.28
T for $\sigma_{\psi N}$=3.5 mb	0.938	0.931	0.908	0.870	0.833	0.751	0.24
T for $\sigma_{\psi N}$=7.0 mb	0.876	0.863	0.816	0.740	0.665	0.502	0.17

The formation length, l_F, over which the $c\bar{c}$ pair evolves into a J/ψ after its interaction with a nucleon, is given by:

$$l_F \cong \frac{2}{m_{\psi'} - m_{J/\psi}} \left[\frac{E_{J/\psi}}{2m_c} \right] \cong 0.22 E_\gamma \tag{29}$$

Near threshold l_F is about 1 fm, closer to the size of the nucleon than to the size of the nucleus. This is the ideal situation for determining the scattering cross section of a full-sized charmed meson on a nucleon, in contrast to the situation at higher energies where the cross section is sensitive to the interaction of a compact $c\bar{c}$ pair with the entire nucleus. The study of the A-dependence of the J/ψ photoproduction cross section at SLAC at 20 GeV [An77b] gave $\sigma_{J/\psi} = 3.5 \pm 0.8 \pm 0.5$ mb. Unfortunately, the need to subtract a large calculated background and the lack of information on the J/ψ kinematics makes it impossible to disentangle coherent and incoherent photoproduction in this experiment. The study [Ge92] of hadroproduction gave $\sigma_{J/\psi} \approx 7$ mb, but after correction [Hu98] for energy loss of the incoming hadron and coherence effects this value went down to ≈ 3.6 mb.

On the theoretical side, QCD calculations [Kr99] predict that $\sigma_{J/\psi} \approx 0.3$ mb at 20 GeV, and that it falls rapidly as the energy is reduced. In contrast, a calculation by Brodsky [Br97] based on the van der Waals potential yielded $\sigma_{J/\psi} \approx 7$ mb at low energies. Both the disagreement between these theoretical estimates and the poor quality of the available data call for a new measurement of J/ψ photoproduction on several nuclei in the range of energy $E_\gamma \approx 10$ GeV, with good process identification and determination of the J/ψ momentum. The systematic error of such a measurement will be smaller than in Ref. [An77b]. The statistical error was estimated using the same model for nuclear transparency as was used for the SLAC experiment [An77b]. This model, based on a semiclassical eikonal approximation for the rescattering [Go69, La72], predicts the values for nuclear transparency, $T = \sigma_{\gamma A}/(A \cdot \sigma_{\gamma N})$, given in Table 3.

Even though the $c\bar{c}$ pair is created with rather high momentum at threshold, it may be possible

Table 4: Experimental resolutions, σ, of important physics variables in the charm experiments possible at JLab

Setup	$\sigma(M)/M$	$\sigma(E_\Psi)/E_\Psi$	$\sigma(E_\gamma)/E_\gamma$	σt (GeV/c)^2
Hall D, tagged beam	0.010	0.004	0.001	0.03
HRS+MAD	0.002	0.001	0.002	0.014
ECAL	0.035	0.007	0.01	0.11

to observe reactions where the pair is captured by the target nucleus, forming "nuclear-bound quarkonium" [Br90]. This process should be enhanced in subthreshold reactions. There is no Pauli blocking for charmed quarks in nuclei, and it has been estimated that there is a large attractive van der Waals potential binding the pair to the nucleus [Lu92]. The discovery of such qualitatively new states of matter would be very significant.

Besides possible applications in connected domains (for instance, the knowledge of the J/ψ-N scattering in the search for the quark-gluon plasma), all these studies select gluonic exchange mechanisms between hadrons or quark clusters. The observation of a gluonic potential between color-neutral states is of utmost importance as it would open up the possibility to trace part of the short-range nucleon-nucleon interaction to such a color force. Only the high intensity and duty factor of the beams that will be available from an upgraded CEBAF make it possible to realize the new experiments that are essential for the exploration of this frontier of our knowledge.

The issue of experimental feasibility has been worked out in detail [Ch01]. Three options were evaluated for the detector: Hall D, HRS+MAD of Hall A, and a dedicated, calorimeter-based experiment called "ECAL" here for brevity. These three options provide the resolutions for the key physics variables as shown in Table 4. The expected particle rates and background estimates are presented in Table 5.

In the open charm sector both Hall D and HRS+MAD would be able to do the measurement, depending on the background levels. The 4π acceptance of the Hall D detector and the energy resolution of its tagged beam could help to reduce the background considerably. However, the HRS+MAD mass resolution would be better. It is not clear yet which option is more advantageous. For J/ψ studies, the best option is the dedicated experiment (ECAL). With ECAL the complete program can be accomplished, including the search for rare phenomena like hidden color. Nevertheless, a pilot measurement of the "elastic production" cross section might be done with Hall D, and the A-dependence can be measured with HRS+MAD.

Table 5: A comparison of the experimental options to study charm at JLab. The background-to-signal ratio was estimated for 11 GeV photons. The last column shows the number of days of data-taking needed to achieve an average relative statistical accuracy of 10% in the cross-section measurement for an energy interval of 0.4 GeV above the threshold. This estimate has not been made for open charm since the background is, at the moment, uncertain.

Process	Setup	Recoil	$\frac{\text{Background}}{\text{signal}}$	$d\sigma/dt \propto (1-x)^2$		$d\sigma/dt \propto (1-x)^0$	
				events/ 90 days	days needed	events/ 90 days	days needed
$\gamma p \to J/\psi p$							
$J/\psi \to e^+e^-$	ECAL	Yes	0.10	$0.6{\cdot}10^5$	10	$3.0{\cdot}10^5$	0.2
$J/\psi \to l^+l^-$	HRS+MAD	No	<0.02	$2.4{\cdot}10^3$	190	$2.8{\cdot}10^4$	45
$J/\psi \to l^+l^-$	D tag	Yes	0.07	$2.6{\cdot}10^2$	640	$2.1{\cdot}10^3$	40
$\gamma p \to \Lambda_c^+ \overline{D}^\circ$							
$\overline{D}^\circ \to K^+\pi^-$	HRS+MAD	No	0.05	$2.9{\cdot}10^3$	-	$2.9{\cdot}10^4$	-
$\overline{D}^\circ \to K^+\pi^-$	D tag	Yes	0.25	$5.4{\cdot}10^2$	-	$3.4{\cdot}10^3$	-

2.C.2 Color Transparency

One of the fundamental predictions of QCD is the existence of color transparency (CT), a novel QCD effect that is predicted to have its most unexpected manifestation in $(e, e'p)$ at very high energy. Under the right conditions, three quarks, each of which would have interacted very strongly with nuclear matter, pass right through it. This can happen because three quarks can have a small color dipole moment. The prediction of color transparency relies on three key elements: (i) the weakness of the interaction of small, color singlet objects at high energies, (ii) the presence of small-transverse-size, pointlike configurations (PLC) in mesons and baryons, and (iii) a large coherence length at high energies which leads to the possibility of considering the scattering states as frozen during the collision.

Experiments at HERA, which studied the production of vector mesons by longitudinally polarized photons, have convincingly confirmed [Ab99] pQCD predictions on the presence of PLC in vector mesons and the smallness of the interaction between a small-size $q\bar{q}$ dipole and a nucleon. Another confirmation of the dominance of PLC and the weakness of small-size $q\bar{q}$-N interaction came from the E971 experiment at FNAL on high-p_t di-jet production from nuclei in the $\pi + A \to 2$ jets $+A$ reaction at $E_\pi =$ 500 GeV [As99]. In this reaction CT effects lead [Fr93a] to a platinum/carbon cross-section ratio seven times larger than expected if soft physics would dominate. Evidence for color transparency effects was also reported in the incoherent vector-meson production in DIS scattering of muons [Ad95]. These observations have firmly established the general concepts of CT. However, there are two fundamental questions yet to be answered: at what energy does CT begin to play a role; and is CT also a characteristic of nonperturbative QCD. These questions are intimately related to the understanding of the mechanism of the transition from the constituent-quark regime to the current-quark regime and to the origin of hadronic (NN) interactions at short distances. The 12 GeV Upgrade will cover the wide range of intermediate energies necessary to pursue an unambiguous answer to these questions. The major directions for the study of CT at intermediate energies are:

- Observation of CT in the propagation of both $q\bar{q}$ and qqq color-neutral states (the last phenomenon is absent in QED).
- Study of the interaction cross sections of small objects.
- Study of the dynamics of the expansion of small sized $q\bar{q}$ and qqq configurations.

The simultaneous investigation of $(e, e'N)$, $(e, e'NN)$ and coherent vector-meson production reactions will significantly contribute to the understanding of those mechanisms.

Color transparency in $(e, e'N)$ and $(e, e'NN)$ reactions

To define the momentum transfers, Q^2, at which the PLC starts to dominate the wavefunction of nucleons, the study of quasiexclusive hard reactions $l(h) + A \to l(h) + p + (A-1)^*$ was suggested in Refs. [Br82, Mu82]. If the energy and momentum transfer are large enough, one expects that both the projectile and the ejected nucleon travel through the nucleus in pointlike configurations, resulting in a cross section proportional to A. To determine the transparency the ratio $T = \sigma^{\mathrm{Exp}}/\sigma^{\mathrm{PWIA}}$ is measured, where σ^{Exp} is the measured cross section, and σ^{PWIA} is the cross section calculated when no final-state interactions are taken into account. An onset of CT would imply an increase of T with the ejectile momentum. Indeed, initial [Ca88] and subsequent [BNL98, BNL00] measurements of T in $A(p, 2p)X$ reactions by the EVA collaboration at BNL support the increase of T for p_{inc} between 6 and 10 GeV/c (but also show a subsequent decrease in T for higher p_{inc}). A set of $A(e, e'p)$ experiments aimed at looking for color transparency were performed at SLAC [Ne95] and JLab [JL99]. The maximum Q^2 in these experiments was ≈ 8 (GeV/c)^2. The data are consistent with calculations that do not include CT effects, but they are not sufficiently accurate or at high enough Q^2 to rule out color transparency at the level predicted by several realistic CT models.

The 12 GeV Upgrade of CEBAF will improve the situation by pushing the measurement of T to

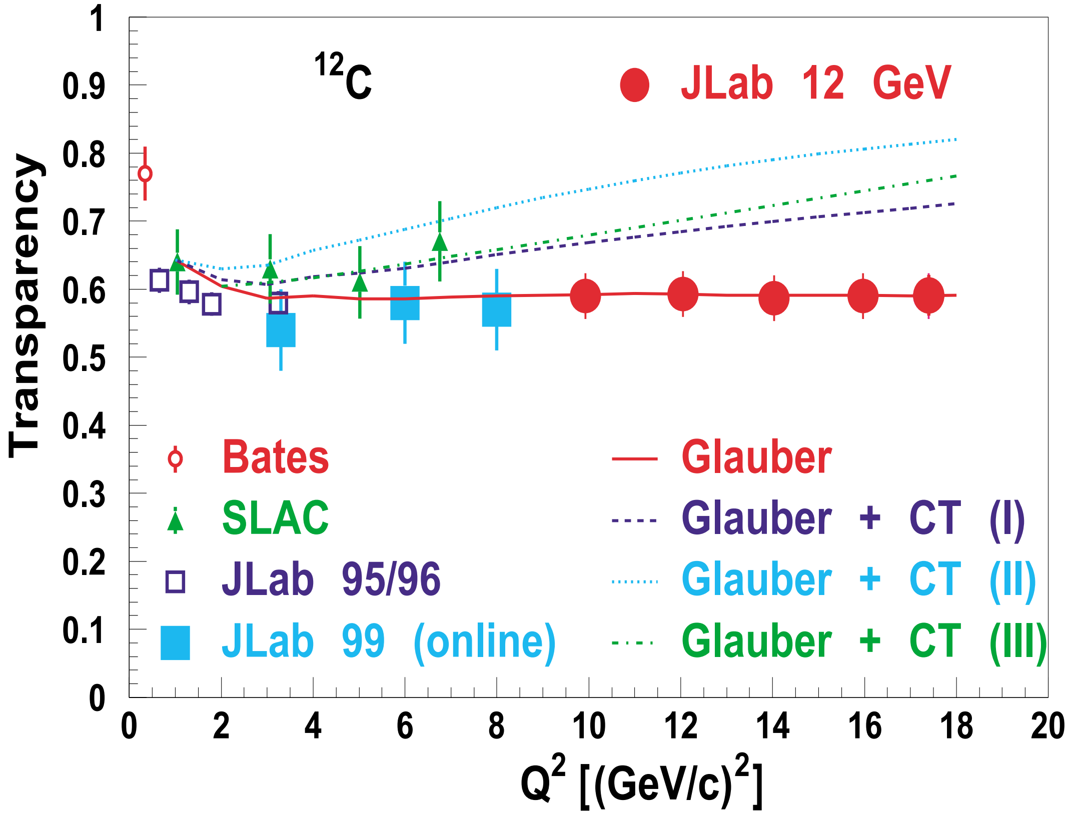

Figure 49: The Q^2 dependence of the nuclear transparency. The data are from Refs. [Ne95, Ab98, JL99]. The calculations are: "Glauber" – conventional Glauber calculation [Fr95]; Glauber+CT(I) and Glauber+CT(II) – minimal and maximal CT effects expected within quantum diffusion model [Fr95]; and Glauber+CT(III) – CT effects calculated in Ref. [Ni94]. A beam time of about one week is assumed.

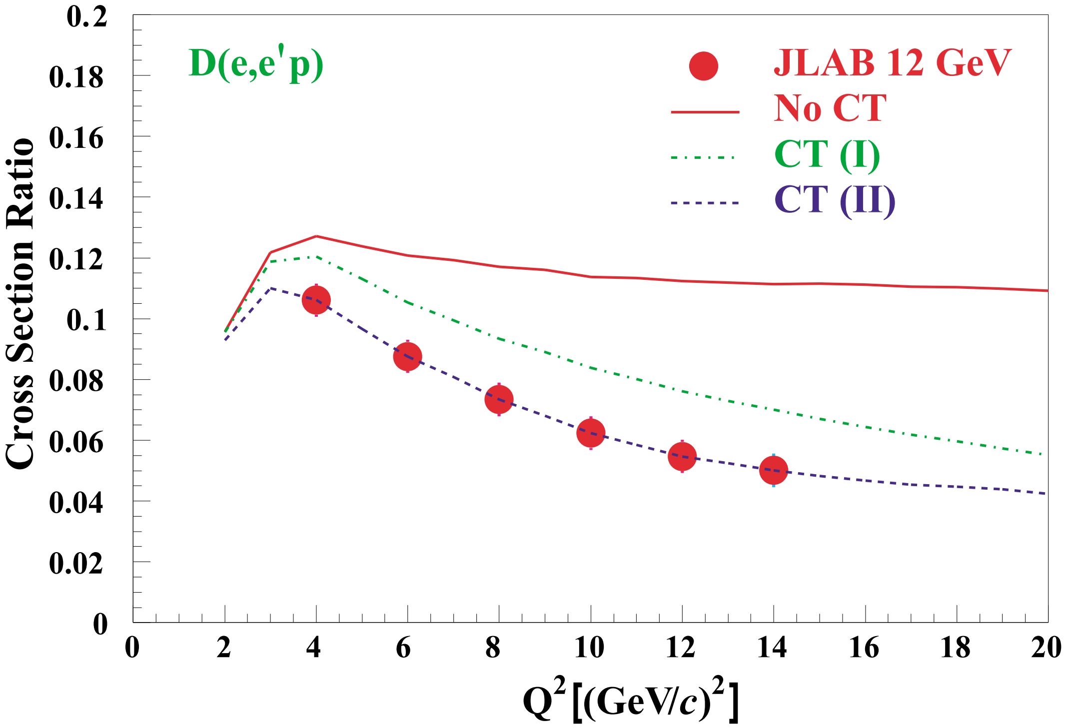

Figure 50: The Q^2-dependence of the ratio $R = \sigma(p = 400\ \mathrm{MeV}/c)/\sigma(p = 200\ \mathrm{MeV}/c)$ for the $(e, e'p)$ reaction on deuterium. The solid line: generalized Glauber approximation. Dashed and dash-dotted lines correspond to the minimal and maximal CT effects expected within the quantum diffusion model [Fr95b]. A beam time of about one month is assumed.

higher values of Q^2 where the CT predictions diverge appreciably from the prediction of conventional calculations, especially as the EVA data establish that, at least for nucleon momenta ≥ 7 GeV/c, the expansion effects are small enough not to mask an increase of T. Hence, measurements at $Q^2 \geq 12\ (\mathrm{GeV}/c)^2$ corresponding to comparable momenta of the ejected nucleon would unambiguously answer the question of whether one has entered the CT regime. These measurements would use the highest-momentum spectrometer available, the SHMS. Figure 49 displays both the present status and expected effects of CT in the measurement of T in $A(e, e'p)$ experiments, together with the typical accuracy expected from experiments feasible with 11 GeV beams from an upgraded CEBAF.

Although $A(e, e'p)X$ measurements will allow an unambiguous check of the existence of CT, a much wider range of reactions will be necessary to answer all three questions raised above. To obtain detailed knowledge of the nuclear interactions of PLCs one should also investigate processes where the ejectile, at low Q^2, interacted a second time during the passage of the nucleus [Eg94, Fr95b, La98]. Here we emphasize the study of recoil nucleons with momenta $k > 300$ MeV/c. As a large fraction of the yield in this range originates from recoil nucleons with lower momenta rescattering, this yield should decrease substantially with the onset of CT, and give a measurable effect at lower Q^2 than in the example given above. An important advantage of this reaction is that the effect can be studied using the lightest nuclei (D, ^{3}He, ^{4}He) for which wavefunctions are much better known. In addition, there is a strong theoretical effort directed towards implementing Glauber theory and eikonal methods for $(e, e'p)$ reactions both on light and medium nuclei, which will aid in the interpretation of these measurements [Be96, Be00, Bi95, Bi96, Bi96a, De00, Gr94, It97, Je99, La91, La94a, Mo99].

The appropriate measure for color transparency in double-scattering reactions is the ratio of the cross section measured in the kinematics where the double scattering is dominant to the cross section measured in the kinematics where the effect of the Glauber screening is more important. Theoretical investigations of these reactions [Eg94, Fr95b] demonstrated that it is possible to separate these two kinematics by choosing two momentum intervals for the recoil nucleon: 300 to 500 MeV/c for double scattering and 0 to 200 MeV/c for Glauber screening. Thus the suggested experiment will measure the Q^2-dependence of the ratio $R = \sigma(p = 400 \text{ MeV}/c)/\sigma(p = 200 \text{ MeV}/c)$. Figure 50 demonstrates the feasibility of such an experiment in the case of the energy upgrade to 12 GeV using the HMS and SHMS spectrometers in Hall C. In addition to the $D(e, e'pn)$ process, one can consider excitation of baryon resonances in the spectator kinematics, such as $D(e, e'pN^*)$ and $D(e, e'N\Delta)$. The latter process is of special interest for looking for the so-called chiral transparency – the disappearance of the pion field of the ejectile.

Color transparency effects in coherent vector-meson production from the deuteron

It is widely expected that one should observe the onset of CT in the electroproduction of mesons earlier than in the case of nucleon knockout. The simple explanation is that it is easier to bring the $q\bar{q}$ pair of a meson close together to form a PLC, than the qqq state of the baryon. We plan to study vector-meson electroproduction from a deuterium target for a beam energy of 11 GeV in the kinematic range of $Q^2 > 1$ (GeV/c)^2 and $x_{Bj} < 0.4$. Measurements of the reaction $e + d \to e' + V + d'$ for transferred momenta $-t$ up to 1 (GeV/c)^2 will allow the investigation of single- and double-scattering mechanisms in the production of vector mesons. The main focus in these measurements will be the study of the rescattering part of the amplitude [Fr98] at different kinematics. CT will diminish the probability of such a rescattering, and the predicted CT effect should be visible already at $Q^2 \sim 2$ (GeV/c)^2.

The fact that such a rescattering channel can be isolated in coherent vector-meson production from deuterium is well known from the photoproduction experiment at SLAC [An71], which demonstrated unambiguously that the cross section is dominated by rescattering of the produced meson off the spectator nucleon at $-t \geq 0.6$ (GeV/c)^2.

The proposed measurements will study the relative change of the slopes in two regions (single and double scattering) as a function of Q^2. As is well known in lepto-production processes, the longitudinal interaction lengths play an important role and have a characteristic Q^2-dependence: $l_c = 2\nu/(Q^2 + m_V^2 - t_{\rm min})$. An important aspect of the measurements here is the separation of l_c effects from color transparency effects [Ac99]. This can be achieved by keeping l_c (or x_{Bj}) fixed in the Q^2 scan of the t-dependence. At 11 GeV beam energy the t-dependence of coherent production can be studied with CLAS up to Q^2 of 5 (GeV/c)^2 at l_c ∼0.8 fm [Cl00a]. Figure 51 shows the expected ratio $R_c = [\sigma(0.8)/dt]/[d\sigma(0.4)/dt]$ of the cross sections for ρ electroproduction at transferred momenta $-t = 0.4$ (GeV/c)^2 (where the cross section is dominated by single scattering) and $-t = 0.8$ (GeV/c)^2 (where the cross section is dominated by double scattering) as a function of Q^2 for different model approximations. It would also be interesting to measure the cross section for ϕ electroproduction, which can give us the information about the interplay of the soft and hard pomeron in QCD.

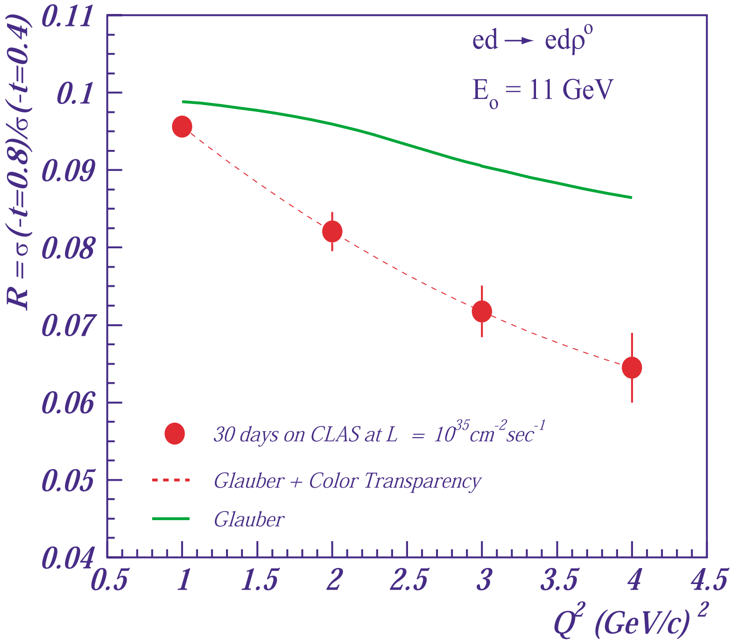

Figure 51: Expected errors on the ratio of cross sections for ρ production at $-t = 0.4$ and 0.8 (GeV$/c$)^2 for 30 days of running on CLAS with an 11 GeV beam. Kinematics is fixed at around $l_c = 0.8$. The solid line is the calculation assuming no CT; the points and dashed line are with CT effects [Fr98].

2.D Campaigns 4 & 5: Testing the Limits of the Meson/Nucleon Description of Nuclei and Probing the Limits of the "Standard Model" of Nuclear Physics

One of the main motivations for building CEBAF was the investigation of the fundamental structure of nuclear matter. The aim was to probe in detail the nucleonic component of nuclear wavefunctions, and to look for manifestations of the underlying quark degrees of freedom. The results of the first investigations (in particular the measurement of the quadrupole deuteron form factor) confirm the presence of high-momentum nucleonic components in the deuteron at least up to momenta of ~ 600 MeV/c, as well as the presence of phenomena such as the large-angle photodisintegration of the deuteron, where one needs to go beyond the description based on hadronic degrees of freedom.

To date our knowledge of the structure of nuclei is limited to their behavior near equilibrium. We have been able to probe nuclei "gently" and to understand their low-energy excitation spectrum in terms of interactions and rearrangements of unperturbed nucleons. The bulk of their high-energy excitation is almost unknown. A natural question is, what happens when an energy of few GeV (comparable to the nucleon mass) is transferred to a nucleus and when nucleons are emitted at large angles? This must involve short-range mechanisms where nucleons overlap and where interactions between their constituents become relevant. This is the field of short-range correlations (SRC).

The pressing questions to be investigated include: the direct observation of SRC in nuclei, the determination of the shortest distance scale for which the notion of meson exchanges remains effective, and the identification of the distance scale at which direct constituent interactions like quark exchanges between nucleons, or "kneading" of the constituents of bound nucleons, becomes important. Average distances between nucleons in SRC are $\sim$ 1–1.2 fm, which is a factor $\sim 1\frac{1}{2}$ smaller than the average internucleon distances. Here the local densities of nuclear matter in SRC exceed the average nuclear densities by at least a factor of 4, so the investigation of the structure of SRC would have astrophysical implications important to our understanding of the dynamics of neutron star cores, which possess similar densities.

These and many related questions have been before us for decades. Why does CEBAF make a difference? The reason is the much better energy and momentum resolution of CEBAF, and its ability to perform correlation experiments for rare processes. Here our experience from nucleon structure studies can serve as a guide. It is well known that the crucial breakthrough in the study of nucleon structure occurred when it became possible at SLAC to study inclusive electron scattering processes at sufficiently high momentum transfer that quarks were knocked out of the nucleons with momenta much larger than those of the spectator quarks. This requires both large Q^2 and sufficiently large missing mass W. Further progress was made when correlation experiments were done, where the leading hadrons were used to tag different flavors. As a result of these studies we now know the single-parton densities in nucleons quite well. In the case of nuclei these conditions correspond to the requirement that to probe the nucleonic structure of SRC it is necessary to reach momentum transfers $|\vec{q}| \gg 2k_N$, where k_N is the momentum of the nucleon in the correlation, and to have $q_0 \gg 1$ GeV/c to ensure that the ejected nucleon moves fast relative to the rest of the nucleus. This corresponds to $Q^2 \geq 1.5 - 2$ (GeV/c)^2 and the energies of the knocked-out nucleons ≥ 1 GeV. This kinematics first became reachable at CEBAF at 4–6 GeV.

To probe the limits of the nucleonic picture of SRC one must go beyond the energy presently accessible at JLab. Previous inclusive measurements of the parton structure of nuclei have demonstrated limits of the standard, many-nucleon model of nuclei. These include the EMC effect [Au83, Bo83], which unambiguously requires the presence of non-nucleonic degrees of freedom in nuclei, and the observation of a suppression of the antiquark distribution in nuclei [Al90], which contradicted predictions of an enhancement based on the mesonic picture of the short-range nuclear forces. To investigate these effects further and to reach an understanding of the parton structure of nuclei, energies higher than 6 GeV are necessary. CEBAF at 11 GeV opens unique opportunities for measuring quark distributions over a broad range of x, exploring the parton structure of superdense nuclear matter, and investigating the parton structure of bound nucleons, which cannot be probed at the available energies (≤ 6 GeV). In this respect, studies at CEBAF will nicely complement the study of the high-temperature, high-density region of the phase diagram of nuclear matter (planned at RHIC and LHC via relativistic heavy-ion collisions) with the exploration of the low-temperature, high-density phase (see Fig. 52).

2.D.1 Probing the Limits of the Standard Model of Nuclear Physics: Few-Body Form Factors

Measurements of the elastic form factors of the deuteron and the helium isotopes are of crucial importance in understanding their electromagnetic structure and testing the "standard model" of light nuclei that is based on the meson-nucleon framework, the impulse approximation (IA), and meson-exchange currents (MEC) [Ca98]. Such measurements offer unique opportunities for studying the short-range nucleon-nucleon interaction, few-body wavefunctions, isobar and three-body force contributions, and effects from possible quark-cluster admixtures. Large-momentum-transfer measurements can also test "nuclear chromodynamics" predictions based on quark dimensional scaling (QDS) and perturbative QCD (pQCD) [Ca97].

The starting point of the conventional theoretical approach of elastic scattering from few-body

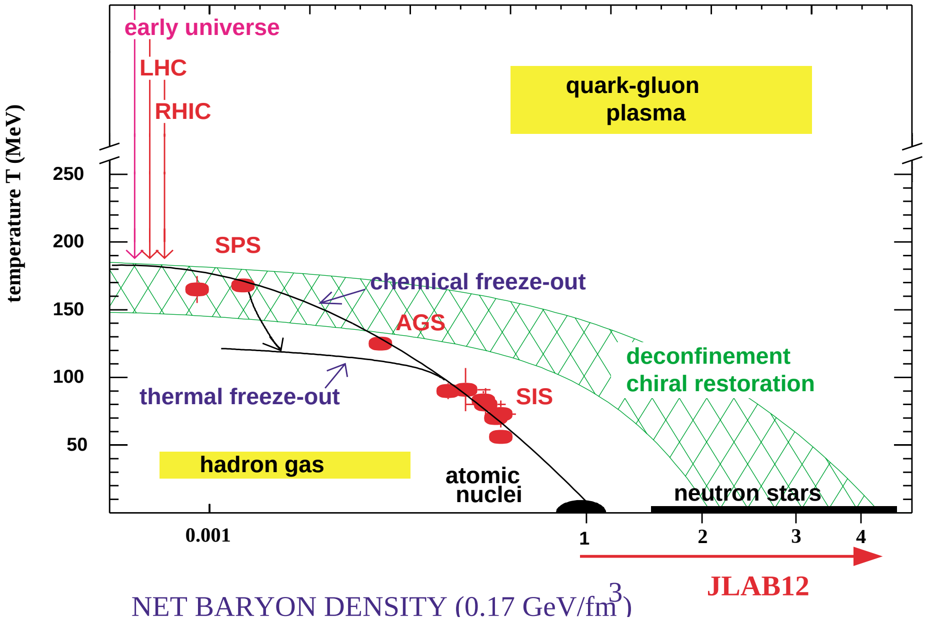

Figure 52: Phase diagram for nuclear matter.

systems is the impulse approximation, where the incident electron interacts with one of the nucleon constituents of deuterium or helium. The form factors of light nuclei are then convolutions of the nuclear wavefunction with the form factors of the constituent nucleons. At large momentum transfers the effects of relativity cannot be ignored, and either corrections must be made to the IA or fully relativistic approaches developed (as has been done in the case of the deuteron [Hu90]. It has long been understood and overwhelmingly supported by the available data that the few-body form factors are sensitive to the presence of meson-exchange currents and isobar configurations that augment the IA picture [Ca98].

At distances much less than the nucleon size, the underlying quark substructure of the nucleons cannot be ignored. This has led to the formulation of so-called hybrid quark models [Di89] that treat few-body nuclei as quark clusters when the internucleon separation becomes smaller than $\sim$1 fm. At sufficiently "large" momentum transfers, the few-body form factors are expected to be calculable in terms of only quarks and gluons within the framework of pQCD. The first attempt at a quark-gluon description of the few-body elastic form factors was based on the dimensional-scaling quark model (DSQM) [Br73], where the underlying dynamical mechanism during elastic scattering is the hard rescattering of the constituent quarks via exchange of hard gluons. The Q^2-dependence of this process is then predicted by simply counting the number n of gluon propagators ($n = 5$ for

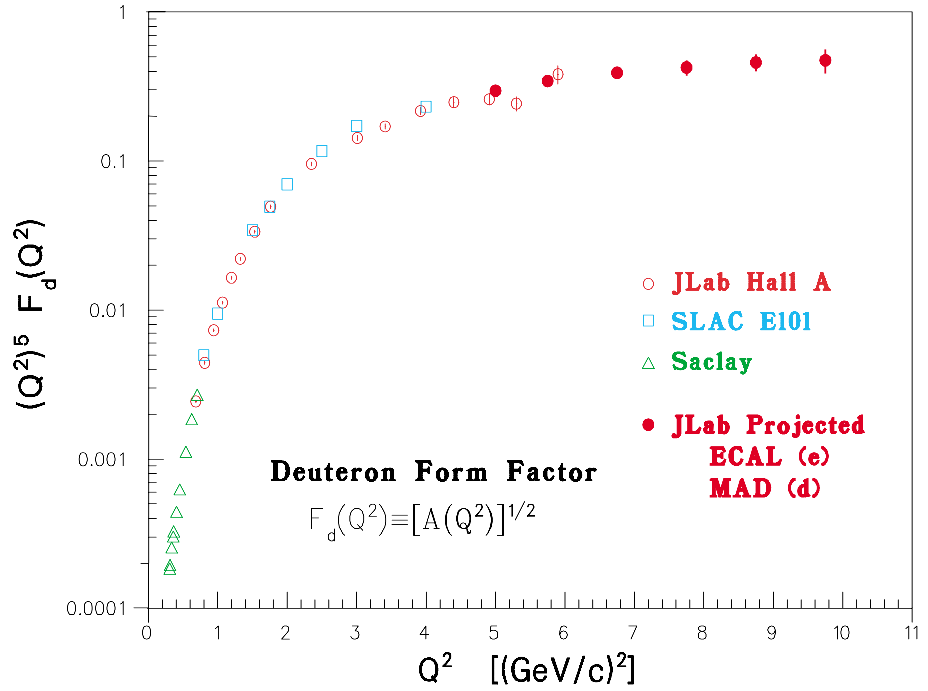

Figure 53: Projected data for the deuteron form factor $F_d(Q^2)$ with an 11 GeV JLab beam. Also shown are existing JLab, SLAC, and Saclay data.

deuterium, 8 for ^{3}He, and 11 for ^{4}He), which implies that the elastic structure functions $A(Q^2)$ of the few-body systems should follow the power law: $\sqrt{A(Q^2)} \sim (Q^2)^{-n}$. This prediction was later substantiated, for the deuteron case, in the pQCD framework, where it was shown [Br83] that to leading order:

$$\sqrt{A(Q^2)} = \left[\alpha_s\left(Q^2\right)/Q^2\right]^5 \sum_{m,n} d_{mn} \left[\ln\left(\frac{Q^2}{\Lambda^2}\right)\right]^{-\gamma_n - \gamma_m},$$

where $\alpha_s(Q^2)$ and Λ are the QCD strong coupling constant and scale parameter, and $\gamma_{m,n}$ and d_{mn} are QCD anomalous dimensions and constants.

The 12 GeV energy upgrade of the JLab electron beam and the proposed spectrometer facility upgrades will be ideal for improving and extending the existing elastic structure function measurements of light nuclei to higher momentum transfers. These measurements will test the limits of the standard model of few-body nuclei, and may uncover a possible transition to a quark-gluon description of the few-body form factors, as predicted by quark dimensional scaling and perturbative QCD.

Figure 53 shows the recent JLab Hall A and older SLAC and Saclay data [Al99] on the deuteron form factor, $F_d(Q^2) \equiv \sqrt{A(Q^2)}$, multiplied by $(Q^2)^5$. It is evident that the data show an approach to a scaling behavior consistent with the power law of DSQM and pQCD. Although several authors have questioned the validity of QDS and pQCD at the momentum transfers of this experiment [Is84], similar scaling behavior has been reported in deuteron photodisintegration at moderate photon energies [Bo98]. It is extremely important to test this apparent scaling behavior by extending the deuteron $A(Q^2)$ measurements to higher momentum transfers. Higher JLab beam energies in the range of 9–11 GeV are essential for such measurements. To separate elastic from inelastic scattering and to suppress backgrounds, recoil deuterons should be detected in coincidence with scattered electrons. A possible scenario would be to use the proposed Medium-Acceptance Device (MAD) to detect recoiling deuterons and a segmented electromagnetic calorimeter (ECAL) to detect scattered electrons. Assuming a 20-cm-long liquid-deuterium target and beam current of 70 μA, $A(Q^2)$ can be measured up to ~ 10 $(\text{GeV}/c)^2$ in one month of beam time, as shown in Fig. 53. Such an experiment will double the Q^2 range of the existing data, which have been acquired over a period of 40 years. The observation of a diffractive structure (which cannot be ruled out from the existing data) would settle in the negative the question of the applicability of the QDS ideas at moderate momentum transfers once and for all. On the other hand, if the predictions are successful, the applicability of these ideas will not be proved: there are alternatives that give essentially the same predictions, and so many failures of the pQCD helicity selection rules at these energies that additional tests of the underlying dynamics will be required.

The existing data [Am94] on the ^{3}He form factor, $F(Q^2) \equiv \sqrt{A(Q^2)}$ (shown in Fig. 54), are in good agreement with the standard model (IA+MEC) calculations [Sc91] at low Q^2 but are fairly inconclusive at the largest momentum transfers. They are consistent with a change in slope at ~ 55 fm^{-2}, indicative of an onset of quark scaling [Ch78], but, at the same time, cannot exclude the presence of a second diffraction minimum as predicted by conventional meson-nucleon theory. As in the case of the deuteron, more measurements at higher Q^2 would be crucial in testing the quark-scaling prediction and a possible breakdown of the meson-nucleon framework. The energy upgrade of JLab will also allow new ^{3}He measurements that could double the Q^2 range of the existing data (taken also over a period of 40 years) in a single experiment with a tenfold better sensitivity. As in the case of the deuteron, recoiling nuclei will be measured with the MAD spectrometer and scattered electrons with a calorimeter. Assuming a 20-cm-long ^{3}He gas cryogenic target and an electron beam of 11 GeV with current of 70 μA, the ^{3}He $F(Q^2)$ can be measured up to ~ 150 fm^{-2} in one month of beam time, as shown in Fig. 54. It is evident that this experiment will be able to show whether the apparent change in slope of the SLAC data can be attributed to a classical diffraction minimum, or a quark-scaling approach as argued in Ref. [Ch78].

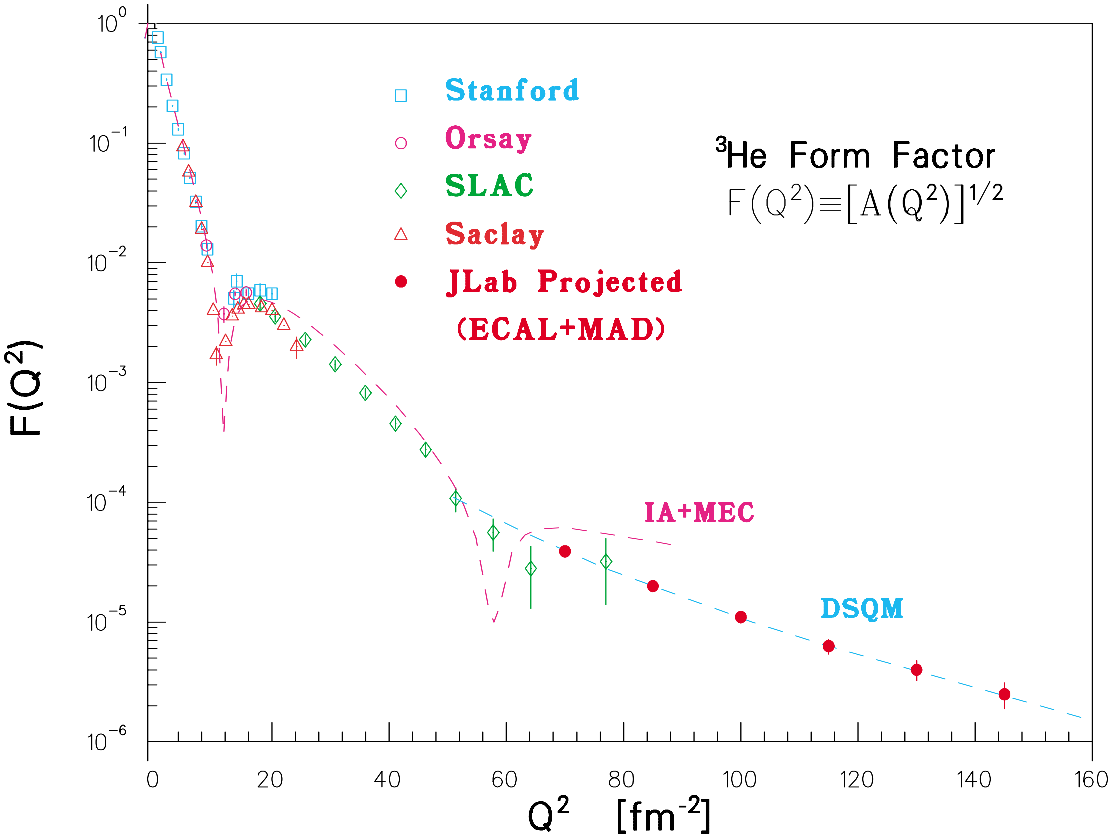

Figure 54: Projected data for the ^{3}He elastic form factor $F(Q^2)$ with an 11 GeV beam. Also shown are existing data and predictions of the standard model (IA+MEC) [Sc91] and the dimensional-scaling quark model (DSQM) [Ch78].

In summary, JLab with an 11 GeV electron beam would the ideal place to perform large-momentum-transfer measurements of the form factors of light nuclei. These measurements will test the limits of the nuclear standard model based on the impulse approximation and meson-exchange currents and are likely to establish the expected transition from the conventional meson-nucleon to the quark-gluon description of the few-body nuclear systems.

2.D.2 Probing the Limits of the Standard Model of Nuclear Physics: Short-Range Correlations in Nuclei

Observing short-range correlations (SRC) in nuclei has been an important goal of experimental nuclear physics for decades [Be99, Be67]. Not that these correlations are small – calculations of nuclear wavefunctions with realistic NN potentials consistently indicate that in heavy enough nuclei about 25% of the nucleons have momenta above the Fermi surface [Pa97]. This corresponds to about 50% of the kinetic energy being due to SRC. The experimental problem has been the unavailability of the high-momentum-transfer kinematics that could discriminate decisively between the effects of SRC in the initial- and final-state interactions. Though the final-state interactions in nucleon knockout do not disappear at large Q^2, two important simplifications occur which make extraction of the information about the short-range nuclear structure possible. First, in high-energy kinematics a "hidden" conservation law exists – the light-cone momentum fractions of slow nucleons do not change if the ejected nucleon elastically scatters off slow nucleons [Fr97]. Second, the rescatterings of a high-energy nucleon can be described by the generalized Glauber approximation, which takes into account a difference in the space-time picture of proton-nucleus scattering (a proton coming from $-\infty$) and the $A(e,e'p)$ process (a proton is produced inside the nucleus) and also accounts for the nonzero Fermi momenta of rescattered nucleons [Fr97].

There is a general consensus that Glauber theory is the appropriate tool for describing final state interactions for $E_p \gtrsim 1$ GeV, which corresponds to $Q^2 \geq 1.5$ (GeV/c)^2. On the other hand, pushing to Q^2 values that are too high is not optimal for the study of the nucleon degrees of freedom in nuclei. Indeed, it was suggested that at $Q^2 \geq 4$ (GeV/c)^2 one may encounter new phenomena related to the EMC effect [Fr88, Fr96]. Hence the optimal range for probing the nucleonic degrees of freedom is $1.5 \leq Q^2 \leq 4$ (GeV/c)^2. CEBAF at 6 GeV reaches the lower end of this range and can provide limited access to its upper part, but at the cost of low counting rates. At 11 GeV this whole range will be easily accessible for the upgraded CLAS while Halls A and C will be able to explore even higher Q^2. Studies of the $(e,e'N)$ and $(e,e'NN)$ reactions in this Q^2 range will allow us to measure directly nucleon momentum distributions up to momenta 500–700 MeV/c, as well as to measure how these momenta are balanced in nuclei: two- and three-nucleon short-range correlation contributions versus those of the mean field.

The starting point for these studies is the simplest reaction $e + {}^2\mathrm{H} \rightarrow e\ p\ n$. It will provide a test of the basic principles of our current understanding of the dynamics of the electro-disintegration processes, especially after the CEBAF measurements of the deuteron form factors over a wide range of Q^2, since the wavefunction of the deuteron will be reasonably well known for a wide range of nucleon momenta for both S- and D-states. The progress in constructing tensor-polarized deuteron targets will make it feasible to study the same reaction using polarized targets at sufficiently large Q^2. In this case a direct separation of S- and D-wave contributions is possible. Since the D-wave is expected to play a key role over a wide range of nucleon momenta both in ^{2}H and in heavier nuclei [Fr81, Fo96], this process will provide an ultimate test of our understanding of the short-distance NN interactions. In particular, it will allow making a clean discrimination between predictions of the Bethe-Salpeter and light-cone approaches to the description of the deuteron as a two-nucleon relativistic system [Fr88].

The $(e, e'N)$ reaction with the ejected nucleon along $\vec{q}$ for $A \geq 3$ is the next natural step in these studies. This process measures at large Q the light-cone density matrix of the nucleus, $\rho_A^N(\alpha, p_t)$, as well as the excitation energy of the residual system. That energy is expected to increase with increasing initial momentum of the knocked-out nucleon. (In the nonrelativistic approximation the average excitation energy is $\langle E_{\mathrm{rec}} \rangle \approx k^2/2m_N$, where $\vec{k}$ is the initial momentum of the knocked-out nucleon.) The availability of a large Q^2 and W range will allow us to perform a stringent test of the many-nucleon approximation in which the cross section should factorize into a product of the elementary eN elastic cross section (which drops in this Q-range by a factor of ~ 10) and the Q^2-independent spectral function. Note that the studies of the $A(e, e')$ processes for many A at $x \geq 1$ and $1 \leq Q^2 \leq 4\ (\mathrm{GeV}/c)^2$ at SLAC and CEBAF have confirmed an expected similarity in the shape of the wavefunction of the short-range correlations. Hence it will be sufficient to restrict the studies of SRC in $(e, e'N)$ and $(e, e'NN)$ processes to the lightest nuclei with $A = 3, 4$ to minimize the effects of the final-state interactions. Polarized ^{3}He targets will play a special role for probing the SRC due to the relative simplicity of the wavefunction of the $A = 3$ system, and present a unique possibility to probe the spin structure of the pp and pn correlations. In particular, there exists kinematics where a minimum in the S-wave pp wavefunction can be probed, and the P-wave can be measured (some of these measurements will be performed already with an unpolarized target, while the polarized target will allow a number of cross checks and bring additional information). These measurements will provide stringent tests of the structure of the $A = 3$ system, and will test the current interpretations of the measurements of ^{3}He form factors at large Q^2.

The $A(e, e'N_fN_b)$ reactions with N_f the forward- and N_b the backward-going nucleons will allow one to investigate how the excitation energy is shared between nucleons. It is expected that the dominant contribution will originate from two-nucleon correlations. In this case N_b should carry most of the excitation energy. A comparison of the yields of (pp), (pn), and (nn) processes will provide a detailed check of the reaction mechanism and provide a quantitative comparison between the wavefunctions of two-nucleon SRC in the isospin zero and one channels. (The former is expected to dominate by a factor ≥ 4 over a large range of momenta.)

Although two-nucleon correlations are expected to produce a dominant part of SRC, the triple and higher SRC (where more than two nucleons come close together) are significant as well; they are likely to constitute $\sim 20\%$ of all SRC. They should manifest themselves in the low-excitation tail of the spectral function for large momenta of the knocked-out nucleon and can be best observed through the $A(e, e'N_f N_b)$ reaction and in processes with two backward-ejected nucleons [Fr88]. The latter reaction is especially interesting since it allows one to study the parton structure of three-nucleon correlations at very high densities. (See the discussion in the next section.)

Overall, this series of experiments at CEBAF can provide a detailed knowledge of the nucleonic component of the spectral function, including the SRC domain, that will constitute a major step forward in our understanding of the physics of the nucleus.

2.D.3 Testing the Limits of Nuclear Many-Body Physics: Probing Non-Nucleonic Degrees of Freedom in Nuclei

With the nucleon size being ~ 0.8 fm it is clear that nucleons start to overlap strongly already when the distance between them becomes ~ 1.2 fm. Hence dense nuclear matter may look very different from a system of densely packed nucleons. The properties of dense nuclear matter are closely related to many outstanding issues in QCD, such as chiral symmetry restoration, deconfinement, the onset of quark-gluon degrees of freedom, and the structure of the phase transition from the hadronic to the quark-gluon state of matter. In QCD, transitions to new phases of matter are possible in different density/temperature regimes. In particular, it has recently been suggested [Al98, Ra98] that nuclear matter could exist in a color superconductivity phase with the condensation of diquarks. Recent estimates suggest that the average nuclear density could be right in between the dilute nucleon phase and superconducting phase [Ca00a]. If so, it is natural to ask whether one can observe precursors of such a phase transition by studying the quark-gluon properties of superdense droplets of nuclear matter, that is, configurations when two, three, or more nucleons come close together.

Since the internucleon distances in these correlations are at least a factor of 1.5 smaller than internucleon distances at average nuclear densities, one can probe droplets of nuclear matter at densities 3–5 times larger than in nuclear matter (see Fig. 52). From this viewpoint it is encouraging that the "EMC effect" data indicate that deviations from the expectations of the nucleon model of nuclei grow approximately linearly with the nuclear density, suggesting that the properties of the quark-gluon droplets could indeed deviate very strongly from those of a collection of nucleons.

These general arguments are in line with measurements of the parton densities in nuclei (the EMC effect, $\bar{q}_A/\bar{q}_N$, etc.), which unambiguously demonstrated that on the parton level a nucleus cannot be viewed as merely a collection of nucleons. Practically all the mechanisms suggested to explain the EMC effect address the question of the quark-gluon structure of SRC and/or the origin of the nuclear forces. These include:

a. Various patterns of mixing quarks (gluons) from different nucleons ranging from the deformation of the bound nucleon wavefunctions to "kneaded" (multiquark) states [Cl83, Ca83, Na84, Ja84, Fr85, Fr96].

b. A loss of momentum by nucleons to some fields that bind *undeformed* nucleons together [Er83, Fr83, Be84, Ak85, Ku89, Du85, Ju88, Ci89, Ka90, Me93, Bi89, Me94, Ku94].

c. The presence of Δ-isobars, N^*'s in nuclei, especially in the SRC [Fr83].

However, inclusive experiments at $x \leq 0.8$ have not allowed us to discriminate between such models. The broad (x, Q^2) range available at 11 GeV and the feasibility of correlation experiments suggest a strategy that will work.

The first step will be to use deep inelastic scattering off nuclei at $x \geq 1$ in the scaling limit to establish in a model-independent way (*i.e.*, not sensitive to the final-state interactions) the presence of superfast quark components in nuclei – quarks that carry a larger momentum fraction than a whole nucleon.

Theoretical estimates indicate that for $x \leq 1.5$ this will require $Q^2 \leq 20$ $(\mathrm{GeV}/c)^2$, so experiments will be feasible with $E_e = 11$ GeV. Several features of CEBAF and its experimental facilities (the good acceptance and high resolution of the CEBAF spectrometers, and the high intensity and small energy spread of the electron beam) are crucial for performing these measurements. Through a study of the Q^2-dependence of the cross section at fixed x it will be possible to observe for the first time the onset of scaling at $x \geq 1$ (Fig. 55), which will be the definitive signature for the existence of superfast quarks in nuclei.

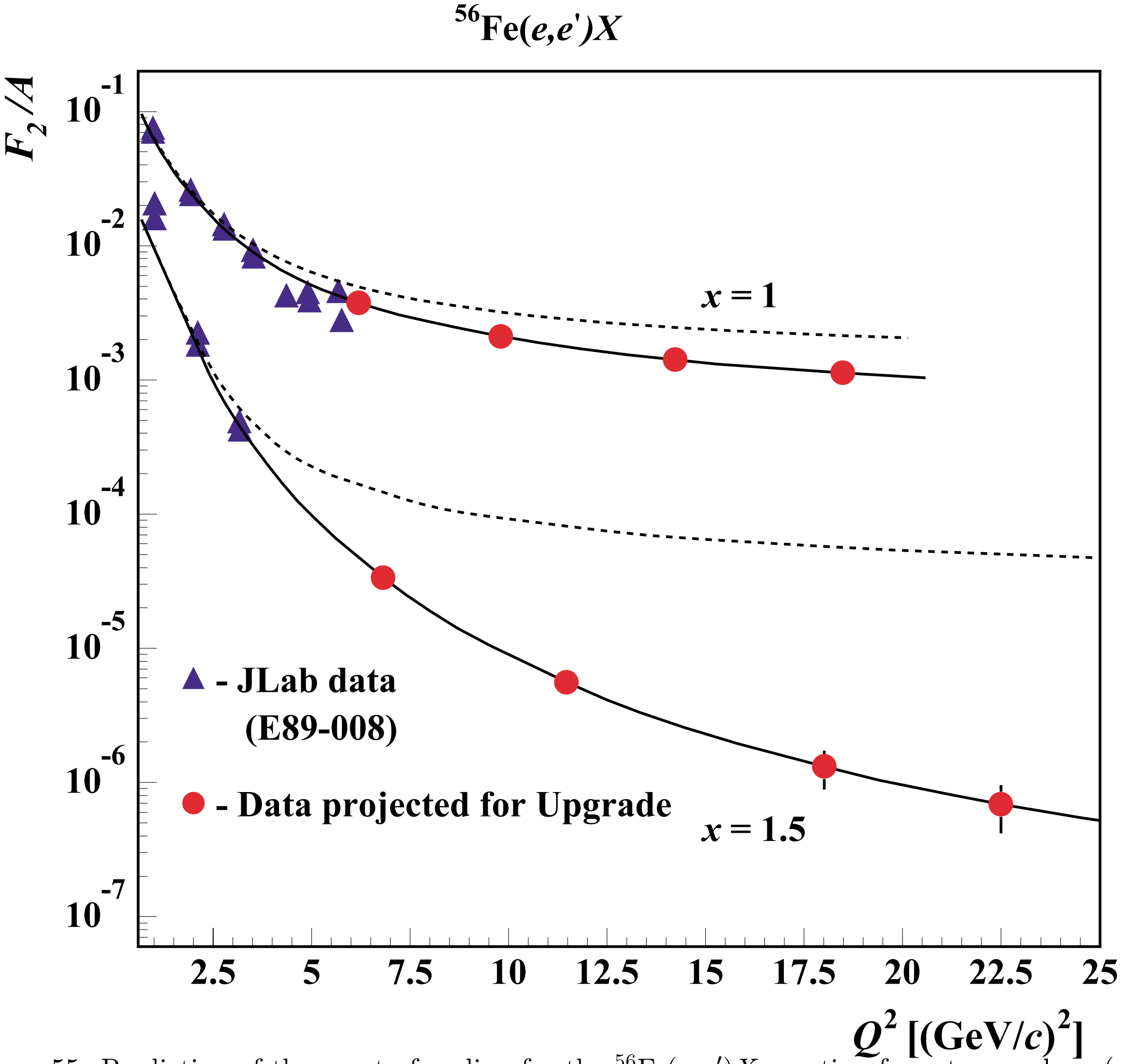

Figure 55: Prediction of the onset of scaling for the $^{56}\text{Fe}(e,e')X$ reaction for a two-nucleon (solid line) and multi-nucleon (dashed line) short-range correlation model. The data shown are from Ref. [Ar99]. With the 12 GeV Upgrade data, measurements can be made to $Q^2 = 20$ (GeV/c)^2, where the solid and dashed lines will have separated by more than an order of magnitude for $x = 1.5$.

Comparing the cross sections for $A = 2$, 3, and 4 and for heavy nuclei will allow the model-independent separation of contributions of two-, three-, or more-nucleon SRC. The two-nucleon correlations are expected to dominate for $1.3 \geq x \geq 1$, leading to quark structure functions for $A \geq 12$ nuclei a factor of 5–6 larger than in the deuteron [Fr81, Fr88]. This ratio should be similar to the cross-section ratio for quasielastic scattering:

$$R_{A/D}(x, Q^2) \equiv \frac{2}{A} \frac{\sigma_{eA}(x, Q^2)}{\sigma_{e^2H}(x, Q^2)}$$

observed at $x \sim 1.5$, $4 \geq Q^2 \geq 1$ $(\mathrm{GeV}/c)^2$ at SLAC [Fr93]. Local nuclear densities probed in this case are three to four times larger than the average value, $\rho_0 \sim 0.17$ fm^{-3}. For larger $x \sim$1.5 higher correlations are expected to dominate, leading to an increase of $R_{A/D}(x \sim 1.5, Q^2 \sim 50\ (\mathrm{GeV}/c)^2)$ [Fr81]. At the same time the local nature of generating $x \geq 1$ quarks will manifest itself experimentally through the same shape and probability per nucleon of the $x \geq 1$ component in ^{4}He and heavy nuclei. In this kinematics we expect to observe densities at least five times larger than ρ_0. Detailed studies of the A-dependence of $q_A(x, Q^2)$ at $1.5 \geq x \geq 1$ will provide important information about fluctuations of the local nuclear density as a function of average nuclear density as well as of the isospin of the correlations.

Measurement of the quark distribution at $x \geq 1$, in combination with the measurements of the light-cone nucleon density matrix (ρ_A^N) described in the previous campaign, will allow a check of whether $F_{2A}(x, Q^2) > 1$ can be described as a convolution of ρ_A^N and the *free* nucleon structure function. At the same time these measurements will establish in a model-independent way the relative importance of two- and three-nucleon SRC by comparing $F_{2A}(x, Q^2)$ for light and heavy nuclei and show the dependence of SRC on nuclear density.

The second step will be to study the tagged structure functions [Fr81, Fr88, Ci93] in order to compare directly the parton structure of the bound and free nucleon. This will start with the $e + ^2$H $\rightarrow e$ + backward nucleon + X reaction in the kinematics, where the momentum fraction carried by the struck quark in the moving nucleon ($\tilde{x}$) is sensitive to the EMC effect [$0.3 \leq \tilde{x} \leq 0.7$ (CEBAF at 11 GeV covers all of this region; see Fig. 56)] and continue to a similar reaction with ^{3}He and the tagging of two backward nucleons to consider deformations in the three-nucleon correlations. In contrast to the case of the inclusive EMC effect, different models predict [Fr88, Ca91, Ca95, Me97] a qualitatively different dependence of the experimental results on the modifications of the bound nucleon wavefunction, which range from a complete absence of modification to an effect comparable to the EMC effect for heavy nuclei in the color screening model, for tagged nucleon momenta $p_N \geq 300$ MeV/c. If the EMC effect for the bound nucleon is observed, one would be able to check whether the theoretical account of such deformations together with a realistic light-cone nucleon

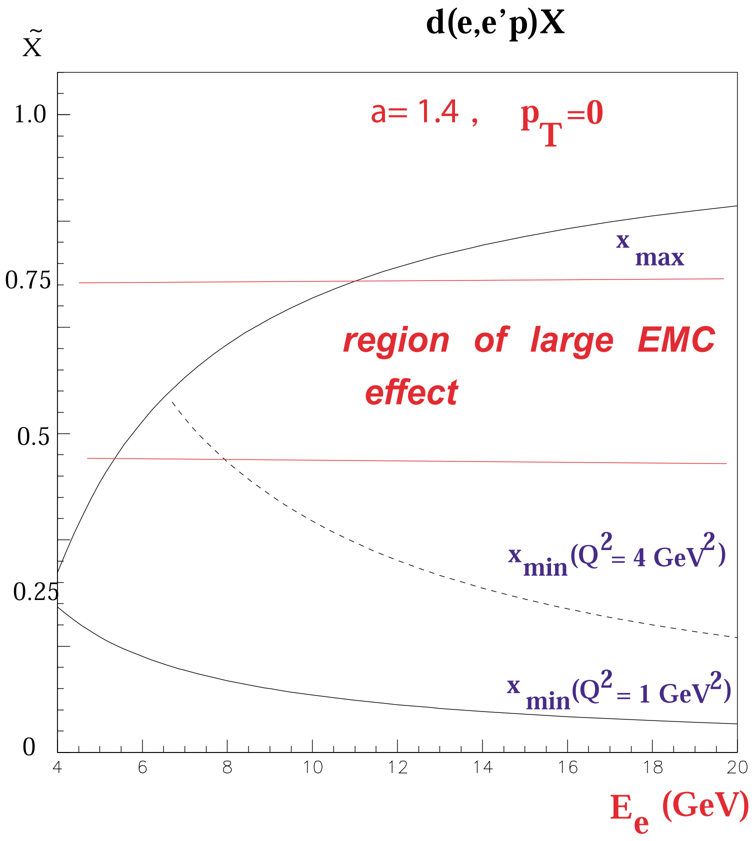

Figure 56: The scaling window for $\alpha = 1.4$, where α is the light-cone fraction of the knocked-out nucleon. The upper curve is defined by the requirement that the mass of the produced final hadronic state $W \geq 2$ GeV.

density (measured in the $A(e, e'p)$ processes) would reproduce $F_{2A}(x, Q^2) > 1$ in the scaling region.

The two-step strategy described above requires related studies that are important to cross-check all aspects of these studies:

- *Investigation of the reaction dynamics at* $Q^2 \geq 4(\text{GeV}/c)^2$ The reaction dynamics of $(e, e'p)$ at GeV energy and momentum transfers has not been explored experimentally so far. It will be quite different from low energy, due to the diffractive nature of the high-energy NN interaction and the role of relativity. With the energy upgrade, one can study, for example, the reaction $e +^2 H \rightarrow e + p + n$ in parallel kinematics for recoil nucleon momenta $p_N = 400 - 500 MeV/c$ up to $Q^2 \approx 8(GeV/c)^2$. A study of this type is essential for our understanding of the baseline color transparency calculations and of short-range structures in the nucleus.

- *A test of the binding models of the EMC effect*, by measuring the position of the quasielastic peak at large Q^2. In these models, a shift of the nucleon spectral function to $\alpha < 1$ is expected, leading to a significant asymmetry in the cross section of the $(e, e'p)$ process in parallel kinematics near the quasielastic peak [Fr92].

- *Studies of special modes of deuteron breakup at high Q^2 using the upgraded CLAS* would be sensitive to meson-exchange currents, *e.g.*, $e + {}^2\mathrm{H} \rightarrow$ two forward protons + leading π^-, and processes such as production of backward Δ's off the deuteron and ^{3}He that are especially sensitive to the presence of Δ-isobar-like color-singlet clusters and six-quark clusters.

- *Probing quark degrees of freedom in large-angle electrodisintegration of the deuteron* will be a natural extension of the CEBAF photodisintegration experiment [Bo98]. This was the first case of a high-energy nuclear physics reaction for which descriptions based on the quark degrees of freedom and on the assumption that *the short-range NN forces are due to quark exchange* quantitatively agree with the data, while all theoretical descriptions invoking hadronic degrees of freedom qualitatively disagree with the data [Fr00]. Study of deuteron electrodisintegration at $E = 11$ GeV will allow a significant extension of the range of the observed energy scaling. A crucial prediction of the quark-exchange picture is that for a wide range of photon virtualities the cross section should depend on the photon virtuality as the pointlike Mott cross section.

In summary, the increase of electron energy to 11 GeV will significantly expand the possibilities for systematic studies of high-momentum-transfer processes with nuclei. The ultimate result of Campaigns 4 and 5 will be a detailed understanding of the hadronic and quark degrees of freedom in nuclear matter at high densities up to 4–5 times the average nuclear density.

3 THE ACCELERATOR UPGRADE

3.A Overview

To deliver a 12 GeV beam, the CEBAF accelerator must be upgraded from its demonstrated 6 GeV capability. The straightforward plan is to utilize the existing tunnel and not change the basic layout of the accelerator. As such, the Upgrade can be categorized as having two major components: 1) additional acceleration in the linacs; and 2) stronger magnets for the recirculation. In this portion of the White Paper, we begin with an overview of the Upgrade. This is followed by a summary description of the changes to the present accelerator necessary to reach 12 GeV (Section 3.B), and a description of the present status and capabilities of the existing CEBAF accelerator (Section 3.C). Section 3.D presents the details of the Upgrade project. Additional information and details are available in an internal JLab report, *Interim Point Design for the CEBAF 12 GeV Upgrade,* May 25, 1999.

Key points of the CEBAF 12 GeV Upgrade

- The highest-energy beam at 12 GeV needs to be delivered only to the planned new experiment hall, Hall D.
- CW operation must be preserved.
- The maximum circulating linac beam current will be 425 μA (corresponding to an 85 μA delivered beam for five-pass operation).
- The maximum installed refrigeration capacity will be 10 kW at 2 K.
- Technical choices should be made that do not preclude the eventual upgrade of CEBAF to 24 GeV.
- No more than three halls receive beam at any time, and each receives a different energy beam.
- Both cost and impact on accelerator operation must be kept to a minimum.

The key parameters of the upgraded accelerator are presented in Table 6.

Table 6: Selected key parameters of the CEBAF 12 GeV Upgrade

Parameter	Specification
Number of passes for Hall D	5.5 (add a tenth arc)
Max. energy to Hall D	12.1 GeV (for 9 GeV photons)
Number of passes for Halls A,B,C	5
Max. energy to Halls A,B,C	11.0 GeV
Max. energy Gain per pass	2.2 GeV
Range of energy gain per pass	2:1
Duty factor	cw
Max. summed current to Halls A,C* (at full, 5-pass energy)	85 μA
Max. summed current to Halls B,D	5 μA
New cryomodules	10 (5 per linac)
Replacement cryomodules	Up to 6 (3 per linac)
Central Helium Liquifier upgrade	10.1 kW (from present 4.8 kW)

*Max. current is 430 μA (north linac) and 425 μA (south linac) and max. *total* beam power is 1 MW.

3.B Highlights of the Changes to the Accelerator

3.B.1 Acceleration

The extensive series of workshops on the 12 GeV Upgrade organized by the JLab nuclear physics users has determined that 12 GeV is required only for Hall D. This is important because it presents the option of placing that hall at the opposite end of the accelerator from the other halls (see Fig. 57) and achieving the needed 12 GeV beam by accelerating through one more linac than is reachable by the beam going to Halls A, B, or C. The advantage is that the total installed accelerating voltage is thereby reduced by 10% relative to what would have been required otherwise.

Presently each of the two linacs provides ∼550 MV of acceleration per pass. To reach 12 GeV, we will need ∼1090 MV, or roughly double the present performance. Fortunately, there is space in the two linacs for a total of ten additional cryomodules. Adding ten cryomodules that are identical to the originals would only bring us to ∼690 MV/linac. To gain the additional acceleration, we have designed and begun prototyping new cryomodules which will provide at least 68 MV (vs. the 28 MV from the existing cryomodules). Ten of these new cryomodules will be installed and six of the existing cryomodules will be replaced with new ones. The most important feature of the new

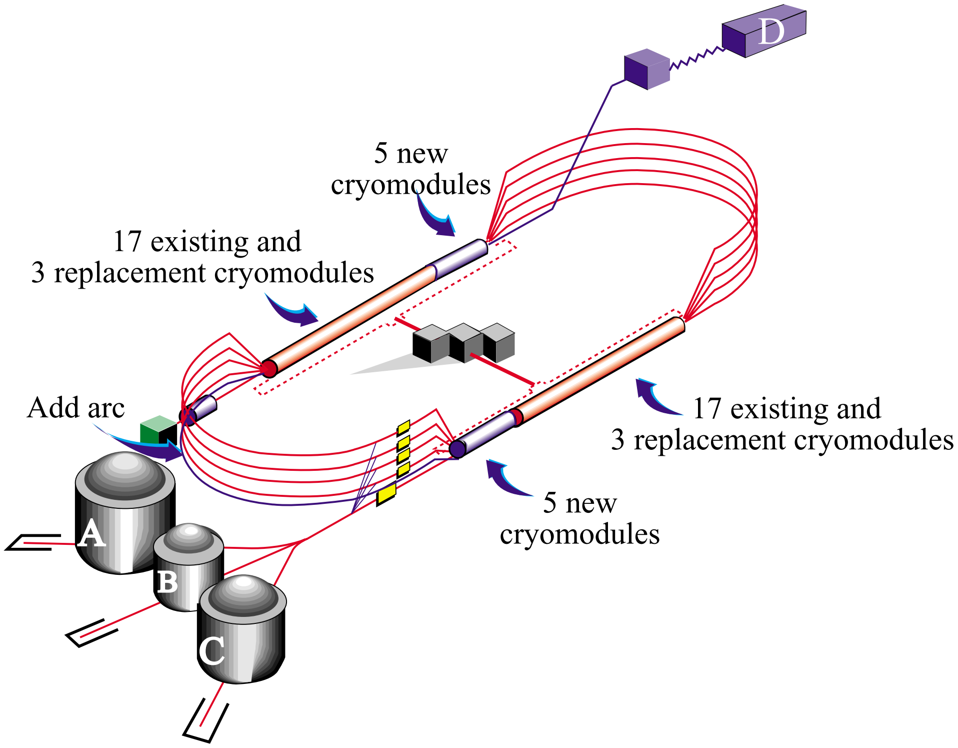

Figure 57: The configuration of the proposed 12 GeV CEBAF upgrade.

cryomodules is a new SRF cavity design. The new cavity has seven cells vs. the five in the present cavity. The cavities will be prepared with improved processes which will result in consistently higher average gradients.

The new cryomodules will increase the static heat load on the cryogenic system. The higher gradients in the cavities in the new cryomodules will increase the dynamic heat load on the system. The result is that the 12 GeV accelerator will require a larger 2 K helium plant than that available for the present accelerator. We plan to increase the 4 K capacity of the helium plant and utilize the already-installed backup 2 K cold box to provide the necessary capacity. The upgraded helium plant will require additional building space, electrical power, and cooling water.

In addition, the behavior of the new cavities will require a change in the rf control. The large Lorentz force at the desired field levels together with a reduced bandwidth to economize power results in a detuning curve that is not single-valued. The present rf control system does not have enough tuning agility to handle this situation. Development has begun of a new rf control module that would not suffer this limitation because it addresses the problem electronically.

3.B.2 Beam Transport

A primary concern of the nuclear physics experimental users is the beam quality. The users have become accustomed to extremely good beam quality. The beam quality will degrade as we push above ~7 GeV because of synchrotron radiation in the bending dipoles. At 12 GeV the spot size will be five times larger than it is at 4 GeV, and the energy spread will be three times larger than it is at 4 GeV. The User Group Board of Directors has endorsed these beam quality specifications.

The beam transport for the recirculation requires no conceptual change. In essence, the fields in the magnets in the primary bending arcs need to be increased. Although the magnets were not designed for operation at these higher fields, simple work-arounds have been identified for almost all of the magnets.

> Dipoles: The dipoles were designed to exhibit minimal saturation effects at fields appropriate for 6 GeV operation of the 5-pass machine. Pushing these fields to values appropriate for 10.9 GeV operation (the equivalent five-pass energy for a 5.5-pass configuration) would lead to considerable saturation and thus require very large power supplies. However, the present dipoles were designed as C magnets; *i.e.*, they have a return yoke on only one side. Our plans call for turning them into H magnets; *i.e.*,

> having return yokes on both sides. This reduces the field levels in the iron to values that are very close to those in the existing C magnets during 6 GeV operation.
>
> Quadrupoles: The prudent engineering margin in the present set of quadrupoles results in their being usable up to ~7 GeV with no changes. Samples of these quadrupoles have been tested up to 170% of their design current and were found to have acceptable field quality. For the majority of the quadrupoles, changing to higher-current power supplies will suffice to reach 12 GeV.

The most obvious change in the beam transport for the accelerator upgrade to 12 GeV is the addition of the tenth recirculation arc. Clearly this requires the construction of new dipoles and quadrupoles. In particular, stronger dipoles and quadrupoles need to be designed. For both we have taken the basic design used in the original construction and have lengthened it to provide the needed field integral.

Less obvious is the need to modify the spreaders and recombiners. (The beams are collinear in the linacs and must be separated at the ends of the linacs and then put back together before entering the next linac.) The topologies in these portions of the machine are sufficiently congested that adding the requisite iron for higher fields will not be possible. Redesign of these sections has been done. Slight adjustments in several magnets' positions were required; replacement of some magnets with longer magnets was also required. Another change was to accommodate the additional beam that will be present in the spreader at the end of the north linac; *i.e.*, the beam going to Hall D. Magnets had to be added in order to separate this beam from the first five passes and to transport it to Hall D.

It should also be noted that unlike the present configuration, which permits delivery of fifth-pass beam to Halls A, B, and C simultaneously, the new configuration requires Halls A, B, and C to receive different energies. Modifications that would permit same-energy beam to be delivered to multiple halls simultaneously are not within the scope of this project.

Clearly, many new power supplies are needed. These will require additions to the building space, more ac power, and more cooling water. In addition, more cooling water will be required for the magnets themselves. The overall requirements for the Upgrade are summarized in Table 7.

Table 7: Summary of major Upgrade items

Number	Item
10	Additional Upgrade CM & supporting rf
6	Replacement Upgrade CM & rf upgrades
-	Double CHL capacity
-	CHL building addition
-	New arc 10
-	Move injector beam line
17	New S/R dipoles
55	Modified S/R dipoles
-	Box PS upgrade (16 regulators, 25 rectifier modules)
5	Modified arcs (C to H style dipoles)
57	New quadrupoles (two new styles)
85	New 17 A, 55 V trim cards
130	New 60 A shunt modules
2	New extraction Lambertsons
5	New (higher-power) rf separator cavities
3	5 kW rf separator tubes
-	New Hall D transport line
-	North and South Access Building additions

3.C CEBAF Today: A Status Report

The Upgrade builds on the present CEBAF accelerator. This section summarizes the status of the accelerator and our operational experience with it. The present accelerator provides a solid platform for the Upgrade. It has already demonstrated the capability of delivering beam near 6 GeV, a full 50% above design specification. The operation of the five-pass recirculation system and the superconducting linacs is now routine, and the accelerator delivers multiple beams with unprecedented polarization and independently controlled current reliably to the three experimental halls. The support systems operate reliably, and the knowledge gained over the past decade of commissioning and operation has provided important insights into the design of the Upgrade.

The design energy of CEBAF is 4 GeV, based on 20 cryomodules in each of the north and south linacs and $2\frac{1}{4}$ modules in the injector. Because the later modules in the production run significantly exceeded the design specification one of the modules was removed from the south linac to study Upgrade options, leaving only 19 modules in that linac. It was with this complement of cavities that CEBAF reached its design beam specification (4 GeV, 200 μA) in 1997. In subsequent years, the cavity trip rate due to arcing on the rf window (that is believed to be caused by charge build-up from electron emission in the cavity) was reduced by the use of helium processing, and the maximum energy of the accelerator has been steadily increasing. In January 2000, a new cryomodule was installed in the last slot of the south linac, and cryomodules were interchanged between the north and south linacs to equalize the energy gain available from each linac. These improvements significantly reduced the rf trip rate during operation at energies up to 5.6 GeV. A test of 6 GeV operation was performed in August 2000 with cw beam. Further improvements and 6 GeV testing are planned, and we expect to deliver 6 GeV beam for physics in the near-term future. The basic operating characteristics of the CEBAF accelerator are outlined in Table 8.

Maintaining the rf systems in optimum condition has required the development of complex algorithms. These maintain the cavities on resonance, and keep the beam on the crest of the cavity fields. In addition, a sophisticated program optimizes the cavity gradient to minimize the arc trip rate and cryogenic heat load for a required total acceleration energy and beam current. A recent problem is that some cavities are now operating in the regime where the Lorenz detuning exceeds the cavity bandwidth, so that recovering a tripped cavity is time-consuming and must be carried out by hand. Semi-automated routines will be written to improve the recovery time, but new rf modules are needed to operate the new cryomodules. Definition of the system requirements and initial engineering discussions on these new rf control modules have been started.

The magnet and power supply systems, as originally installed, were limited to settings cor-

Table 8: Key parameters of the present CEBAF accelerator

Parameter	Specification
Number of passes for Halls A,B,C	1–5
Max. Energy to Halls A,B,C	≤ 6 GeV
Duty factor	cw
Beam emittance at full energy:	
transverse	3×10^{-7}mm
longitudinal	$\delta p/p \leq 1 \times 10^{-4}$
Max. summed current to Halls A,C*	180 μA
Max. current to Hall B	5 μA
# of cryomodules	$42\frac{1}{4}$
Central Helium Liquifier capacity	4.8 kW (at 2.07 K)

*Max. linac current is 1 mA

responding to slightly above 4 GeV, with the limitation coming from some of the power supplies. These have been upgraded, so the accelerator may now be considered a 6 GeV machine. The stability of the magnet system has undergone several rounds of improvements as the requirements of the users became more demanding. This required the development of off-line analysis tools to find unstable magnets and/or power supplies. Most of the problems were traced to the way the hysteresis loops were handled, and these have now all been changed to a new protocol that provides both short- and long-term stability.

The polarized injector now has two fully operational, horizontally mounted polarized guns. All beam operation, polarized or unpolarized, is now conducted with high-polarization cathodes. When polarized beam is not required, shorter-wavelength lasers are used to take advantage of the higher quantum efficiency at these wavelengths. This has been very successfully demonstrated as of mid-2000, with unpolarized beam up to 130 μA delivered to Hall A while high-polarization beam was delivered to Hall B at 5 nA. The only known problem is that tails on the high-power laser pulses for Halls A and C can produce electrons within the acceptance for Hall B. Typical values for this feedthrough from Hall A to Hall B are about 50 pA. The photocathode lifetime in the new horizontal guns is excellent. The present value is over 10^5 C/cm^2. Though this long lifetime makes absolute statements difficult, our present experience is that the cathode deterioration can be completely removed by a simple heat treatment and reactivation. This cathode recovery can be accomplished during a normal maintenance period, which implies that a single cathode could be used essentially without limit. During the past year, over 280,000 μA-hours were delivered from the polarized guns.

During January 2000, a test run was conducted with a new Ti-sapphire laser, which delivered ~400 μA of high-polarization beam. The final version of this laser will allow this current to be more than doubled. We installed this laser during the shutdown in August 2000. Once this laser is operational, we will be able to deliver high-polarization beam at full current to one hall. A second laser of this type will be prepared, to allow high-polarization operation to both Halls A and C. Based on the very successful operation of the new guns, and the coming installation of this new laser, we have removed some of the components that allowed beam to be delivered from the thermionic gun. While we could restore these components and operate the thermionic gun again, there is no plan for any further running with unpolarized (or low-polarization) beam.

Over the last three years, most of the operations have been scheduled with polarized beam required in more than one hall. There are only two beam energies (2.115 and 4.230 GeV) at which purely longitudinal spin can be delivered simultaneously to all three halls when the halls have the same energy. There are, however, many combinations of passes and linac energies at which it is possible to deliver beams with perfectly longitudinal polarization to two halls simultaneously, and many combinations at which it is possible to deliver nearly (¿90%) longitudinal polarization to all three halls.

3.D Details of the 12 GeV Upgrade of the CEBAF Accelerator

In this section we address, in turn, the changes necessary to the CEBAF accelerator to upgrade it to the 12 GeV capability required for the physics program. We address, in turn, new accelerating structures, rf power and control, the optics and beam transport, magnet power supplies, instrumentation and control systems, cryogenics, and civil construction. A final section addresses the schedule for the Upgrade.

3.D.1 Accelerating Structures

The Upgrade Cryomodule is clearly the key component of the upgrade of the acceleration system. Its design is also somewhat insensitive to the details of the Upgrade, once the top-level parameters have been defined, and it can be viewed as a building block that can be applied to a large number of Upgrade paths. For these reasons, most of the development efforts in support of the Upgrade are directed toward the development and demonstration of prototype Upgrade cryomodules. Table 9 compares the original CEBAF linac parameters with those of the upgraded linac with the new cryomodules added.

Table 9: CEBAF linac parameters: 4 GeV vs. 12 GeV

Parameter	Linac CMs for 4 GeV (original)	Linac CMs for 12 GeV Retained original	Upgrade
Acceleration	400 MeV	544 MeV	544 MeV
Maximum linac current (at maximum E)	1000 μA	430 μA	430 μA
Linac slot length	9.6 m	9.6 m	9.6 m
CM* slot length	8.25 m	8.25 m	8.71 m
Warm vac. slot length	1.35 m	1.35 m (also 1.12 m)	0.89 m
# CM/linac	20	$\geq$17	$\leq$8
Voltage/CM	20 MV	32 MV	68 MV
E_{acc} average	5 MV/m	8 MV/m	12.2 MV/m
$Q_\circ$ @ E_{acc}	2.4×10^9	5.0×10^9	6.5×10^9
rf windows/cavity	2	Same	1
FPC coupling	$\lambda/2$ stub on stub	Same	$\lambda/4$ stub
Q_{ext} FPC	6.6×10^6	Same	2.2×10^7
HOM coupling	Waveguide	Same	Coaxial
B.L. bellows/CM	5	Same	2
Vac. valves/CM	10	Same	4
Freq. tuner/cavity	Single	Same	Dual (coarse/fine)
Cryounits (CU)/CM	4	Same	1
Cavities/CU	2	Same	8
2 K rf heat load	45 W	72 W	160 W
50 K rf heat load	20 W	40 W	120 W
2 K static heat load	15 W	15 W	25 W
50 K static heat load	140 W	140 W	180 W

*CM = cryomodule

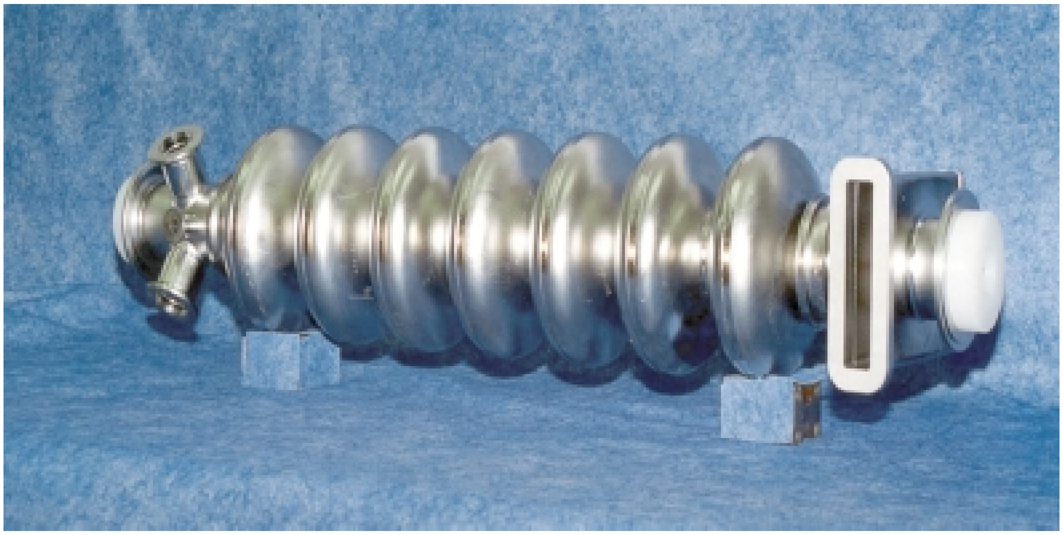

Figure 58: Prototype seven-cell cavity.

Cavities

In order to increase the voltage that is provided by a cryomodule within a given length, one can either increase the gradient at which the cavities are operating, or increase the effective accelerating length, or both. While it may be argued that adding accelerating length is the approach that presents the least technological risk, for cw accelerators such as CEBAF, maximizing the length instead of the gradient has the added advantage of lowering the dynamic load on the refrigeration system.

For this reason, it was decided early that the Upgrade Cryomodule would still include eight cavities, but that these would be seven-cell cavities (70 cm) instead of the present five-cell (50 cm). Meeting the overall system performance goals calls for these cavities to provide a minimum voltage of 8.75 MV with a maximum power dissipation of 17.5 W; *i.e.*, their Q_0 must be at least 6.5×10^9 at 12.5 MV/m. Thus the greatest challenge is not so much in achieving a high gradient but in maintaining a high Q_0 at that high gradient. Given the constraint imposed by the available refrigeration, cw operation at 15 MV/m would be practical only if the Q_0 at that field were at least 10^{10}.

While the CEBAF cavity cell design could be improved, the potential benefits do not seem critically important, and the first seven-cell cavity prototype was built using the existing cell design (see Figs. 58 and 59). The first prototype met the requirement of a Q_0 of 6.5×10^9 at 12.5 MV/m.

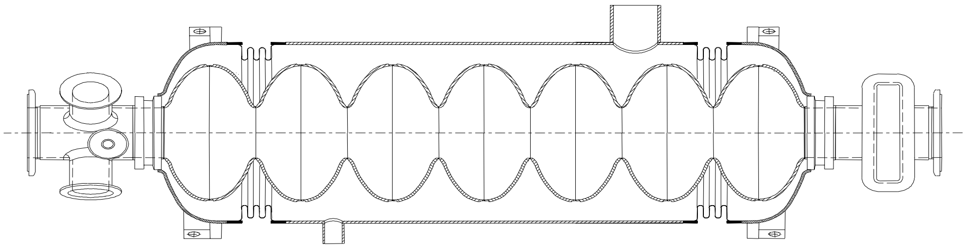

Figure 59: A seven-cell cavity in its helium vessel.

The existing cell shape is characterized by ratios peak fields to accelerating fields, $E_{\mathrm{p}}/E_{\mathrm{acc}} = 2.6$ and $H_{\mathrm{p}}/E_{\mathrm{acc}} = 47$ Oe/(MV/m). Designs with lower ratios exist; however, as was mentioned before, the greatest challenge is not so much high gradient as low power dissipation. In that respect, the shunt impedance of the existing design compares well with that of others. Another attractive feature of the existing cell design is the relatively high cell-to-cell coupling coefficient (3.3%), which reduces the sensitivity of the field profile to mechanical tolerances and mechanical stability as the number of cells is increased. A redesign of the cells is still an option, although a low-priority one.

Cryomodule design

The existing CEBAF cryomodule is constructed from four cryounits, each containing a sealed cavity pair. These cryounits are then joined with bridging sections. In order to increase the number of cells from five to seven while maintaining the same cryomodule length, this approach had to be abandoned. Several cryostat concepts were explored:

- Cylindrical cryostat with radial penetrations for the power couplers.
- Cylindrical cryostat with axial (through the end plates) penetrations.
- Bathtub-type cryostat where all the internal components are suspended from a top plate.

While all designs had advantages and disadvantages, a cost/benefit analysis did not reveal an obviously preferred option. The radial design was chosen, as it was the one that would require the least amount of development given the on-site experience with the radial design. The Upgrade Cryomodule will include a continuous eight-cavity string assembly without isolation valves between the cavities. The present Upgrade design calls for a 30 cm separation between cavities into which must fit the fundamental power coupler, the higher-mode extraction system, the pick-up probe, connecting flanges, and connections to the helium tank and mechanical tuners. The design does

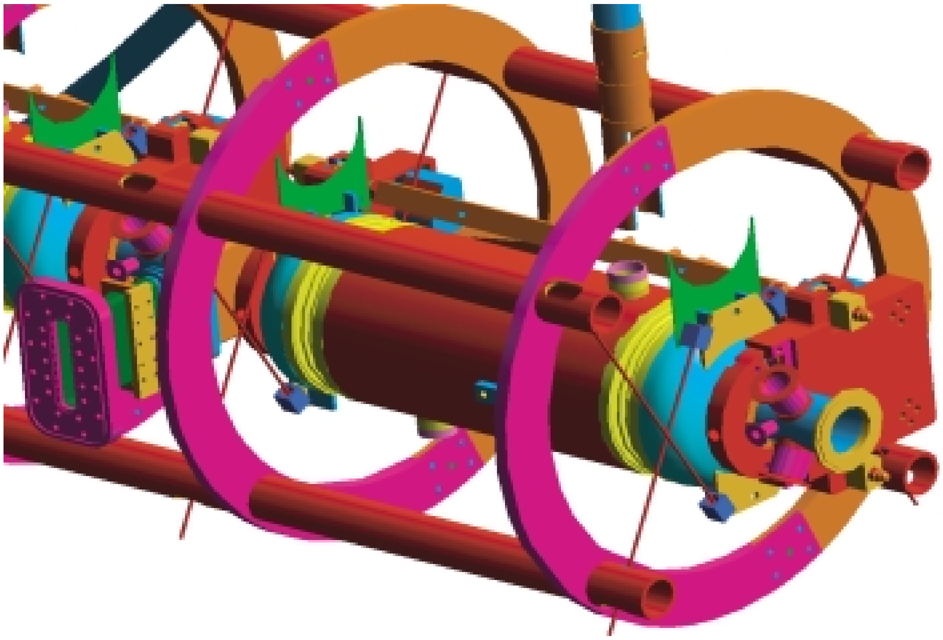

Figure 60: A CAD drawing of the helium vessel in its space-frame.

not include bellows between the cavities. Figure 60 shows the helium vessel in its space-frame. Figure 61 shows a cut-away view of the assembled cryomodule.

Cryomodule components and design choices

Fundamental power coupler Both coaxial and waveguide couplers were explored. The waveguide concept was retained because of its simplicity and flexibility at 1500 MHz. Unlike the present design, though, we have decided to completely separate the functions of fundamental power coupling and higher-mode extraction. This produces a coupler design (Fig. 62) that, unlike the existing CEBAF design, is free of transverse kick imparted to the beam and allows a cryostat design where all the power couplers are on the same side.

Higher-order mode damping The requirements for higher-order mode (HOM) damping for the 12 GeV Upgrade have been substantially relaxed from the original CEBAF design. Not only is the energy increased from 4 to 12 GeV, but the maximum circulating current is being reduced from 1000 to 425 μA. Additionally, the experience acquired during CEBAF operation has led to a

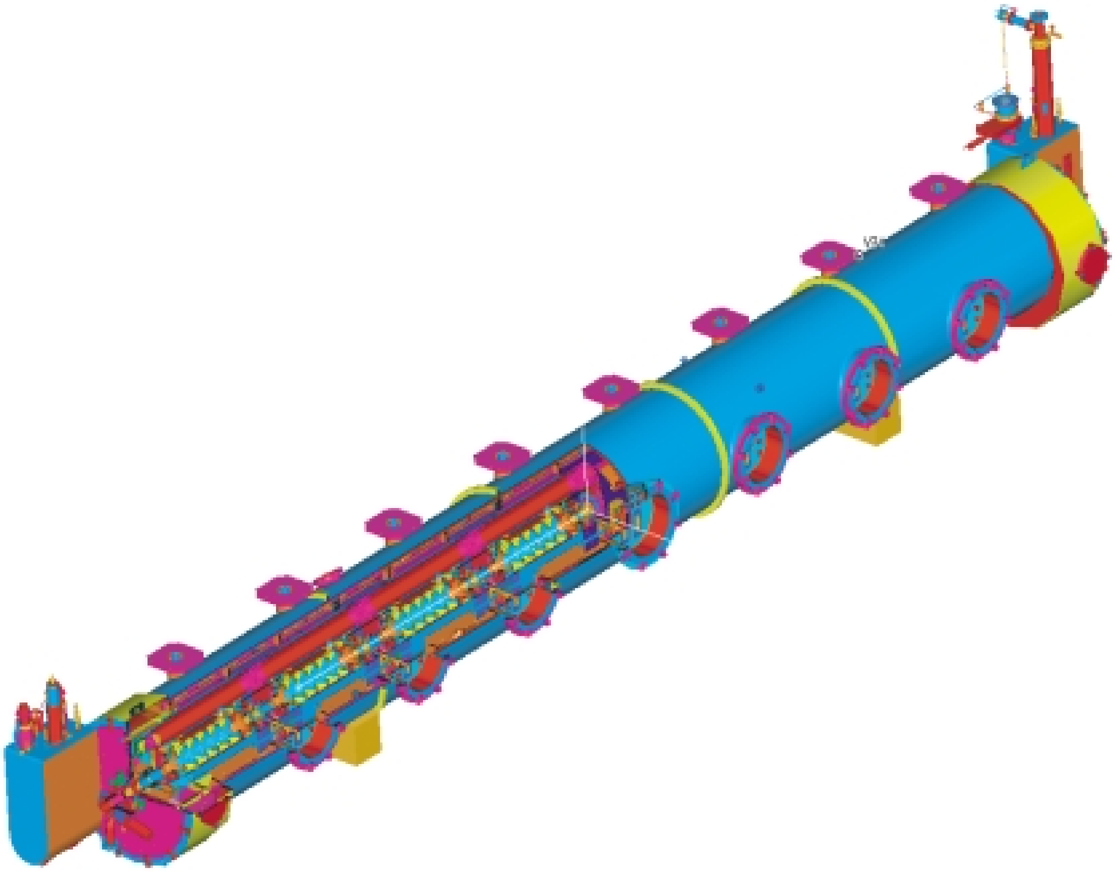

Figure 61: A CAD cut-away drawing of the assembled cryomodule.

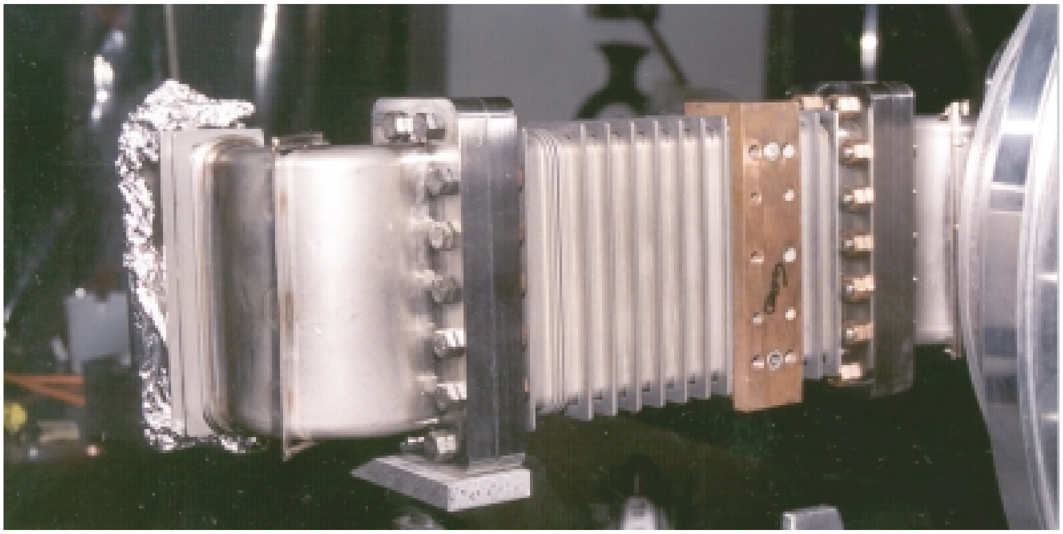

Figure 62: Prototype fundamental power coupler.

reduction of the "safety factor" for the stability threshold current. As a result an upper limit of 10^6 was adopted for the Q_{ext} of the HOMs. The design of the HOM couplers (Fig. 63) is a departure from the existing design in that we do not rely on any HOM extraction with the fundamental power coupler. The new design uses two coaxial-type couplers as opposed to the present waveguide type. These couplers are located outside the helium tank, permitting deposition of the HOM power at a temperature other than 2 K and thereby minimizing the refrigerator load.

Thermal design When 2 K is involved, heat load is always a concern. All supports and penetrations reaching the 2 K volume have been designed to minimize the heat load. The projected static heat load is 25 W per cryomodule.

Frequency tuning The frequency tuners perform several functions: bringing the cavities on resonance after installation, detuning the cavities that are not operating, and tracking the changes in frequency due to Lorentz detuning pressure and temperature fluctuations. For the Upgrade Cryomodule, the bandwidth will be small (~75 Hz), the Lorentz detuning large (~500 Hz), and we want to track the frequency accurately (~2 Hz) in order to minimize the rf power requirements. For this reason the baseline design incorporates two different tuning schemes: a coarse mechanical tuner with 400 kHz range and 100 Hz resolution that will be used infrequently, and a fine piezoelectric tuner with 1 kHz range and 1 Hz resolution that will provide the fine, frequent tracking. Figure 64

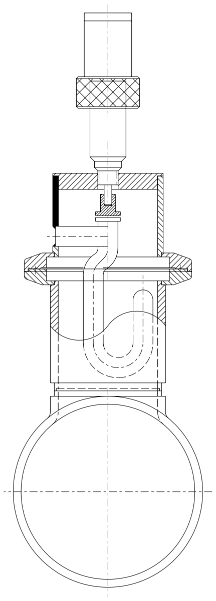

Figure 63: A drawing of the new HOM coupler design.

shows a prototype of the cavity tuning mechanism containing hardware for both schemes.

Processes and procedures While the gradients required are modest compared to those for proposed linear colliders, a high Q_0 is of primary importance. Furthermore, since rf power will be a hard constraint, "outstanding" cavities cannot operate at higher gradient in order to compensate for "weaker" ones. For these reasons our main goal is to achieve consistent performance. We are engaged in a complete review of all the processes and procedures involved in the fabrication and assembly of cavities and cryomodules. Modifications to the processing and assembly facilities, such as implementation of final chemistry and rinsing in the clean room, are under way.

Microphonics, rf control, and rf power Cost containment was a major goal in the overall system design. In order to contain the cost of the Upgrade we have adopted as a goal only a modest increase of the rf power per cavity from 5.0 to 8 kW for the Upgrade cryomodules. This has two effects:

- Total required rf power is a major driver in the cost of the new rf systems and in operational cost. In order to minimize the required rf power at the design gradient and circulating current, a cavity-coupling factor was chosen: 2.2×10^7. A $\lambda/4$ stub waveguide coupler intersecting

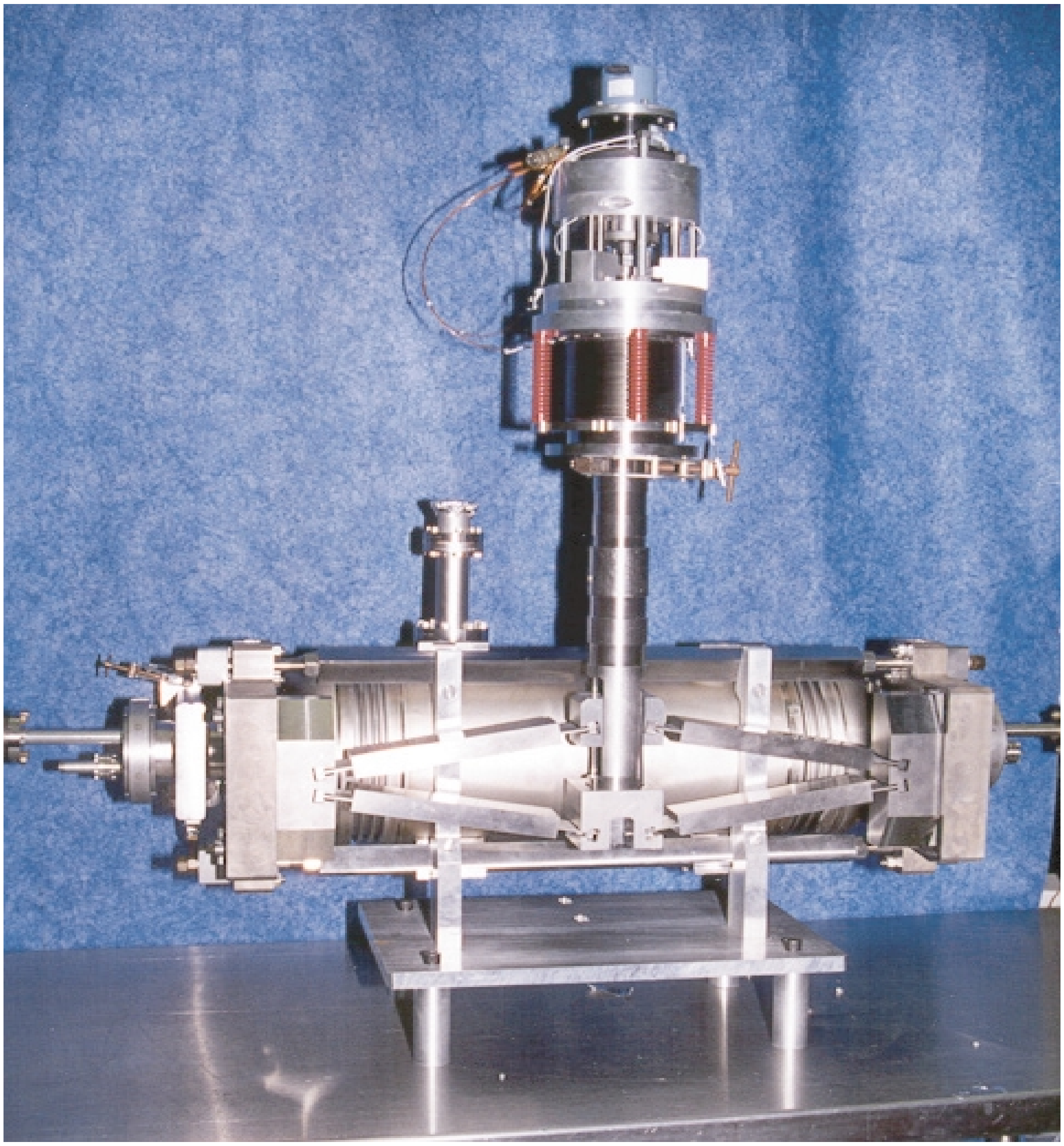

Figure 64: Prototype cavity tuning mechanism.

the beam pipe couples the TE_{01} waveguide mode to the evanescent TM_{01} cavity mode. The waveguide-coupler-to-cavity separation was selected to achieve the desired coupling.

- This puts stringent requirements on microphonics and the control system. At an accelerating gradient of 12.5 MV/m and 400 μA circulating current, the maximum allowable amount of detuning (including static and microphonics) is 25 Hz. The optimum Q_{ext} is 2×10^7, and the Lorentz detuning is much larger than the loaded bandwidth; for this reason a new low-level rf control system will be required. The baseline concept is an agile digital system capable of implementing a self-excited loop on I/Q feedback.

3.D.2 RF Power and Control

To meet the beam energy requirement for the Upgrade, the linacs must be expanded and additional rf systems procured. Presently the CEBAF rf system consists of an injector (warm-temperature chopper, buncher, and capture sections followed by a superconducting quarter-cryomodule and two full cryomodules) plus two linacs of 20 superconducting cryomodules each. A total of 42 eight-cavity cryomodules are powered by 42 identical rf systems. Each zone comprises both low- and high-level rf equipment located in the service buildings above the tunnel. Each cavity has its own klystron and low-level controls.

The energy upgrade will require new rf systems for the additional ten new cryomodules and six upgraded rf systems for replacement cryomodules. The new rf systems will require 8 kW klystrons (vs. the original 5 kW). To control the new higher-gradient cavities the rf phase and amplitude controls will be redesigned to handle the higher loaded Q and hence increased fluctuations from microphonics.

Control

The most significant change in the rf system is the new control module. The need for a major change is due to the dramatically different resonance curve for the new cryomodule vs. the existing ones. The curve for the new cryomodule is shown Fig. 65. As can be seen readily, the curve is not single-valued, whereas it was single-valued for the existing cryomodule. The change is due to the large Lorentz detuning of the cavities at the anticipated higher gradients. An effect of this detuning curve is that should a cavity trip off, the cavity is at the wrong frequency. With the present cavity control, the mechanical tuner would have to be used to bring the cavity back onto resonance; this is a slow process (minutes) and would seriously degrade the overall beam availability. The new

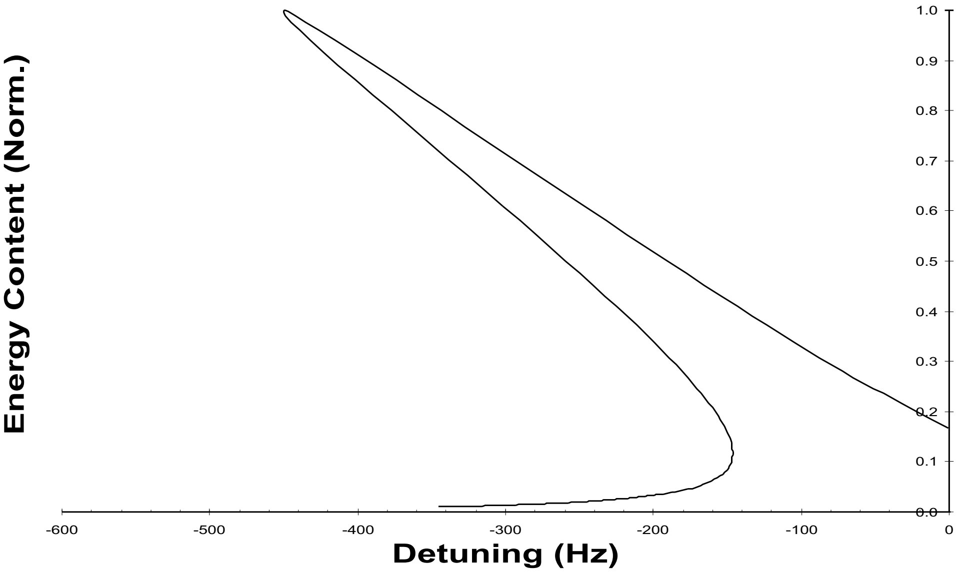

Figure 65: The detuning curve for the seven-cell cavities.

control module will handle this without use of the mechanical tuner.

The existing rf controls and interfaces include a separate rf control module plus CAMAC crate and modules: CAMAC-to-CM interface, CAMAC I/O for other analog and digital functions (status, interlocks, controls, tuning), and CAMAC-to-IOC interface for connection to the EPICS control system. The rf control design is over 10 years old, with CAMAC substantially older still. The years are beginning to show, and some replacement parts have become extremely limited or completely obsolete and unavailable. Additionally, critical eurocard connectors are about to exceed their rated lifetime insertions. Induced power-line noise makes numerous modules unable to meet full specifications. Duplicating the present design for new zones with higher-performance SRF cavities is not appropriate because the higher gradient of the new seven-cell SRF cavities will likely be uncontrollable using the present rf module design.

A proposed new control module retains the concept of the "individual microprocessor per klystron rf source", but replaces the other hardware with an FPGA- and DSP-based design, and eliminates CAMAC entirely. Much of the present analog function will be created using stable digital circuitry. This allows greater flexibility in refining rf control algorithms, plus opens the capability of running true pulse-mode operation in addition to cw.

Moving the functionality of the multiple CAMAC modules into the rf control block more tightly

Table 10: Components for an 8 kW rf power zone

Item	#/Zone	Description
(High-power amplifier)	1	HPA w/ auxiliary power supplies (heater, mod anode, etc.), LCW manifold, WG pressurization manifold and interlock
Klystron	8	Rated 8 kW cw @ 1497 MHz
Waveguide components		Includes 8 each, circulators, couplers, transitions, HOM, sweeps, flexes, and straight waveguide
(Cathode power supply)	1	14 kV @ 14.5 A power supply, variable output w/crowbar
Control module	8	New design modules (replaces CAMAC as well)
Power supplies	1	dc power for control modules and interfaces
MOPS	1	(Multi-output power supply) for controls and interlocks
Rack cooling	1	Filtered, forced air cooling for low-level racks
Racks	3	Low-level rack assembly

integrates all of the rf controls, makes all rf signals immediately available to the control module, and reduces the number of interconnects by reducing the number of separate chassis and associated cabling. The effects of improved reliability and maintainability are also enhanced through better built-in, on-board diagnostics. The new digital design reduces the analog component count greatly, thereby reducing the time required for calibration to achieve, and maintain, design goals.

Power

8 kW rf systems To support the higher-gradient cavities, 8 kW of rf power is needed. This will include a modified klystron tube (modified gun and collector) beyond our present 5 kW tubes. In addition the dc power supply will be larger to support the additional power requirements. The new rf phase and amplitude controls will be based on modern digital receiver technology to take advantage of commercial, industrial, and military improvements. Sixteen 8 kW systems are needed for the energy upgrade. Table 10 summarizes the components of an “8 kW” rf power zone.

Master reference oscillator and drive line The base frequency of the master oscillator (MO) is 499 MHz. This frequency and 70 MHz are distributed around the complex. At each service building, the 499 MHz is tripled to 1497 MHz and then mixed with the 70 MHz to get a 1427 MHz signal. The 1427 MHz and 70 MHz are distributed throughout each service building with a thermally stabilized drive line. Directional couplers deliver the signals to each zone where it is further split for each cavity's control module.

The new controls will use the same frequencies as presently used: 10 MHz, 70 MHz, and 1427 MHz. The drive line in one linac will need to be extended and couplers added. As described in the section on beam transport, the new MO system (being tested as of fall 2000) will have a large (0.001%) base frequency adjustment capability.

3.D.3 Optics and Beam Transport

Beam transport for the 12 GeV Upgrade project is straightforward. The basic layout and optics need not be changed. As such the changes amount to ensuring that all deflecting/focusing elements can reach the higher fields that are required, adding arc 10, adding the Hall D beam line, and adjusting the fifth-pass extraction. One additional feature of the Upgrade is to recirculate the beam in the injector before injection into the main accelerator. All magnets are "resistive" – *i.e.*, not superconducting.

Layout and optics

Beam quality The existing CEBAF accelerator has delivered outstanding beam quality. The unnormalized rms (4σ) emittances for the full-energy five-pass beam are 2.9×10^{-7} mm in both the horizontal and vertical planes. The energy spread is ~0.01%. With the upgraded accelerator, these values will be larger due to the greatly increased synchrotron radiation emitted in the bends. The 12 GeV emittances are projected to be $\epsilon_x = 9 \times 10^{-6}$ mm and $\epsilon_y = 1.9 \times 10^{-6}$ mm; the energy spread is projected to be 0.02%. (See Table 11.)

Spot sizes would nominally scale with the square roots of the emittances; there is flexibility in the final optics before the targets, so it is possible to overcome some of the problems that are strictly spot-size-related. These values have been reviewed by the User Group Board of Directors (UGBOD) and approved as being consistent with the needs of the physics program. Some changes in local optics/central orbits may be required to ensure there is no beam scraping with the enlarged beams.

Table 11: Unnormalized rms transverse emittances and momentum spreads for a $5\frac{1}{2}$-pass, 12 GeV CEBAF.

Area	δp/p $\times 10^{-3}$	ϵ_x (mm)	ϵ_y (mm)
Chicane	0.200	4.17×10^{-06}	4.17×10^{-06}
Arc 1	0.200	4.34×10^{-07}	4.34×10^{-07}
Arc 2	0.106	3.13×10^{-07}	2.63×10^{-07}
Arc 3	0.078	2.89×10^{-07}	2.83×10^{-07}
Arc 4	0.069	3.15×10^{-07}	4.15×10^{-07}
Arc 5	0.074	5.81×10^{-07}	4.81×10^{-07}
Arc 6	0.097	1.41×10^{-06}	6.44×10^{-07}
Arc 7	0.110	2.21×10^{-06}	7.03×10^{-07}
Arc 8	0.140	3.58×10^{-06}	1.03×10^{-06}
Arc 9	0.178	6.67×10^{-06}	1.12×10^{-06}
Arc 10	0.213	9.43×10^{-06}	1.91×10^{-06}

It should be noted that a study determined that it is indeed possible to decrease the emittances. In order to achieve the improvement, the last two or three arcs would have to be completely replaced. The UGBOD did not view the improvements worth the projected several-million-dollar cost or worth the loss of beam time associated with the required additional facility down time. This option could be considered for a future project.

Injector One inconvenient feature of a several-pass recirculating linac is the fact that the highest-pass beam experiences the same focusing magnets as does the first-pass beam as they transit the linacs. In our 4 GeV baseline, the ratio of injected beam energy to final-pass beam energy is 3200 MeV/45 MeV $\simeq$ 71. As a result, the higher-pass beams experience essentially no focusing while transiting the north linac. To deal with this it is necessary to set up large beta functions in the final recombiner, with the resulting sensitivity to magnet settings.

The problem is exacerbated if the linac energy is increased but the injector energy is not. The present injector cryomodules cannot reach the total energy gain needed to maintain the present injector-linac energy ratio. Several options have been examined to deal with this problem. Although the studies are not complete, the likely solution will be to retain the present cryomodules and recirculate the beam; this option is much cheaper than replacing the cryomodules and rf systems, for example.

Linacs The optics in the linacs consists of a single quadrupole dividing each pair of cryomodules. The quadrupoles are set for a FODO with 120°/cell phase advance for the first-pass beam. The exact settings of the quads are adjusted to incorporate the focusing from the SRF cavities. An additional focusing effect of the cavities' fields is a skew quadrupole component; this component is compensated by small, air-core skew magnets located between the cryomodules.

As a consequence of multipass recirculation, beams with quite different energies "see" the same magnets (*e.g.*, $E_{\text{pass6}}/E_{\text{pass1}} \cong 90$ at the entrance to the north linac). Since focal lengths scale proportionally with the beam energy, the focusing on the higher passes is quite different from what the first-pass beam experiences. The problem is particularly acute in the north linac, which has both the lowest-energy beam – *i.e.*, that from the injector – and the highest, *i.e.*, the sixth-pass beam. The linacs are essentially optical drifts for the higher-pass beams. Thus, the beta functions need to be set up specifically for each pass through a linac; this is done in the recombiners.

Spreaders/recombiners At the exit of each linac, the collinear beams (one for each pass) are spread apart vertically for transport through the recirculation arcs. These beam lines carry the beams through 180°, after which they are recombined into collinear beams before entering the subsequent linac. Both the spreaders and recombiners on a given "end" of the machine have dispersion suppression. The spreaders and recombiners are essentially mirror images of each other. Matching into the 180° arcs is functionally included in the spreaders; likewise matching into the linacs is included in the recombiners. There is one recombiner in the beam switchyard that can put beam from any pass onto the correct trajectory to reach any of the original three experimental halls.

The spreaders and recombiners are very congested physically. The magnets are not small, and the space is limited, so a lot of effort was expended getting everything to fit. Unfortunately, even larger magnets are needed for the Upgrade. The limited space precludes simply going to higher fields, as this would require more return yoke. A longer-magnet alternative was chosen. This results in small changes in the central beam path that must be accommodated with slight shifts in about 50% of the magnet positions. The northeast spreader (which includes the sixth-pass beam) is shown in Fig. 66.

Recirculation The nine original CEBAF recirculation arcs perform the function of achromatic, linearly isochronous[5] transport of beam for re-injection into the linacs. An effort was made

---

[5] In practice the optics within the arc is tuned such that the overall momentum compaction including spreader, arc, and recombiner is zero.

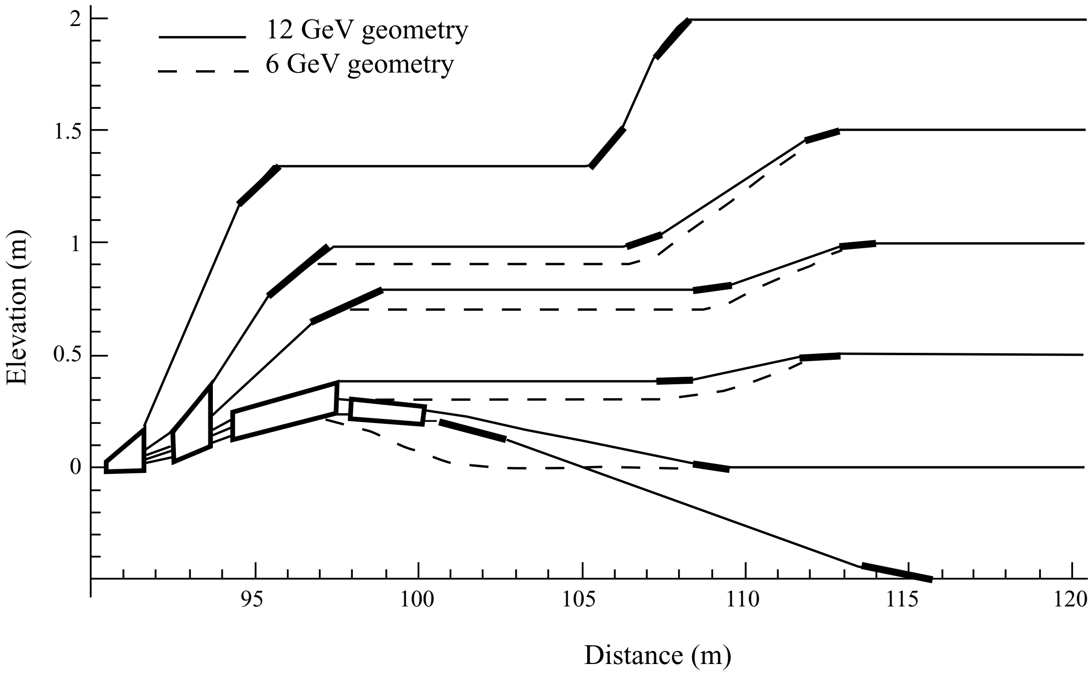

Figure 66: The original and upgraded versions of the northeast spreader.

in the original design to minimize quantum excitation and error sensitivity. Each arc consists of four super-periods, each with four FODO cells. The design of each super-period is based on a pair of back-to-back 90° dispersion suppressors which were re-tuned for overall isochronicity (including compensating for the effects of the spreaders and recombiners), providing minimal betatron function mismatch, and giving phase advance appropriate[6] to generate a second-order achromat. The lattice allows independent tuning of horizontal dispersion and momentum compaction. The first two arcs have been tuned to moderate (6 m) dispersion modes in recent running to provide high-resolution signals for energy monitoring and stabilization. The optics in the original nine arcs will be unchanged by the Upgrade. Magnetic fields are required which exceed the capability of the presently installed magnets. The plans for accommodating this will be addressed below.

A significant change in the recirculation is the addition of arc 10, which brings the beam to the north linac for its sixth pass through. The optics for this arc is the same as for the original nine arcs.

---

[6] This results in 5/4 of the horizontal and 3/4 of the vertical betatron wavelength per super-period.

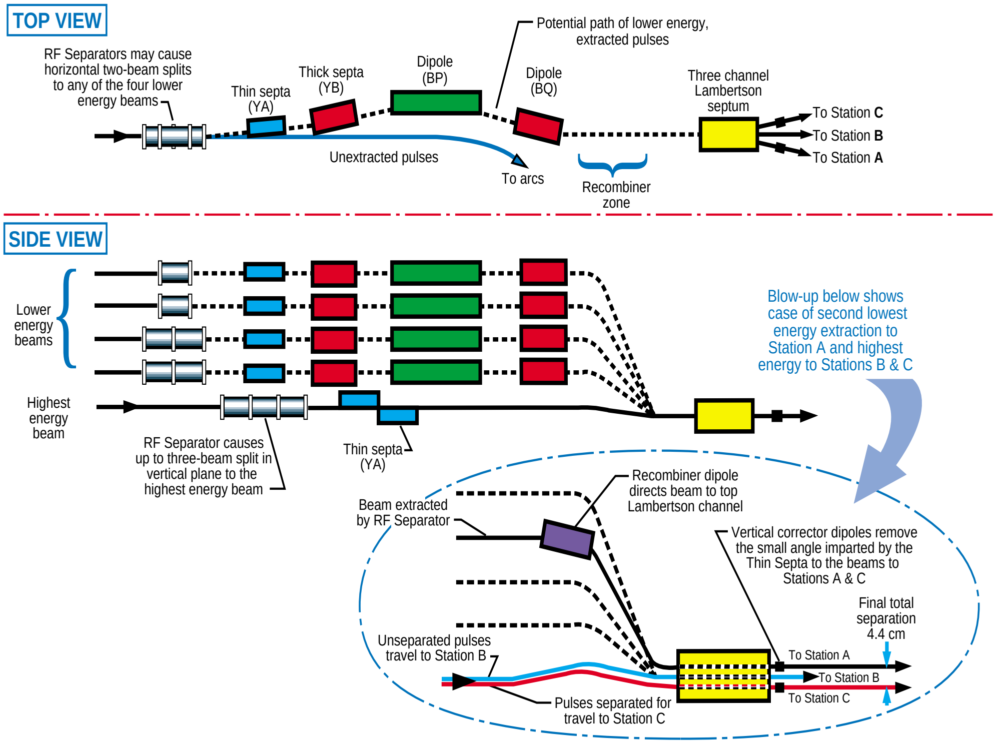

Figure 67: The extraction scheme for the present CEBAF accelerator.

Extraction The extraction region consists of a pair of 33.1-m-long FODO cells tuned to one quarter-wavelength phase advance. Thus the entire unit comprises a $(-I)$ transform in both planes. The large horizontal beta function is exploited for beam extraction using rf separator kicks in all the west-end extraction regions. Pass-by-pass path-length control is also realized within the extraction region with three-magnet chicanes (doglegs) located in the second half-cell. The layout is illustrated in Fig. 67.

For the Upgrade, the extraction scheme will be unchanged for passes 1–3. Additional field will be needed for the rf separators and magnets. The separator performance will be upgraded by adding cavities to passes 2 and 3 and by increasing the rf power for each cavity.

Passes 4 and 5 will have their present configurations changed noticeably. There will be four separator cavities in each line. They will be followed by horizontal-kick Lambertson magnets. Pass 5 will have an extraction chicane added that parallels the ones used in passes 1–4. The change in pass 5 eliminates the present capability of delivering the same energy to all three experimental halls simultaneously. Adding a three- or four-way split is not within the scope of the Upgrade.

However, it could potentially be done in the out-years.

Hall D beam line The beam trains (there are three, each at 499 MHz) that are not extracted by the two-way rf separators in passes 1 to 5 will enter arc 10. The northwest recombiner re-injects them into the north linac for their final gain of 1.09 GeV. The northeast spreader does a six-way momentum separation with Hall D beam being 0.5 m below the fifth-pass beam (arc 9). It then goes straight to the northeast stub, passing under the doglegs for arcs 1, 3, 5, 7, and 9 and the arcs themselves. The beam line to the Hall D radiator is dispersion-suppressed and has a matching section so that beta functions can be adjusted to meet the needs of experimenters.

Magnet and power supply changes

Overview The CEBAF accelerator contains over 2200 magnets, including approximately 415 bending dipoles, 650 quadrupoles, 96 sextupoles, and 1050 corrector dipoles. These magnets were designed and magnetically mapped to support 6 GeV. The total number of families of magnets was kept to a minimum to reduce construction costs. This resulted in the magnets of a given family operating over a wide dynamic range and in various regions of the accelerator. Thus, when planning an upgrade to higher energies, only those magnets operating at the upper end of their original design range need consideration. The sections below detail the magnet changes required to support the 11 GeV Upgrade of the existing five-pass machine and the additional magnets required for transporting the sixth-pass, 12 GeV beam to Hall D.

Field quality requirements Unlike during the original design of CEBAF, we now benefit from several years of operating experience and have well-established procedures for machine setup and monitoring. The field quality specifications for the Upgrade are based on this experience and are aimed at accommodating the present procedures. The new procedures focus on uniformity of any focusing component in a magnet when experience-based estimates of beam motion are included.

Arc dipoles As mentioned previously, many of the present magnets do not provide sufficient fields without becoming extremely saturated. This is particularly true for the arc dipoles. They were designed for efficient performance up to ∼300 A; 550 A would be required for 12 GeV operation. However, there is a fairly easy and inexpensive remedy for this. Figure 68 shows a cross section of an arc dipole. The basic design is that of a C. This means that all the flux must route through

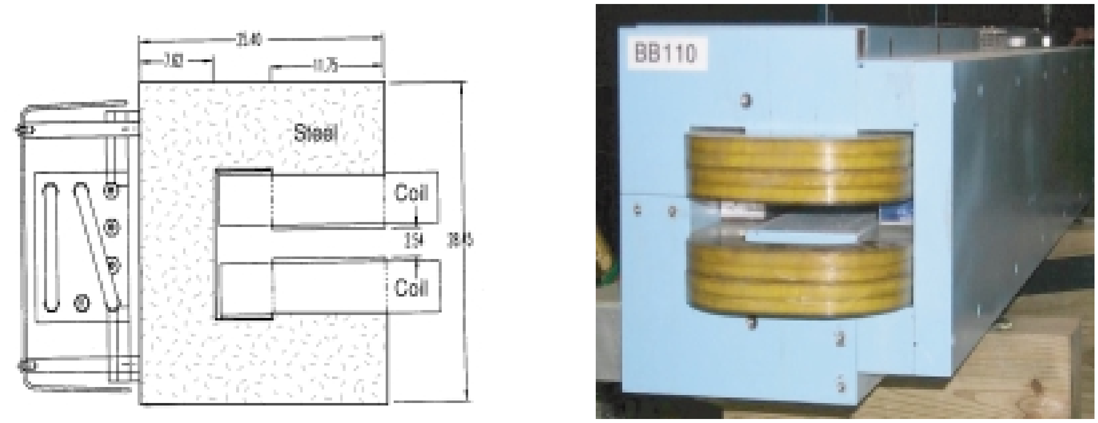

Figure 68: The cross section of a typical arc dipole (left); and a photo of the dipole modified from the C to H configuration by the addition of three iron plates (right).

one side of the magnet. It is the backleg of the return iron that saturates. We can add a C on the open side (right side in this figure) which turns them into H style dipoles, thereby increase the area for flux return, and essentially eliminate the saturation. Computer modeling has been done and verified by a prototype. The modification is sufficiently simple that the magnets can be modified in situ. The modification will be made to the dipoles in arcs 3, 5, 6, 8, and 9 and the dipoles in the beam line leading to Hall B. Arc 10 will have brand new dipoles that will be manufactured as H magnets; in addition, they will be 4 m long, whereas the longest magnet in the existing machine is 3 m.

Spreader/recombiner dipoles Most of the S/R dipoles are built using a C-shaped steel core. Several of these cores are limited by return legs and can be improved with the H-steel modification, as described earlier. All cores are limited by saturation in the pole. Several of the families of the pole-limited dipoles use a common core cross section and vary the number and turn-counts of coils. This produces an air pocket in the coil gap for families with fewer coils. Filling these gaps with steel, such that the coils are flush with the pole, reduces the saturation in the poles. Further, the coil stacking order of some families can be inverted to place the higher-turns coils closer to the gap. In some cases, it will be necessary to completely replace S/R dipoles. Typically, the required change is to lengthen the magnet. In some cases it is also necessary to modify the coil package and/or pole shape to achieve acceptable field quality over the full operating range.

The northeast spreader – *i.e.*, the one at the end of the north linac – will have magnets added to accommodate the separation and transport of the sixth-pass beam to Hall D.

Table 12: Summary of magnet changes needed to upgrade existing beam lines.

Action	Using existing designs	Using new designs
Procure and install	16 (including 3 spares)	60 (including 10 spares)
Relocate	81	
Remove/salvage	28	
Re-cable	60	
New power supplies	25	60

Quadrupoles Of the ~650 quadrupoles in the existing beam lines – *i.e.*, injector, recirculation through five passes and delivery to Halls A, B, and C – relatively few need to be modified for the Upgrade. In most cases nothing needs to be done. Eighty-five need larger power supplies. We need to procure 76 new magnets (including 13 spares), 60 of which will be built using one of two new designs which provide more field than existing designs. In addition, 60 of the quads need to be re-cabled with larger cables so that total load impedance is matched to the power supply I/V. Some of the magnets will be moved to match operating ranges with needs. The Hall D beam line will receive new quadrupoles using one of the new designs.

The scale of the total job associated with upgrading the existing beam lines is summarized in Table 12.

Path-length adjustment For optical energy spread and stability, the beam should run on the crest of the rf wave. The machine layout includes nine locations where the path length can be adjusted so that the beam will meet this criterion as it transits each linac on each pass. The adjustment is done with a three-magnet chicane, referred to as "doglegs".

It has been our experience that the path length is stable over the short term (days). Slight adjustments are needed to correct for changes in the beam's central orbit from one setup to the next. We have also observed an overall "breathing" to the path lengths. This "breathing" is seen in all passes of the recirculation; it closely follows a sine curve with a one-year period and a peak-peak amplitude of 5.5 mm (equivalent to 10° of 1497 MHz) for each pass. The source has not been identified.

We have determined that new dogleg magnets and power supplies will not be needed if the "breathing" can be handled separately. The plan for dealing with it is to slightly adjust the master oscillator frequency and thereby cause the path length to become an integer number of rf wavelengths. A new master oscillator has been installed with this feature, and frequency adjustment tests started in October 2000.

3.D.4 Magnet Power Supplies

Overview

The ∼2200 magnets in the CEBAF accelerator are powered by ∼1800 separate power supplies. The vast majority are 10A/30V “trim” supplies which power individual quadrupoles, sextupoles, and steering dipoles (“correctors”). The primary bending dipoles are powered in strings, with one large power supply (“box”supply) for each string. Some of the dipoles need individual adjustment capability; these receive an electronic shunt controller (“shunt regulator”). The 12 GeV Upgrade will require replacement of a number of the supplies, particularly the box supplies. The required changes are outlined below.

Box power supplies

There presently are 35 box supplies in the CEBAF beam transport system, ranging from 13.5 kW to 266 kW output power. All are of the SCR pre-regulator with transistor post-regulator configuration. Regulation is 0.001%. All supplies are from one vendor and use many interchangeable parts to minimize spares count and ease maintenance.

The energy upgrade will require replacing all eleven of the box supplies for the arc dipole strings and adding a supply for arc 10, as summarized in Table 13. To economically meet this wide range of voltages and currents, a planned modular system of power supply “building blocks” will use a common design of rectifier modules and transistor post-regulator modules which can be “stacked” into either series or parallel configurations to meet the required output. A block diagram is shown in Fig. 69.

Each rectifier module will utilize a 12-phase thyristor bridge with L-C filtering and have 0–800 VDC @ 600 A maximum output. The passbank module will have ∼400 power transistors configured to handle the maximum 1200 A. A current transductor, strappable 600/1200 A, will provide a feedback signal from the output. Regulation will be 0.001%. Interface to the PSS, magnet thermal interlocks, and shunts will remain unchanged.

All arc magnet strings will be grounded at their midpoint, via a ground fault detector circuit.

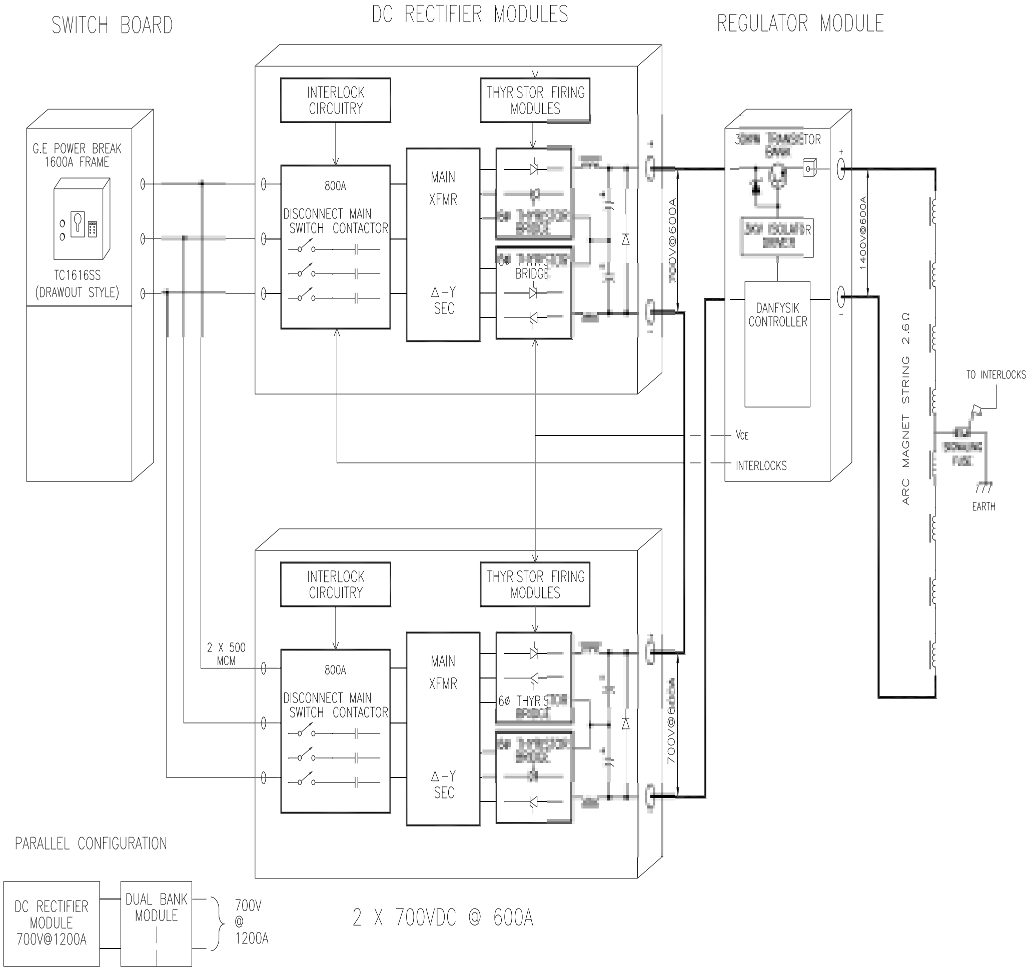

Figure 69: Block diagram of modular power supply.

Table 13: Major box supplies required for 12 GeV

Location	Present $E_{\max}$ (GeV)	Supply Requirements for 12 GeV Current (A)	Voltage (V)	Power (kW)
EAST ARC				
Arc 1	7.1	390	415	162
Arc 3	7.1	549	781	428
Arc 5	7.8	456	955	435
Arc 7	8.1	423	1132	478
Arc 9	6.5	546	1471	803
Recirculation septa	6.5	1081	401	433
WEST ARC				
Arc 2	7.1	386	612	235
Arc 4	7.3	365	941	343
Arc 6	7.1	543	1167	634
Arc 8	7.0	483	1384	668
Arc10	-	575	1495	860
Recirculation septa	6.5	1188	567	674

This will lower the conductor-to-ground potentials throughout the string, placing less stress on magnet and cable insulation and lowering the safety hazard associated with the required voltages. It will be necessary to double up on the 500 MCM cables serving arcs 3, 5, 6, and 9.

Additional electrical power

The maximum ac power requirements for the arc box supplies will increase from 2.28 MVA to an estimated 9.92 MVA. Two additional 5 MVA unit substations will be required, one near the North Access Building, one near the South Access Building. Each of these locations will require two new 2,000 A switchboards. The existing 12.47 kV feeder loops serving these new substations have sufficient capacity. New concrete pads and duct banks will be required for the new substations.

LCW cooling requirements for magnets and power supplies

Low-conductivity water (LCW) cools the magnets and power supplies. The heat load will increase as identified in Table 14.

Table 14: Increased LCW cooling requirements for magnets and power supplies

	South Access Bldg. South Linac Cooling Loop	South Access Bldg. East Arc Cooling Loop	North Access Bldg. North Linac Cooling Loop	North Access Bldg. West Arc Cooling Loop
6.0 GeV Heat Load	147 kW	774 kW	182 kW	959 kW
12.0 GeV Heat Load	588 kW	3095 kW	729 kW	3873 kW

Required civil construction

The footprint of the new arc box supplies will be approximately three times that of the present units. Adding a 20 ft extension on the 60 ft width of the existing North and South Access Buildings will provide sufficient floor space both for the new box supplies and for the required additions to the LCW system, which presently share common space. These building additions have been designed and were bid in early fall 2000.

Other box supplies

The remaining 24 box supplies are distributed around the accelerator, the extraction region, and beam switchyard. With a single exception, they have less than 66 kW outputs. Where present supplies would be inadequate for the new energies, they will be replaced with units surplused from the arcs. In some cases, surplus supplies may be rebuilt to provide different voltage/current output capability while staying within the basic power rating of the unit. Such rebuilding has already been proven successful for supplies for the Hall A, B, and C transport lines.

Trim power supplies

There are approximately 1800 bipolar trim power supplies serving the quadrupoles, solenoids, and small corrector dipoles. Each supply output is realized as a single, plug-in printed circuit board. The nominal output from each channel is presently ±30 V at 10 A.

For the energy upgrade, approximately 75 channels will have to be upgraded to ±65 V at 17 A output capability. The new supply is envisioned as a separate chassis, utilizing hybrid switching technology and post-transistor regulation to achieve the required 0.01% regulation. The chassis would be powered directly from the ac line, rather than from common bulk supplies.

Shunt regulators

In the large dipole magnet strings, individual control over certain magnets is achieved by shunt regulators, which can divert up to 5% (20 A) of the current around a given magnet. Presently, each of the 84 shunt regulators is realized as a plug-in module. The energy upgrade will double the current in these magnet strings, requiring increased power dissipation in the shunts to achieve the same percentage of control. A new regulator module, to be realized as a single chassis per channel, will have a current-shunting capacity of 60 A and a power dissipation of 1.2 kW. The design will closely approximate the existing circuitry; however, the power-dissipation transistors will be water-cooled to increase their dissipation capability.

Control interface and software

The present box supplies and trim racks interface to the EPICS control system via an RS-232 link to CAMAC or VME serial ports. In general, the data communications interface for all power supplies and shunts will be upgraded to purchased VME hardware. Software changes will be minimal, with a few new driver routines being required for the 480 kW box supplies, 17 A trim supplies, and 60 A shunts. The EPICS operator screens should remain unchanged.

3.D.5 Instrumentation and Control

I&C for the Upgrade will require the fewest changes of all the systems from the present configuration. The beam diagnostics, machine protection system, and personnel protection systems associated with delivery of five-pass beam to Halls A, B, and C will require no changes.

Beam delivery to Hall D will require an expansion of all the I&C systems. In all cases copies of the existing system can be used. For example, additional beam position monitors will need to be installed for arc 10, but their signals can be simply added to the existing multiplexers.

The control network will have to be extended to Hall D. The associated electronics and racks will share space in a new surface service building with the magnet power supplies for the Hall D beam line.

3.D.6 Cryogenics

Overview

The cryogenic requirements for the 12 GeV Upgrade are: 7155 W at 2 K and 16,270 W at 50 K. The existing JLab cryogenic system is capable of 4600 W at 2 K and 12,000 W at 50 K for both the north and south linacs. The 12 GeV-capable cryogenics complex will distribute liquid helium as shown in Fig. 70 using two parallel systems:

> One system will utilize the existing JLab cryogenic system, which presently serves both the north and south linacs and the FEL, to provide cryogens to the north linac only. JLab's primary 2 K cold compressors will be modified from four-stage to five-stage compression to provide the reduced-flow turndown capability required for the north linac loads.

> A second cryogenic system will be installed which will provide cryogens for the south linac and the FEL. The new south linac/FEL cryogenic system will consist of subsystem components of the former MFTF-B test facility at Lawrence Livermore National Laboratory. These subsystems include warm helium gas compressors and a 4 K refrigerator. They will be coupled to an existing JLab spare five-stage, 2 K cold compressor, and an expanded control system to provide a complete operating cryogenic plant. A warm helium compressor building and utilities will be provided for the compressors of the former MFTF-B system.

A small satellite 4 K refrigerator will installed at the Hall D location for the hall cryogen load requirements. A summary of the cryogenic plant upgrades is presented in Table 15. A summary of linac heat loads for the Upgrade is presented in Table 16.

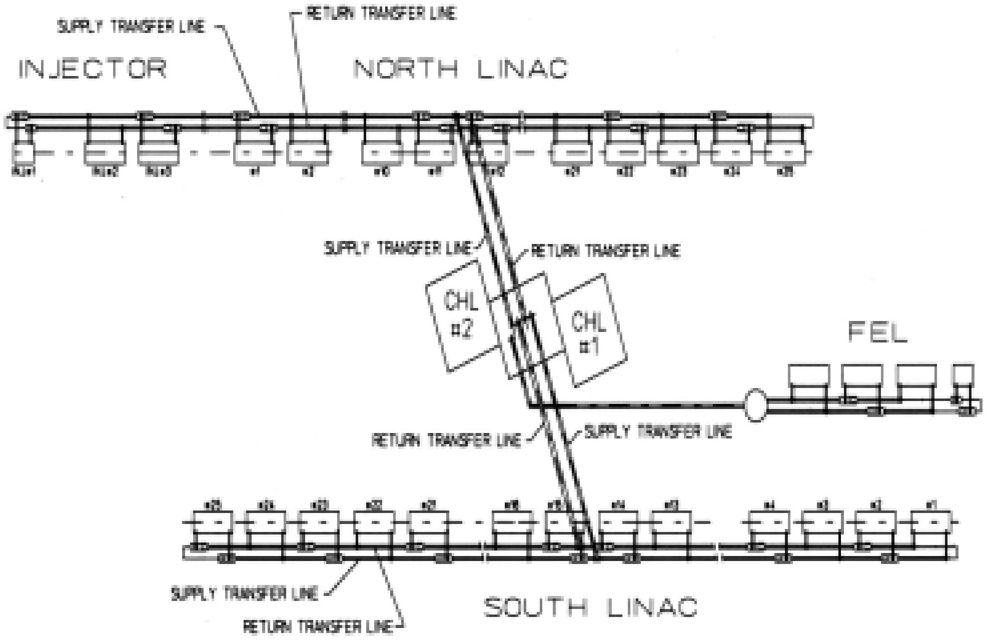

Figure 70: The layout of the 12 GeV cryogenics distribution system.

Table 15: Upgraded CHL refrigeration capacities

	He Temp. (K)	Capacity	Pressure (atm)	Flow (g/s)
CHL #1				
Linac shields	35–52	12,000 W	4.0	136
Linac cavities	2.0	4800 W	0.031	240
Liquefaction	4.5	288 l/hr	2.8	10
SBR				
Linac shield	35–52	12,000 W	4.0	136
Linac cavities	4.5	1900 W	1.3	150
CHL #2				
Linac shields	35–52	12,000 W	4.0	136
Linac cavities	2.0	5280 W	0.031	264
Liquefaction	4.5	280 l/hr	2.8	10
Hall D*				
Magnet shields	85	LN2	3.0	NA
Target	20	10 W	?	?
Magnet	4.5	160 W (@ 2 g/s)	2.8	10
Magnet power leads	4.5	84 l/hr	2.8	3

*Capacity in satellite mode with liquid from CHL

Table 16: Linac heat loads (W)

	Unit Loads		6 GeV Loads			12 GeV NL Loads			12 GeV SL Loads		
	2 K	50 K	#	2 K	50 K	#	2 K	50 K	#	2 K	50 K
Static											
Transfer line	250	2950	2	500	5900	1	250	2950	1	250	2950
CEBAF CM	16	110	42.5	680	4675	27.5	440	3025	25	400	2750
FEL CM	16	110	1.5	24	165	0		0	3.5	56	385
Dynamic rf load											
@ 30 MV	72	49	42.25	3042	2070	0.25	18	12	0	0	
@ 32 MV	72	49	1.25	90	61	17	1224	833	17.25	1242	845
@ 68 MV	175	120				8	1750	1200	8	1925	1320
Total required			43.5	4336	12872	27.25	3682	8020	28.25	3873	8250
Capacity											
CHL#1				4800	12000		4800	12000			
% of required				111%	93%		130%	150%			
CHL#2										5280	12000
% of required										136%	145%

12 GeV cryogenic upgrade summary

A) North linac refrigeration loads
  - a) 3282 W at 2 K, 8020 W at 50 K
  - b) Use existing CHL compressors, 4 K cold box, and modified original 2 K cold box (five stage)

B) South linac refrigeration loads
  - a) 3873 W at 2 K, 8250 W at 50 K
  - b) Use modified MFTF-B compressors, modified MFTF-B 4 K cold box, new 80 K cold box, and the newly commissioned 2 K cold box, and new oil removal system
  - c) Requires additional CHL compressor building, 4160 V electrical and cooling water utility, 4 K cold box pit construction, and expanded control system

C) Hall D satellite refrigerator
  - a) New satellite 4 K refrigerator, transfer and gas lines from CHL, expanded controls

3.D.7 Civil Construction

Additional beam energy requires additional cooling capacity electrical capacity and building space to house and maintain the extra equipment. The following items are required:

Electrical

For the North and South Access Buildings, two new 5 MVA substation will be required including bus duct and bus work. The CHL will require a 12 MVA substation with primary duct bank, plus a 1.5 MVA substation, associated duct banks, switch boards, and motor control centers.

Mechanical

Mechanical systems capacity increases will be required to extract unwanted heat from the arc magnets. This includes low-conductivity water (LCW) upgrades (Table 17) and arc environmental control. The LCW will be improved by increasing the motor size in both the arc magnet circuits and

Table 17: LCW system parameters

Requirement	**North Access**		**South Access**	
	Magnets (W. arc & BSY)	Magnet Power Supplies(W. arc, N. linac rf)	Magnets (E. arc & Hall D)	Magnet Power Supplies (E. arc & BSY, S. linac rf)
Existing flows @ 6.0 GeV	510 gpm	1300 gpm	410 gpm	1650 gpm
Needed flow @ 12.0 GeV	610 gpm	1750 gpm	510 gpm	2375 gpm

the service building circuits. An additional heat exchanger will be required for the arc magnets as well as piping and valve reconfiguration of the existing heat exchangers to accommodate the service building loads. An extra cooling tower is required at each location. Existing service building air conditioning is sufficient.

To avoid a major revamping of existing magnet cooling circuits, it has been deemed advisable to allow the LCW water differential temperature to rise to accommodate the extra heating. Pipe insulation and mechanical cooling must be used to counteract the tunnel air temperature rise. This will allow maintenance personnel access to the tunnel without a protracted cooldown period. Since space is at a premium, a direct expansion unit is planned. With careful positioning of the evaporator, buoyantly driven flow would eliminate the need for fans and fan-induced noise.

Building space

Additions to the North and South Access Buildings are required to accommodate the larger magnet power supplies and larger LCW systems; each addition will be 20'× 60'. An addition to the existing CHL will be required to house compressors for "CHL #2". A pit will also be needed in the northeast corner of the existing cold-box room to house the 80 to 4.5 K "CHL #2" cold box (MFTF refrigerator).

3.D.8 Schedule

While the final schedule for the Upgrade is contingent on special funding from DOE, it is possible to present information about early work aimed at the final goal. Also we can address how to accomplish the Upgrade with minimal impact on the ongoing research program. The 12 GeV Upgrade is part of DOE's 20 Year Plan, and is also central to Jefferson Lab's Institutional Plan. Nevertheless, as a practical matter in the present funding climate, a fully operational prototype of the primary high-tech component is required in order to submit a proposal to DOE. In our case this means the Upgrade Cryomodule. Much of the technology that must be validated will come naturally from the JLab involvement in the SNS project. However, development of a 1497 MHz cryomodule that delivers 68 MV is critical to the credibility of the Upgrade project. We are presently working toward the following schedule:

Cavity string complete: 10/00
CM assembled: 4/02
CM testing complete: 8/02
CM installed SL21: 9/02

Critical path issues

The critical path for the Upgrade starts with the civil engineering building design. A two-year timeline for the two access building additions, including PS installation, is needed in the energy region below 7.5 GeV–an intermediate energy stage in the operational progression of CEBAF from its originally specified 4 GeV towards 12 GeV. CHL#2 is the most time-sensitive, as we estimate that it will require a minimum of four years' lead time. This includes building design, building construction, CHL#2 assembly and installation, commissioning, and burn-in. This work has not been started. We currently have much of the CHL#2 hardware from the SSC and MFTF-B. It could be started early as an AIP project, as the early availability of CHL#2 will support higher end station target loads for our ongoing (4 to 6 GeV) research program, and also support high CHL#1 availability as we push the limits of the present installation (5.5 to 6 GeV operation).

Installation and major shutdown scheduling

The installation of the new cryomodules in the linacs can be accomplished easily during routine maintenance shutdowns, and the commissioning of their rf power and control systems can be accomplished with no impact on beam delivery. Indeed, early installation of a few new cryomodules would improve accelerator performance at the present limit of 6 GeV. Completion of the Upgrade project will require one major shutdown. The shutdown has four main goals:

1. Install the 12 GeV magnet modifications in the five spreader/recombiner regions (including moving the injection beam line and start of the chicane).

2. Install the 11 GeV Hall A, B, and C extraction magnets.
3. Install the tenth arc.
4. Install the new Hall D beamline.

It probably will be possible to complete at least portions of some of these tasks during maintenance periods and during the semi-annual shutdowns associated with routine accelerator operations, with no effect on beam availability; this would relieve the duration of the major shutdown which would otherwise require about six months for hardware installation and six months for recommissioning the accelerator.

4 EXPERIMENTAL EQUIPMENT FOR THE 12 GeV UPGRADE

4.A Overview

In this chapter we outline the upgrades and additions to the equipment in the present experimental halls, and the equipment needed for the new hall (Hall D) that is being added to support the meson spectroscopy initiative. The equipment makes efficient use of much of the base equipment from the original CEBAF complement. Both high-resolution spectrometers are retained in Hall A, all of the CLAS components (with the exception of the drift chambers) are retained in Hall B, and the High-Momentum Spectrometer (HMS) is retained in Hall C. These devices are complemented by the addition of a medium-acceptance spectrometer in Hall A (to be called MAD, Medium-Acceptance Device), an upgrade of the central region and tracking system for CLAS in Hall B, a new high-momentum spectrometer in Hall C (the SHMS, Super-High-Momentum Spectrometer), and the new Hall D equipment. These items, and related ancillary equipment, are described in detail in the sections below.

4.B Hall A

4.B.1 Overview

The present base instrumentation in Hall A has been used with great success for experiments that require high luminosity and high resolution in momentum and/or angle for at least one of the reaction products. The central elements are the two High-Resolution Spectrometers (HRS). Both of these devices provide a momentum resolution of better than 2×10^{-4} and an angular resolution of better than 1 mrad. The design maximum central momentum, 4 GeV/c, is available in one of the HRS, but in the other the central momentum is administratively limited to 3.2 GeV/c to avoid possible damage from a short in the copper component of one of the superconducting coils.

The Jefferson Lab 12 GeV (11 GeV for Halls A, B, and C) Upgrade opens several new physics windows. In particular, a large kinematic domain becomes available for studies of deep inelastic scattering. The combination of high luminosity and high polarization of beam and targets will place Jefferson Lab in a unique position to make significant contributions to the understanding of nucleon and nuclear structure and of the strong interaction in the high-x region.

Theoretically, the high-x region provides a relatively clean testing ground for our understanding of nucleon structure in terms of valence quarks, which will dominate this region. Precision data are scarce in this region (especially for the spin-dependent nucleon structure), due to the fact that the quark distribution functions drop rapidly when x becomes large. Such data at relatively low Q^2 are not only important for understanding this structure, but would also have a significant impact on a search for new physics beyond the standard model at very high energies. To fully utilize the high luminosity available at CEBAF, a well-matched spectrometer with large momentum and angular acceptance and moderate momentum resolution is crucial for obtaining precision information in the high-x region.

Table 18 lists the physics requirements of a number of experiments that need a large-acceptance spectrometer, mainly in the high-x region. A brief explanation of these experiments is given in the following paragraphs. Several are discussed in more detail in Chapters 1 and 2. The first experiment uses unpolarized inclusive electron scattering on ^{3}H and ^{3}He [Pe00]. Precision measurements of the d-quark-to-u-quark ratio at high x, through the study of the ratio of the ^{3}H and ^{3}He structure functions, will resolve a long-standing issue of different predictions from pQCD and constituent quark models. This experiment also requires the implementation of a ^{3}H target. The second will provide a precise measurement of the spin structure functions g_1 and A_1 of the neutron by using a polarized ^{3}He target [Me00]. It will unambiguously establish the trend of A_1^n for $x \to 1$, which will

Table 18: Instrumentation requirements for experiments needing a large-acceptance detector.

Nr.	Exp.	P_{max} (GeV/c)	Angle acc. (msr)	Mom. acc. (%)	Mom. res. (%)	Hor. ang. res. (mrad)	Vert. ang. res. (mrad)	Min. angle (degrees)
1	^{3}H/^{3}He	6	15-30	30	0.3	1	3	15-30
2	A_1^n, g_1^n	5-7	15-30	30	0.3	2	3	15-30
3	g_2^n	5	20-30	30	0.3	2	3	15-25
4	A_1^p, g_1^p	5-7	15-30	30	0.3	2	3	15-30
5	DIS-PV	6	30	30	0.3	1	3	15-25
6	Semi-π	6-7	10-30	30	0.3	2	3	12-15
7	Semi-K	6-7	10-30	30	0.3	2	3	12-15
8	Charm	6.5	30	30	0.3	1	2	12-15
9	b_1	6	15-30	30	0.3	1	3	20-30
10	Recoil p	5-7	10-30	30	0.3	1	3	15-25

provide a benchmark test of pQCD and constituent quark models. Precision measurements of g_1 will also provide vital information on nucleon spin structure.

The third experiment [Av00] will measure the g_2^n spin structure function and its moments. This measurement will be a clean measure of a higher twist effect (twist 3), which is related to the quark-gluon interaction. The fourth is the equivalent of the second for the proton [Mi00]. Parity violation in deep inelastic scattering (the fifth experiment) can be used to selectively study nucleon structure, quark-quark correlations, or the standard model [So00].

With high luminosity and well-matched spectrometers, a new window opens in the study of nucleon structure and the strong interaction: semi-inclusive reactions can be used to probe the structure of the parton distributions. Experiments six and seven are examples of a potentially very rich program using semi-inclusive reactions to test factorization and to study the flavor decomposition of the nucleon spin structure, the asymmetry of the sea quark distribution, and the Generalized Parton Distributions [Gi00].

With an 11 GeV beam, the threshold of charm production is crossed. Threshold charm production (experiment 8, [Chpc]) allows one to study the role of the gluons in nucleon structure and some other novel phenomena, such as hidden color. A measurement of the charm-nuclear cross sections will also provide important information for RHIC physics.

The measurement of b_1 (experiment 9, [Mi00]) studies the spin 1 system with a tensor-polarized

Table 19: Summary of major design specifications for the large-acceptance spectrometer

Angular acceptance	30 msr (at a scattering angle of 30°) to 15 msr (at 15°)
Momentum acceptance	30%
Maximum central momentum	5–7 GeV/c
Minimum scattering angle	12–25° (reduced solid angle at small angles)
Moderate resolutions	0.3% in momentum, 1 (3) mrad in hor. (vert.) angle.

deuteron target. This provides a unique channel for a study of the difference between the deuteron system and a trivial bound state of two spin 1/2 objects coupled to spin 1. Many other experiments, such as real and deeply virtual Compton scattering (experiment 11, [Wopc]), will also benefit from a large-acceptance, moderate-resolution spectrometer. Compton scattering experiments also require a high-performance electromagnetic calorimeter.

Three major instrumentation upgrades are proposed to allow an optimal study of the experiments listed in the previous section: a large-acceptance spectrometer, a high-resolution electromagnetic calorimeter, and a ^{3}H target. The spectrometer would provide a tool for high-x studies of the properties of nucleons with an 11 GeV beam, where a large acceptance in both solid angle and momentum coupled to a moderate momentum resolution is needed.

The availability of a high-intensity 11 GeV beam will offer unique possibilities for studying both real and virtual Compton scattering. These experiments require the construction of a large, highly segmented, electromagnetic calorimeter. Other experiments besides Compton scattering will no doubt also benefit from such a detector. The proposed measurement of the d-quark-to-u-quark ratio requires a tritium target.

4.B.2 A New, Medium-Acceptance Device (MAD)

General characteristics

The proposed MAD (Medium-Acceptance Device) detector is a magnetic spectrometer built from two combined-function, quadrupole and dipole, superconducting magnets with a maximum central momentum of 6 GeV/c and a total bend angle of 20°. Extra versatility can be achieved by varying the drift distance to the first magnet. Larger drift distances allow smaller scattering angles at the cost of reduced acceptance.

Table 20: Performance parameters of the MAD spectrometer

Minimum angle 35°		Minimum angle 25°	
Acceptance	Resolution	Acceptance	Resolution
$\theta_0 \pm 207$ mrad	$\sigma_\theta = 3.5$ mrad	$\theta_0 \pm 165$ mrad	$\sigma_\theta = 3.0$ mrad
$\phi_0 \pm 38$ mrad	$\sigma_\phi = 0.8$ mrad	$\phi_0 \pm 35$ mrad	$\sigma_\phi = 1.0$ mrad
$y_0 > \pm 5$ cm	$\sigma_y = 2.5$ mm	$y_0 > \pm 5$ cm	$\sigma_y = 4.0$ mm
$\delta \pm 15\%$	$\sigma_\delta = 0.26\%$ @ $\delta = 15\%$	$\delta \pm 15\%$	$\sigma_\delta = 0.26\%$ @ $\delta = 15\%$

Depending on the details of the detector package, scattering angles as small as 12° might be possible. The quadrupole components provide the focusing necessary to achieve the desired solid angle while the dipole components provide the dispersion needed for momentum resolution. Optical properties and their impact on the performance have been studied. A description of those studies and their results follows. Table 20 shows the estimated performance parameters based on TRANSPORT [Br80a] calculations of the optical properties.

Optical design

A working model of the MAD spectrometer has been developed using the raytracing code SNAKE [Ve87]. The magnetic fields in the magnets are determined using TOSCA [TOSCA]-generated maps. The first was generated by running TOSCA on the magnet with only the quadrupole coil energized and the second with only the dipole element energized. These two maps are then added together with scale factors to simulate tuning the relative excitation of the quadrupole and dipole components of each of the magnets, until the first-order properties expected from the TRANSPORT studies are reproduced. Then, a large number (2000) of random trajectories spanning the full acceptance of the spectrometer are traced through the spectrometer. These trajectories are then used as input to a fitting program that determines the best-fit polynomials which reproduce the target parameters $(\delta, \theta_0, y_0, \phi_0)$ of the input trajectories based on their positions and angles $(x_f, y_f, \theta_f, \phi_f)$ in the detectors. The sensitivity to measurement errors in the detectors can then be explored in a Monte Carlo fashion using a new set of trajectories generated in the same manner as those used in the fitting. In general there is a reasonable match between the Monte Carlo analysis and the TRANSPORT-based predictions.

A set of simulations has been performed to evaluate the performance of the MAD spectrometer using the existing polarized ^{3}He target in the 25° configuration. The spectrometer was equipped with an H_2 bag in the body of the spectrometer followed by two wire chambers separated by just

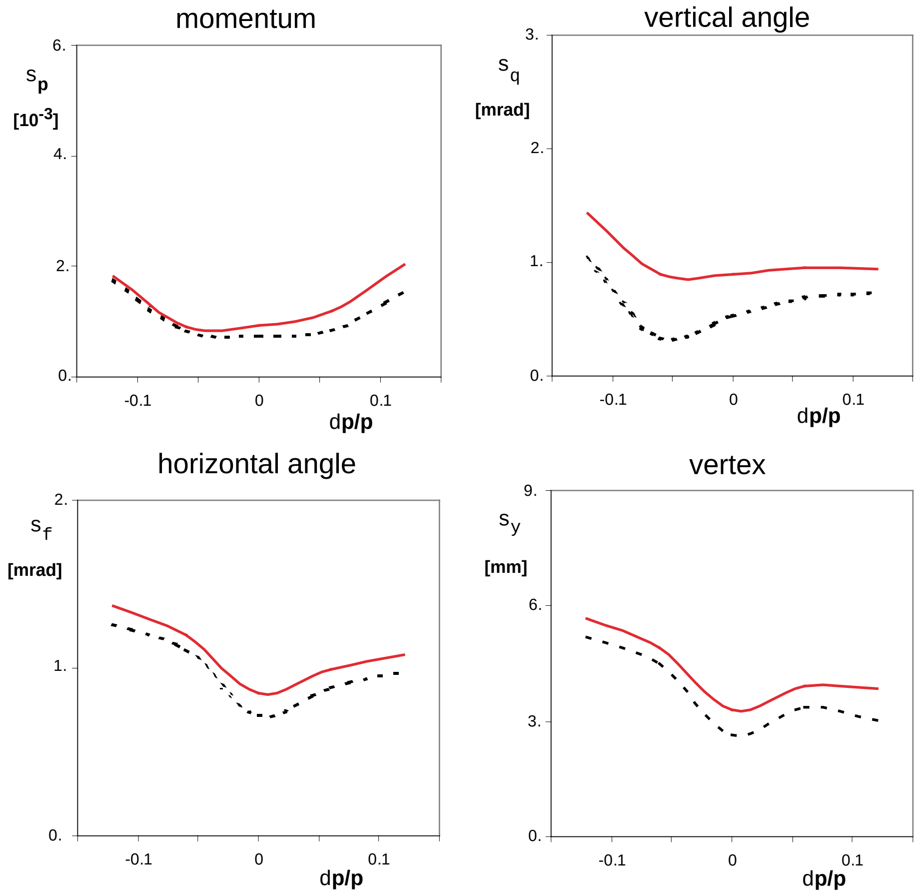

Figure 71: Resolution in δ, θ_0, y_0, and ϕ_0 as a function of the particle momentum. Dashed line: optical resolution, assuming a 200-μm-diameter beam spot. Solid line: result of the full Monte Carlo simulation, including multiple scattering.

over 1 m. Trajectories spanning the full momentum acceptance were evaluated in five momentum bins centered at δ = -12, -6, 0, 6, and 12%. The effect of multiple scattering in the target on the initial trajectories and of multiple scattering in the H_2 bag, the exit window, the first wire chamber, and the air between the wire chambers on the determination of the final trajectories $(x_f, y_f, \theta_f, \phi_f)$ was evaluated. Then the effect of those uncertainties on the original trajectory parameters (δ, θ_0, y_0, and ϕ_0) was evaluated, assuming a 200 μm beam spot, in a Monte Carlo fashion using $\sim$ 400 random trajectories spanning the full acceptance of the spectrometer in each momentum bin. The effects from the target and the rest of the spectrometer on δ, θ_0, y_0, and ϕ_0 were then added in quadrature. Multiple scattering was evaluated separately for the central momentum of each bin.

Figure 71 shows the resolution of δ, θ_0, y_0, and ϕ_0 generated in the Monte Carlo analysis for two cases: (1) No measurement error. This demonstrates how well the optics are understood and incorporates the effect of a 200 μm beam spot. (2) Full MC results taking into account multiple scattering in the target, various windows, and detector components.

The large fields and field gradients in the magnets in the 6 GeV/c version of the MAD preclude the possibility of achieving a higher central momentum by simply increasing the fields in the magnets. Therefore, to reach a higher central momentum the magnets must be lengthened. For example, increasing the maximum central momentum to 8 GeV/c results in a loss of angular acceptance of $\approx 25\%$ unless the apertures are increased proportionately. However, the large fields and field gradients needed in the magnets also preclude an increase in the apertures. A decrease in the bend angles of both magnets will also accommodate an increase in the maximum central momentum at an expected moderate loss of resolution. However, this would increase the acceptance region with a direct line-of-sight between target and detector, the effect of which requires further study.

Magnet design

This spectrometer requires a pair of identical combined-function superconducting magnets that can simultaneously produce a 1.5 T dipole field and a 4.5 T/m quadrupole field inside a warm bore of 120 cm (QD120SC). A magnetic design using TOSCA3D has been performed to establish the basic magnetic requirements, provide 3D field maps for optics analysis, and produce basic engineering information about the magnets. A two-sector $\cos(\phi)/\cos(2\phi)$ design with a low nominal current density (5750/4111 A/cm^2) with a warm bore and warm iron has been selected and analyzed. These low current densities are consistent with the limits for a cryo-stable winding. Coils of this type are generally the most conservative that can be built, and the large size and modest field quality requirements (3×10^{-3}) ensure that construction tolerances (1–2 mm) are easily achievable. Other relevant parameters of the QD120SC magnet are given in Table 21.

The magnetic design uses TOSCA-generated $\cos(\phi)$ type coils with "constant perimeter ends". These coils closely approximate the ideal cosine geometry that is well established as a "perfect" generator of high-purity fields. Practical considerations (finite current distributions, limited number of sectors, and TOSCAs internal approximations) contribute to deviations from the ideal geometry and are the sources of higher-order field errors in the design. The yoke is modeled as truly nonlinear iron with the nominal properties of 1010 steel. The present yoke design is a simple 3.0-m-long annulus with a 3.2 m OD and a 2.0 m ID. The yoke variations that have been studied are a full-coverage 4.0 m cylinder, beveled ends, a truncated 3.0 m cylinder, and a beam tube slot. Due

Table 21: Magnet properties

Type	Combined-Function QD
Aperture	120 cm warm bore
NI:	
dipole	2.3×10^6 A turns
quad	4.9×10^6 A turns
Central field	1.5 T
Dipole $\int Bdl$	3.6 Tm
Quadrupole $\int Gdl$	13.0 (T/m)m (gradient $G = 4.2$ T/m)
Effective length:	
Dipole	2.4 m
Quad	3.1 m
Overall length	4 m (3.2 m central length with 0.4 m step ends)
Yoke	130 metric tons warm iron (1010 steel) (3.2 m OD × 2.0 m ID × 3.0 m long)
Coil and cryostat:	25 metric tons stainless steel (2.0 m OD × 1.2 m ID × 4.0 m long)
Peak linear force density:	
dipole coil	36,000 lbs/in (peak pressure 1100 psi)
quad coil	39,000 lbs/in (peak pressure 1300 psi)
Total peak pressure:	2400 psi
Stored energy:	15 MJ

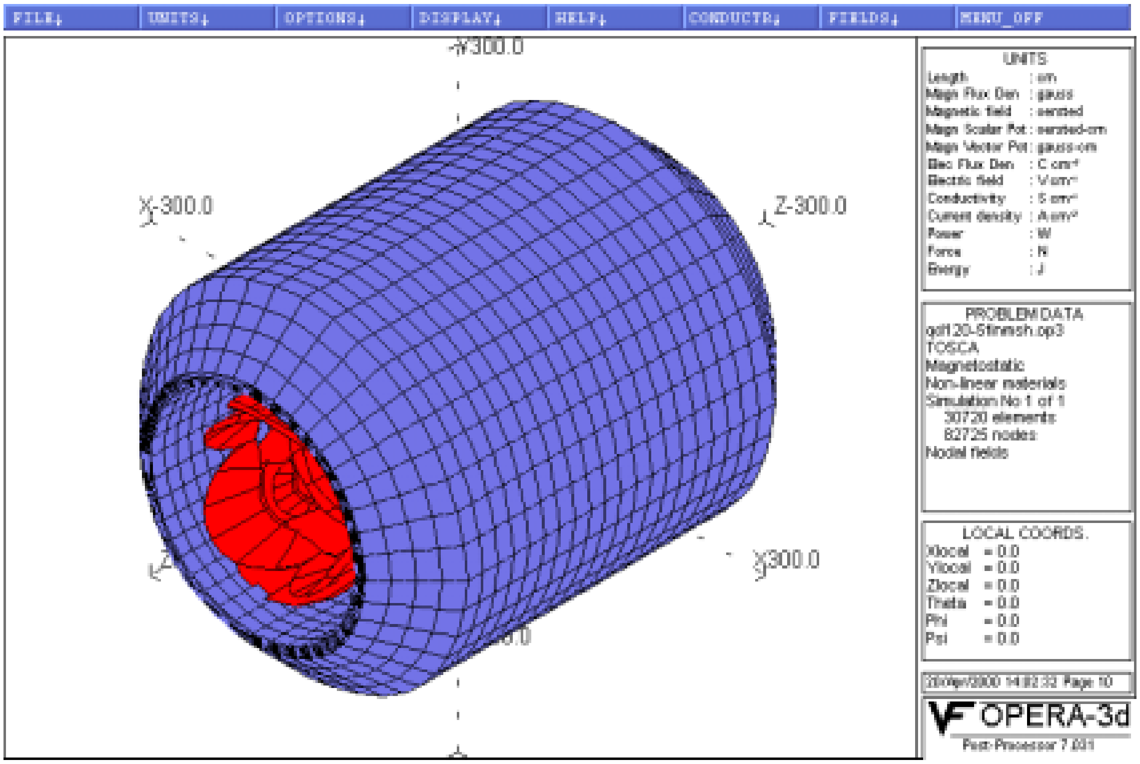

UNITS
Length : cm
Magn Flux Den : gauss
Magnetic field : oersted
Magn Scalar Pot : oersted-cm
Magn Vector Pot : gauss-cm
Elec Flux Den : C cm^{-2}
Electric field : V cm^{-1}
Conductivity : S cm^{-1}
Current density : A cm^{-2}
Power : W
Force : N
Energy : J

PROBLEM DATA
qd120-5finmsh.op3
TOSCA
Magnetostatic
Non-linear materials
Simulation No 1 of 1
30720 elements
82725 nodes
Nodal fields

LOCAL COORDS.
Xlocal = 0.0
Ylocal = 0.0
Zlocal = 0.0
Theta = 0.0
Phi = 0.0
Psi = 0.0

20/Apr/2000 14:02:32 Page 10

Figure 72: TOSCA 3D grid of the iron yoke with the coil package inside.

to the nature of current-dominated coils and largely unsaturated iron, these variations have little effect on the internal fields, allowing a maximum freedom of choice in the final design. The present results of the optics analysis based on this magnetic design indicate that the field quality achieved is already at a level that meets the requirements, so no further “trimming” is anticipated. Relevant results of the TOSCA calculations are shown in Figs. 72 and 73.

The QD120SC combined-function magnet produces peak fields in the warm bore of 4 T and peak fields in the windings of 5 T. These fields are comparable to those achieved in large-bore magnets produced 20 years ago for MHD (Magneto-Hydro-Dynamics) research, particle spectroscopy, and coal sulphur separation (see Table 22). There are significant differences as well between the present magnet and these “prototypes”. For example, the stored energy of the QD120SC is typically less even though the field volumes are comparable. This is due to the fact that the superposed quadrupole field produces significantly less stored energy for a given maximum field. The combined fields also produce a very asymmetric field and force distribution. The fields add on the bottom of the magnet and subtract on the top, resulting in fields across the bore ranging from -1 to 4 T.

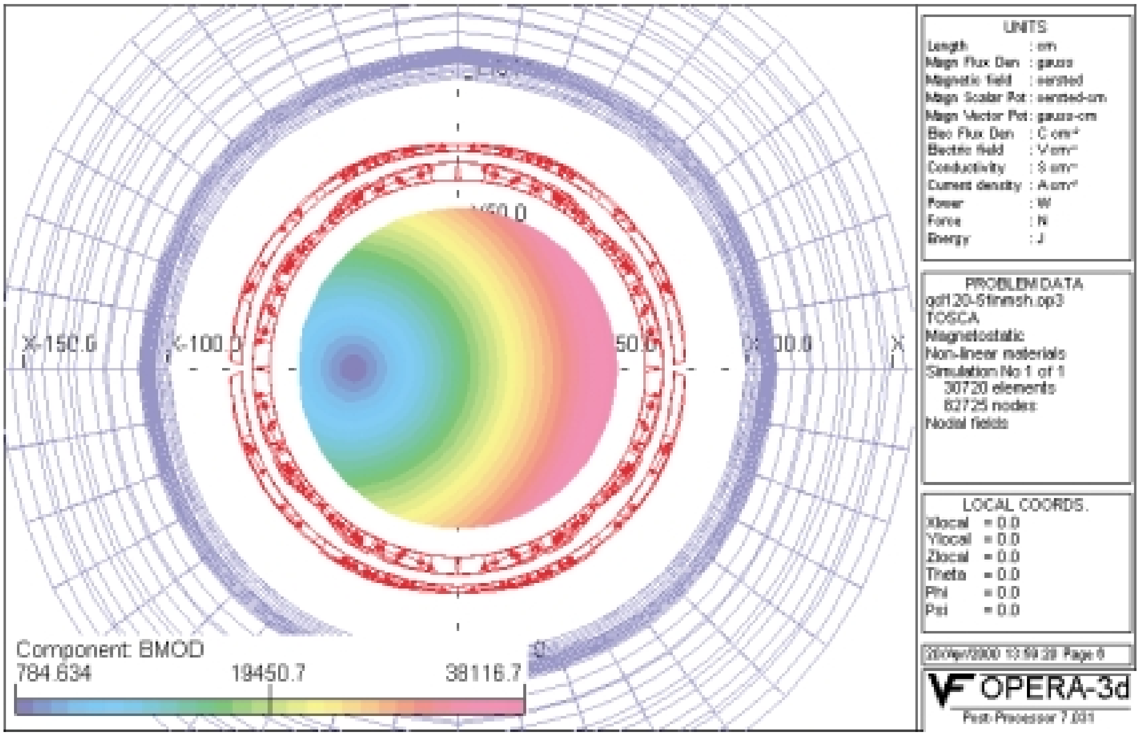

UNITS

Length : cm
Magn Flux Den : gauss
Magnetic field : oersted
Magn Scalar Pot : oersted-cm
Magn Vector Pot : gauss-cm
Elec Flux Den : $C\ cm^{-2}$
Electric field : $V\ cm^{-1}$
Conductivity : $S\ cm^{-1}$
Current density : $A\ cm^{-2}$
Power : W
Force : N
Energy : J

PROBLEM DATA

gdf120-6finmsh.op3
TOSCA
Magnetostatic
Non-linear materials
Simulation No 1 of 1
30720 elements
82725 nodes
Nodal fields

LOCAL COORDS.

Xlocal = 0.0
Ylocal = 0.0
Zlocal = 0.0
Theta = 0.0
Phi = 0.0
Psi = 0.0

20/Apr/2000 13:59:28 Page 6

Figure 73: TOSCA-generated modulus of the magnetic field in the aperture, showing a quadrupole field configuration offset to the left of the magnet center.

Table 22: Large-aperture superconducting magnets

Magnet	Reference
U25 SC Dipole Magnet for MHD	[Ne77]
UTSI SC Dipole Magnet for MHD	[Wa82]
CFFF SC Dipole Magnet for MHD	[Wa80]
Omega Spectrometer SC Dipole	[Mo70]
Large SC Dipole Spectrometer Magnet	[Mo79a]
Large SC Dipole for Spectrometer	[Wo81]
Super Benkei SC dipole magnet for spectrometer	[In84]

Hence, there is a net force between the yoke and coil. The peak linear forces add on one side and subtract on the other, yielding peak pressures that range from 2400 psi to 300 psi. Due to the large radial thickness (12 cm) of the windings and cryostat (40 cm), the required 11-cm-thick pressure shell is easily accommodated without stressing the coil cold mass. The large size of the cryostat will allow separate fluid pressure vessels in accordance with the ASME code. A fully clamped winding is planned for the final construction. This combined with the very conservative cryo-stability will result in a highly reliable design.

The cryogenics for the combined-function magnets will be based on the very successful thermal-siphon cooling that has been incorporated in nearly all the superconducting magnets at JLab. The very high (100 g/s) internal flow rates and simple reservoir level control ensure very reliable operation with simple controls. The heart of this system is a somewhat complex control reservoir that contains JT valves, bayonet connections, phase-separating reservoirs, current leads, relief valves, and instrumentation including level sensors. There are four of these control reservoirs at JLab and three more being delivered. The standardization of design and function of components will ensure compatibility and reliability. The control reservoir will be mounted on the downstream ends of the magnets and will be located on the side to keep the overall spectrometer profile low enough to fit through the truck access door of Hall A. The cryogenic valving allows for top and bottom fill of helium and nitrogen for level operation and cooldown. There will also be a separate valve for variable-temperature cooldown gas made locally in an LN2 to He gas heat exchanger (also standard design). This will be used to cool down and warm up the magnets to minimize thermal stress due to relative contraction and to increase the overall efficiency of cryogenic operations.

Helium at 3.0 atm and 4.5 K is supplied from the End Station Refrigerator (ESR) and JT expanded in the magnet to fill the reservoir. The on-board phase separator allows efficient return of cold gas to the ESR while filling the reservoir without disturbing the level indication. Cold return and warm return shutoff valves are included to allow a smooth transition from cooldown to regular closed-cycle operation. Similarly, LN2 is supplied at 80 K and 2 to 4 atm. Gaseous N2 is vented at the magnet to a sealed exhaust line. Separate flow control and measurement for each current lead is a normal part of this design. Finally, the reservoirs contain dual relief devices, an ASME coded mechanical relief, and a rupture disc set at a 25% higher pressure. Exhaust lines for pressure relief, separate from cooldown lines, are used so that there is no chance of a contamination blockage in these important pressure relief paths. The reservoirs contain temperature sensors, liquid level sensors and voltage taps. Generally, all internal instrumentation is routed to the reservoir through a set of vacuum feedthroughs. Strain gauges in the cold-to-warm support system will be essential due to the force between yoke and coil especially considering the asymmetry of these forces. Vacuum gauging and system pressure sensors will also be located in the control reservoir. JLab owns the design for the installed and to-be-delivered control reservoirs, all of which were built commercially; thus a repeat order could be easily accomplished.

Tuning of the MAD spectrometer requires both relative polarities, so the magnets must be identical and the quadrupole/dipole components must be independently operable. DC power for the magnets is presently designed around low-voltage, high-current commercial power supplies. A DC current of 5 kA at 10 V would be a safe choice due to the relatively low inductance (1.2 H) and provide easily for a charge time under 30 minutes. JLab has three power supplies obtained from SSC surplus that could easily be used. Fast discharge voltages under 500 V are easily obtained with a high-current design, thus reducing the risk of exposure to high voltages. The very large cold mass and low current density ensure that sufficient material is available in the cold mass to absorb most of the stored energy at a low temperature during a quench discharge.

A conceptual design for the MAD support structure has been completed, the result of which is shown in Fig. 74. The support structure was required to allow positioning the MAD spectrometer through a range of angles including the lower-acceptance 15° to 30° range and the 35 msr acceptance 30° through 90° range. This is accomplished by the use of a sliding suspension that permits the magnets and detector to be moved closer to or further away from the pivot.

The construction of the support structure must allow assembly inside Hall A. The structure is comprised of about 20 pieces each under the 20 ton crane capacity. The magnets and detector are carried on transport carts to permit angle changes. They can also be withdrawn up the truck ramp one at a time so that the major MAD components can be "parked" at large angles out of the way of the normal HRS operating range. This is accomplished by steerable Hillman rollers on each transporter and a track in the truck entrance. The magnets are "driven" onto the support

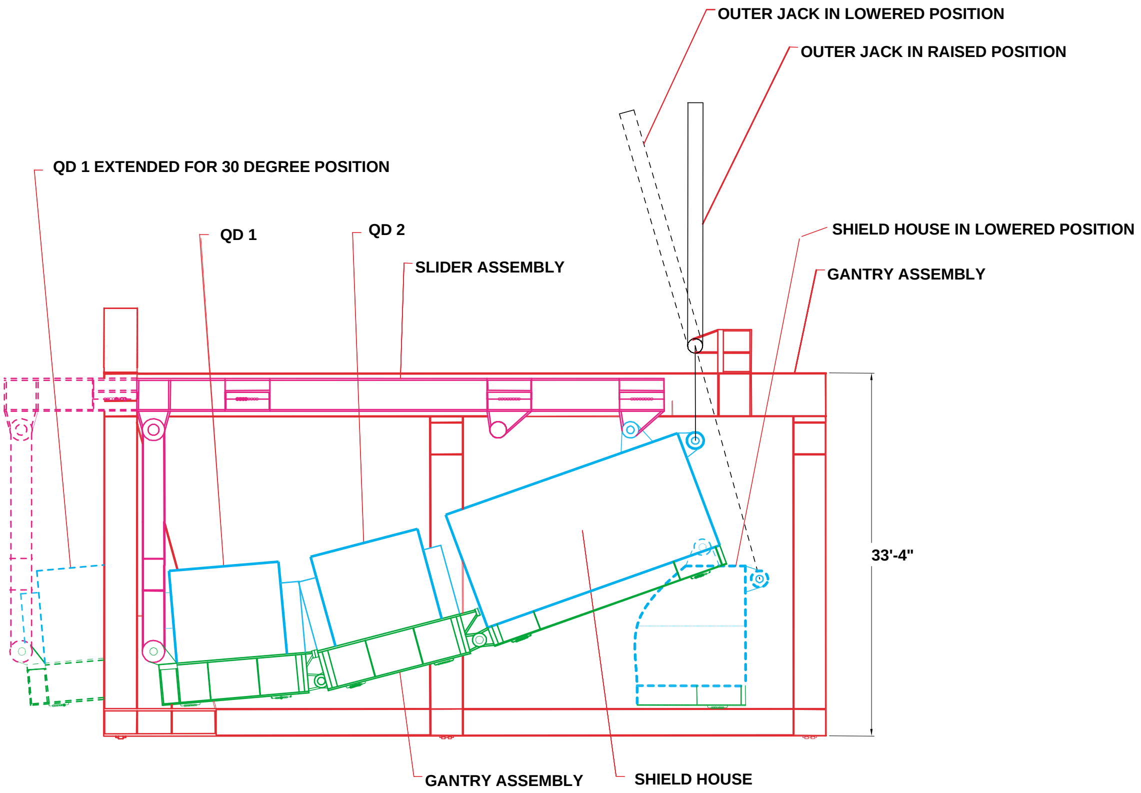

Figure 74: Side view of the support structure for MAD.

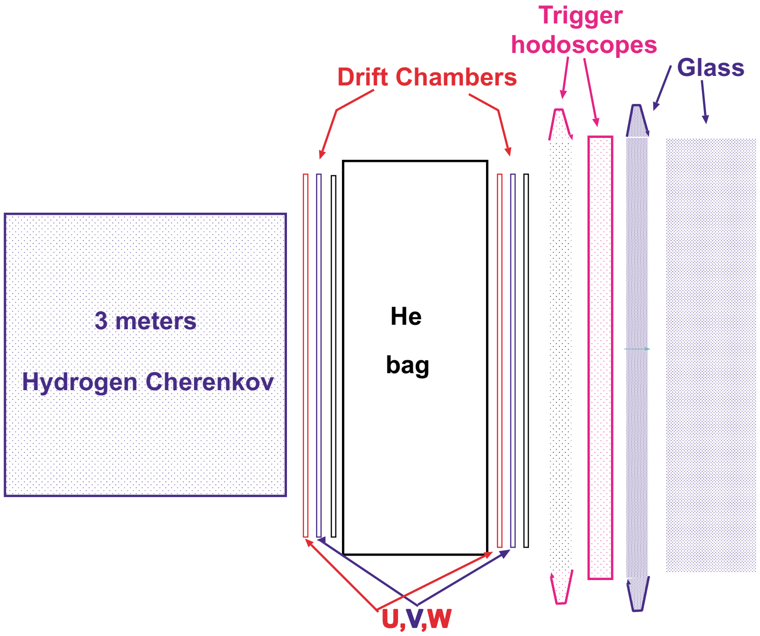

Figure 75: Schematic layout of the basic detector system planned for the proposed MAD spectrometer.

structure and linked together to put them into use. The linked components can then be lifted to their proper attitude with a hydraulic system, which uses components similar to those in the Hall C SOS system. Remote operation of angle changes is not anticipated at this time. The conceptual design as presented meets all operating requirements and assembly and disassembly conditions.

The detector system

The proposed basic detector package for the MAD spectrometer will serve for most electron scattering experiments. The detectors have been designed to cover the full momentum and angular acceptance. The design includes an optional hadron configuration with a flexible particle identification system in the trigger and a very powerful PID in the off-line analysis.

The main components of the detector package are as follows (with rms values of perfomance parameters for 6 GeV electrons listed):

- High-resolution drift chamber – 75 μm per plane and 0.30 mrad angular.
- Hydrogen gas Čerenkov counter – 2 m long, ten photoelectrons, $P^{\pi}_{\rm threshold} \sim 8$ GeV/c.

- Trigger scintillator counters – 70 ps, two layers, each 5 cm thick, of BC408 scintillating material.
- Lead glass hadron rejector – a hadron suppression factor of a few ×100.

The main components of the hadron configuration are:

- Variable-pressure gas Čerenkov counter – 100 cm long, $\gamma_{\text{threshold}}$ range of 8 to 32.
- Diffuse reflective aerogel counter A1, $n = 1.008$ (1.015) – 50 cm long.
- Diffuse reflective aerogel counter A2, $n = 1.030$ (1.060) – 50 cm long.
- Ring imaging Čerenkov counter – 140 cm long.

Triggering and tracking For triggering, two plastic scintillator hodoscopes will be located behind the drift chambers. Each hodoscope will have 16 paddles ($2 \times 5 \times 60$ cm^3) viewed by two XP2282 PMT's. A classical pair of drift chambers 1 m apart with 1 cm drift distance will be used for particle tracking. Each drift chamber contains three groups (4U,4V,4W) with wires oriented differently, each with four wire planes. The four planes in each direction provide high efficiency and resolution. The extra group W enhances high-rate operation. The total number of wires in each chamber is about 1700.

The lead glass shower counter A lead glass preshower/shower combination will provide identification of electrons. The preshower layer consists of 40 modules, each $13 \times 13 \times 35$ cm^3, arranged in four layers. The shower layer consists of 100 similar modules.

The hydrogen gas Čerenkov counter The refractive index (n-1) of hydrogen gas is 1.4×10^{-4} at atmospheric pressure, which corresponds to a threshold gamma factor of 58. The number of Čerenkov photons detected by a PMT from a 3 m pass through hydrogen will be about ten. This value is based on our experimental results with the Hall A gas Čerenkov counters. The advantages of the hydrogen radiator are very low multiple scattering, reduced delta ray production, and low scintillation light yield. In the present design the front window is inside the magnetic field so that delta rays produced in the window are deflected away from the PMT's. With this feature a high rejection factor for hadrons (few $\times 10^4$) can be achieved.

A variable-pressure gas Čerenkov counter The refractive index (n-1) of isobutane is 1.9×10^{-3} at atmospheric pressure which corresponds to a threshold gamma factor of 16. The number of Čerenkov photons detected by a PMT from a 1 m pass through this gas will be about 40. With a pressure range between 0.25 and 2 atm the counter will provide pion discrimination in a momentum range of 1.6–4.5 GeV/c.

The aerogel trigger Čerenkov counter The radiator has ten layers of 100 aerogel modules, each $11 \times 11 \times 1$ cm^3. Twenty 5" XP4582B PMT's are used for light collection.

The ring imaging Čerenkov counter PID over a wide momentum range coupled to a high-selection PID factor $\sim 10^5$ (*e.g.*, for semi-exclusive kaon production) can be provided by a Ring Imaging Čerenkov counter. In the last few years several successful RICH systems were developed at CERN/SLAC/DESY. A CsI photocathode-based detector is under construction for a Hall A HRS by the INFN/SANITA group. An aerogel and a gas radiator, read out by multi-anode phototubes, are being considered for the present proposal.

4.B.3 High-performance electromagnetic calorimetry

A highly segmented total absorption calorimeter is proposed for use in conjunction with the magnetic spectrometers in high-luminosity Compton experiments (real and virtual) at 11 GeV. The calorimeter must combine high spatial resolution, good energy resolution, fast time response, and substantial radiation hardness.

A calorimeter of 1000 PbF_2 crystals, each $2.5 \times 2.5 \times 15$ cm^3 is proposed. Each crystal will be coupled to a mesh PMT, *e.g.* Hamamatsu R5900 for optimum time resolution. The PMT signals will be digitized by a 1 GHz fast-sampling ADC system, for off-line suppression of pile-up.

PbF_2 is an attractive Čerenkov medium for electromagnetic calorimetry. Some basic properties of PbF_2 are listed in Table 23 and compared with the Pb-Glass already in use for the calorimeter for the Real Compton Scattering Experiment E99-114. The table also illustrates $PbWO_4$, which is a scintillator, and can achieve high energy resolution. However, as a scintillator, $PbWO_4$ is much more sensitive to neutrons and other hadronic background. Additional tests are required to evaluate the selection of calorimeter material.

The calorimetry requirements are most stringent for Deeply Virtual Compton Scattering

Table 23: Comparison of Pb-glass, PbF_2, and $PbWO_4$ properties.

	Pb-Glass TF-1	PbF_2	$PbWO_4$	
Radiation length X_0 (cm)	2.5	0.93	0.89	
Moliere radius r_0 (cm)	3.3	2.2	2.2	
Density ρ (g/cm^3)	3.86	7.77	8.28	
Mass/element (g)	2980	990	1010	$\rho \times (1.33 r_0)^2 \times 16 X_0$
Photoelectrons/GeV	1100	1600	5000	
Critical Energy (MeV)	15	8.6		

(DVCS) in which an energetic photon must be detected in the direction of the $\vec{q}$-vector (angles as small as 10°) and with a luminosity of at least $10^{37}/\text{cm}^2/\text{s}$. It is important to resolve the exclusive DVCS process from competing inelastic processes such as $ep \to e'p'\pi^0 \to e'p'\gamma\gamma$ or $ep \to e'N^*\gamma \to e'N\pi\gamma$. For different calorimetry materials, Fig. 76 illustrates the kinematic limit for separation of the exclusive channel by $p(e, e'\gamma)X$ double coincidences alone. Beyond the limits illustrated in the figure, the exclusive $ep \to ep\gamma$ channel can be resolved by detecting the recoil proton in triple coincidence. In the DVCS limit, the angular resolution required on the detection of the proton is approximately a factor of 10 less stringent than the requirements for the photon. A high-performance calorimeter can greatly enhance the capabilities for real and virtual Compton scattering experiments at 11 GeV.

4.B.4 A ^{3}H Target

Several experiments have been discussed which require a tritium target. Tritium targets have been used in the past 15 years at Bates [Be89], Saclay [Am94], and most recently at Saskatoon. Those designs have been reviewed, and options have been discussed with knowledgeable people from each of the labs. The target is technically straightforward, but some modifications of the hall will be required for safety purposes.

The three types of targets which have been used are sealed-liquid (Saclay) and high-pressure cold gas (225 psi at 45 K) with a uranium getter storage bed (Bates), and medium-pressure warm gas with a uranium storage bed (Saskatoon). The luminosity requirements of the JLab target will require either a liquid or high-pressure cold gas target.

The major considerations in the target design are to minimize the amount of tritium, minimize

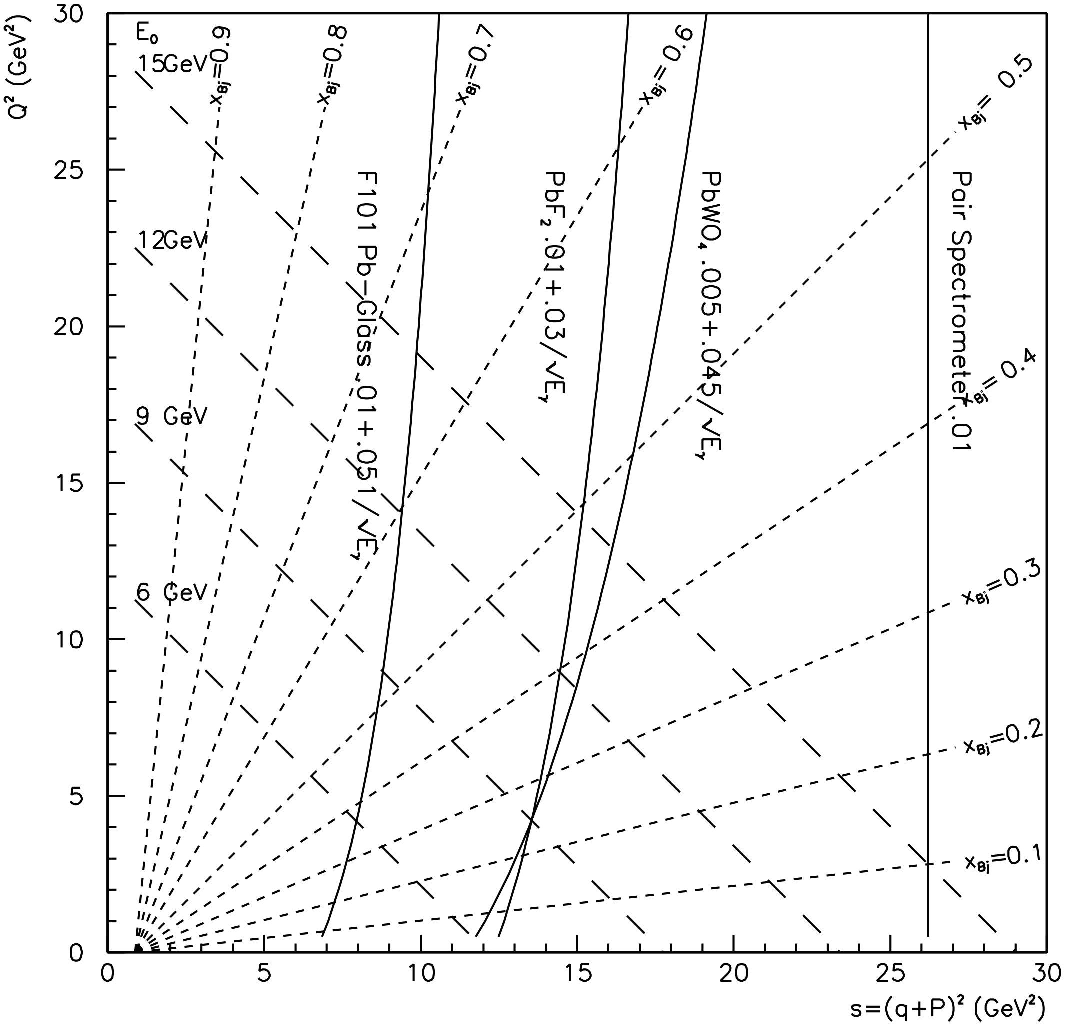

Figure 76: Photon resolution on a plot Q^2 vs. s. The curves labeled by different photon energy resolution values correspond to the kinematic limit at which the $p(e,e'\gamma)p$ and $p(e,e'\gamma)N\pi$(threshold) reactions are separated by 1-σ in the forward (DVCS) limit. DVCS kinematics corresponds to Q^2 and $s=(q+P)^2$ large, and $t=(P'-P)^2 \ll Q^2$. For each resolution curve, the entire kinematic region to the left is accessible with the exclusive channel resolved by $p(e,e'\gamma)X$ double coincidence. Each calorimetry material is labeled with its resolution in $\sigma(E_\gamma)/E_\gamma$. Contours of constant $x_{\rm Bj}$ and constant incident energy E_0 are also indicated separately.

Table 24: Some properties of tritium gas and liquid targets. Activity per cm assumes 1.5-cm-diameter gas target and 1-cm-diameter liquid target. Cooling power listed is due to beam heating only at maximum current. The luminosity is at maximum current. The liquid density is given at 225 psi and 45 K.

State	Density (g/cm^3)	Current (μA)	Cooling (W/cm)	Luminosity ($cm^2 s^{-1}$)	Activity/cm (kCi)
Gas	0.028	80	2.9	2.8×10^{36}	0.5
Liquid	0.27	15	5.5	5.1×10^{36}	2.2

the uncertainty in density, match the spectrometer acceptance, and maximize the luminosity. For safety considerations, the maximum amount of tritium should be no more than 20–30 kCi. This limits the maximum target length to around 10 cm for liquid and 40 cm for gas.

Adequate cooling of a liquid target requires most of the target to be surrounded by a copper heat transfer shield, which means only one spectrometer can be used, and the maximum current is about 15 μA. The advantage of liquid is a well-known density (to about 0.5%) and higher luminosity than gas at larger spectrometer angles. The effective density decreases by about 1.5%/μA. The gas target has the advantages that it can be made longer, thus taking advantage of the full acceptance at smaller angles, can take more current, has a more stable density (although presently the density of cold gas is known to only around 1.5–2%), and can be used for coincidence experiments. At large angles the luminosity is about half of that for the liquid one.

The properties of liquid and gas targets are summarized in Table 24. Because of the ability to do coincidence experiments, the better match to the spectrometer solid angle, less stringent cooling requirements, and the more stable density as a function of current, the gas target is preferred. The absolute density can probably be determined by comparing with measurements at higher temperatures and lower pressures where the gas properties are more reliably calculated.

The other question is whether to use a sealed target or storage beds. The advantage of a storage bed is that it provides the possibility to remove the tritium from the target to a mechanically strong container for work on the target or for safety reasons. Storage beds appear to be the best option. The major improvement required for the hall will be a tritium exhaust stack, which would, in the worst case of a complete target rupture, vent the tritium out of the hall with sufficient height and speed to keep the exposure at ground level to an acceptable level (less than 100 mrem at the site boundary).

4.C Hall B

4.C.1 Overview

The Upgrade of CEBAF to 12 GeV will provide opportunities for exciting new physics. The existing CLAS detector in Hall B was designed to study multiparticle, exclusive reactions with its combination of large acceptance and moderate momentum resolution. Studying exclusive reactions at high energy offers a new window on quark subprocesses; the extra information gained from measuring the hadrons' three-momenta allows the controlled study of an additional internal degree of freedom. For example, we can study the perpendicular as well as the parallel component of the quark momentum distributions by analyzing the exclusive production of mesons in the Deep Exclusive Scattering (DES) regime (high Q^2 and W, small t), impossible to deduce from the more limited information content of Deep Inclusive Scattering (DIS). High-energy exclusive events are characterized by higher-momentum, forward-going particles produced in conjunction with the typically lower-energy, larger-angle recoil nucleon system. Moreover, many reactions of interest, such as DES processes, have low cross sections on the order of nb/GeV^2 which will require high-luminosity operation.

To systematically study these high-energy exclusive processes, an upgraded CLAS will retain its toroidal magnet, time-of-flight counters, Čerenkov detectors, and shower counter. The present drift chamber system will be replaced with higher-granularity forward tracking chambers covering the angular range of 5° to 40°. The smaller drift cells result in a smaller sensitive time, making high-rate data collection possible, and also afford better spatial and hence, momentum resolution. The additional electromagnetic background at high luminosity (primarily Møller electrons) will be handled by a solenoidal magnetic shield. A cylindrical drift chamber followed by time-of-flight scintillators and a high-density shower counter will be located within the solenoid, forming the central detector (CD) whose primary role will be detecting the recoil nucleon and other large-angle tracks (35° to 120°). The target location will be moved upstream 1 m to provide coverage down to lab angles as small as 5°. Special (GAP) tracking chambers and shower counters located in front of the main torus coils will enable full azimuthal coverage for photons as well as charged track angular reconstruction down to 5°. These changes will enable efficient reconstruction of exclusive events at luminosities up to 10^{35} cm^{-2} s^{-1}.

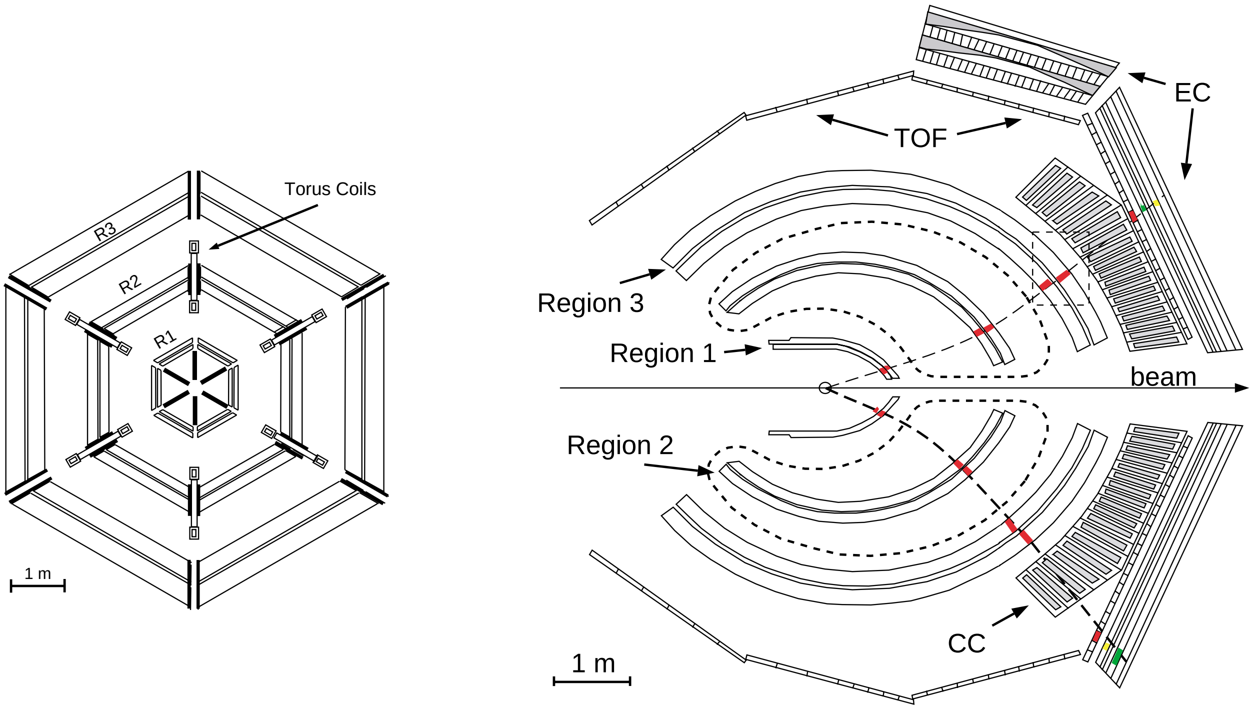

Figure 77: a) View of the CLAS in the beam direction, cut at the target z-position, showing three layers of tracking chambers (left). b) Top view; shown are the three regions of drift chambers, and the CC, EC, and TOF counters (right). A projection of the magnet's cryostat onto the midplane is shown as a dashed line.

4.C.2 Present CLAS Spectrometer

CLAS is a magnetic six-gap spectrometer with a toroidal magnetic field which is generated by six superconducting coils arranged around the beam line to produce a field which is primarily azimuthal; each gap is referred to as a sector. A view of the particle detection system in the direction of the beam (cut in the target region) is given in Fig. 77a, a top view in Fig. 77b. The detection system consists of drift chambers to determine the tracks of charged particles, gas Čerenkov counters for electron identification, scintillation counters for the trigger and for measuring time of flight, and electromagnetic calorimeters to detect showering particles like electrons and photons. The sectors are individually instrumented to form six independent magnetic spectrometers. This facilitates pattern recognition and track reconstruction at high luminosity.

In each sector, charged particles are tracked by drift chambers whose wires are arranged in 3 regions: Region 1 chambers are in the field-free volume close to the target, Region 2 are between the coils, and Region 3 lie outside of the coils. Each drift chamber region defines an independent track segment. The combination of axial wires oriented perpendicular to the beam axis, and stereo wires oriented at 6° with respect to the axial wires, allows a complete geometric reconstruction of charged tracks. For electron scattering experiments, a small normal-conducting toroid ("mini-torus") surrounding the target and nested within Region 1 keeps (low-momentum) charged electromagnetic background from reaching the Region 1 drift chamber.

The threshold gas Čerenkov counters are sensitive to particles with $\beta \geq 0.998$. In combination with the electromagnetic calorimeters they give good electron identification, sufficient even at large electron scattering angles where the π/e ratio becomes large. The location of the Čerenkov counters in front of the scintillation counters minimizes photon conversion and knock-on electrons.

The scintillation counters serve the dual purpose of contributing to the first-level trigger and providing time-of-flight information. Each counter is viewed by phototubes at both ends for improved timing and position resolution. Both the amplitude and time signals are measured.

The electromagnetic calorimeters are used for the identification of electrons and the detection of photons from the decay of hadrons, such as π^0, η, η', and Λ^*. The calorimeters are made of alternating layers of lead sheets as showering material and plastic scintillator strips. Six forward calorimeter segments provide coverage up to 45° in all six sectors; two additional segments cover the angular range up to 75°.

A Møller polarimeter to measure the polarization of the incident electron beam is located in the upstream beam tunnel. It is followed by a bremsstrahlung tagging spectrometer which occupies an enlarged tunnel section at the entrance of the hall. For tagged photon experiments, the primary electron beam is deflected downward into a low-power beam dump. Equipment to monitor the tagged photon beam – *e.g.*, a pair spectrometer and a total absorption counter – is located behind CLAS in the downstream tunnel section.

4.C.3 CLAS Performance

CLAS was commissioned in 1997, and started taking production data in December 1997. Major production runs were executed in the following categories:

- Electron scattering off hydrogen (e1 run group), deuterium (e1 and e5 runs), helium and nuclear targets (e2 run group); typically using a single-arm trigger on inclusive, scattered electrons; most runs done with polarized electrons.

- Tagged photons on hydrogen (g1 and g6 run groups), deuterium (g2 run group), helium (g3 run group); typically triggered on a single charged particle in CLAS in coincidence with the bremsstrahlung tagging system.
- Polarized electron scattering off solid-state polarized hydrogen and deuterium targets (eg1 run group).

The electron scattering experiments using CLAS have been typically conducted at a luminosity of 10^{34} cm^{-2}s^{-1}, slightly lower for a hydrogen target, slightly higher for deuterium and light nuclei. Tagged photon experiments were operated at around 10^7 tagged photons/s, typically limited by accidental coincidences between CLAS and the bremsstrahlung tagging system. The capabilities of the data-acquisition system have been steadily improved; data rates of 3,000 events/s and data throughput of 14 MB/s have been reached.

Angular coverage

Some fraction of the full solid angle is obstructed by the torus coils. Therefore, magnetic analysis is possible in the open gaps, only. Since the width of the torus coils is constant, the relative loss in ϕ-coverage increases with decreasing polar angle θ. Figure 78 shows the CLAS acceptance for full magnetic analysis of π^+ and π^- in the $(\theta - \phi)$ plane. Note that the acceptance depends on the charge of the particle, extending to smaller values of polar angle for the outward-bending (positive) particles.

Particle identification

Electron identification in CLAS relies on the combination of a signal from the threshold Čerenkov counter, as well as energy deposition in the electromagnetic calorimeter which matches the momentum as determined by the tracking chambers.

Neutral particles (photons and neutrons) are detected in the electromagnetic calorimeters (EC). The momentum and direction of photons are determined from the EC signals. The calorimeters provide photon energy measurements with a resolution $\sigma_E/E \leq 0.1/\sqrt{E(\mathrm{GeV})}$, and provide an angular resolution of ≤ 10 mrad. Mass determination for charged hadrons, π, K, p, and D, is accomplished by measuring the particle's momentum and velocity. The tracking chambers determine the track's momentum and path length, while the scintillator counters provide the time-of-flight measurement. As an example, Fig. 79 shows the mass distribution for charged particles produced in

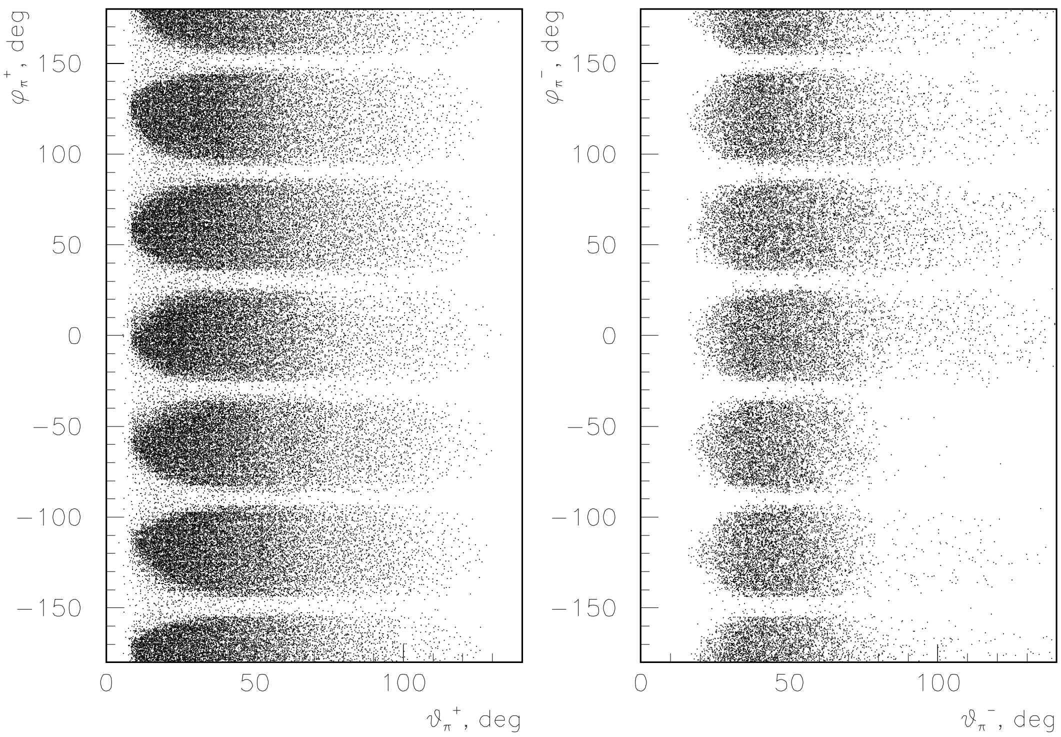

Figure 78: The angular acceptance if CLAS for π^+ (left) and π^- (right) plotted versus lab angles.

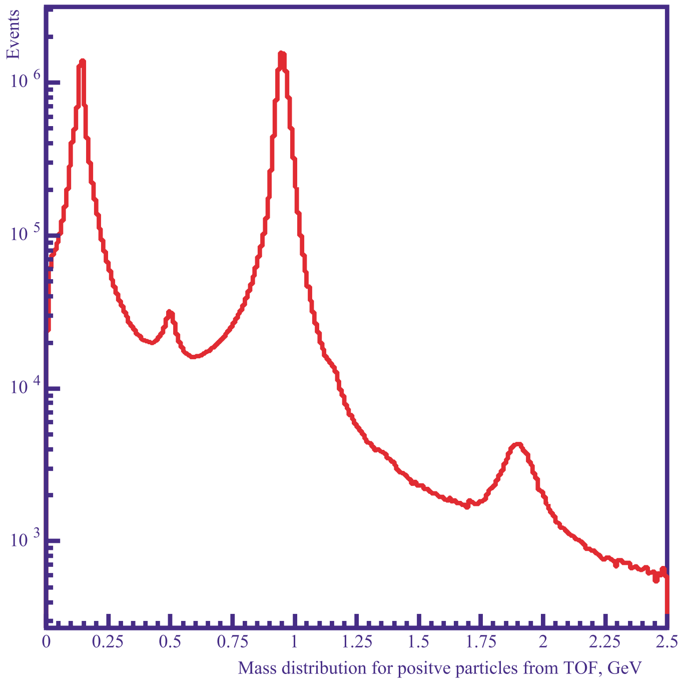

Figure 79: Mass distribution for charged particles produced in the $ep \to eX$ reaction at $E_o =$ 2.4 GeV.

coincidence with electrons in the process $ep \to e'X$. The mass spectrum shows clear contributions from pions, kaons, and protons as well as a peak from deuterons.

Missing-mass technique

Much of the CLAS experimental program relies on the missing-mass technique to identify exclusive processes, especially for the identification of neutral particles in the final state such as:

$$ep \to ep\pi^0\ ,\ ep\eta,\ e\pi^+n$$

or

$$\gamma p \to K^+\Lambda,\ K^+\Sigma^0,\ K^+\Lambda^*.$$

As an example, Fig. 80a shows the missing mass recoiling from the scattered electron and a π^+, showing the neutron and Delta peaks, while Fig. 80b shows the missing-mass distribution for the process $ep \to epX$. The missing-mass spectrum shows clear contributions from π^0, η, ρ, and ω production.

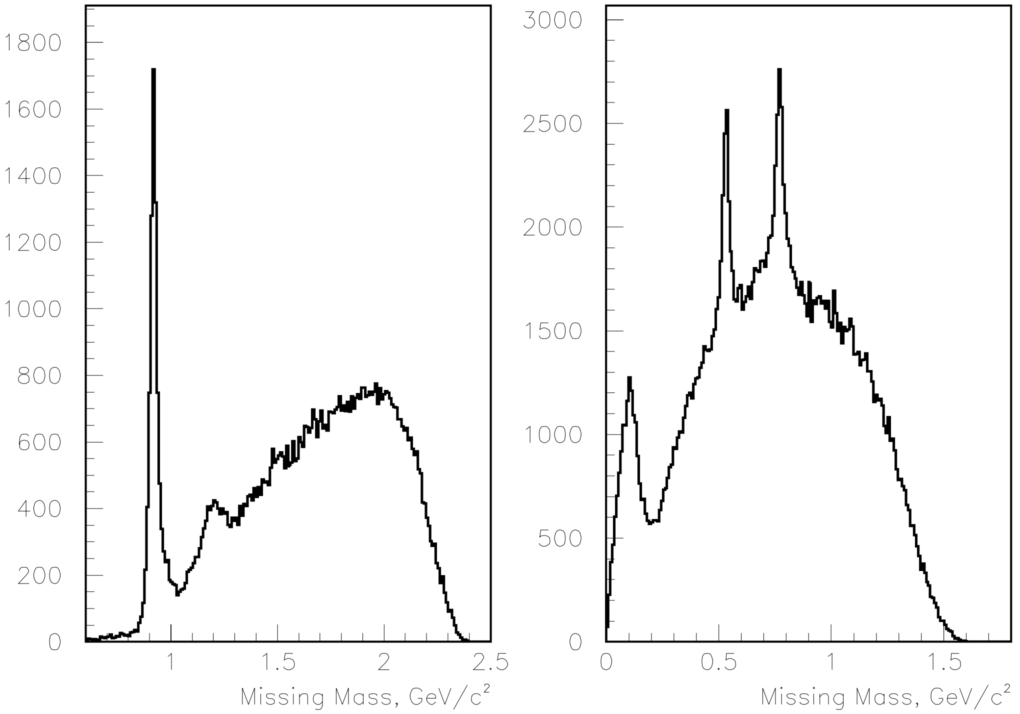

Figure 80: Missing-mass distribution for $ep \to e\pi^+X$ (left) and $ep \to epX$ (right) at $E_o = 4$ GeV.

4.C.4 Physics Program for an Upgraded CLAS

The main physics goal for an upgraded CLAS detector is a systematic investigation of exclusive scattering cross sections. The higher available beam energy will allow exclusive studies in unique kinematic ranges, for example, high-Q^2 studies of nucleon excitation, high-W studies of polarization transfer to hyperons, and a large range of formation time and distance in color-coherent studies, to name a few.

Among the most interesting studies are those in the Deep Exclusive Scattering (DES) regime, in which a forward meson is produced at small t but at large $Q^2$and W. These studies are expected to provide quantitative measures of the full quark wavefunctions (perpendicular as well as parallel momentum distributions) using the framework of the recently developed Generalized Parton Distribution (GPD) functions. (This is in contrast to deep inelastic inclusive measurements which give access only to the longitudinal momentum distribution.) To carry out this new DES program the following processes need to be investigated:

- Deeply virtual Compton scattering: $e\,p \;\rightarrow\; e'\,p\,\gamma$.
- Electroproduction of pseudoscalar mesons: $e\,p \;\rightarrow\; e'\,\pi^+\,n$ and $e\,p \;\rightarrow\; e'\,\pi^o\,p$.
- Electroproduction of vector mesons, in particular $e\,p \;\rightarrow\; e'\,\rho\,p$.
- Single-spin beam asymmetries in deeply virtual Compton scattering and target polarization asymmetries in pion production from protons.

The typical kinematic regime that needs to be covered is $W \geq 2$ GeV (to avoid the resonance region), $Q^2 \approx 2$ GeV/c^2 and higher, and small t.

In addition to the DES program, there will be logical extensions of the present CLAS program to higher masses for the final states, and to higher momentum transfers (see Ref. [Bu98] for details). Particularly important measurements are:

- The neutron form factor G_m^n to $Q^2 \approx 14$ (GeV/c)^2.
- Higher moments of spin structure functions; *i.e.*, determining $\int g(x, Q^2) \cdot x^n$.
- Flavor tagging of polarized spin structure functions.
- Meson transition form factors, *e.g.* $\omega \rightarrow \pi^0\gamma^*$, $A_2 \rightarrow \rho\pi$.

- Multi-nucleon knockout, and meson and N^* production and propagation in nuclei.
- Measurements of spin transfer from polarized electrons to hyperons at large W.
- Color coherent effects.

4.C.5 Design Goals for Higher Energy

The main goal of the CLAS upgrade is to maintain its capability to obtain high statistics data for exclusive electron scattering reactions at high energies. Many of the desired event samples (and the DES events in particular) form a medium-multiplicity (three to five final-state particles), low cross-section sample in a background of higher-multiplicity events. They are also typified by higher-momentum tracks emitted at smaller lab angles. A successful study of these exclusive reactions requires several major improvements in the CLAS's capabilities:

- The missing-mass technique needs to be augmented by a more complete detection of the hadronic final state.
- Efficient detection of the events requires complete photon reconstruction (energy and angle) over the complete azimuth for angles down to 5°.
- Similarly, partial charged track reconstuction (track identification and angle determination) is required over the full azimuth for angles greater than 5°.
- The luminosity of CLAS needs to be increased by about one order of magnitude over the present value to $L = 10^{35}$ cm^{-2} s^{-1}.

The small cross sections for the processes of interest mean that efficient background rejection is quite important. The primary backgrounds will likely be due to higher-multiplicity events with missing particles as well as events contaminated by out-of-time accidentals (not much of a problem at the present CLAS luminosity, but this will become important at 10^{35}). The primary strategy will be to positively identify the background, and to rely on missing-mass methods to pick out single, low-momentum particles (*e.g.*, recoil neutrons or slow π^-'s) that might otherwise escape detection. These requirements prescribe a more hermetic detector than the present CLAS as well as detectors capable of identifying that all particles came from the same event in both space and time.

Table 25 lists some of the characteristics of exclusive events at 12 GeV and the ensuing requirements for an efficient detector:

Table 25: CLAS upgrade plans: design goals

Event Characteristics	**Detector Requirements**
Higher multiplicity	More hermetic detector
	Good missing-mass resolution
Higher momentum	Easier electron identification
	π/p separation by TOF only to 3 GeV/c
Smaller lab angles	Move target back 1 m
Small cross sections	Better Møller shield
→ high luminosity	Smaller sensitive time for wire chambers

4.C.6 CLAS Upgrade Plan

We will retain most of the present CLAS detector with the exception of the drift chambers, which will be replaced by new forward tracking chambers with smaller granularity. Moving the target upstream 1 m will enable particle detection down to 5°. Forward-going photons within the gap between torus coils will be detected by the EC counter; an auxilliary pre-radiator in front of the shower counter will improve the spatial resolution for photons. Forward tracking for charged particles in the inter-gap region will be accomplished by three stations of new drift chambers with smaller granularity. Special "gap" counters located in front of the main torus coils will restore full azimuthal coverage for forward-going photons and charged tracks, though full momentum reconstruction will be possible only for tracks penetrating the forward tracking stations. A central detector located within the superconducting solenoid will provide charged-particle tracking and photon detection for large-angle particles.

Table 26 recapitulates the design features required by the characteristics of DES events, and the new detector elements chosen to satisfy them. A conceptual design of the upgraded CLAS is shown in Fig. 81. The components of the upgrade plan will be discussed in more detail in the following sections.

Central detector

The dual need for more complete solid angle coverage as well as more robust shielding against the electromagnetic background of Møller electrons is satisfied with the addition of a new superconducting solenoidal magnet and associated central drift chamber and shower counters. This central

Table 26: CLAS upgrade plans: design choices

Requirement	**Design Element**
Better Møller shield Hermeticity requirement	Solenoid with central tracker and central calorimeter
Better missing-mass resolution Lower sensitive times	Tracking chambers with smaller cell sizes
Particle identification at higher momentum	Fine-grain pre-radiator before EC Use Čerenkov for pi/p separation
Smaller angle coverage	Move target back 1 m

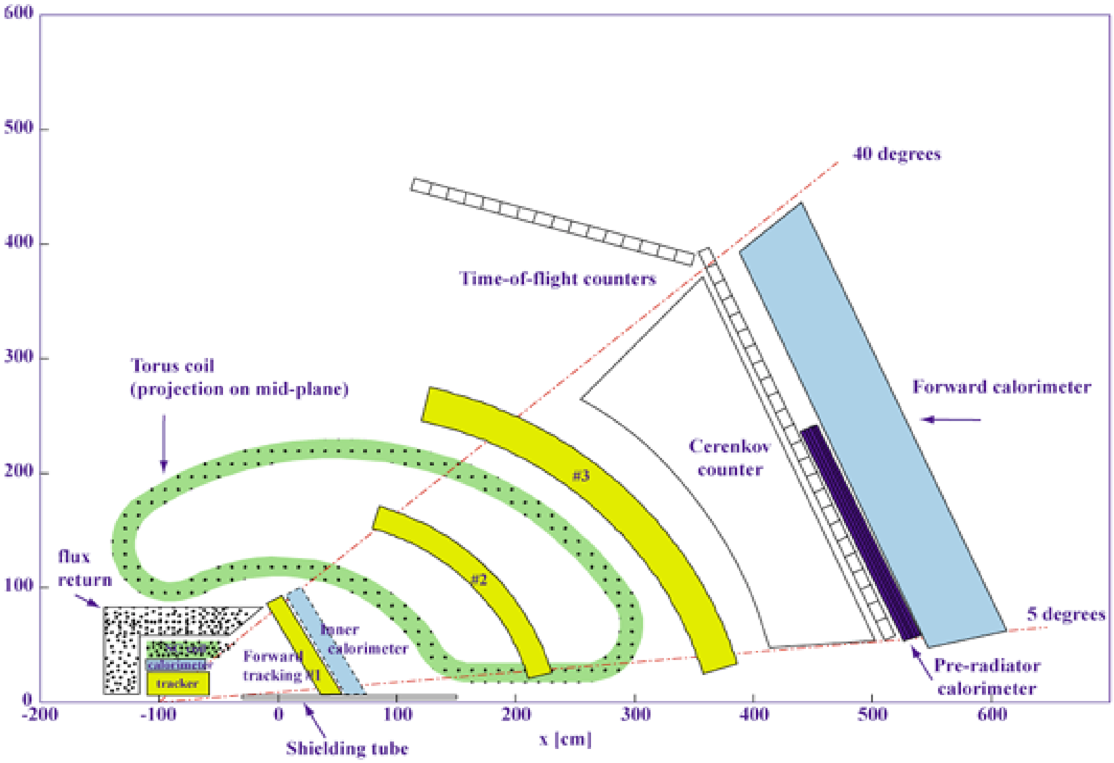

Figure 81: Conceptual view of the CLAS upgrade.

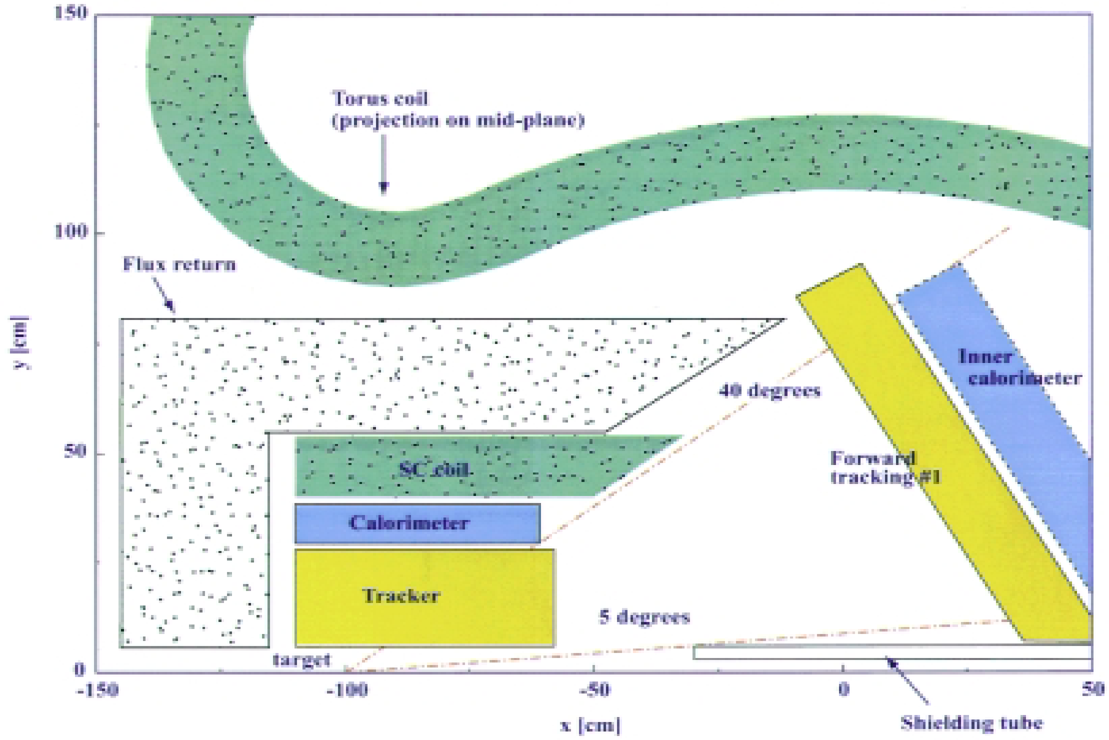

Figure 82: Conceptual view of the CLAS central detector.

detector (CD) allows the detection of charged and neutral tracks in the central region (35°$\leq\theta$ $\leq$120°) with a moderate fractional momentum resolution of $\delta p/p \approx$2%. A close-up view of the central detector is shown in Fig. 82. Note that the nominal target location has been shifted upstream by 1 m.

The detector uses a superconducting solenoid to provide a 1.5 – 5 T longitudinal magnetic field for the following functions:

- Keep Møller scattered electrons from reaching the detectors by guiding them along the magnetic field lines till they hit the inside of a heavy metal shielding pipe. This technique has been used successfully during the eg1 run, with the magnetic field provided by the 5 T polarized target magnet. This arrangement resulted in better shielding than the standard mini-torus magnet.
- Determine charged-particle momenta and charge via tracking in a central cylindrical drift chamber.

- Additionally provide the magnetic field for a solid-state dynamically polarized target. Polarized target operation adds homogeneity constraints which will require correction coils.

The flux return increases the field homogeneity and reduces the fringe field. Since shielding the Møller electrons relies on the fringe field the shaping of the flux return will be optimized for this purpose.

The central tracker uses gas-filled drift cells, either a standard drift chamber or straw tubes, to track charged particles over a radial distance of 25 cm. The expected transverse momentum resolution is $\delta p/p \approx 2\%$ (rms). A preliminary design uses an average cell radius of 3.5 mm, allowing three superlayers of wires of six layers each for a total of 18 wire layers. Each wire layer would have 180 wires in azimuth, yielding a total count of 3240 instrumented wires. Each wire will need a distance resolution of about 150 microns in order to achieve the desired 2% fractional momentum resolution. The expected hadronic accidental occupancy at a luminosity of 10^{35} $\mathrm{cm}^{-2}\mathrm{s}^{-1}$ should only be about 0.5% per wire for a 100 ns time window. An interesting straw tube solution to a similar problem has been developed for the WASA detector at CELSIUS.

The function of the central calorimeter is to detect photons and neutrons, and to give some range information for charged particles (mainly to help identify recoiling protons). The calorimeter is located inside the coil and needs to be very compact to keep the coil diameter small. A promising construction technique that is presently being studied is to embed scintillating fibers into a high-density tungsten powder matrix. Another vital function of the central calorimeter is to determine the event time for all tracks in order to reject out-of-time accidentals.

Forward tracker

The small cross-sections expected for exclusive processes will require running at luminosities of $\approx 10^{35}$ $\mathrm{cm}^{-2}\mathrm{sec}^{-1}$. Sucessful use of the missing-mass technique at higher energy will also require better momentum resolution than the present detector for forward-going particles. We accomplish these two goals by redesigning our main drift chambers to have smaller cell sizes than the present chambers; this reduces the accidental occupancy by a factor of 4 (for tracks) or 8 (for isolated X-rays) and will also provide better position resolution and hence, better momentum resolution.

The resulting forward tracking system covers the angular range of 5–40 degrees for high-momentum particles. The proposed design uses three tracking stations located at the same positions as the present CLAS chambers. However, the angular range is smaller and the cell diameters are half the present size, yielding about the same total wire count.

Construction and mounting techniques are envisioned to be similar to the present drift chambers. The station 1 chambers will need to cover the full ϕ range; the goal, of course, being to detect as many tracks as possible from the high-multiplicity events, even if we don't measure the momentum accurately, in order to veto these events. To achieve this full coverage in azimuth for the station 1 chambers we plan to build six independent trapezoidal chambers with light-weight frames coupled mechanically to support the wire tension (analogous to our present Region 1 chambers).

The dead area of the station 1 tracking chambers will covered by six additional (narrow) rectangular chambers, referred to as the "gap" chambers. The detectors in this "gap" area are covered in the next section.

GAP detectors

In the present CLAS detector, charged or neutral particles heading for the coils are not detected. One would like to determine the directions and make a coarse energy measurement for all photons, and to determine the direction for charged tracks in this region. This requires instrumenting the inside of the torus coils with the so-called inner photon detectors and the "gap" tracking chambers.

The gap chambers must not intrude into the intra-coil region for which the forward tracker will measure momentum. It must also measure accurately the radial coordinate in order to measure the angle (but not the charge or momentum) of track segments. One concept is to have radial wires with the signals picked up by azimuthal cathode strips. An alternate strategy has wires running azimuthally with only low-profile capacitors in the sensitive region and the pre-amplifiers and signal cables hidden behind the chambers.

The inner photon detector will have to be very compact since there is little space available. Ideally, the detector should also give some information on charged particles, like energy deposition, range, etc. A possible solution is to install short-radiation-length crystals (*e.g.*, lead tungstate) in the angular range between 5° and 45° to complement the forward calorimeters (see Ref. [Bu98a] for more details). An important open question is the choice of the readout technique.

Particle identification strategy

For e/π separation the present technique of combining energy deposition in the calorimeter and a signal in the Čerenkov counter will be limited to $p \leq 2.7$ GeV/c since the Čerenkov counters will record pion events at the higher operating energies. The solution is to rely on the electromagnetic calorimeter alone for e/π separation. The relative calorimeter resolution improves with increasing energy; in addition, one can make better use of the longitudinal and transverse energy deposition patterns, which are different for e and π.

Typical exclusive events at high energy will naturally have higher-momentum particles than those in present experiments, making particle identification more difficult. To study DES adequately, we will need to extend π/p separation up to 6 or 8 GeV/c. Pion-proton separation by time of flight works up to about 3 GeV/c momentum. Pions with higher momenta give a signal in the Čerenkov counter, distinguishing them from protons. Kaon-pion separation can likewise be accomplished up to 2 GeV/c by time of flight, and above 3 GeV/c by using the Čerenkov counter to indicate a pion. There will be a gap in positive kaon-pion separation between 2 and 3 GeV/c momentum. We plan to accomplish effective kaon identification in this range by using constrained fitting, or in some cases, by detecting the hyperon directly. We can also enhance our detection of the weakly decaying strange particles by detection of a detached vertex.

The position resolution of the present electromagnetic calorimeter (EC) is insufficient to separate single photons (*e.g.* from the DVCS process) from two photons from the decay of high-momentum π^0's since the half-angle of photons from the decay of an 8 GeV/c π^0 is less than 1^0. The two-photon separation will be enhanced by adding a smaller-granularity, four-radiation-lengths pre-shower calorimeter in front of the existing EC. Using the same lead-scintillator sandwich construction technique as for the EC, but with scintillator strips of half the width, will give the desired position resolution. Since the maximum π^0 energy falls steeply with increasing polar angle, only half of the forward calorimeter face needs to be covered by the pre-shower radiator. The new detector elements necessary to complete the upgrade are listed in Table 27.

Trigger and data acquisition

Triggering at high energy will be challenging since the Čerenkov counters will be less effective in enriching the event sample with electrons. At a luminosity of 10^{35} cm^{-2}s^{-1} the total hadronic production rate is about 10^7s^{-1}. Assuming a data-acquisition capability of 5,000/s, the trigger has to provide a factor of 2000 rejection of hadronic events. The following requirements will be used in the Level I and II trigger:

- High energy in the calorimeter, with independent thresholds in the front and rear elements.
- Matching signal in the Čerenkov counter, which will eliminate contributions from high-energy

Table 27: CLAS upgrade plans: new detector elements

New Detector	**Description, Expected Performance**
Central solenoid	Superconducting, 1 m diameter, 0.5 m length, up to 5 T field for tracking, Møller shield
Central tracker	Cylindrical chamber, 18 layers × 180 wires stereo and axial wires, 150 μm accuracy
Central calorimeter	Lead tungstate, $10\%/\sqrt{E}$ energy resolution
Inner calorimeter	Lead tungstate, covers coil faces
Gap tracker	Finds track segments, determines track angle Covers coil face
Forward tracker	3 regions of drift chambers with small granularity Same coverage as present DC's, twice the granularity
EC pre-radiator	Covers inner angular range of EC's Gives better spatial resolution for photons

photons hitting the calorimeter.

- Negative polarity track matching the energy deposition in the calorimeter.

On-line event analysis in a Level III trigger will reduce further the number of events that have to be written to tape.

Bremsstrahlung tagging system

The present bremsstrahlung tagging system is limited to $E_o \leq 7$ GeV by the requirement to bend the primary electron beam into the 30° dump line. The present plan is that tagged photon experiments at higher energies will generally be performed in Hall D.

We have considered ways to upgrade the maximum energy of the tagging system by using alternative beam dumping schemes. We are also investigating possible ways to detect and trigger on very small-angle scattered electrons in coincidence with a hadronic event, providing tagged photons with $Q^2 \approx 0$. For now, we have no plans to upgrade the tagging system.

Expected performance: CLAS upgraded detector We have done some simple simulations of various components of the CLAS upgrade under expected experimental conditions. We

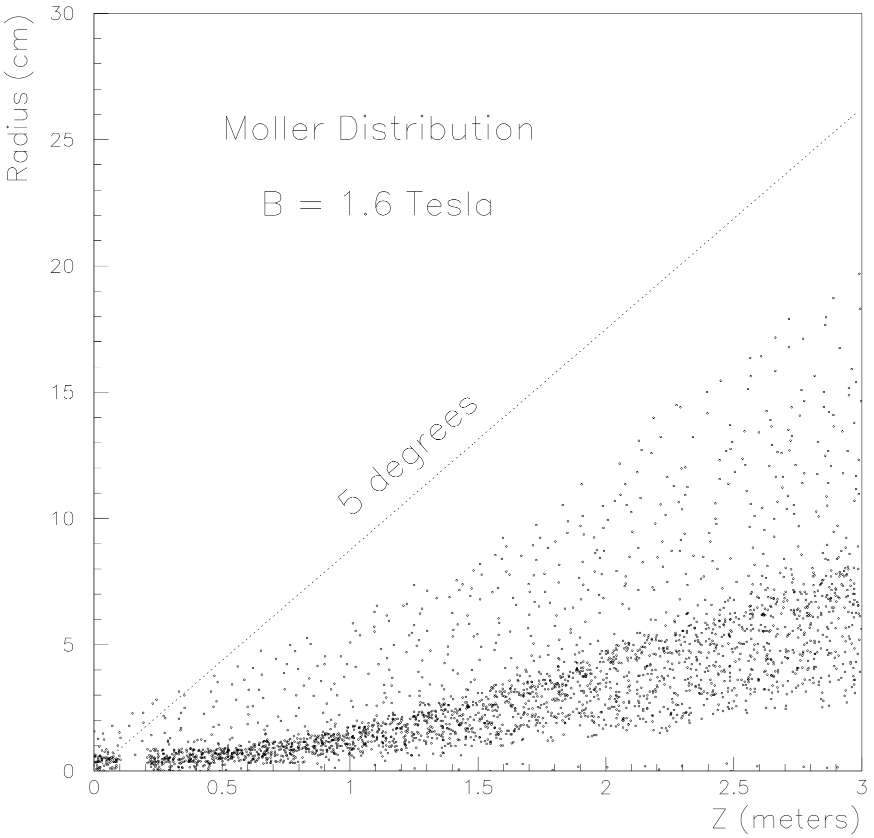

Figure 83: Møller flux rate as a function of the z coordinate along the beam versus the radial position. A 5° line is shown for comparison.

have broadly specified the size and current density of the central solenoid by considering its effect on the expected flux of Møller electrons from the target. The strategy is to confine the Møllers to widening spiral trajectories using the solenoid's magnetic flux lines, and to absorb these electrons when they strike the inner face of a cylindrical shielding tube. We note that this shielding technique has been successfully used in the EG1 experiments in the present CLAS setup.

In Fig. 83 we plot the expected flux density of Møller electrons as a function of the z coordinate along the beam line in meters and the radial coordinate in centimeters. The shielding of the Møller electrons for this study is accomplished by a 1-m-diameter and 0.5-m-long solenoid with a maximum field strength of 1.6 T. Note that for z positions greater than about 0.5 m, all Møllers are confined to a cone smaller than 5°. For higher B fields, the cone angle is smaller still.

We have estimated the resolution for the perpendicular momentum component of charged

Table 28: CLAS upgrade plans: expected performance

	Resolution		
Component	**Spatial**	**Time**	**Energy**
Central tracker	150 microns/layer	na	na
Central calorimeter	10 cm	1 ns	10%
Gap calorimeter	10 cm	1 ns	10%
Gap tracker	100 microns	na	na
Fwd. tracker	150 microns/layer	na	na
TOF banks	1 cm	100 ps	na
EC (with pre-radiator)	5 cm	1 ns	5%

particles traversing the CD's drift chamber by dividing the expected spatial accuracy (150 microns per layer) by the sagitta of a charged track traversing a solenoidal field. We obtain an estimate of $\delta p/p = 2\%$. Likewise we estimate that new EC with preceding pre-radiator should be able to achieve the same energy resolution as the present EC, that is $\approx 7\%/\sqrt{E}$, but should have much better position accuracy, down to an uncertainty of only 1 cm. Table 28 lists the individual detector components and their expected resolution in position, time, and energy where applicable.

Since the missing-mass technique will be employed to identify exclusive events with a missing recoil neutron from, for example, a recoil delta baryon, we have simulated the momentum and angular resolution of the forward tracking system to see what spatial resolution is required. Fig. 84 shows a plot of the missing mass recoiling from the scattered electron and forward-produced pion in $ep \rightarrow e'\pi^+(N)$ events. These events were simulated with a beam energy of 11 GeV. Overplotted are two spectra, obtained from assuming that the tracking chambers have 100 and 400 micron accuracy, respectively.

4.C.7 Hall B Summary

The planned Hall B physics program at 12 GeV requires an upgraded CLAS detector which has better magnetic shielding, more complete angular coverage, better momentum resolution in the forward tracking region, smaller time windows in the tracking system, and coverage down to smaller polar angles than the present detector. We accomplish these design goals by: adding a central solenoidal magnet instrumented with a cylindrical drift chamber and inner shower counter (to provide hermetic coverage of slow recoil particles while giving good magnetic shielding for Møller electrons); replacing the current tracking system by three stations of forward tracking chambers

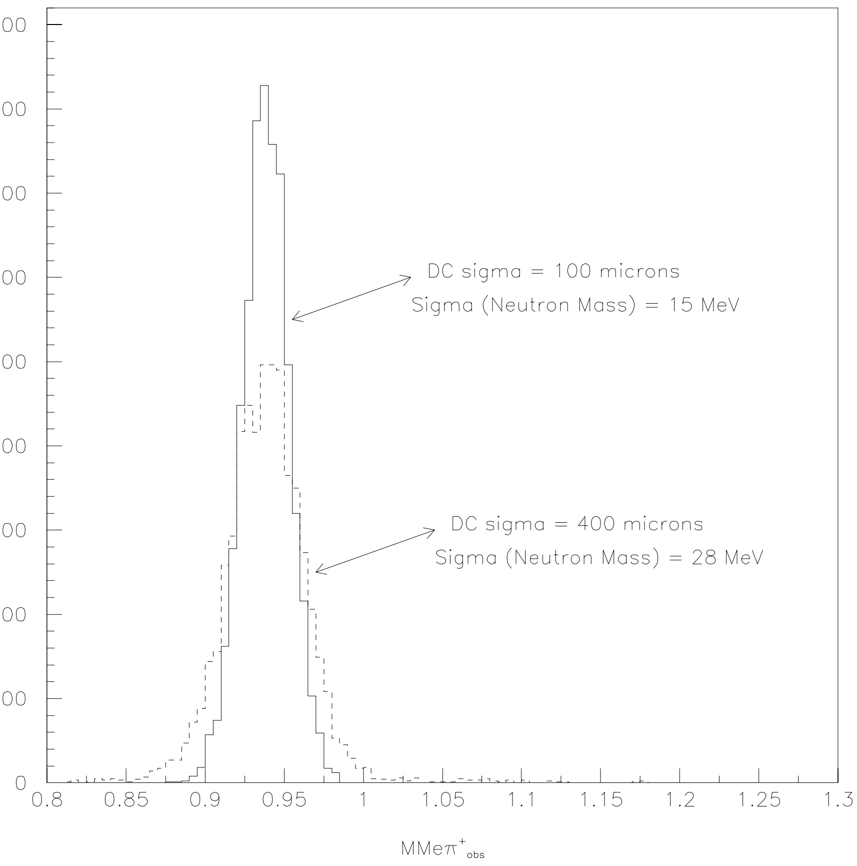

Figure 84: Simulated missing mass for the reaction $ep \to e'\pi^+N$.

(which have half the cell size and hence, lower sensitive time and better resolution, than the present system); augmenting the electromagnetic calorimeters with a fine-grained pre-radiator; and moving the target position back a meter to gain access to tracks with polar angles down to 5°.

These changes should allow the efficient detection of exclusive events, representing the majority of the planned program, at luminosities up to 10^{35} $\mathrm{cm}^{-2}\mathrm{sec}^{-1}$. With these changes, the exciting program of investigating Deep Exclusive Scattering and thereby beginning the next-generation studies of the nucleon's quark wavefunction should be within our experimental grasp.

4.D Hall C

Hall C at Jefferson Lab has generally been used for experiments which require high luminosity and good resolution. Since the beginning of operations at JLab, the core spectrometers have been the High-Momentum Spectrometer (HMS) and the Short-Orbit Spectrometer (SOS). These two devices have been used flexibly in the experimental program as either electron or hadron arms, in coincidence with one another or with a third user-supplied arm. The HMS has $P_{\text{max}} = 7.6$ GeV/c and is compatible with the 12 GeV Upgrade, but the SOS has only a limited maximum momentum of 1.7 GeV/c. The HMS will be in need of a new, high-momentum companion spectrometer: the Super-High-Momentum Spectrometer (SHMS), which will have the flexibility and dynamic range to carry out a broad physics program.

4.D.1 Overview

The Super-High-Momentum Spectrometer (SHMS) will play a vital role in the overall JLab physics program at 12 GeV. An inevitable consequence of relativistic kinematics is that much of the interesting physics at 12 GeV will only be accessible provided at least one of the spectrometers can achieve angles significantly below 10°. The SHMS will achieve a minimum scattering angle of 5.5° with acceptable solid angle and do so at high luminosity. The maximum momentum will be 11 GeV/c, well matched to the maximum beam energy available in Hall C. These three characteristics (high luminosity, small scattering angle, and high momentum) are essential for carrying out a program of electron-hadron coincidence experiments at large $z = E_h/\nu$ where ν is the electron energy loss. (For orientation, in the limit of $z \to 1$, one approaches the exclusive limit.) At large z (*i.e.*, $z \simeq 1$), sensitivity to the valence quark structure of the hadron is maximized and the reaction mechanism is simplified. The HMS-SHMS spectrometer pair will be rigidly connected to a central pivot which permits both rapid, remote angle changes and reproducible rotation characteristics which simplify accurate measurements. From its inception, the SHMS momentum and target acceptances were designed to be very flat, with similar performance to the HMS, which also will greatly simplify making accurate measurements. Finally, for experiments which are willing to trade off small-angle performance for increased solid angle, this can be achieved by pulling the first two quads forward and retuning the spectrometer. In the remainder of this section we will discuss several physics examples which drive the SHMS requirements.

Measurements of the charged pion form factor at large Q^2

The long-term interest in this subject is due to the calculation of Farrar and Jackson [Fa75], who showed that the pion form factor (F_π) is rigorously calculable in pQCD at asymptotic values of Q^2. Such a rigorous prediction is almost unique in QCD. However, for the finite values of Q^2 where experiments are actually performed, the situation is more complex. Nonperturbative "soft scattering" contributions must be explicitly taken into account. After years of theoretical effort, there has been considerable progress in our understanding of the smallest value of Q^2 for which the hard scattering amplitude may dominate (*e.g.*, [Is84, Ja90, Ti92, It92, Ja93, Mu95, Do97]). The pion is the laboratory of choice for these studies because the smaller number of valence quarks in the pion means that the asymptotic regime will be reached at lower values of Q^2 for F_π than for the nucleon form factors. Thus the pion "laboratory" may eventually provide the same level of insight into light-quark QCD that the deuteron "laboratory" has provided for studies with nucleon and meson degrees of freedom.

The high-quality, continuous electron beam of Jefferson Lab makes it the only place to seriously pursue these measurements. Completed JLab experiment 93-021 explored F_π to $Q^2 = 1.6$ with 4 GeV beam using the HMS-SOS combination in Hall C. However, a serious test of QCD-based models requires the construction of the SHMS and the 12 GeV electron beam Upgrade. The reaction used is exclusive $p(e, e'\pi^+)n$ and the longitudinal response function $d\sigma/dt$ must be isolated via a Rosenbluth separation. The most stringent requirement this experiment imposes upon the SHMS design is the 5.5° forward angle capability. An accurate and reproducible coupling to the present pivot is also needed, as well as relatively flat acceptances in phase space. Figure 40 shows the size of the anticipated error bars with the SHMS+HMS combination and 12 GeV beam. It is easily seen that the JLab Upgrade would allow a dramatic advance in the understanding of the pion form factor.

Color transparency

The Color Transparency (CT) conjecture by Mueller and Brodsky [Mu83] has stimulated great interest. CT was first discussed in terms of perturbative QCD considerations. However, later work [Fr92a] indicated that this phenomenon occurs in a wide variety of situations with nonperturbative reaction mechanisms. The existence of CT requires that high-momentum-transfer scattering take place via selection of amplitudes in the initial- and final-state hadrons characterized by a small transverse size. Furthermore, this small object should be "color neutral" outside of this small radius in order not to radiate gluons. Finally, this compact size must be maintained for some distance in traversing the nuclear medium. Unambiguous observation of CT would provide a new means to study the strong interaction in nuclei.

Jefferson Lab has several advantages to offer in searching for CT effects via quasielastic $A(e, e'p)$ measurements. First, data from experiments NE18 at SLAC [Ma94] and completed JLab experiments E91-013 [Ab98] and E94-139 will provide a baseline for conventional Glauber calculations. Second, the fundamental electron-proton scattering cross section is smoothly varying and accurately known in this kinematic range. Finally, the high duty factor, high luminosity, and large solid angle of the high-momentum Hall C spectrometers all contribute to making high-quality, precision measurements feasible.

Upgrading to a 12 GeV beam energy would allow measurements at even higher momentum transfers. With the planned Hall C upgrades a momentum transfer of about 18 $(\mathrm{GeV}/c)^2$ could be obtained. The most stringent requirement this experiment places on the SHMS design is that the proton momenta approach the beam momentum, so a reasonable maximum SHMS momentum is 11 GeV/c. In Fig. 49 we show an overview of previous results from nuclear transparency measurements in combination with the projected uncertainty using the HMS-SHMS combination for the $^{12}\mathrm{C}(e, e'p)$ reaction. The highest Q^2 point assumes a data-taking period of 80 hours. As shown, such a precise data set will allow us to distinguish between conventional Glauber calculations and the state-of-the-art CT predictions of Nikolaev *et al.* (CT(I); Ref. [Ni94]) and Frankfurt *et al.* (CT(II); Ref. [Fr94]).

$N \rightarrow N^*$ form factors at high Q^2

The upgraded Hall C will have a unique role to play in studies of neutral meson electroproduction at high Q^2. As in the completed JLab experiment 94-014, high-Q^2 studies of the resonant amplitudes of the $\Delta(1232)$ and $S_{11}(1535)$ via $e+p \rightarrow \Delta(1232) \rightarrow p+\pi^0$ and $e+p \rightarrow S_{11}(1535) \rightarrow p+\eta$, respectively, can be executed (Fig. 39). For the single meson decay channel, measuring only one of the decay hadrons completely determines the kinematics of the entire reaction, including the other undetected hadron. In particular, the neutral single meson is identified by the missing mass of the detected proton and electron, and its CM kinematics by missing momentum. An important property of high-Q^2 reactions which Hall C can take advantage of is that the hadronic reaction products are boosted into a narrow cone relative to the momentum transfer, so that large CM angular acceptances in θ and ϕ can be obtained with relatively modest angular-acceptance spectrometers. This is especially true for the recoil protons in single neutral meson production, $p(e, e'p)\pi^0$ and $p(e, e'p)\eta$. The protons emerge in a narrow cone around the momentum transfer $\vec{q}$. For example, if we consider π^0 production at the delta peak, $W = 1232$ MeV, at $Q^2 = 10$ (GeV/c)^2 the cone angle in the lab corresponding to 4π in the CM is 2.7° (47 mr). For η's at the peak of the $S_{11}(1535)$ resonance the angle is 2.5° (43 mr). With modest solid angle acceptance spectrometers one can obtain almost all of the decay proton cone, and then select the π^0 and η channels by reconstructing their missing mass.

In experiment 94-014 the HMS detected the protons with momenta up to about 3.5 GeV/c, and the SOS detected the scattered electrons with a momentum about 1.5 GeV/c. At much higher Q^2 [*e.g.*, ~ 15 (GeV/c)^2], the SOS must be replaced by a new spectrometer, the SHMS. At these increased Q^2 both spectrometers must have high maximum-momentum capabilities. In addition *both* must have adequate resolution ($\simeq 0.1\%$ in momentum and $\simeq 1$ msr in θ and ϕ) and adequate solid angle.

Duality and fragmentation

In the early 1970s Bloom and Gilman made the phenomenological observation that there is a duality between electron-proton scattering in the resonance and in the deep inelastic regions [Bl70]. Duality in this situation means that resonance bumps observed in the structure functions at low Q^2 average out to mimic the smooth scaling functions measured at higher Q^2. This implies that the single-quark scattering process determines the scale of the reaction, even in the nucleon resonance region, provided one averages over a suitably wide region of kinematics. Bloom-Gilman duality has recently been verified to hold to high precision down to very small values of Q^2 [$<$ 1 (GeV/c)^2] [Ni99]. This last observation, if reliably understood, could allow one to use duality to study structure functions in hitherto difficult to access kinematics regions, *e.g.*, the region of Bjorken $x \to 1$.

Carlson *et al.* have argued that duality should also hold in the longitudinal structure function for inclusive scattering, and in pion photoproduction for semi-exclusive scattering [Ca90, Af00]. Related to the latter case may be semi-exclusive deep inelastic scattering with parallel kinematics. Here duality would manifest itself with an observed scaling in the meson plus resonance final state. Assuming one is in a kinematic region that mimics single-quark scattering, in analogy to the inclusive case, the question here is whether the remaining part of the process can be described as hadronization of the struck quark into the detected meson. In such a factorization approach, the cross section decomposes into a part dependent on the photon-quark interaction and an independent part on the quark fragmentation functions $D^h_{q_i}$ (or the probabilities that a quark of flavor q_i hadronizes into a hadron h).

One would assume this factorization to be strictly valid at asymptotic energies only; however, similar to the inclusive case where the nucleon resonances quickly heal to the scaling curve, here the conspiracy of the nucleon resonances remaining in the final state after having produced a fast meson may heal to a fragmentation function. A pictorial example is given in Fig. 43. Data of HERMES and JLab seem to indicate that the factorization assumption works at lower than asymptotic energies, provided one additionally makes a cut in z [Ac98, Mkpc].

For $\pi^{\pm}$ and $K^{\pm}$ electroproduction at large $z = E_h/\nu$, it is essential that the hadron arm accesses angles of about 6°. This will enable us to test meson duality, and, if also quantified, access fragmentation functions and parton distribution functions through a flavor decomposition in hitherto inaccessible regions. The HMS-SHMS combination fully exploits the high-luminosity 12 GeV energy domain here!

4.D.2 SHMS Optical Design

The design of the SHMS was primarily driven by the needs of the coincidence physics program described briefly above. Happily, the resulting constraints resulted in a buildable device with enough flexibility to carry out a broader physics program, including many other experiments described in detail in Chapter 2.

Here we list the constraints on the SHMS design. The first five are hard, imposed by the physics objectives (in parentheses). The next two constraints match the SHMS to the existing HMS:

- Maximum momentum of 11 GeV/c (CT, $N \to N^*$).
- Minimum central angle of 5.5° (pion form factor, fragmentation).
- Maximum angle of 30° ($N \to N^*$).
- Moderate resolutions in momentum ($\simeq 0.1\%$) and angle ($\simeq 1$ mrad).
- Moderate solid angle (2–3 msr in small-angle mode).
- Full acceptance of a 15 cm cryotarget cell at $\Theta_{\rm SHMS} = 30^\circ$ (*i.e.*, $Y_{\rm tar} = \pm\ 3.75$ cm).
- Minimum opening angle of the SHMS-HMS pair to be $5.5^\circ + 10.5^\circ = 16^\circ$.
- Distance to the focal plane less than 19 m.

- Bend angle of the dipole larger than 15° (no line of sight to target!).
- Larger vertical than horizontal angular acceptance.

The final three constraints in the list are imposed to leave sufficient space for detectors and shielding, prevent single-scattering events from reaching the focal plane, and emphasize coverage in the out-of-plane angle ϕ essential for interpreting $(e, e'h)$ measurements. For convenience in commissioning we employ a point-to-point tune. To simplify the design and procurement effort the two first quadrupoles are taken to be HMS Q1-type, which have a horizontally slim design and maximum gradient of 8.4 T/m.

We have arrived at a magnetic optical design for the SHMS that fulfills all of the above constraints and preferences. The design consists of two superconducting quadrupoles and one combined-function magnet consisting of a dipole-quadrupole combination (DQ). The DQ magnet consists of a $\cos(\Theta)$ dipole and a concentric $\cos(2\Theta)$ quadrupole. The third quadrupole element, located inside the dipole, is needed to obtain a larger vertical than horizontal angular acceptance in combination with the moderate-resolution requirement. (Recall that both the HMS and HRS spectrometers employ a Q^3D design.) Combining the dipole and third quadrupole element into a single package also makes the total spectrometer shorter.

We have modeled the combined-function (DQ) magnet in COSY by incorporating the TOSCA field map calculation. COSY is used to provide the forward and reconstruction matrix element sets to fifth order, which are then used in a FORTRAN Monte Carlo simulation of the SHMS spectrometer including finite resolution position measurements in twelve wire chamber planes and multiple scattering in all the windows and detector elements. The size of the beam envelope in the dispersive (x) and nondispersive (y) directions is given in Fig. 85.

Typical resolutions in the reconstructed target quantities (δ, $\phi \equiv dx/dz$, $Y_{\rm tar}$, and $\theta \equiv dy/dz$) are shown in Fig. 86 as a function of $\delta \equiv (p-p_0)/p_0$ for a 2.5 GeV/c electron. This is obviously at the low end of operations for an 11 GeV/c spectrometer, and so nearly worst case, but it demonstrates the flexibility of the SHMS. The solid curves are our best estimate of the real-world resolutions under conditions which are far from ideal. The dashed curves neglect multiple scattering and demonstrate the importance of including this effect. The dot-dash curves further neglect the finite resolution of (very conservatively) 150 μm per wire-chamber plane, thus demonstrating the ultimate resolution when the optics are limited to fifth order. At higher momenta (*e.g.*, 7.5 GeV/c), some experiments requiring good $e^- - \pi$ discrimination will install a long, low-pressure gas Čerenkov which must go before the drift chambers due to space constraints. Despite the additional material before the

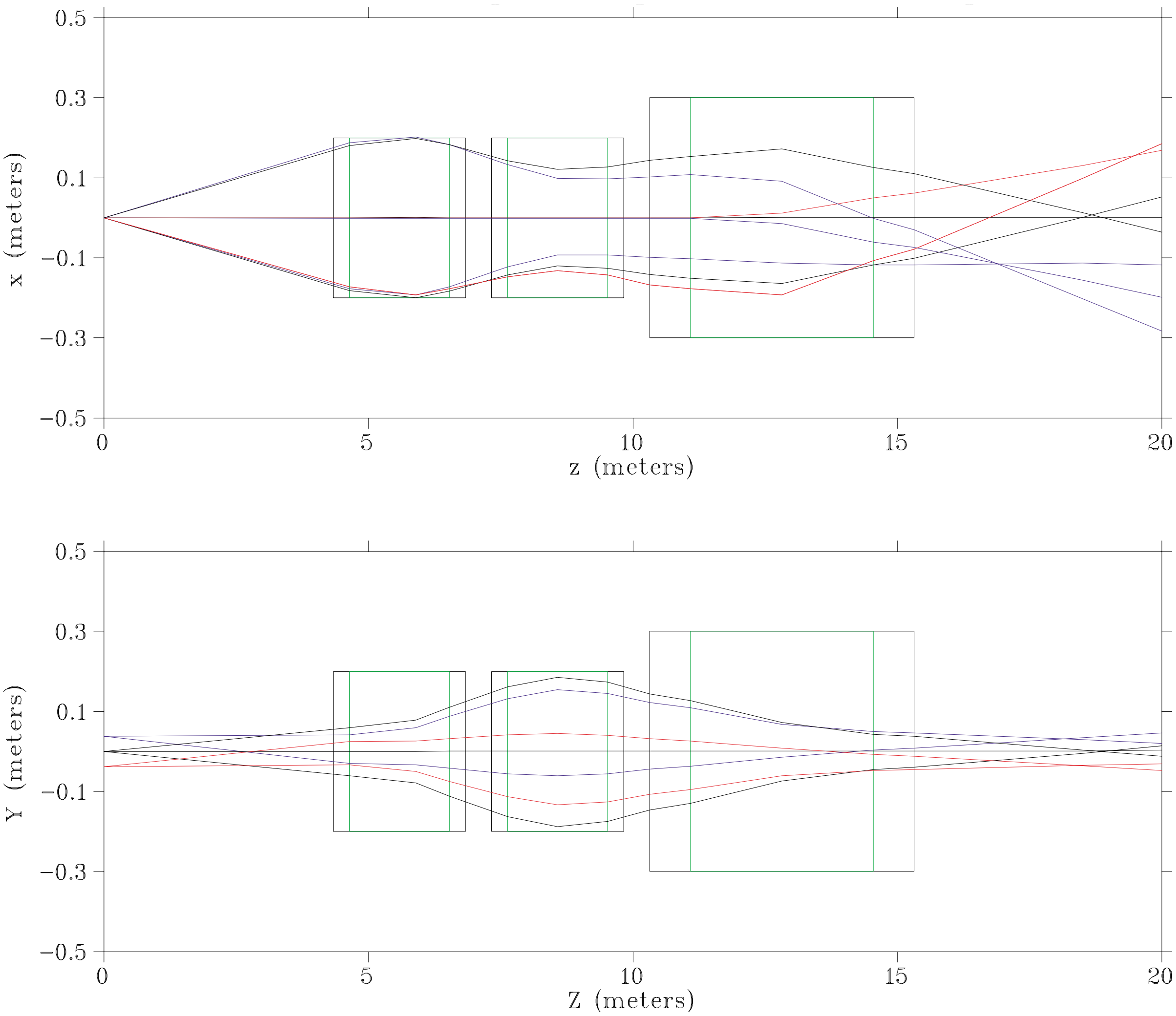

Figure 85: Beam envelopes through the SHMS in the dispersive (upper figure) and nondispersive (lower figure) planes. In the dispersive direction, rays were generated for $\delta = 0, \pm 10\%$. In the transverse direction, rays were generated for $Y_{\text{tar}} = 0, \pm\ 3.75$ cm.

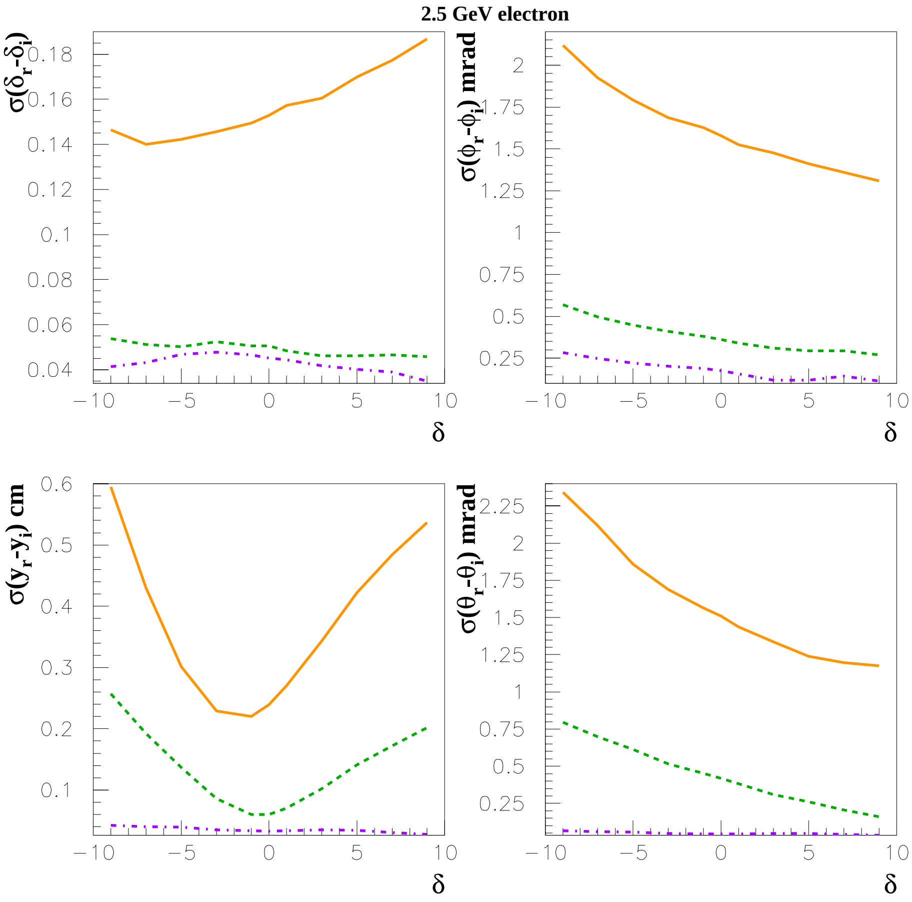

Figure 86: Typical resolutions in the reconstructed target quantities (δ, ϕ, $\mathrm{Y_{tar}}$, and θ) are shown as a function of $\delta \equiv (p - p_0)/p_0$ for a 2.5 GeV/c electron. The solid curves are our best estimate of the real-world resolutions. See text for a detailed explanation of the other curves.

Table 29: The basic parameters of the SHMS; resolutions are quoted for 2.5 GeV/c electrons.

Max. central momentum	11 GeV/c
Min. scattering angle	5.5°
Momentum resolution	0.15%–0.2%
Xptar,yptar resolution	1–2 mrad, 1–2 mrad
Ytar resolution	0.2–0.6 cm
Vertical acceptance	±42 mrad
Horizontal acceptance	±14 mrad
Solid angle	2 msr (small angle mode)
Momentum acceptance	20%
Opening angle with HMS	16°
Configuration	QQ(DQ)
Bend angle	18.4°
Focusing mode	Double
Max. rigidity	400 kG-m
Dispersion	1.764 cm/%
D/M	1.20 cm/%
Mx	1.47
My	1.02
Focal plane angle	4.88°
Focal plane dimension	40 cm (X) × 20 cm (Y)
Optical length	18.5 m

drift chambers, the reduction in multiple scattering means that the resolutions are comparable to or better than those in Fig. 86. The basic parameters of the SHMS of primary concern to experimentalists are summarized in Table 29.

4.D.3 Magnet Engineering

The SHMS requires a combined-function superconducting magnet that can simultaneously produce 4.0 T dipole fields and a 3.0 T/m quadrupole field inside a warm bore of 30 cm. A magnetic design using TOSCA 3D has been performed to establish the basic magnetic requirements, to provide three-dimensional field maps for optics analysis, and to produce basic engineering information about the magnets. A four-sector $\cos(\theta)$ current distribution and a two-sector $\cos(2\theta)$ quad design with warm bore and warm iron have been analyzed. A cutaway view of the combined-function dipole DQ is seen in Fig. 87. The basic parameters of the DQ are given in Table 30.

The yoke is modeled as truly nonlinear iron with the nominal properties of 1006 steel. The present design yoke is 4.2 m long with an outer elliptical shape with semi-major and minor radii of 120 cm by 100 cm and a cylindrical bore with a 60 cm inside radius. The yoke has been optimized to achieve a 5.5° scattering angle at fields capable of 11 GeV/c. The detailed shape of the yoke is less important in a cosine-type magnet as the design requires an unsaturated yoke for good internal fields. The high-field region is either on top or on the bottom depending on the relative sign of the dipole and quadrupole coils; therefore an elliptical yoke represents an ideal solution.

The DQ combined-function magnet produces peak fields in the warm bore of 4.3 T and peak fields in the windings of 5.4 T. These fields are comparable to those achieved in large-bore magnets produced 20 years ago for MHD research, particle spectroscopy, and coal sulphur separation. However, the stored energy of the DQ is somewhat less (even though the field volumes are comparable) due to the superposed quadrupole field.

The combined fields also produce a very asymmetric field and force distribution. The fields add on the bottom of the magnet and subtract on the top, so the fields across the bore range from $\simeq 0$ to 5 T. Similarly the fields in the windings are highest where the fields add, giving 5.4 T winding fields and nearly -2 T where they subtract. There is thus a net force between the yoke and coil that must be dealt with due to the asymmetry. The peak linear force densities are 40,000 pounds per inch for the dipole winding and 11,000 pounds per inch for the dipole winding. These forces add on one side and subtract on the other, yielding peak pressures that range from 4680 psi to 2100 psi. Simple pressure-vessel computations in which we limit the material stress to 20KSI yield a 6.0 in thickness for the cold mass force collar. Due to the large radial thickness (3.5 in) of the windings and cryostat (11.8 in) the required 6 in pressure shell is easily accommodated without stressing the coil cold mass. Obviously in a real cold mass the stress will be distributed and the resulting stresses lowered. The large size of the cryostat will allow separate fluid pressure vessels in accordance with the ASME code. This will greatly simplify the final design and result in a much more conservative magnet. A fully clamped winding is planned for the final construction.

DC power for the SHMS magnets is presently designed around low-voltage, high-current commercial power supplies. A DC current of 5000 A at 10 V would be a reasonable choice for SHMS due to the relatively low inductance (0.72 H) and provide easily for a charge time under 30 minutes. The large cold mass and moderate current density ensure that sufficient material is available to absorb a large fraction of the stored energy at a low final temperature during a quench discharge, resulting in a safer overall magnet.

The main characteristics of the superconducting quadrupoles are listed in Table 31. These magnets are identical to the Q1 quadrupole in use as part of the HMS spectrometer in Hall C.

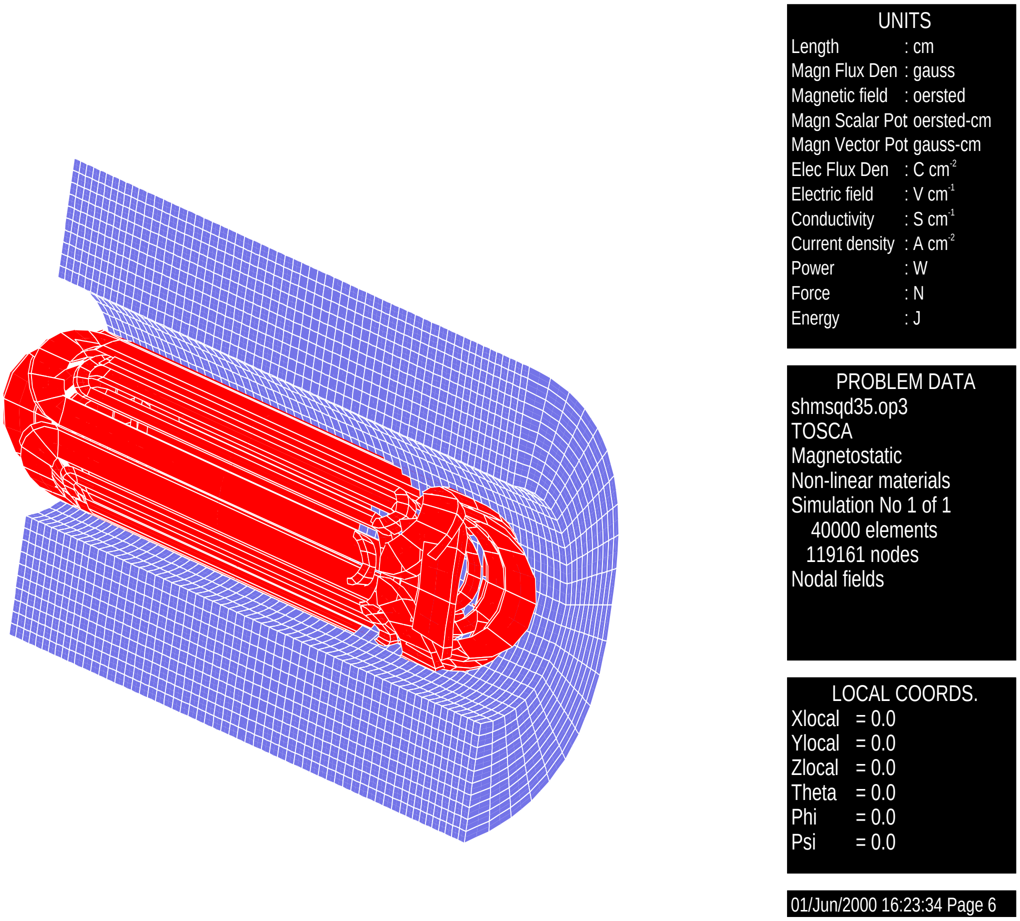

UNITS

Length	: cm
Magn Flux Den	: gauss
Magnetic field	: oersted
Magn Scalar Pot	oersted-cm
Magn Vector Pot	gauss-cm
Elec Flux Den	: C cm^{-2}
Electric field	: V cm^{-1}
Conductivity	: S cm^{-1}
Current density	: A cm^{-2}
Power	: W
Force	: N
Energy	: J

PROBLEM DATA
shmsqd35.op3
TOSCA
Magnetostatic
Non-linear materials
Simulation No 1 of 1
40000 elements
119161 nodes
Nodal fields

LOCAL COORDS.
Xlocal = 0.0
Ylocal = 0.0
Zlocal = 0.0
Theta = 0.0
Phi = 0.0
Psi = 0.0

01/Jun/2000 16:23:34 Page 6

Figure 87: Cutaway view of the combined-function SHMS dipole.

Table 30: Basic parameters of the combined-function dipole for the SHMS.

Overall length	5 m
Warm bore radius	30 cm
Stored energy	11 MJ
Dipole:	
Configuration	4-sector $\cos(\theta)$ superconducting
$\int B \cdot dl$	11.9 T-m
Effective Length	3.45 m
$B(0,0,0)$	3.446 T
Field uniformity dB/B	1×10^{-3} inside 30 cm
Current density	11,000 A/cm^2
Peak force on coil	40,000 lbs/in
Peak pressure	3390 psi
Quadrupole:	
configuration	2-sector $\cos(2\theta)$ superconducting
Gradient (G) (0,25,0)	3.337 T/m
$\int G \cdot dl$	10.99 (T/m)m
Effective length	3.29 m
Gradient uniformity dG/G	1×10^{-3} at 30 cm
Current density	4000 A/cm^2
Peak force on coil	11,000 lbs/in
Peak pressure	1290 psi

Table 31: Main characteristics of the SHMS superconducting quadrupoles.

Effective length	1.89 m
Maximum gradient	8.4 T/m
Warm bore diameter	40 cm
Current at max. grad.	1200 A
Higher-order multipoles	$< 1\%$ at 1000 A
Overall length	2.5 m

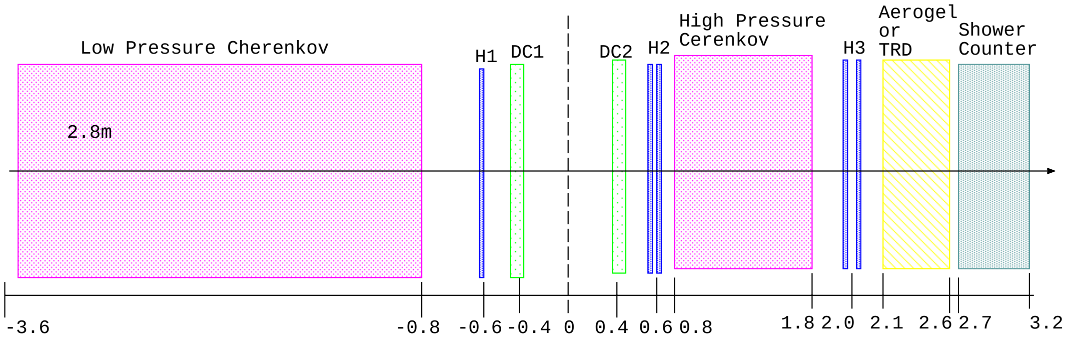

Figure 88: The detector stack of the SHMS. Dimensions along the bottom axis are in meters.

4.D.4 Detectors

The key characteristic of the SHMS detector stack will be flexibility. While the wire chambers, scintillator hodoscopes, and lead glass calorimeter would be more or less permanent fixtures, other detectors may be swapped in and out as experiments require (in some cases remotely). Figure 88 shows a typical SHMS detector stack. Detectors will be designed so as to accept 100% of the beam envelope in the detector stack for a ±10% momentum bite and extended target. The SHMS acceptance will therefore be defined by a limited number of upstream apertures (all easy to measure and survey) facilitating accurate cross-section measurements. The modest size of the SHMS beam envelope at several key points in the detector stack is shown in Fig. 89.

The design of a flexible 11 GeV/c detector stack is fundamentally different than that of the original HMS-SOS detector stacks. First of all, above roughly 3 GeV/c, it becomes very difficult to distinguish hadrons by time of flight over a several-meter baseline even with excellent (*e.g.*, 100 ps) time resolution. This means that one is increasingly reliant upon other technologies such as threshold Čerenkovs. Second, when one designs an experiment it becomes clear that, if threshold Čerenkovs are to be used, then greater flexibility is needed in adjusting the beta threshold. Finally, a gas Čerenkov for electron-pion discrimination at 7.5 GeV/c or above needs to be 2–3 m long to have adequate photoelectron number, so space must be reserved for this, or other technologies must be pursued.

The SHMS detector elements and the collaborating institutions that have expressed an interest in participating in their design, construction, installation, and testing are listed in Table 32.

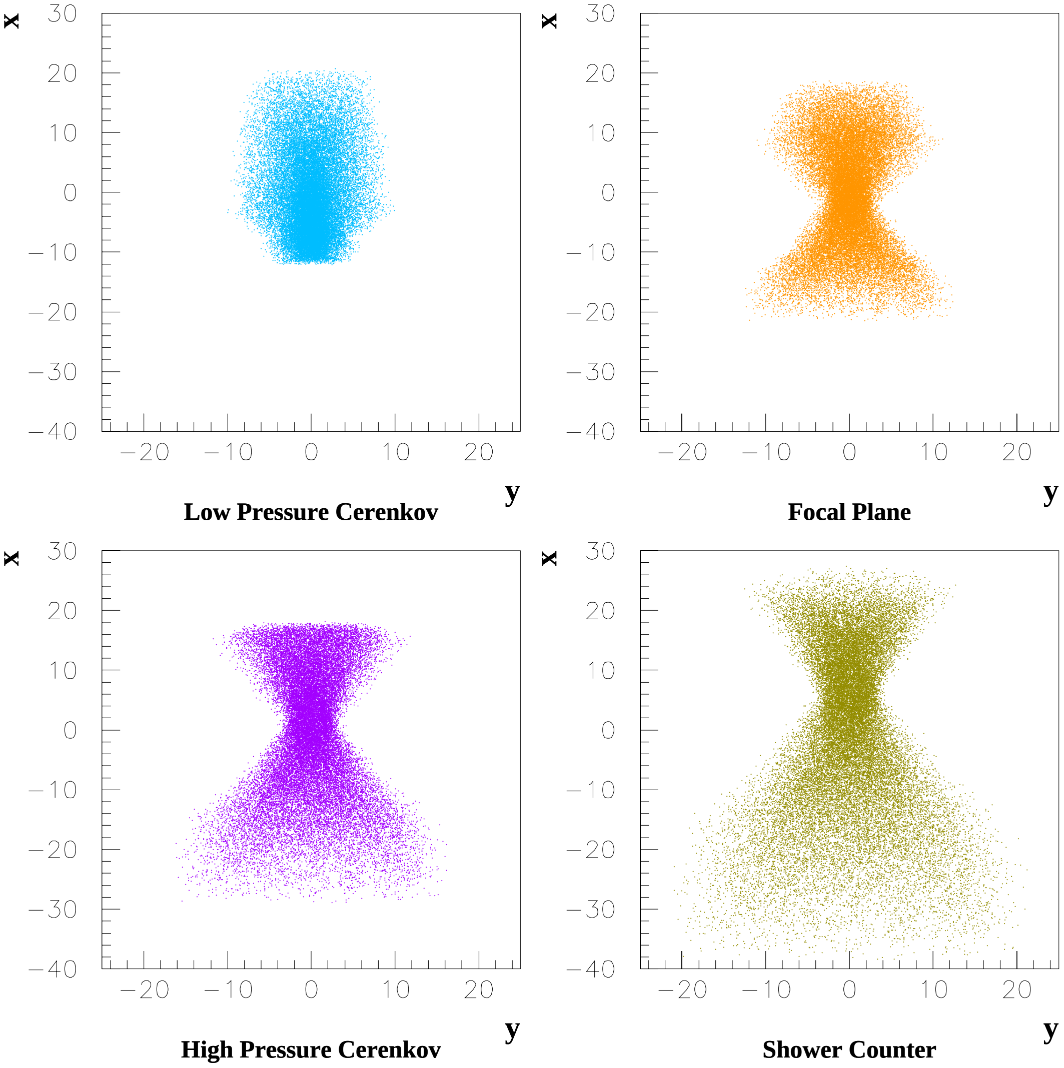

Figure 89: Beam envelope in the detector stack at 2.5 GeV/c for the full momentum bite and full $Y_{\rm tar}$ acceptance at the middle of the low-pressure gas Čerenkov ($z = -2.3$ m), the focal plane ($z = 0$ m), the high-pressure gas Čerenkov ($z = +1.3$ m), and the shower counter ($z = +2.95$ m).

Table 32: The following institutions have expressed interest in writing specifications for the SHMS detectors. These study groups may evolve into design, construction, installation, and commissioning teams. Additional user support or new suggestions for the detector stack are encouraged.

Detector	Institution
Wire chambers	Jefferson Lab
Scint. hodoscope	Jefferson Lab
Calorimeter	Yerevan
Low-pressure Čerenkov	Yerevan
High-pressure Čerenkov	U. Regina
Aerogel	Hampton U.
TRD	Mississippi State U.

Tracking and basic trigger

Particle tracking will be done with a pair of drift chambers, each with six planes of position measurements. The resolution goal would be 100 μm (rms) as in the present HMS wire chambers. The scintillator telescope trigger will be similar to that now used in the HMS, namely a threefold coincidence of four separated planes of scintillator hodoscopes (S1X, S1Y, S2X, and S2Y). These planes will contain 8-cm-wide, overlapping scintillator elements of 1 cm thickness. Although in principle capable of yielding 50 ps (rms) focal plane timing resolution, we have found that such a system is realistically limited to 100 ps (rms) focal plane timing resolution without heroic measurement to correct for TDC drifts. As demonstrated in the present HMS-SOS setup, this will still provide more than 10-sigma separation of real and random coincidence peaks.

Particle identification

Electron-hadron discrimination A lead glass shower counter will provide a tag for electrons. This would normally be augmented by a gas Čerenkov when electron-pion discrimination is needed. Below roughly 6 GeV/c, the shorter (so-called high-pressure) gas Čerenkov downstream of the wire chambers would be used. At higher momenta, a gas Čerenkov would have to operate well below atmospheric pressure. This means that the device would require an active length of 2–3 m (several times longer than the existing HMS gas Čerenkov) to achieve a reasonable photoelectron yield. Due to limited space in the detector hut, this low-pressure (LP) gas Čerenkov must be located upstream of the drift chambers. Simulations demonstrate that the resolutions at 7.5 GeV/c using the LP gas Čerenkov (filled with 1/3 atm C4F10) are comparable to or better than those obtained at 2.5 GeV/c with the LP gas Čerenkov under vacuum as in Fig. 86.

Distinguishing species of hadrons Experiments which detect pions will make use of a high-pressure (HP) gas Čerenkov employing C4F10. This gas has been used successfully for years in the HMS gas Čerenkov for electron and pion detection at pressures of 0.5–1 atm. In reality the HP gas Čerenkov device would have variable pressure with a nominal operating range of 0.5–2 atm, which would typically be adjusted remotely except when the windows needed to be changed.

Experiments where kaons are detected will generally benefit from an aerogel detector. Covering a large momentum range will require aerogels with indices ranging from 1.01-1.06. We have reserved sufficient room such that two or three aerogel counters could be used simultaneously in the detector stack.

Other detector technologies Transition radiation occurs when a charged particle crossing a dielectric boundary is ultrarelativistic [Gi46]. The number of transition radiation photons is increased by increasing the number of boundary crossings. Due to interference effects created by the periodic arrangements of the boundaries, only charged particles with a Lorentz factor $\gamma >$ 1000 produce transition radiation [Ar75]. At JLab Upgrade energies this means that a transition radiation detector (TRD) could be used to distinguish between electrons and more massive particles. One nice feature of transition radiation is that the energy of the radiation increases with γ and is not proportional to its velocity, β. This makes TRD's increasingly useful at high energies (in contrast to time-of-flight techniques or gas Čerenkov detectors, whose length must increase as the square of the momentum for an equivalent number of photoelectrons). The transition radiation photons are emitted in the X-ray range; hence the radiator needs to be made of low-Z material. Typically, a TRD will consist of multiple modules, where a module contains a radiator followed by a proportional chamber filled with xenon to detect the photons.

A TRD is well suited for the SHMS – a 50-cm-long detector should produce a pion rejection factor of 200–300 at 90% electron efficiency. The C TRD would utilize cluster-counting particle identification. This particle ID method has an advantage over a total-charge method since the distribution of the number of ionization clusters is better behaved than the total ionization energy.

We are also considering the use of a ring-imaging Čerenkov counter (RICH) combining both gas and aerogel radiators as employed by HERMES. While interesting in that it could provide definite signatures for multiple particle species through measurement of the Čerenkov angle (unlike a threshold Čerenkov), much more study is needed. Such a device would be most useful if fast

PID-trigger information could be obtained (*e.g.*, kaons only) and the RICH counter covered a very broad range of momentum.

4.E Hall D

4.E.1 Introduction

The purpose of the Hall D experiment is to search for so-called gluonic mesons with masses up to 2.5 GeV/c^2. The identification of such states requires knowledge of their production mechanism, the identification of their quantum numbers, J^{PC}, and measuring their decay modes. These in turn require a partial wave analysis of exclusive final states. The decay products of produced mesons must be identified and measured with good resolution and with full acceptance in decay angles. In many cases, the decays of mesons involve a chain of particle decays. The Hall D detector must therefore be hermetic with an effective 4π coverage with the capability of measuring directions and energies of neutral particles (γ, π^0, η) and momenta of charged particles with good resolution. Particle identification is also required.

The partial wave analysis technique also depends on high statistics and, in the case of incident photons, also requires linear polarization. As discussed in Section 2A, the latter is needed to identify the production mechanism. The linear polarization is achieved by the coherent bremsstrahlung technique. The degree of linear polarization and flux of photons in the coherent peak fall dramatically as the photon energy approaches the endpoint energy. On the other hand, it is desirable to have photon energies high enough to produce the required masses with sufficient cross section and with sufficient forward-boost for good acceptance. For a fixed incident momentum and a fixed resonance mass, it is also desirable to have a fairly constant $\mid t \mid_{\mathrm{min}}$ over the natural width of the resonance. This also requires sufficiently high incident photon energy. An operating photon energy between 8.0 and 9.0 GeV produced from a 12.0 GeV electron beam represents an optimization of beam flux, cross section, and degree of polarization. The Hall D detector is optimized for this energy range. Extensive Monte Carlo simulation has been performed to optimize the detector's ability to reconstruct exclusive final states. Acceptances are nearly 90% for many complicated channels, and the detector resolutions have been balanced to facilitate excellent reconstruction of the events, and allow kinematic fitting to reduce background contamination of events, thereby facilitating the partial wave analysis.

4.E.2 The Photon Beam and Polarization

Linearly polarized photons can be produced in the desired energy range by using the technique of coherent bremsstrahlung. A horizontal plan view of the photon beam line is shown in Fig. 90 with the major components labeled. The electron beam enters the figure from below ground at the left

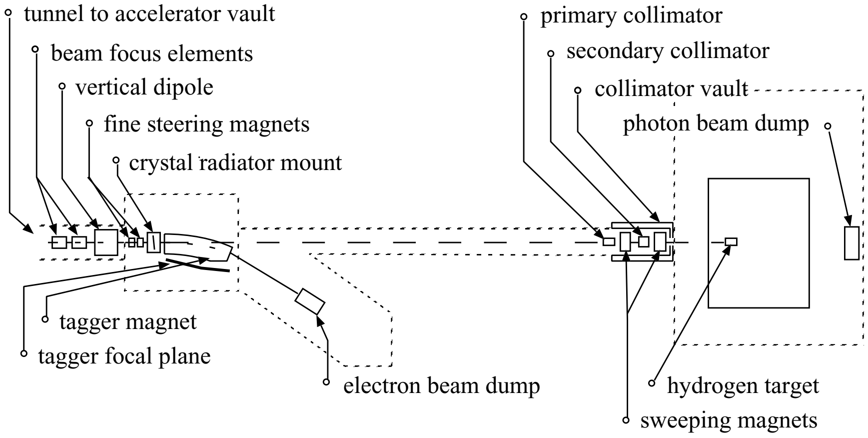

Figure 90: A schematic plan view of Hall D photon beam line, shown in the horizontal plane as viewed from above. The objects in this figure are not drawn to scale.

and is bent into the horizontal plane to enter the tagger building. There it passes through two small dipoles to impinge upon the bremsstrahlung radiator.

The photon tagger and beam collimation

After its exit from the radiator, the electron beam passes into the tagger magnet where the primary beam is bent in the direction of the electron beam dump. The radiator crystal is thin enough that most of the electrons lose less energy in traversing the radiator than the intrinsic energy spread of the incident beam. Those electrons which lose a significant fraction of their initial energy inside the radiator do so by emitting a single bremsstrahlung photon. These degraded electrons are bent out of the primary beam inside the tagger magnet and exit the vacuum through a thin window, passing through air for a short distance to strike the focal plane of the spectrometer. The primary electron beam is contained inside vacuum all the way to the dump.

The Hall D tagging system will consist of a dipole magnet spectrometer with a set of plastic scintillation counters in the focal plane to tag photon energies between 50% and 95% of the incident electron energy. The tagging spectrometer magnet envisioned for Hall D is modeled closely on the existing tagger magnet in Hall B. Although the Hall D tagger will operate at a much higher energy, the combination of smaller deflection angle and smaller dynamic range (50% to 95% of the incident energy instead of 20% to 95%) results in a device which is comparable to the Hall B tagger in most of its dimensions, allowing the use of existing solutions to many engineering problems.

Such a tagging system will allow us to measure the photon energy to an accuracy of 0.1%, a limit which is set by detector constraints on reconstructing missing masses. The collaboration is also investigating a sliding tagger counter. This would facilitate diagnostics and calibration including the measurement of the crystal angle. It could also reduce the electronics costs associated with the tagger readout.

The photons that are produced in the radiator pass through a small hole bored in the return yoke of the tagger magnet to exit the vacuum through a thin window in the forward direction. They then pass into a transfer pipe, which may either be evacuated or filled with helium to reduce photon beam degradation due to interactions, and travel to the experimental hall. Just before entering the hall the photon beam passes through a system of collimators and sweeping magnets. In the figure they are shown in a separate enclosure for shielding purposes. The primary collimator defines the part of the photon beam that is allowed to reach the target. Debris from interactions along the inside surface of the collimator bore forms a halo around the photon beam that exits the collimator. The charged component of the halo is deflected away from the beam axis by a dipole "sweeping" magnet just downstream of the collimator. A secondary collimator follows the sweeping magnet to stop the deflected shower particles and block the halo of secondary photons generated by the first collimator. The secondary collimator is of a larger diameter than the primary and so sees a reduced rate of secondary interactions on the inner surface of the hole. What new showers are generated there are cleaned up by a second sweeping magnet. The beam then passes through a final collimating aperture into the experimental hall. This triple-collimation system was copied from the setup developed at SLAC [Ka75].

The collimated photon beam, now only a few millimeters in diameter, is delivered to the experimental target. After passing through of order 3% radiation lengths of target, the photon beam passes through the detector and into the photon beam dump at the back of the hall. Based upon a design upper limit of 60 kW (5 μA at 12 GeV) being delivered to the electron beam dump, the total power in the photon beam is at most 1.5 W in the experimental hall and at most 15 W in the collimator enclosure. The safety issues of such a beam have been reviewed by Jefferson Lab's RadCon group. As an additional safety constraint, permanent magnets are being installed in the photon beam downstream from the tagger building to prevent an accidental loss of the electron beam into Hall D. These magnets have been obtained as surplus from FermiLab.

The effects of collimation and the thickness of the radiator are demonstrated in the calculated spectra shown in Figs. 91 and 92. First, note that the collimation angles are very small, which requires a long flight path of 80 m in order that the collimator can be larger than the intrinsic beam spot size; otherwise the collimator is cutting in transverse coordinate instead of in angle.

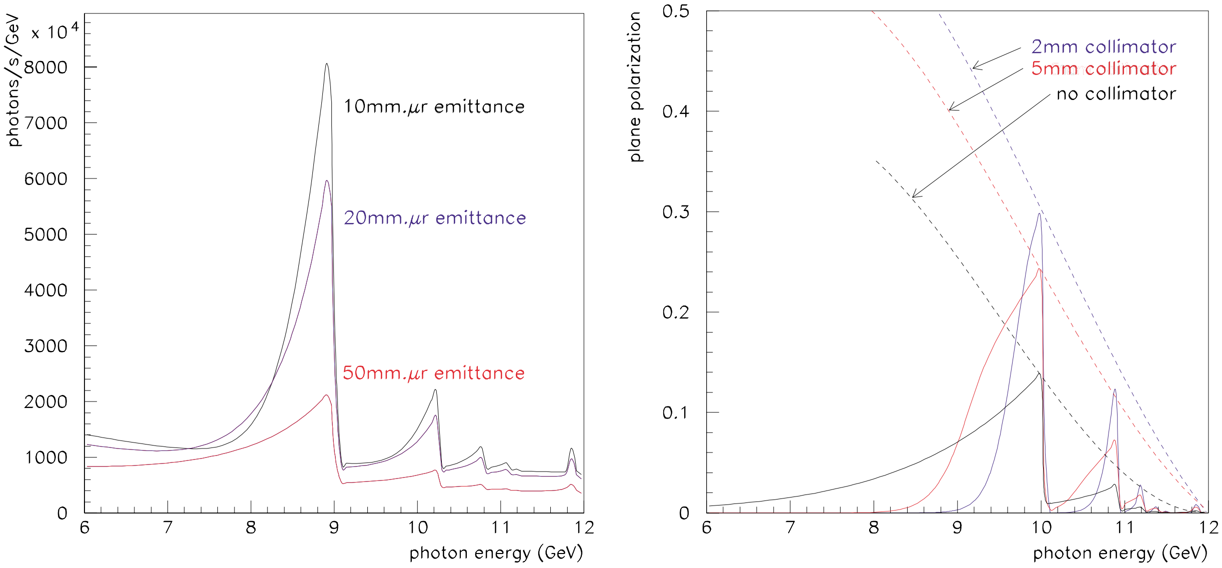

Figure 91: Left: The effect of collimation on the coherent bremsstrahlung spectrum (various collimation diameters are given). Right: Plane polarization of the coherent bremsstrahlung.

This distance is, in fact, a sensitive function of the electron beam emittance from the machine, and must be increased in inverse proportion to the beam emittance if the effectiveness of collimation is to be maintained.

Polarization via coherent bremsstrahlung

The net polarization of the beam under different collimation conditions is shown in Fig. 91. The dashed curves show how the maximum polarization in the peak varies as the peak energy is changed by rotating the crystal. The polarization in all cases is zero at the endpoint. Without collimation it rises as $(k-E)^2$, one power coming from the intensity of the coherent peak relative to the incoherent component going to zero linearly at the endpoint, and the other from the intrinsic polarization of the coherent photons also behaving like $(k-E)$ near the endpoint. Collimation allows one to essentially isolate the coherent component, so that the polarization available to the experiment rises from zero at the endpoint in a linear fashion. The dashed curves in Fig. 91 demonstrate this point.

In order to obtain the full polarization enhancement from collimation, it is necessary to have a distance between the radiator and collimator of about 80 m. This distance scale is set by the requirement that the collimator aperture must be large compared to the size the electron beam

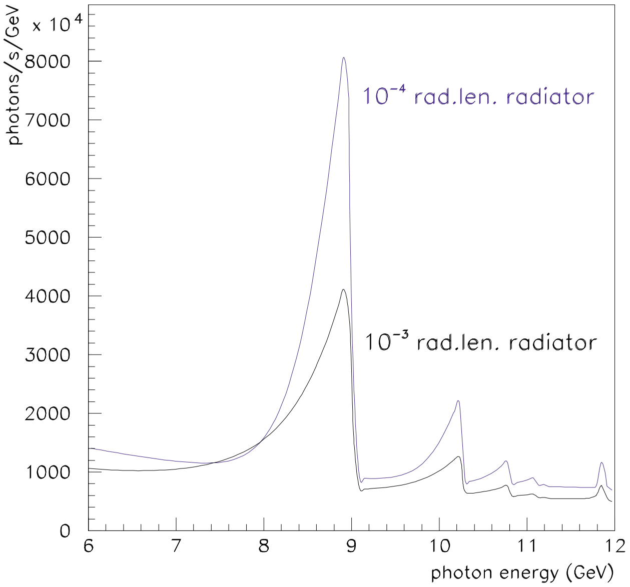

Figure 92: The collimated coherent bremsstrahlung spectrum for two crystal radiator thicknesses.

spot would be on the collimator, but small compared to the actual photon spot size. Fig. 91 shows the maximum polarization as a function of radiator-collimator distance for a coherent peak at 9 GeV. The collimator diameter is adjusted in this calculation to keep the collimation half-angle at $0.5\, m_e/E$. At zero distance the collimator has no effect except to attenuate the beam, and so the uncollimated polarization from coherent bremsstrahlung is obtained. At 100 m separation distance the polarization enhancement has saturated. The design for Hall D calls for a radiator-collimator distance of 80 m.

The thicknesses of the crystal radiator is limited by multiple scattering of the electron beam as it passes through the radiator, which causes the divergence of the incident beam to grow, thereby enlarging the photon beam spot on the collimator face and degrading the degree to which collimation discriminates against the incoherent component in favor of the coherent part. It is bounded from below by the fact that the crystal must be of some minimum thickness in order to achieve the full coherent gain. For a 12 GeV beam energy and a 6 GeV coherent photon the coherence length is 18 nm. The coherence length does not impose a practical limit on how thin the radiator should be. The effects of multiple scattering are best presented by showing the calculated spectra for various radiator thicknesses. In Fig. 92 is shown the photon spectrum for a 20 μm (10^{-4}) and a 100 μm (10^{-3}) radiator to demonstrate the effect. The 100 μm spectrum is scaled down by a factor of 5 to facilitate the comparison, but it is clear that for a significant coherent gain, the crystal thickness must be near 20 μm.

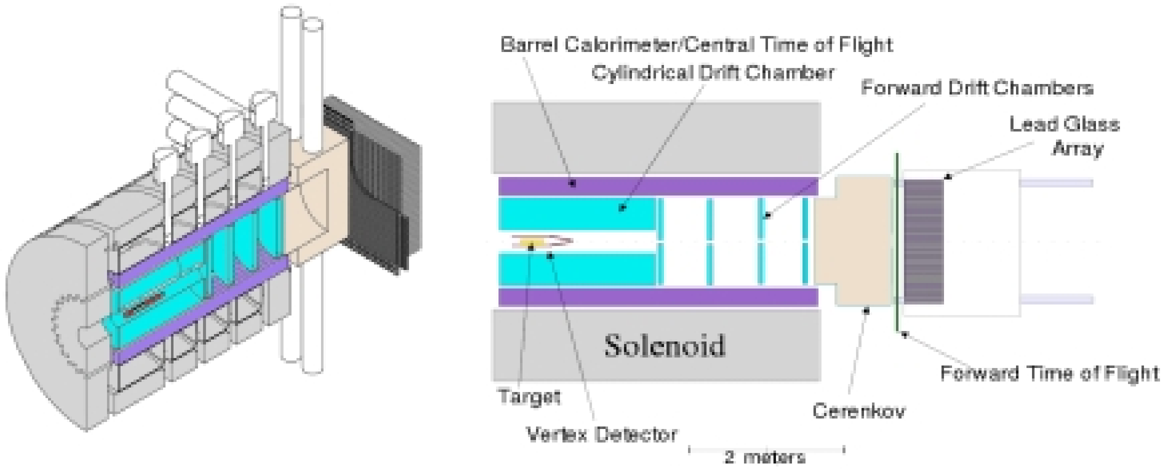

Figure 93: A 3D cut-away view of the Hall D detector (left) and schematic diagram of its major subsystems (right).

A committee chaired by David Cassel (Cornell) and consisting of Frank Close (Rutherford Laboratory), John Domingo (Jefferson Lab), William Dunwoodie (SLAC), Donald Geesaman (Argonne), David Hitlin (Caltech), Martin Olsson (Wisconsin), and Glenn Young (Oak Ridge) reviewed the project plans in December 1999 [Ca00]. The Cassel committee identified the availability of thin diamond crystals as one of the critical R&D areas for Hall D. Should it prove impossible to achieve the proposed level of linear polarization, the committee believed, it will be necessary for the collaboration to make the appropriate modifications to the proposed physics program. In response to this concern, *Hall D collaborators have obtained diamond wafers that are sufficiently thin for Hall D purposes; these wafers will be tested at Mainz in 2001.*

4.E.3 The Hall D Detector

The Hall D detector has been optimized to provide nearly hermetic acceptance for both charged particles and photons. In addition, a combination of particle identification systems will allow very good K-π separation. Optimization will allow the detector to fully reconstruct exclusive many-body final states. In conjunction with high statistics, this will allow us to do excellent partial wave analyses of many final states. Figure 93 is a schematic representation of the proposed detector; the individual subsystems are discussed in more detail below. A more detailed description can be found in the Hall D Design Report [HD99].

The superconducting solenoid

Momentum analysis of charged particles will be achieved using a superconducting solenoid and tracking chambers. The superconducting solenoid already exists. It was built for the LASS detector at SLAC and later moved to LANL where it was used for the MEGA experiment. The magnet is described in a technical note [As87]. The solenoid magnet provides a 22.4 kG magnetic field parallel to the beam direction. The inside diameter of the magnet is 185 cm and its overall length is 465 cm. The fiducial region within the bore is 320 cm in length and 75 cm in radius. Within this region the field homogeneity is better than ±3.1%. Along the beam axis the homogeneity improves to ±0.9%.

The Cassel committee [Ca00] identified that the R&D area of greatest concern was to ensure that the magnet is still functional, particularly the fourth coil, which has not been used for at least 15 years. *In March 2000, an assessment team went to Los Alamos to check the magnet. The team found that all coils appeared to be in working order and estimated that the magnet had at least another 25 years of life* [ML00].

Moving and refurbishing costs of the magnet are estimated at about $1M, while replacement costs are estimated to be $12M. Negotiations between Jefferson Lab and LANL are underway to have the magnet transfered to JLab.

Particle tracking and particle identification

The system of tracking chambers in the Hall D detector must cover as close to an effective 4π solid angle as possible over a wide range of particle momenta and have sufficient momentum resolution to be able to identify missing particles. In the solenoid region, the chambers are inside the barrel calorimeter. The location of the target very near the entrance to the solenoid, coupled with the energies involved which force the reaction products into forward angles, result in an effective 4π coverage, even though the geometrical coverage around the target is less than that. The chambers also must extend as close to the beam line as possible. Near the target, this will provide very accurate vertex information which will be important in identifying decaying particles (*e.g.*, K_S, Λ, Σ, ...). In the forward region, this is needed to reconstruct very fast small-angle particles (down to nearly 0°). Finally, it is necessary that near the target, the tracking be able to separate π's and K's up to momenta of about 0.5 GeV/c – a regime where dE/dx measurements will work. To satisfy the tracking requirements a starting point based on the LASS detector [As87] was taken. A series of three different tracking elements is taken, with each element optimized for a particular region in the detector as shown in Fig. 93.

The vertex system (VTX) surrounds the target, and detects outgoing particles at angles from 1° to 90° for the full length of the target. The VTX has several purposes. First it will be used to provide accurate tracking information very close to the target. These track elements must be sufficiently well defined to be connected to the other tracking chambers. Second, the VTX must provide a fast signal which can be used in the level 1 trigger of the experiment, in particular a start signal for the event. Finally, it is a critical element of all time-of-flight systems. The vertex detector will consist of two detector packages. One will be optimized for timing purposes, and the other will provide fast tracking information. (See Fig. 94.)

The timing detector will consist of a cylindrical array of ten scintillator paddles. This will allow us to cover scattering angles between 1° and 90° for the full length of the target. The scintillators have a thickness of 5 mm, which reduces to 2 mm in the forward direction. This will provide a good light output and therefore a good timing signal. Using Bicron BC-404 scintillating material in combination with fast photomultipliers, we expect to achieve better than 120 ps overall timing resolution. The collaboration is investigating the trade-off between material thickness and time resolution.

The fast tracking detector will consist of three super-layers of fibers, each containing two layers to minimize dead space. The central layer will be arranged around the target and parallel to the beam. It will determine the azimuthal angle. The z position is deduced from the two outer layers. They will be wound in two opposite helices around the first layer. In order to function in the high magnetic field, we are studying the possibility of using visible light photon counters (VLPC) developed by Rockwell in collaboration with Fermilab [Pe89]. The spectral sensitivity of the VLPC's requires us to use SCSF-3HF multi-clad scintillating fibers from Kuraray which are also the least susceptible to radiation damage. One of the main advantages of using VLPC's is their large quantum efficiency of approximately 80% [Wa97] for the light produced by the fibers together with a very high rate capability of 10^8 single photoelectrons per second. The design of this detector system will closely follow the prototype system developed [Ba96] by the D0 collaboration at FNAL. The expected position resolution will be at least 1 mm.

The cylindrical drift chamber (CDC) surrounds the VTX and provides very good $r - \phi$ information and moderate to good z information. This chamber also provides dE/dx information for tracks which do not reach any time-of-flight detectors. The CDC is used to accurately track particles between polar angles of 20° back to 170°. To minimize material in the forward end plate of the chamber, one would like a self-supporting chamber. This leads to a straw chamber, where the straw walls support much of the wire tension. The disadvantage of this design is the difficulty

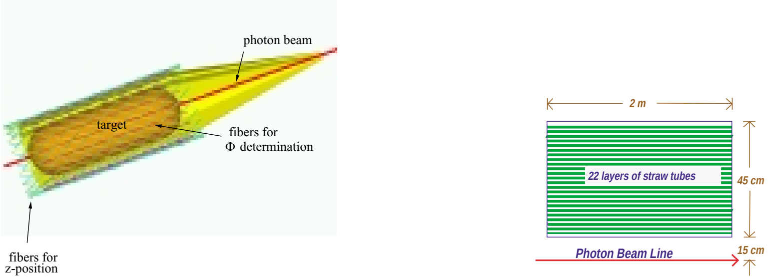

Figure 94: The start counter/vertex chamber (left) and the straw tube chamber (right).

of making dE/dx measurements in a circular straw tube. The planned design has the chamber filled with 5200 1-cm-diameter straw tubes arranged in 22 layers. The tubes are assumed to have an $r - \phi$ resolution of $200\,\mu$m, while resolution along the wire length will be obtained by placing about half of the layers at a 6° stereo angle. A typical hydrocarbon drift gas will have v_d on the order of $5\,$cm$/\mu$s, meaning maximum drift times will be on order of 100 ns.

The forward drift chambers (FDC) are disk-shaped drift chambers. The basic drift package is a plane of wires with $150\,\mu$m spatial resolution between two planes of cathode strips. The strips are arranged in a u and v geometry with respect to the wires, allowing the reconstruction of a 3-D space point from each hit. The chambers are arranged in packages of six to provide a small track segment to facilitate later linking of tracks. Given the number of spiraling tracks, it is critical that these chamber packages not only provide good spatial resolution, but also reasonable direction information. The basic chamber element is a disk of outer radius 60.0 cm, the wires strung as chords across the chamber. With a 1.0 cm wire spacing, each chamber will contain 119 wires. In addition, there will be an equal number of cathode strips on each face. These are arranged in a u–v pattern with respect to the wires. The wires that cross through the beam line will be deadened out to a radius of about 3.5 cm by placing material such as styrofoam in the chambers.

Monte Carlo studies show that the combined tracking system provides very good momentum resolution for the event topologies in Hall D. The system is sufficient to identify undetected particles by missing-mass cuts. In particular, a missing neutron can be separated from a completely missing recoil Δ for most kinematic regions. Detailed information on resolutions can be found in Ref. [HD99].

Electromagnetic calorimetry (EM) in the barrel region of the Hall D detector covers the approximate polar angular range $14^\circ < \theta < 138^\circ$ (indicated as barrel calorimeter in Fig. 95). The goal of the calorimetry is to detect and measure photons from the decays of π°'s and η's, which, in turn, can come from the decays of produced mesons, or from an excited baryon (N^* or Δ). The positions and energies of the photons must be of sufficient accuracy to allow for a complete kinematic reconstruction of the event. Finally, for events with only charged particles, it is essential to be able to veto on neutral missing energy. Hence, nearly hermetic coverage is critical. For selected triggers, neutral energy requirements (or vetoes) are relatively easy to implement.

The barrel calorimeter, shown schematically in Fig. 95, will utilize scintillating fibers embedded in a lead (or possibly tungsten) matrix to make a relatively high-resolution sampling calorimeter. Advantages include speed, cost, ease of readout, and the fact that it is based on a proven technology. This technology has been used in calorimeter design and operation for more than a decade. The ratio of the active scintillator to the passive high-Z material, as well as the diameter of the fibers, can be tuned to enhance resolution, to determine the radiation length, and to achieve uniformity in the electromagnetic to hadronic response (the e/h ratio). For high-resolution EM performance, the Jetset detector developed at Illinois [He90] was the first designed specifically to optimize EM resolution. The recipe produced a detector comparable to lead glass at a considerably lower cost and with approximately half the radiation length. Our design for Hall D follows this concept but would be a full 12.5–15 X_0 thick at normal incidence and considerably longer. Realization of these changes fortunately can be based on the KLOE calorimeter at DAΦNE, where they have been building a device of this length with an even larger inner diameter [An96]. They have achieved an excellent energy resolution parameterization of $\sigma/E \approx 4.4\%/\sqrt{E}$ in a half-length prototype.

An important feature of these detectors is the signal rise-time and overall duration. Because fast plastic scintillator is used, integrated signal time can be kept below 100 ns with shorter times possible if deemed necessary for rate considerations. At the expected maximum luminosity, no problems are anticipated. With rise-times of a few nanoseconds, excellent timing can be expected for each of the PMTs involved in collecting the light from a shower. Time differences from the two ends produce the z coordinate of the hit. The mean time of the two readout ends can be used

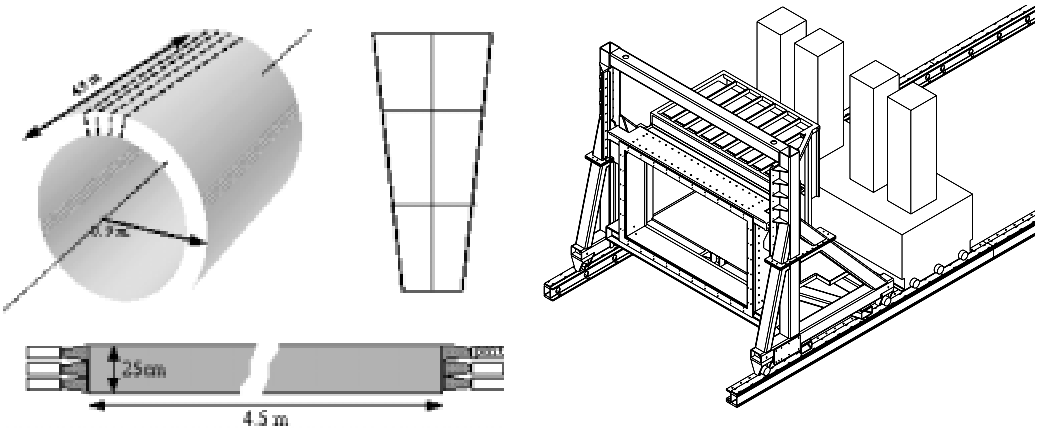

Figure 95: Left: Schematic diagrams of the barrel calorimeter. The 4.5-m-long elements will be stacked in wedges. Right: A sketch of the Pb-glass array as modified for the Hall D detector. The glass will be stacked in a circular arrangement to match the solenoidal geometry.

to determine the particle time of flight (TOF). TOF coupled with the track length and momentum then yields particle mass. In the KLOE design, timing of $\approx$ 250 ps (rms) was achieved, and improvements are possible.

A circular lead glass array will serve as the forward electromagnetic calorimeter for the Hall D detector. The Brookhaven National Laboratory E852 lead glass calorimeter [Cr98], (LGD), will be salvaged and, with minor modifications, will be configured for Hall D use.

Operating an electromagnetic calorimeter, like the LGD, near a photon beam line could be a concern given the backgrounds one might expect with a tagged bremsstrahlung photon beam. For this reason, the experience with the LGD used in the Radphi experiment in the Hall B photon beam is of particular relevance. Because of the high quality of the photon beam, beam-associated backgrounds were manageable, even when operating at an endpoint energy of 4 GeV. At higher energies the beam spot size will be even smaller, and the LGD energy resolution will improve.

Charged particle identification (PID) separates $\pi^{\pm}$ from $K^{\pm}$ from p (and the occasional $\bar{p}$). (We do not consider $e^{\pm}$ nor $\mu^{\pm}$ identification explicitly, but they can be separated from hadrons at some level using the electromagnetic calorimeters.) Two detector systems will be constructed explicitly for this purpose, namely the time-of-flight hodoscope and the Čerenkov detector. Both of these address PID in the forward region, where velocities are close to c, and the separation is most difficult. In the solenoid, we expect to make use of dE/dx in the drift chambers and timing in the barrel calorimeter. Furthermore, constrained fitting is a generally useful tool for identifying

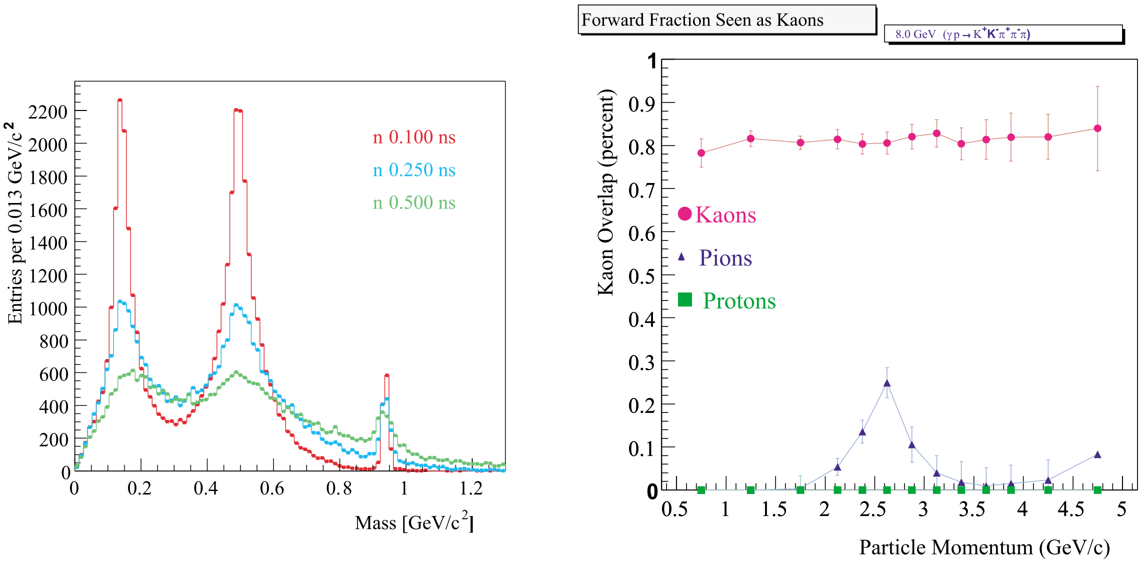

Figure 96: Left: Particle mass as reconstructed from the particle momentum and the time of flight for several timing resolutions. Right: K-π-p separation for individual tracks in the Hall D detector, (timing resolution of 100 ps is used).

the event topology as a whole.

If the particle momentum is not too high, time of flight is useful for PID in the forward region. For TOF scintillators that are ≈ 2 m long, rms time resolutions on the order of 100–120 ps are typically achievable using well-established techniques [Mo79, Be82]. With improvements in photomultiplier design, however, one can achieve 50 ps rms for detectors with long, narrow geometry. Superior time resolution has also been achieved with mesh PMTs which will work well in a high magnetic field. In Fig. 96 is shown the reconstructed particle mass from time of flight and charged tracking for several different time resolutions. Hall D is aiming for timing resolutions in the forward direction of about 100 ps, which when combined with the start counter would yield an overall resolution of about 150 ps. Beam tests of prototype designs are bing carried out in collaboration with the group at Protvino; early results indicate we are well on the way to achieving the needed time resolution.

The Čerenkov detector is planned to be a gas-filled threshold detector running at atmospheric pressure. It will be used to identify high-energy pions when TOF measurements cannot distinguish between pions and kaons. Current studies suggest that a C_4F_{10}-filled Čerenkov detector ($n = 1.0014$) will be a good match to the kinematics of Hall D reactions. For individual tracks, the results of the Čerenkov detector coupled with the time-of-flight system are shown in Fig. 96.

Because the Hall D experiment will be reconstructing exclusive final states, perfect K-π separation for all tracks is not necessary. Detailed Monte Carlo studies using the above detectors and imposing additional constraints such as the total strangeness in an event, and kinematic fitting have been performed. We find that combining all available information will make for a very efficient particle identification system for Hall D events.

4.E.4 Rates, Trigger, and Data Acquisition

Table 33 gives the total hadronic rate, and the tagged hadronic rate for fixed electron beam conditions for various energies of the coherent peak. For $E_\gamma = 9\,\mathrm{GeV}$ and $10^8\,\gamma/s$ in the peak, the experiment will have a total hadronic rate of 365 kHz and a tagged hadronic rate of 14 kHz. Initial operating conditions will be at about 10% of these values, ($10^7\,\gamma$/s), but as the trigger improves, and the detector is better understood, rates will be pushed up towards the 10^8 number.

An essential feature of the Hall D design is to build pipelining into the entire trigger, digitizer, and data-acquisition systems at the outset. This has the virtue of allowing us to upgrade from initial photon fluxes of $10^7\,\gamma$/s to eventual fluxes of $10^8\,\gamma$/s. The level 1 trigger makes a decision based on detector elements which measure hadronic multiplicities (track counts) and energies. The start counter and barrel and forward TOF detectors provide the track count while the barrel and forward calorimeters determine the energy. A tight tagger OR/start counter coincidence also is used as input to the level 1 trigger for low photon fluxes of $\approx 10^7\,\gamma$/s. For high photon fluxes ($\approx 10^8\,\gamma$/s), the tagger OR/start counter coincidence is not a useful requirement. It will be necessary to impose a software level 3 trigger which uses input from all detectors.

The data-acquisition goal for Hall D is to accept the level 1 trigger rate without incurring any DAQ system dead-time. The high rate of 70–180 kHz drives the design of the trigger, the front-end electronics, and the DAQ system. When the level 1 trigger is asserted, a time slice of each ring buffer will be copied, compressed, and stored. Events will be buffered into groups of at least ten on each electronics board and then transferred first across a backplane to be built into crate event fragments and then to a computer farm to be built into complete events. The farm will perform a quick analysis to reduce the event rate by approximately a factor of 10 before recording to magnetic media. This design allows Hall D to start running with a modest tagged-photon rate and then to scale up by an order of magnitude.

The goal of the level 3 trigger is to reduce the event rate given by the level 1 trigger to an

Table 33: Operating parameters for an experiment using the coherent bremsstrahlung beam. The calculation assumes a 12 GeV electron beam energy and a 3.4 mm collimator 80 m downstream from a radiator of thickness 10^{-4} radiation lengths. The electron beam current is taken to be 3 μA. The rates in the detector (last two rows) are calculated for a 30 cm hydrogen target and an open hadronic trigger.

E of peak	8 GeV	9 GeV	10 GeV	11 GeV
N_γ in peak	185 M/s	100 M/s	45 M/s	15 M/s
Peak polarization	0.54	0.41	0.27	0.11
(f.w.h.m.)	(1140 MeV)	(900 MeV)	(600 MeV)	(240 MeV)
Peak tagging efficiency	0.55	0.50	0.45	0.29
(f.w.h.m.)	(720 MeV)	(600 MeV)	(420 MeV)	(300 MeV)
Power on collimator	5.3 W	4.7 W	4.2 W	3.8 W
Power on target	810 mW	690 mW	600 mW	540 mW
Total hadronic rate	385 K/s	365 K/s	350 K/s	345 K/s
Tagged hadronic rate	26 K/s	14 K/s	6.3 K/s	2.1 K/s

acceptable on-tape rate. In low-intensity running (10^7 tagged photons/s) the level 1 trigger rate is expected to be 15 kHz. Since the DAQ system is being designed to handle this rate to tape, the level 3 trigger farm will not have to cut any events, although it may be used to reduce the event rate somewhat. In high-intensity mode where the level 1 rate is 70 to 180 kHz, the level 3 trigger must be able to reduce the event rate by a factor of 10.

Most of these unwanted events result from an untagged (mostly lower-energy) photon interacting in coincidence with a tagged photon. Rejecting these events means that level 3 must be able to calculate, with reasonable accuracy, the energy of the photon which produced the event. This involves accurately reconstructing tracks, matching them with the calorimeters, and adding additional energy deposited by neutral particles in the calorimeters.

Because of the accuracy requirements and the demands of linking information from different detectors, we have decided to use a processor farm architecture for level 3 instead of building a dedicated hardware processor. All events passing the level 1 trigger will be read into the level 3 processor farm where they will be reconstructed; events passing the cuts applied will then be written to tape. This approach allows for algorithmic flexibility and improvements, and the ability to cost-effectively adjust to higher rates, but it does put pressure on the DAQ system.

An estimate of the processing power required can be made using the Hall B full event analysis as a model. Hall B has similar-sized events, and their reconstruction time should be quite similar to

Table 34: Rates, sizes, and processing requirements for the level 3 trigger. A 35 SpecInt95 processor corresponds to a PIII 750 MHz machine. Moore's law scaling will lead to 350 SpecInt95 processors by early 2005, and such a box will cost about $2K.

	Low Rate	**High Rate**
Event size	5 kB	5 kB
Event rate to farm	10 kHz	180 kHz
Data rate to farm	50 Mbytes/s	900 Mbytes/s
Link technology	100 megabit Ethernet	Gigabit Ethernet
SpecInt95 for L3	2500	45,000
Num 35 SpecInt95 processors/link	70	1280
Num 350 SpecInt95 processors/link	7	128
Total Num dual 350 SpecInt95 nodes	4	64

Hall D. Currently, Hall B is able to fully reconstruct an event off-line in 100 ms on a 12 SpecInt95 computer, (PIII 300 MHz). We nominally assume that the level 3 Hall D code will be about 10% as complicated as off-line code. We then double the requirements to account for overhead. This gives us that 0.25 SpecInt95 of processing power will allow us to analyze a level 3 event in 1 s. PIII 750 MHz processors available at the start of 2000 are rated at 35 SpecInt 95, and given the rapid advances in computer speeds, Moore's law predicts that 350 SpecInt95 processors will be available at the start of 2005, and 700 SpecInt95 processors would be available by the middle of 2006. Table 34 summarizes the needs of the Hall D level 3 system. These can easily be met by a reasonable number of processors, particularly by using dual processor nodes. We note that these numbers are small compared to FNAL experiments currently running, and very small compared to expected LHC needs. Careful and timed purchases of processors will allow us to easily accommodate the level 3 trigger. Finally, we have left open the possibility of a clever level 2 hardware trigger. If such hardware could be designed, it would reduce the requirements on the level 3 farm.

4.E.5 Data Handling

The overall strategy for handling the large volume of data produced by the Hall D detector is straightforward and similar to other large fixed-target experiments. The amount of data generated by Hall D, essentially 15 kHz, is ambitious by today's standards but should be achievable at a reasonable cost in the near future. Current technology is exemplified by the CLAS detector at

Jefferson lab, which can handle a sustained rate to tape of up to 3 kHz. The movement of data from the DAQ to the computing center for Hall D will be identical to CLAS. On-line data are staged to disk in the counting house, and moved to the computing center where it is written directly to tape. The off-line analysis will place a heavy reliance on automated tape silos to access the data for both track reconstruction and higher-level analysis.

Hall D software must be developed not only to orchestrate the movement of data but to provide an integrated reconstruction and analysis environment. A design feature of this environment must include the ability to perform the same analysis of the data in the on-line and off-line environments, to allow for extensive data-quality monitoring. This requires a common set of software tools to be used throughout the on-line and off-line software. From an organizational point of view this implies an integrated on-line and off-line software environment.

4.E.6 Partial Wave Analysis

In order to identify the J^{PC} quantum numbers of a meson, it is necessary to perform a *partial wave analysis*. In the simplest terms, a partial wave analysis is an attempt to determine production amplitudes by fitting decay angular distributions. The fit may include information on the polarization of the beam and target, the spin and parity of the resonance, the spin and parity of any daughter resonances, and any relative orbital angular momenta. The analysis seeks to establish both the production strengths and the relative phase motion between various production amplitudes. Phase motion is critical in determining if resonance production is present.

While the implementation of a partial wave analysis is, in principle, straightforward, there are both empirical and intrinsic difficulties. Empirically, instrumentation effects, such as detector acceptance and resolution, can conspire to make one distribution look like another. These similar distributions lead to leakage in the partial wave analysis. Here, cropping, smearing, or incorrect acceptance corrections of two physically different distributions may lead to distributions which are apparently indistinguishable. These difficulties can be minimized by properly designing the experiment. Full angular coverage in the distributions can be achieved by using a nearly 4π detector with excellent resolution. In addition, high statistics are critical to be able to accurately separate these partial waves. A thorough partial wave analysis requires nearly 4π coverage, excellent resolution, high statistics, and a very good understanding of the detector.

The PWA method is subject to intrinsic mathematical ambiguities for certain final states. Two or more different choices of amplitudes lead to identical observables. Here there are at least two approaches. The first assumes some *a priori* physics knowledge that allows one to choose one solution over another. The second, and cleaner approach is to simultaneously examine several final states to which the resonance can decay. While the distributions may be confused in one final state, such as $\eta\pi$, such ambiguities are likely to be absent or different in a second such as $\rho\pi$. This latter approach assumes that the detector has been optimized for many different final states, and that relative normalizations between these are understood.

This latter approach of looking at multiple final states not only would allow one to separate different waves, but in itself yields key information about the relative decay rates of mesons. It is this latter information that is critical to understanding the underlying wavefunctions of the mesons – their content, and mixing with other states. This ability to accurately measure many final states and perform a simultaneous partial wave analysis is a key feature of the Hall D spectrometer for doing excellent spectroscopy.

The use of photon polarization will also allow one to both simplify the analysis parameterization and access additional information on the production of mesons. It will also provide key checks on the stability of the analysis itself. While circularly polarized light may yield some information in a few special cases, the true gain comes from linear polarization. Linear polarization defines a *new spatial direction* beyond the photon direction, while for circular polarization, the polarization and the momentum are in the same direction. Secondly, linearly polarized light is a coherent sum of circularly polarized light, which leads to new interference terms.

Finally, there is always a problem of background in a partial wave analysis. This limits one's ability to measure phase motion, and can be particularly severe in a region of dense overlapping resonances. Backgrounds involve a different final state accidentally reconstructing as the channel under study. Either a particle is missed by the detector, or when putting the final state back together, multiple interpretations are possible. This can be minimized with a good 4π detector with high efficiency for detecting all final-state particles with good resolution. One needs all particles to be reconstructed well enough to allow for a complete kinematic identification of a specific final state.

As part of the Hall D design studies, the group has carried out a partial wave analysis on simulated data for the reaction: $\gamma p \to \pi^+\pi^+\pi^- n$, for 8.5 GeV photons. Studies have been done with photon polarizations ranging from 0% up to 100%. The simulated data include several 3π resonances which decay via $\rho^\circ\pi^+$ to the 3π final state. The data are assumed to proceed via purely one-pion exchange. Two different packages for partial wave analysis have been used, each with a different formalism for fitting the data. The results between the two agree. The use of more than

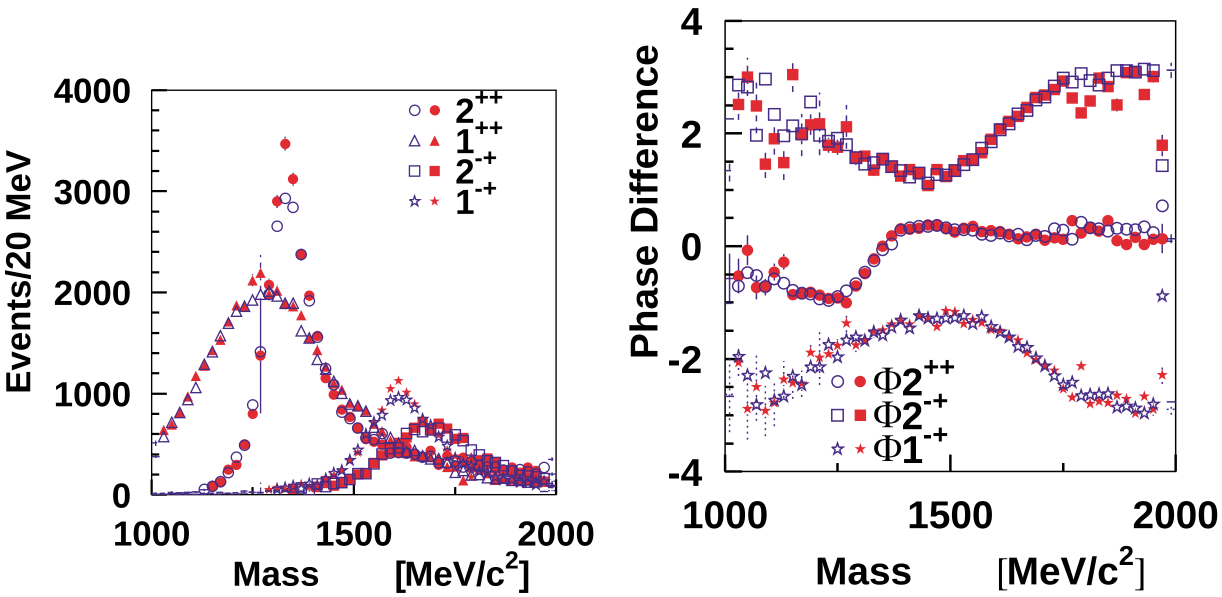

Figure 97: Partial wave analysis results for simulated 3π data. The solid figures correspond to fits to generated data, while the open figures correspond to fits to events which have been run through the Hall D Monte Carlo program. The left-hand figure shows the intensities of several waves, while the right-hand figure shows the phase difference using the 1^{++} wave as a reference.

one analysis package on real data will allow us to better access the systematics associated with the fitting of the data. The data used in these fits correspond to a couple percent of one year's reconstructed sample using 10^7 photons per second. It should be noted that this channel has a large photoproduction cross section, while the goal of the experiment is to simultaneously study channels with much smaller cross sections.

Figure 97 shows the results of fits to the simulated data. The solid figures correspond to simple generated data, while the open figures are for data which have been run through the Hall D Monte Carlo program to simulate both acceptance and resolution effects. The small differences between the two curves are due mostly to resolution, particularly for the fast π's in the events. It should be noted that the 3π channel, while one of the stronger photoproduction channels, is also one of the more difficult as far as resolution goes. The curves correspond to the $a_2(1320)$, ($J^{PC} = 2^{++}$), the $a_1(1260)$, (1^{++}), the $\pi_2(1670)$, (2^{-+}), and an exotic $\pi_1(1600)$, (1^{-+}). The phase differences are plotted with respect to the $a_1(1260)$ wave.

In addition, two small partial waves that together represent less than 1% of the total intensity have also been fit. In this model, these waves correspond to a second decay modes for the $a_1(1260)$

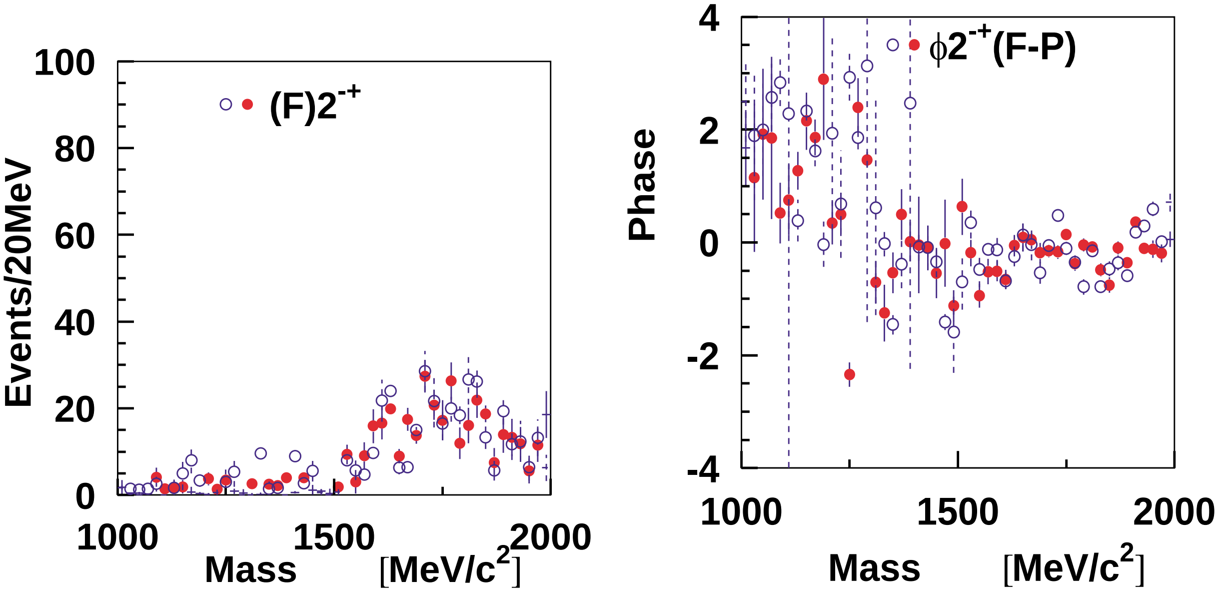

Figure 98: Partial wave analysis results for simulated 3π data. The solid figures correspond to fits to generated data, while the open figures correspond to fits to events which have been run through the Hall D Monte Carlo program. These figure correspond to the F-wave decay of the $\pi_2(1670)$, which is less than 1% of the entire signal. The two important features are the small signals in the intensity and the phase difference plot. The phase difference is relative to the dominant decay of the π_2 and should be zero (as it is).

in which the $\rho\pi$ have two units of angular momentum between them, and for the $\pi_2(1670)$ in which the $\rho\pi$ have three units of angular momentum between them. The ratios of these second modes to the main mode are important quantities in their own right. The main issue here is that the partial wave analysis has been able to extract these signals from the data. Figure 98 shows the intensity and phase difference for the $\pi_2(1670)$. The phase difference is measured with respect to the dominant $L = 1$ decay of the π_2 and should be near zero. This is clearly the case where there is strength in the intensity plot.

Similarly, a study on the effect of linear polarization in determining the production mechanism has been undertaken. In the Gottfried-Jackson frame of the decaying resonance, the angle α is defined to be the angle between the polarization vector of the photon and the normal to the production plane of the reaction. In the case of unpolarized photons, this angle is not defined. When α is either 0° or 90°, the photon is in a well-defined state of reflectivity. In the case of single pion exchange (the naturality of the π is negative), the produced reflectivity state of the resonance is opposite to that of the photon. In the case of natural parity exchange (such as ρ exchange), the

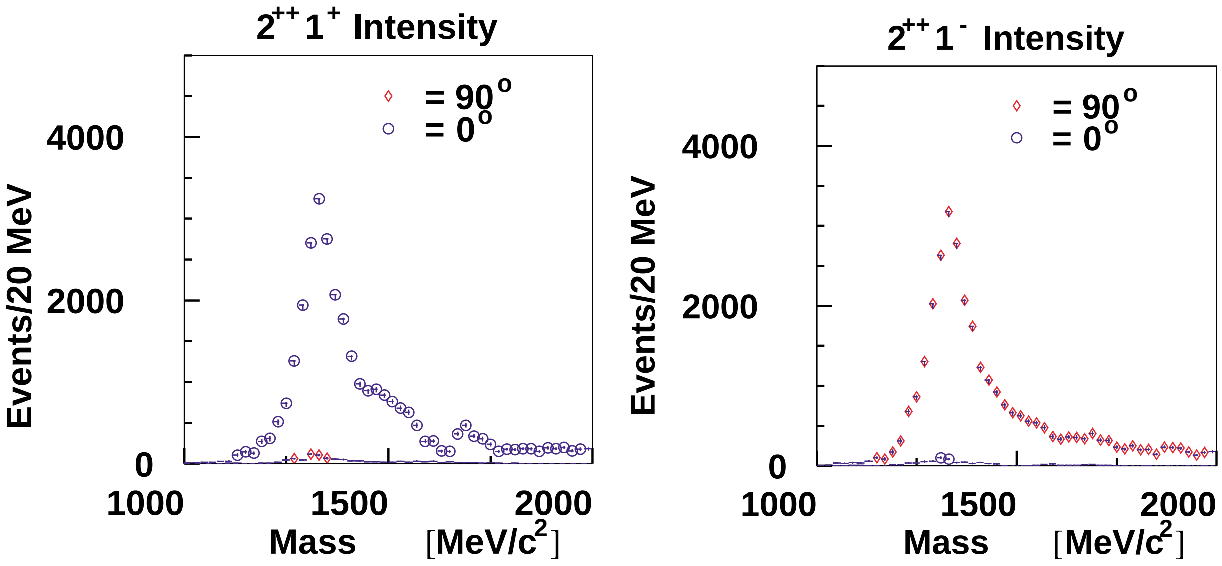

Figure 99: Left: The fit to the positive reflectivity part of the 2^{++} intensity for events near $\alpha = 0°$ and $90°$. Right: The same for the negative reflectivity waves. They key point is that the positive reflectivity wave is produced near $\alpha = 0°$ while the negative reflectivity is produced near $\alpha = 90°$. See the text for a more complete discussion.

two reflectivities will be the same. A pair of partial wave analyses has been done in which we have selected only events near $\alpha = 0°$ or $\alpha = 90°$. Figure 99 shows the results for the 2^{++} wave. The figure on the left shows the positive reflectivity 2^{++} wave, $\mid M \mid^{\epsilon} = 1^{+}$. Only the events near $\alpha = 0°$ contribute, while the $\alpha = 90°$ gives nearly no contribution. The exact opposite happens in the $\mid M \mid^{\epsilon} = 1^{-}$ wave on the right. Had the production mechanism been of opposite naturality to the pion, these figures would have been reversed. If both mechanisms had been present, then the exact mixture could have been read directly off these plots. Of course the real data will involve a more general fit to this in which the degree of linear polarization is used. However, linear polarization allows the naturality of the exchange particle to be trivially known, while for no linear polarization, there is no such handle on this.

4.E.7 Hall D Summary

The Hall D beam and detector have been optimized to perform a good partial wave analysis of mesons and baryons produced with an 8 to 9 GeV linearly polarized photon beam. Even with rates of only $10^7\,\gamma/s$, the experiment will collect at least an order of magnitude more data than existing π beam experiments during its first year of running. Such an increase in statistics coupled with a new production mechanism will not only allow us to map out the gluonic excitations, but to measure their decay properties and production mechanisms as well.

5 SUMMARY

There is a clear need today for a CEBAF-class facility operating at 12 GeV. Such an upgrade will make profound contributions to the study of strongly interacting (*i.e.*, nuclear) matter. It will open up qualitatively new and vital research capabilities on:

- the origin and nature of quark confinement by discovering the flux tubes responsible for quark confinement in the form of the gluonic excitations of $q\bar{q}$ systems, and
- the quark-gluon structure of the nuclear building blocks by mapping out for the first time quark momentum distributions in the valence quark region and by opening the door to mapping out the quark-gluon *wavefunctions* of the nucleons by exploiting the rigorous methods opened up by the newly discovered Generalized Parton Distributions.

It will also open up major new research capabilities on:

- the transition from the hadronic approximation to strongly interacting matter to the fundamental quark-gluon description through the study of quark-hadron duality in the region of the onset of deep inelastic scaling;
- delineating the forces between quarks by examining the high-momentum components of the quark-gluon wavefunctions of hadrons through measurements of the high-Q^2 behavior of their elastic and transition form factors;
- using the threshold ψN interaction as a probe of color van der Waals forces that are expected to play an important role in the NN interaction;
- using deep inelastic scattering to map out the short-range correlations in nuclei;
- learning about the basic nature of hadronic interactions by searching for the phenomenon of “color transparency”;
- examining the dependence of hadron structure on the quark mass by exploiting the $s\bar{s}$ spectrum as a bridge between heavy quarkonia and heavy-light systems, which are both well understood, and the complex light quark world; and

- providing important new data on the form factors and couplings of the Goldstone bosons of QCD, including the η'.

Jefferson Lab can realize the required accelerator upgrade cost-effectively by building on the remarkable performance of CEBAF's superconducting radio-frequency cavities, on free space in the linacs made available when it became possible to build a five-pass machine, and on a physical layout that was designed to accommodate a much higher energy than CEBAF's 4 GeV design energy. The existing experimental equipment can also be readily upgraded to accomplish the physics objectives that drive the Upgrade. Moreover, the required Hall D equipment is remarkably economical because its major components are already in hand.

References

[Ab96] K. Abe *et al.* Phys. Rev. Lett. **76**, 587 (1996).

[Ab97] K. Abe *et al.* [SLAC E154], Phys. Rev. Lett. **79**, 26 (1997).

[Ab98] A. Abele *et al.*, Phys. Lett. **B423**, 175, (1998).

[Ab98] D. Abbott *et al.*, Phys. Rev. Lett. **80**, 5072 (1998).

[Ab98b] K. Abe *et al.* [SLAC E143], Phys. Rev. D **58**, 112003 (1998).

[Ab99] H. Abramowicz and A. Caldwell, Rev. Mod. Phys. **71**, 1275 (1999).

[Ab99a] K. Abe *et al.* [SLAC E155], Phys. Lett. **B463**, 339 (1999).

[Ac98] K. Ackerstaff *et al.* [HERMES Collaboration], Phys. Rev. Lett. **81**, 5519 (1998).

[Ac98a] M. Acciarri *et al.*, Phys. Lett. **B418**, 399 (1998).

[Ac99] K. Ackerstaff *et al.* [HERMES Collaboration], Phys. Rev. Lett. **82**, 3025 (1999).

[Ac00] K. Ackerstaff *et al.*, hep-ex/0002016 (2000).

[Ad93] B. Adeva *et al.*, Phys. Lett. **B302**, 533 (1993); D. Adams *et al.*, Phys. Lett. **B329**, 399 (1994); B. Adeva *et al.*, Phys. Lett. **B357**, 248 (1995).

[Ad94] G. Adams, Workshop on CEBAF at Higher Energies, N. Isgur and P. Stoler, eds, CEBAF (1994), p. 65.

[Ad94a] D. Adams *et al.* [SMC Collaboration], Phys. Lett. **B329**, 399 (1994).

[Ad95] M. R. Adams *et al.* [E665 Collaboration], Phys. Rev. Lett. **74**, 1525 (1995).

[Ad96] J. Adomeit *et al.* [Crystal Barrel Collaboration], Z. Phys. **C71**, 227 (1996).

[Ad98] G. S. Adams *et al.*, Phys. Rev. Lett. **81**, 5760 (1998).

[Af00] A. Afanasev, C. E. Carlson, and C. Wahlquist, Phys. Rev. D **62**, 074011 (2000).

[Af00a] A. Afanasev, C. E. Carlson, and C. Wahlquist, Phys. Rev. D **61**, 034014 (2000).

[Af00b] I. R. Afnan *et al.*, Phys. Lett. B **493**, 36 (2000).

[Af94] A. Afanasev, J. Gomez and S. Nanda, Workshop on CEBAF at Higher Energies, *op. cit.*, p. 184.

[Af98] A. Afanasev and P. R. Page, Phys. Rev. D **57**, 6771 (1998).

[Ak85] S. V. Akulinichev, S.A. Kulagin and G.M. Vagradov, Phys. Lett. **B158**, 485 (1985)

[Al76] M. J. Alguard *et al.* [SLAC E80], Phys. Rev. Lett. **37**, 1261 (1976); **41**, 70 (1978).

[Al90] D. M. Alde *et al.*, Phys. Rev. Lett. **64**, 2479 (1990).

[Al98] M. Alford, K. Rajagopal and F. Wilczek, Phys. Lett. **B422**, 247 (1998).

[Al99] L. C. Alexa *et al.*, Phys. Rev. Lett. **82**, 1374 (1999); and references therein.

[Al00] S. I. Alekhin and A. L. Kataev, Nucl. Phys. **A666-667**, 179 (2000); and references therein.

[Am94] A. Amroun *et al.*, Nucl. Phys. **A579**, 596 (1994); and references therein.

[Am95] C. Amsler and F. E. Close, Phys. Lett. **B353**, 385 (1995).

[Am96] C. Amsler and F. E. Close, Phys. Rev. D **53**, 295 (1996).

[Am98] M. Ambrogiani *et al.*, Nucl. Phys. B **61**, 384 (1998).

[An71] R. L. Anderson *et al.*, Phys. Rev. **D4**, 3245 (1971).

[An77] R. Anderson *et al.*, SLAC-PUB-1741, *Invited talk presented at Int. Conf. on Production of Particles with New Quantum Numbers, Wisconsin U., Madison, Apr. 22-24, 1976.*

[An77b] R. L. Anderson *et al.*, Phys. Rev. Lett. **38**, 263 (1977).

[An93] P. L. Anthony *et al.* [SLAC E142], Phys. Rev. Lett. **71**, 959 (1993).

[An95] V. V. Anisovich *et al.*, Phys. Lett. **B323**, 233 (1994).

[An96] A. Antonelli *et al.*, Nucl. Inst. and Meth. A **370**, 367 (1996).

[An96a] M. Anghinolfi *et al.*, Nucl. Phys. **A602**, 405 (1996).

[Ar75] X. Artru *et al.*, Phys. Rev. D **12**, 1289 (1975).

[Ar97] R. Arnold and J. McCarthy, *A Proposal for Extension of E155 to Measure the Transverse Spin Structure Functions of the Proton and Deuteron* , SLAC E155x, September 1997.

[Ar99] J. Arrington *et al.*, Phys. Rev. Lett. **82**, 205 (1999).

[Ar00] C. S. Armstrong *et al.*, submitted to Phys. Rev. D (2000).

[As87] D. Aston *et al.*, *The LASS spectrometer*, Technical report, 1987, SLAC-Report-298.

[As88] J. Ashman *et al.* [EMC Collaboration], Phys. Lett. **B206**, 364 (1988).

[As89] J. Ashman *et al.* [EMC Collaboration], Nucl. Phys. **B328**, 1 (1989)

[As89a] D. Aston *et al.*, SLAC-PUB-5145; Nucl. Phys. (Proc. Suppl.) **B8**, 32 (1989).

[As99] D. Ashery [E791 Collaboration], Proceedings of the Int. Workshop on Physics with Electron Polarized Ion Colliders, Bloomington, 1999, p. 322.

[Au83] J. J. Aubert *et al.* [EMC Collaboration], *Phys. Lett.* **B123**, 275 (1983).

[Av00] T. Averett, Proceedings of the HiX2000 workshop, J.P. Chen and Z.E. Meziani, eds.

[Ba77] Exotic hybrids were apparently first described in a bag model context by T. Barnes, Ph.D. thesis, California Institute of Technology, 1977 (unpublished).

[Ba82] "The Role of Electromagnetic Interactions in Nuclear Science", a report of the DOE/NSF Nuclear Science Advisory Committee (1982).

[Ba83] G. Baum *et al.,* [SLAC E130] Phys. Rev. Lett. **51**, 1135 (1983).

[Ba93] G. S. Bali *et al.*, Phys. Lett. B **309**, 378 (1993).

[Ba95] T. Barnes, F. E. Close, and E. S. Swanson, Phys. Rev. D **52**, 5242 (1995).

[Ba96] B. Baumbaugh *et al.*, IEEE Trans. Nucl. Sci. **43**, 1146, (1996).

[Ba97] G. Bali *et al.* [SESAM Collaboration], Nucl. Phys. Proc. Suppl. **63**, 209 (1997).

[Ba00] G. S. Bali *et al.* [SESAM/TCL Collaboration], Phys. Rev. D **62**, 054503 (2000).

[Be67] H. A. Bethe, Ann. Rev. Nucl. Sci. **21**, 93 (1971).

[Be69] J. S. Bell and R. Jaciw, Nuovo Cimento **60A**, 47 (1969); S. L. Adler, Phys. Rev. **177**, 2426 (1969).

[Be75] C. J. Bebek *et al.*, Phys. Rev. Lett. **34**, 759 (1975); Phys. Rev. Lett. **37**, 1525 (1976); Phys. Rev. D **15**, 3085 (1977).

[Be78] C. J. Bebek *et al.*, Phys. Rev. D **13**, 1693 (1978).

[Be82] B. Bengston and M. Moszynksi, Nuclear Inst. and Meth. **204**, 129, (1982).

[Be84] E. L. Berger, F. Coester, and R. B. Wiringa, Phys. Rev. D **29**, 398 (1984).

[Be89] D. Beck *et al.*, Nucl. Instr. Methods in Phys. Res. **A277**, 323 (1989).

[Be91] H. J. Behrend *et al.*, Z. Phys. **C49**, 401 (1991).

[Be95] V. M. Belyaev and A. Radyushkin, Phys. Lett. **B359**, 194 (1995).

[Be96] O. Benhar, S. Fantoni, N. N. Nikolaev, J. Speth, A. A. Usmani and B. G. Zakharov, J. Exp. Theor. Phys. **83**, 1063 (1996);

[Be97] C. Bernard *et al.* [MILC Collaboration], Phys. Rev. D **56**, 7039 (1997).

[Be99] H. A. Bethe, Rev. Mod. Phys. **71**, S6 (1999).

[Be00] O. Benhar, N. N. Nikolaev, J. Speth, A. A. Usmani and B. G. Zakharov, Nucl. Phys. **A673**, 241 (2000).

[Bi88] J. Bijnens, A. Bramon and F. Cornet, Phys. Rev. Lett. **61**, 1453 (1988).

[Bi89] R. P. Bickerstaff and A. W. Thomas, J. Phys. G **15**, 1523 (1989).

[Bi95] A. Bianconi, S. Jeschonnek, N. N. Nikolaev, and B. G. Zakharov, Phys.Lett.**B343** (1995), 13.

[Bi96] A. Bianconi, S. Jeschonnek, N. N. Nikolaev, and B. G. Zakharov, Nucl.Phys. **A608** (1996), 437.

[Bi96a] A.Bianconi, S. Jeschonnek, N. N. Nikolaev, and B. G. Zakharov, Phys. Rev. C **53** (1996), 576.

[Bl69] E. D. Bloom *et al.*, Phys. Rev. Lett. **23**, 930 (1969), and M. Briedenbach *et al.*, Phys. Rev. Lett. **23** 935 (1969)

[Bl70] E. D. Bloom and F. J. Gilman, Phys. Rev. Lett. **25**, 1140 (1970); Phys. Rev. D **4**, 2901 (1971).

[BNL98] Y. Mardor *et al.*, Phys. Rev. Lett. **81**, 5085 (1998).

[BNL00] A. Leksanov *et al.* [E850 Collaboration], Proc. of 7th. Conf. CIPANP2000, Quebec, p. 306.

[Bo81] A. Bodek and J. L. Ritchie, Phys. Rev. D **23**, 1070 (1981).

[Bo83] A. Bodek *et al.*, Phys. Rev. Lett. **50**, 1431 (1983).

[Bo98] C. Bochna *et al.* [E89-012 Collaboration], Phys. Rev. Lett. **81**, 4576 (1998)

[Bo00] P. Bosted, "Spin Structure Functions of the Nucleon Measured at SLAC", *Circum-Pan-Pacific RIKEN Symposium on High Energy Spin Physics* (Wako, Japan, November 1999), RIKEN Review 28 (May, 2000) (No. 13); P. Bosted, private communication.

[Br73] S. J. Brodsky and G. R. Farrar, Phys. Rev. Lett. **31**, 1153 (1973); V. A. Matveev, R. M. Muradyan and A. N. Tavkhelidze, Lett. Nuovo Cimento **7**, 719 (1973).

[Br79] E. L. Berger and S. J. Brodsky, Phys. Rev. Lett. **42** (1979) 940.

[Br79a] S. J. Brodsky and G. P. Lepage, Phys. Lett. **B87**, 359 (1979).

[Br80] S. J. Brodsky and G. P. Lepage, Phys. Rev. D **22**, 2157 (1980).

[Br80a] K. L. Brown, "TRANSPORT, A computer program for designing charged particle beam transport systems", CERN 80-04, Geneva, 1980.

[Br82] S. J. Brodsky, in *Proceedings of the Thirteenth Int'l Symposium on Multiparticle Dynamics*, ed. W. Kittel, W. Metzger and A. Stergiou (World Scientific, Singapore, 1982) 963.

[Br83] S. J. Brodsky, C. Ji and G. P. Lepage, Phys. Rev. Lett. **51** (1983) 83.

[Br90] S. J. Brodsky, G. F. de Teramond and I. A. Schmidt, Phys. Rev. Lett. **64** (1990) 1924.

[Br92] S. J. Brodsky *et al.*, Nucl. Phys. **B369** (1992) 519.

[Br97] S. J. Brodsky and G. A. Miller, Phys. Lett. **B412**, 125 (1997).

[Br99] S. J. Brodsky, M. Diehl, P. Hoyer, and S. Peigne, Phys. Lett. **B449**, 306 (1999); A. Afanasev, C. E. Carlson, and C. Wahlquist, Phys. Rev. D **58**, 054007 (1998) and Phys. Lett. **B398**, 393 (1997); C. E. Carlson and A. B. Wakely, Phys. Rev. D **48**, 2000 (1993).

[Br01] S. J. Brodsky, E. Chudakov, P. Hoyer and J.-M. Laget, Phys. Lett. **B498**, 23 (2001).

[Br00a] V. M. Braun, A. Khodjamirian, M. Maul, Phys. Rev. D **61**, 073004 (2000).

[Bu98] V. Burkert, "Physics with CLAS at Energies up to 12GeV", in *Physics & Instrumentation with 6-12 GeV Beams*, a Thomas Jefferson National Accelerator Facility report, S. Dytman, H. Fenker and P. Roos, eds., June 1998, p. 407.

[Bu98a] V. Burkert, "Electromagnetic Calorimeter Upgrade Possibilities for CLAS", in *Physics & Instrumentation with 6-12 GeV Beams"* (ibid.) p. 425.

[Ca75] U. Camerini *et al.*, Phys. Rev. Lett. **35** 483 (1975).

[Ca75a] R. Carlitz, Phys. Lett. **B58**, 345 (1975).

[Ca83] C. E. Carlson and T. J. Havens, Phys. Rev. Lett. **51**, 261 (1983).

[Ca88] A. S. Carroll *et al.*, Phys. Rev. Lett. **61**,1698 (1988).

[Ca90] C. E. Carlson and N. C. Mukhopadhyay, Phys. Rev. D **41**, 2343 (1990).

[Ca91] C. E. Carlson, K. E. Lassila, and U. P. Sukhatme, Phys. Lett. **B263**, 377 (1991).

[Ca91a] C. E. Carlson and N. C. Mukhopadhyay, Phys. Rev. Lett. **67**, 3745 (1991).

[Ca95] C. E. Carlson and K. E. Lassila, Phys. Rev. C **51**, 364 (1995).

[Ca95a] C. E. Carlson and N. Mukhopadhyay, Phys. Rev. Lett. **74**, 1288 (1995).

[Ca97] C. E. Carlson, J. R. Hiller, R. J. Holt, Ann. Rev. Nucl. and Part. Sci. **47**, 395 (1997); and references therein.

[Ca00] D. Cassel, F. Close, J. Domingo, W. Dunwoodie, D. Geesaman, D. Hitlin, M. Olson and G. Young, *Review of the Jefferson Laboratory "Hall D Project"*, January 2000, (http://www.phys.cmu.edu/halld/halld_notes/Note_024/).

[Ca00a] G. W. Carter and D. Diakonov, Nucl. Phys. B **582**, 571 (2000).

[Ch77] V. L. Chernyak and A. R. Zhitnitsky, JETP Lett. **25**, 510 (1977); V. L. Chernyak, A. R. Zhitnitsky and V. G. Serbo, JETP Lett. **26**, 594 (1977).

[Ch78] B. T. Chertok, Phys. Rev. Lett. **40**, 1429 (1978); S. J. Brodsky and B. T. Chertok, Phys. Rev. **D14**, 3003 (1976).

[Ch96] E. Chen, M. Saulnier, W. Sun, and H. Yamamoto, *Tests of a high resolution time-of-flight system based on long and narrow scintillator*, hep-ex/9606007, (1996).

[Ch99] E. Christova and E. Leader, Phys. Lett. **B468**, 299 (1999).

[Ch01] E. Chudakov *et al.*, Letter of Intent for CEBAF12, JLab technical note: JLAB-TN-01-007, January 2001.

[Chpc] E. Chudakov, private communication

[Ca98] J. Carlson and R. Schiavilla, Rev. Mod. Phys. **70**, 743 (1998); and references therein.

[Ci89] C. Ciofi degli Atti and S. Liuti, Phys. Lett. **B225**, 215 (1989).

[Ci90] C. Ciofi degli Atti and S. Liuti, Phys. Rev. C **41**, 1100 (1990).

[Ci93] C. Ciofi degli Atti and S. Simula, Phys. Lett. **B319**, 23 (1993).

[Ci93a] C. Ciofi degli Atti, S. Scopetta, E. Pace, and G. Salme, Phys. Rev. C **48**, 968 (1993).

[Cl73] F. E. Close, Phys. Lett. **B43**, 422 (1973); Nucl. Phys. **B80**, 269 (1974).

[Cl79] F. E. Close, *An Introduction to Quarks and Partons* (Academic Press, 1979).

[Cl83] F. E. Close, R. G. Roberts, and G. G. Ross, Phys. Lett. **B129**, 346 (1983).

[Cl88] F. E. Close and A. W. Thomas, Phys. Lett. **B212**, 227 (1988).

[Cl95] F. E. Close and P. Page, Nucl. Phys. **B443**, 233 (1995).

[Cl95a] F. E. Close, private communication, advocates using the *positive* term “strong QCD” instead of the negative “nonperturbative QCD”.

[Cl00] F. E. Close and A. Kirk, Phys. Lett. B **483**, 345 (2000).

[Cl00a] Proposal for CLAS Upgrade at High Energies.

[Co97] J. C. Collins, L. Frankfurt, and M. Strikman, Phys. Rev. D **56**, 2982 (1997).

[Co98] C. Coriano, H-N. Li, and C. Savkli, J. High En. Phys. 9807, 008 (1998).

[Cr97] J. A. Crittenden [ZEUS Collaboration], presented at Photon ’97, May 1997.

[Cr98] R. R. Crittenden *et al.*, Nuclear Inst. and Meth. **387**, 377 (1998).

[Da94] S. Dasu *et al.*, Phys. Rev. D **49**, 5641 (1994).

[De00] D. Debruyne, J. Ryckebusch, W. Van Nespen, and S. Janssen, *Phys. Rev. C* **62**, 024611 (2000).

[Di88] M. Diemoz *et al.*, Z. Phys. **C39**, 21 (1988).

[Di89] H. Dijk and B. L. G. Bakker, Nucl. Phys. **A494**, 438 (1989); Z-J. Cao and L. Kisslinger, Phys. Rev. C **41**, 647 (1990), and references therein.

[Do97] J. F. Donoghue and E. S. Na, Phys. Rev. D **56**, 7073 (1997).

[Du85] G. V. Dunne and A. W. Thomas, Nucl. Phys. **A446**, 437c (1985).

[Du91] M. Dueren and K. Rith, *Polarized Electron Nucleon Scattering at HERA: The HERMES Experiment*, in "Hamburg 1991, Proceedings, Physics at HERA, vol. 1" 427-445.

[Ef80] A. V. Efremov and A. V. Radyushkin, Theor. Math. Phys. **42**, 97 (1980).

[Eg94] K. S. Egiyan, L. L. Frankfurt, W. R. Greenberg, G. A. Miller, M. M. Sargsyan, M. I. Strikman, Nucl. Phys. **A580**, 365 (1994).

[Ei84] E. Eichten, I. Hinchliffe, K. Lane and C. Quigg, Rev. Mod. Phys. **56**, 579 (1984).

[Ei99] M. Eides, L. Frankfurt, and M. Strikman, Phys. Rev. D **59**, 114025 (1999).

[En00] R. Ent, C. E. Keppel, and I. Niculescu, Phys. Rev. D. **62**, 73008 (2000).

[En00a] R. Ent, H. Mkrtchyan, and G. Niculescu, JLAB Proposal E00-004 (2000).

[Er83] M. Erikson and A. W. Thomas, Phys. Lett. **B128**, 112 (1983).

[Fa75] G. R. Farrar and D. R. Jackson, Phys. Rev. Lett. **35**, 1416 (1975).

[Fa79] G. R. Farrar and D. R. Jackson, Phys. Rev. Lett. **43**, 246 (1979); and D. R. Jackson, Thesis, CALTECH, 1977 (unpublished);

[Fe72] R. P. Feynman, *Photon Hadron Interactions* (Benjamin, Reading, Massachusetts, 1972).

[Fo96] J. L. Forest, V. R. Pandharipande, S. C. Pieper, R. B. Wiringa, and R. Schiavilla, Phys. Rev. C **54**, 646 (1996).

[Fr81] L. L. Frankfurt and M. I. Strikman, Phys. Rep. **76**, 215 (1981).

[Fr83] B. L. Friman, V. R. Pandharipande, and R. B. Wiringa, Phys. Rev. Lett. **51**, 763 (1983)

[Fr85] L. L. Frankfurt and M. I. Strikman, Nucl. Phys. **B250**, 1585 (1985).

[Fr88] L. L. Frankfurt and M. I. Strikman, Phys. Rep. **160**, 235 (1988).

[Fr90] J. L. Friar *et al.*, Phys. Rev. C **42**, 2310 (1990).

[Fr92] L. L. Frankfurt, G. A. Miller and M. I. Strikman, Phys. Rev. Lett. **68**, 17 (1992).

[Fr92a] L. L. Frankfurt, G. A. Miller, and M. I. Strikman, Comm. Nucl. Part. Phys. **21**, 1 (1992).

[Fr93] L. L. Frankfurt, G. A. Miller and M. Strikman, Phys. Lett. **B304**, 1 (1993)

[Fr93a] L. L. Frankfurt, D. B. Day, M. M. Sargsian and M. I. Strikman, Phys. Rev. C **48**, 2451 (1993).

[Fr94] L. L. Frankfurt *et al.*, in Workshop on 'CEBAF at Higher Energies', Eds. N. Isgur and P. Stoler, Conf. Proc. p. 499 (1994).

[Fr94a] B. Frois and P. J. Mulders, Workshop on CEBAF at Higher Energies, Thomas Jefferson National Accelerator Facility, Eds. N. Isgur, P. Stoler, p. 309 (1994).

[Fr95] L. L. Frankfurt, E. J. Moniz, M. M. Sargsyan, M. I. Strikman, Phys. Rev. C **51**, 3435 (1995).

[Fr95b] L. L. Frankfurt, W. R. Greenberg, G. A. Miller, M. M. Sargsian and M. I. Strikman, Z. Phys. **A352**, 97 (1995).

[Fr96] M. R. Frank, B. K. Jennings and G. A. Miller, Phys. Rev. C **54**, 920 (1996); B. K. Jennings and G. A. Miller, Phys. Lett. **B318**, 7 (1993).

[Fr97] L. L. Frankfurt, M. M. Sargsian and M. I. Strikman, Phys. Rev. C **56**, 1124 (1997)

[Fr98] L. Frankfurt, G. Piller, M. Sargsian, and M. Strikman, Eur. Phys. J. **A2**, 301 (1998).

[Fr98a] V. V. Frolov *et al.*, Phys. Rev. Lett. **82**, 45 (1998).

[Fr00] L. L. Frankfurt, G. A. Miller, M. M. Sargsian and M. I. Strikman, Phys. Rev. Lett. **84**, 3045 (2000)

[Ge92] C. Gerschel and J. Hufner, Z. Phys. **C56** (1992) 171.

[Ge93] P. Geiger and N. Isgur, Phys. Rev. D **47**, 5050 (1993); D **44**, 799 (1991).

[Ge95] D. F. Geesaman, K. Saito and A. W. Thomas, Ann. Rev. Nucl. and Part. Sci. **45**, 337 (1995).

[Gi46] V. L. Ginzburg and I. M. Frank, JETP **16**, 15 (1946).

[Gi75] B. Gittelman *et al.*, Phys. Rev. Lett. **35**, 1616 (1975).

[Gi00] R. Gilman, Proceedings of the HiX2000 workshop, J.P. Chen and Z.E. Meziani, eds (ibid); P. Mulders, ibid; H. Gao, private communication

[Gl98] M. Glück, E. Reya, and A. Vogt, Eur. Phys. J. **C5**, 461 (1998).

[Go69] K. Gottfried and D. R. Yennie, Phys. Rev. **182** (1969) 1595.

[Go94] J. Gomez *et al.*, Phys. Rev. D **49**, 4348 (1994).

[Gr75] L. V. Gribov and L. Lipatov, Yad. Fiz. **20**, 181 (1975); G. Altarelli and G. Parisi, Nucl. Phys. **B126**, 298 (1977); Dokshitzer, Sov. Phys. JETP **46**, 641 (1977).

[Gr94] W. R. Greenberg and G. A. Miller, *Phys. Rev. C* **49**, 2747 (1994).

[Gr98] J. Gronberg *et al.* [CLEO Collaboration], Phys. Rev. D **57**, 33 (1998).

[Gupc] M. Guidal "*Computer Code for DVCS and BH calculations*", private communication.

[Ha98] E. A. Hawker *et al.*, Phys. Rev. Lett. **80**, 3715 (1998).

[HD99] The Hall D Collaboration, *Photoproduction of Unusual Mesons: The Hall D Project at Jefferson Lab*, Design Report version 2, August 1999, (http://www.phys.cmu.edu/halld/cdr/).

[He90] D. W. Hertzog *et al.*, Nucl. Inst. and Meth., **A294**, 446 (1990).

[Ho55] R. Hofstadter and R. W. McAllister, Phys. Rev. **98**, 183 (1955).

[Ho97] P. Hoyer, Nucl. Phys. **A622**, 284c (1997).

[Hu90] E. Hummel and J. A. Tjon, Phys. Rev. Lett. **63**, 1788 (1989); Phys. Rev. C **42**, 423 (1990); J. W. Van Orden, N. Devine and F. Gross, Phys. Rev. Lett. **75**, 4369 (1995); D. R. Phillips, S. J. Wallace and N. K. Devine, Phys. Rev. C **58**, 2261 (1998); F. M. Lev, E. Pace and G. Salme, Phys. Rev. C **62**, 064004 (2000).

[Hu98] J. Hufner and B. Kopelovich, Phys. Lett. **B426**, 154 (1998).

[In84] T. Inagaki *et al.*, Cryogenics **24**, 83 (1984).

[Is81] N. Isgur, G. Karl, and D. W. L. Sprung, Phys. Rev. D **23**, 163 (1981).

[Is84] N. Isgur and C. H. Llewellyn Smith, Phys. Rev. Lett. **52**, 1080 (1984); Phys. Lett. **B217**, 535 (1989); G. R. Farrar, K. Huleihel and H. Zhang, Phys. Rev. Lett. **74**, 650 (1995).

[Is85] N. Isgur, and J. Paton, Phys. Rev. D **31**, 2910 (1985); N. Isgur, R. Kokoski and J. Paton, Phys. Rev. Lett. **54**, 869 (1985).

[Is91] N. Isgur and M. B. Wise, Phys. Rev. D **43**, 819 (1991).

[Is99] N. Isgur, Phys. Rev. D **59**, 034013 (1999).

[Is99b] N. Isgur, Phys. Rev. D **60**, 114016 (1999).

[It92] H. Ito, W. W. Buck, and F. Gross, Phys. Lett. **287B**, 23 (1992).

[It97] H. Ito, S. E. Koonin and R. Seki, *Phys. Rev. C* **56**, 3231 (1997).

[Ja84] R. L. Jaffe, F. E. Close, R. G. Roberts, and G. G. Ross, Phys. Lett. **B134**, 449 (1984).

[Ja90] O. C. Jacob and L. S. Kisslinger, Phys. Lett. **243B**, 323 (1990).

[Ja93] R. Jakob and P. Kroll, Phys. Lett. **315B**, 463 (1993).

[Je99] S. Jeschonnek and T. W. Donnelly, Phys. Rev. C **59** (1999), 2676.

[Je00] S. Jeschonnek, N. Isgur, W. Melnitchouk, and J. W. Van Orden, to be submitted to Phys. Rev.

[Ji95a] X. Ji and P. Unrau, Phys. Rev. D **52**, 72 (1995).

[Ji97] X. Ji, Phys. Rev. Lett. **78**, 610 (1997); Phys. Rev. D **55**, 7114 (1997).

[JL99] JLab Experiment E94-139, preliminary results.

[Jo00] M. K. Jones *et al.*, Phys. Rev. Lett. **84**, 1398 (2000).

[Ju88] H. Jung and G. A. Miller, Phys. Lett. **B200**, 351 (1988).

[Ju97] K. Juge, J. Kuti, and C. J. Morningstar, Nucl. Phys. Proc. Suppl. **63**, 326, (1997).

[Ka75] W. Kaune, G. Miller, W. Oliver, R. W. Williams, and K. K. Young, Phys. Rev. D **11**, 478 (1975).

[Ka90] L. P. Kaptari *et al.*, Nucl. Phys. **A512**, 684 (1990).

[Ko97] N. I. Kochelev, *Proc. of Workshop on Physics with Polarized Protons at HERA*, 1997, Hamburg, p. 225, hep-ph/9711274.

[Kopc] N. Kochelev, private communication.

[Kr99] D. Kharzeev, Eur. Phys. J. **C9**, 459 (1999).

[Ku89] S. A. Kulagin, Nucl. Phys. **A500**, 653 (1989).

[Ku94] S. A. Kulagin, G. Piller, and W. Weise, Phys. Rev. C **50**, 1154 (1994).

[Ku00] S. Kuhlmann *et al.*, Phys. Lett. **B476**, 291 (2000).

[La72] J.-M. Laget, Nucl. Phys. **A194**, 81 (1972).

[La91] J.-M. Laget, in *Modern Topics in Electron Scattering*, edited by B. Frois and I. Sick (World Scientific, 1991) 290, and references therein.

[La94] J.-M. Laget and R. Mendez-Galain, Nucl. Phys. **A581**, 397 (1995).

[La94a] J.-M. Laget, Nucl.Phys. **579** (1994) 333.

[La95] H. L. Lai *et al.* [CTEQ Collaboration], Phys. Rev. D **51**, 4763 (1995); H. L. Lai *et al.*, Eur. Phys. J. **C12**, 375 (2000).

[La97] P. Lacock *et al.* [UKQCD Collaboration], Phys. Lett. **B401**, 308, (1997).

[La98] J.-M. Laget, in *Proceedings of workshop on Jefferson Lab Physics & Instrumentations with 12 GeV Beams*, Newport News, 1998, p. 57.

[La98a] B. Lampe and E. Reya, hep-ph/9810270; S. D. Bass and A. W. Thomas, Prog. Part. Nucl. Phys. **33**, 449 (1994).

[Li00] S. Liuti, R. Ent, C. E. Keppel, and I. Niculescu, to be submitted to Phys. Rev. D.

[Lu81] M. Luscher, Nucl. Phys. **B180**, 317 (1981).

[Lu92] M. Luke, A. V. Manohar and M. J. Savage, Phys. Lett. **B288**, 355 (1992).

[Ma91] A. V. Manohar, Phys. Rev. Lett. **66**, 289 (1991).

[Ma94] N. C. R. Makins *et al.*, Phys. Rev. Lett. **72**, 1986 (1994).

[Ma94a] A. D. Martin, R. Roberts and W. J. Stirling, Phys. Rev. D **50**, 6734 (1994).

[Ma98] A. D. Martin, R. G. Roberts, W. J. Stirling and R. S. Thorne, Eur. Phys. J. **C4**, 463 (1998).

[Ma00] P. Maris and P. C. Tandy, Phys. Rev. C **62**, 055204 (2000).

[Me93] W. Melnitchouk and A. W. Thomas, Phys. Rev. D **47**, 3783 (1993).

[Me94] W. Melnitchouk, A. W. Schreiber, and A. W. Thomas, Phys. Rev. D **49**, 1183 (1994).

[Me96] W. Melnitchouk and A. W. Thomas, Phys. Lett. **B377**, 11 (1996).

[Me97] W. Melnitchouk, M. Sargsian, and M. I. Strikman, Z. Phys. **A359**, 359 (1997).

[Me00] Z.-E. Meziani, *Proceedings of the HiX2000 Workshop*, J.P. Chen and Z.-E. Meziani, eds.

[Mi00] J. Mitchell, *Proceedings of the HiX2000 Workshop*, J.-P. Chen and Z.-E. Meziani, eds.

[Mkpc] H. Mkrtchyan *et al.*, JLab test run results, 1999 (private communication).

[ML00] *Assessment of the MEGA/LASS Magnet at LANL,20 March, 2000,* (http://www.phys.cmu.edu/halld/halld_notes/Note_026/).

[Mo70] M. Morpurgo *et al.*, Particle Accelerators **1**, 255 (1970).

[Mo79] M. Moszynski and B. Bengston, Nucl. Inst. and Meth., **158**, 1 (1979).

[Mo79a] M. Morpurgo *et al.*, Cryogenics **19**, 411 (1979).

[Mo95] B. Moussallam, Phys. Rev. D **51**, 4939 (1995).

[Mo97] C. J. Morningstar and M. Peardon, Phys. Rev. D **56**, 4043 (1997).

[Mo99] H. Morita, C. Ciofi degli Atti, and D. Treleani, Phys. Rev. C **60**, 034603 (1999).

[Mopc] M. Morlet and J. Van de Wiele, private communication.

[Mu83] A. H. Mueller, in *Proceedings of the Seventeenth Recontre de Moriond Conference on Elementary Particle Physics*, Les Arcs, France, 1982, edited by J. Tran Thanh Van (Editions Frontieres, Gif-sur-Yvette, France,1982); S. J. Brodsky, in *Proceedings of the Thirteenth International Symposium on Multiparticle Dynamics*, Volendam, The Netherlands, 1982, edited by W. Kittel *et al.* (World Scientific, Singapore, 1983).

[Mu82] A. H. Mueller, in *Proceedings of the Seventeenth Rencontres de Moriond*, ed. J. Tran Thanh Van (Editions Frontieres, Gif-sur-Yvette, France, 1982) **Vol. I** 13.

[Mu95] C. R. Munz *et al.,* Phys. Rev. C **52**, 2110 (1995).

[Na70] Y. Nambu, Univ. of Chicago Report No. 70-70 (1970) (unpublished); lectures at the Copenhagen Summer Symposium (1970) (unpublished).

[Na84] O. Nachtmann and H. J. Pirner, Z. Phys. **C21**, 277 (1984).

[NA99] *Nuclear Physics: The Core of Matter, The Fuel of Stars,* The Committee on Nuclear Physics of the Board on Physics and Astronomy of the Commission on Physical Sciences, Mathematics, and Applications of the National Research Council, National Academy Press, Washington, D.C. (1999).

[Ne77] R. Nieman *et al.*, IEEE Trans. on Magn., **13**, 632 (1977).

[Ne95] T. G. O'Neill *et al.*, Phys. Lett. **B351**, 87 (1995).

[Ni00] I. Niculescu *et al.*, Phys. Rev. Lett. **85**, 1186 (2000).

[Ni00a] I. Niculescu *et al.*, Phys. Rev. Lett. **85**, 1182 (2000).

[Ni94] N. N. Nikolaev, A. Szczurek, J. Speth, J. Wambach, B. G. Zakharov and V. R. Zoller, Phys. Rev. C **50**, 1296 (1994).

[Ni99] I. Niculescu, C. Keppel, S. Liuti, and G. Niculescu, Phys. Rev. D **60**, 094001 (1999).

[NS96] "Nuclear Science: A Long Range Plan", a report by the DOE/NSF Nuclear Science Advisory Committee, February, 1996.

[Pa97] V. R. Pandharipande, I. Sick, and P. K. A. deWitt Huberts, Rev. Mod. Phys. **69**, 981 (1997).

[Pa00] E. Pace, G. Salme and S. Scopetta, to appear in *Proceedings of the XVII-th European Few-Body Conference*, Evora, Portugal (2000).

[Pe89] M. D. Petroff and M. Atac, IEEE Trans. Nucl. Sci. **NS-36**, 163 (1989).

[Pe00] G. Petratos, *Proceedings of the HiX2000 Workshop*, J.-P. Chen and Z.-E. Meziani, eds.

[Po99] M. V. Polyakov and C. Weiss, Phys. Rev. D **60**, 114017 (1999).

[Ra77] A. V. Radyushkin, JINR report P2-10717, Dubna, 1977 (unpublished).

[Ra96] A. V. Radyushkin, Phys. Lett. **B380**, 417 (1996); Phys. Lett. **B385**, 333 (1996); Phys. Rev. D **56**, 5524 (1997).

[Ra98] R. Rapp, T. Schafer, E. V. Shuryak and M. Velkovsky, Phys. Rev. Lett. **81**, 53 (1998)

[Ra98a] A. V. Radyushkin, Phys. Rev. D **58**, 114008 (1998).

[Ra99] A. V. Radyushkin, Phys.Rev.D **59**, 014030 (1999).

[Ri98] G. Ricco *et al.*, Phys. Rev. C **57**, 356 (1998).

[Ru75] A. de Rújula, H. Georgi and H.D. Politzer, Ann. Phys. **103**, 315 (1975).

[Sa69] J. J. Sakurai, Phys. Rev. Lett. **22**, 981 (1969).

[Sc91] R. Schiavilla and D. O. Riska, Phys. Rev. C **43**, 437 (1991); R. Schiavilla, V. R. Pandharipande and D. O. Riska, Phys. Rev. C **41**, 309 (1990); and references therein.

[Sc93] R. W. Schulze and P. U. Sauer, Phys. Rev. C **48**, 38 (1993).

[Se95] J. Sexton *et al.* [IBM Collaboration], Phys. Rev. Lett. **75**, 4563 (1995).

[Sl88] T. Sloan, G. Smadja, and R. Voss, Phys. Rep. **162**, 45 (1988).

[So00] P. Souder, *Proceedings of the HiX2000 Workshop*, J.-P. Chen and Z.-E. Meziani, eds.

[St93] P. Stoler, Phys. Rep. **226**, 103 (1993).

[St95] E. Stein, P. Gornicki, L. Mankiewicz, and A. Schafer, Phys. Lett. **B353**, 107 (1995).

[Ta96] L. Tao *et al.*, Z. Phys. C **70**, 387 (1996).

[tH76] G. 't Hooft, Phys. Rev. Lett. **37**, 8 (1976); and Phys. Rev. D **14**, 3432 (1976).

[Th84] A. W. Thomas, Adv. Nucl. Phys. **13**, 1 (1984).

[Th97] D. R. Thompson *et al.*, Phys. Rev. Lett. **81**, 5760, (1997).

[Ti92] P. C. Tiemeijer and J. A. Tjon, Phys. Lett. **277B**, 38 (1992).

[TOSCA] 3-D Non-linear magnetostatics computer program, SCARPIA pre-processor and OPERA post-processor, Vector Fields, Oxford, U.K.

[Uc88] T. Uchiyama and K. Saito, Phys. Rev. C **38**, 2245 (1988).

[Va98] M. Vanderhaeghen, M. Guidal, J.-M. Laget, Phys. Rev. C **57**, 1454 (1998).

[Va99] M. Vanderhaeghen, P. A. M. Guichon, and M. Guidal, Phys. Rev. D **60**, 094017 (1999).

[Vapc] M. Vanderhaeghen, private communication. The calculations were done using the double distribution of Radyushkin [Ra99] with and without the D"-term of Polyakov and Weiss [Po99].

[Ve87] P. Vernin, RPAC (II), CEBAF, January 1987, p. 615.

[Vi92] M. Virchaux and A. Milzstajn, Phys. Lett. **74B**, 221 (1992).

[Vo88] M. B. Voloshin and M. A. Shifman, Sov. J. Nucl. Phys. **47**, 511 (1988); N. Isgur, Phys. Rev. D **40**, 101 (1989); Phys. Lett. **B448**, 111 (1999).

[Vo00] J. Volmer *et al.*, nucl-ex/00/0009.

[Wa77] S. Wandzura and F. Wilczek, Phys. Lett. **B72**, 195 (1977).

[Wa80] S. T. Wang *et al.*, Adv. in Cryogenics Engineering **25**, 19 (1980).

[Wa82] S. T. Wang *et al.*, Cryogenics **22**, 335 (1982).

[Wa97] M. R. Wayne, Nucl. Inst. and Meth. **A386**, 278 (1997).

[We71] G. B. West, Phys. Lett. **B37**, 509 (1971); W. B. Atwood and G. B. West, Phys. Rev. D **7**, 773 (1973).

[We94] D. Weingarten, Nucl. Phys. **B34** (Proc Suppl.), 29 (1994).

[We96] G. West, hep-ph/9612403.

[Wh92] L. Whitlow *et al.*, Phys. Lett. **B282**, 475 (1992).

[Wo81] R. C. Wolgast *et al.*, IEEE Trans. on Magn. **17**, 195 (1981).

[Wo89] R. M. Woloshyn, Nucl. Phys. **A496**, 749 (1989).

[Wopc] B. Wojtsekhowski and C. Hyde-Wright, private communication; K. Abe *et al.*, Phys. Lett. **B404**, 404 (1997); P. L. Anthony *et al.*, Phys. Lett. **B458**, 529 (1999).

List of Figures

List of Tables

Contributors to the White Paper

Name	Institution
Abbott, D.	Jefferson Lab
Ambrozewicz, P.	Temple University
Abu-raddad, L.J.	Florida State University
Adams, G.	Rensselaer Polytechnic Institute
Afanasev, A.	North Carolina Central University/Jefferson Lab
Ahmidouch, A.	North Carolina A&T State University
Akushevich, I.	North Carolina Central University
Amatuni, T.	Yerevan Physics Institute
Ananyan, S.	College of William and Mary
Angelescu, T.	Bucharest University
Anghinolfi, M.	Istituto Nazionale di Fisica Nucleare, Genova
Anklin, H.	Jefferson Lab
Annand, J.	University of Glasgow
Anselmino, M.	Istituto Nazionale di Fisica Nucleare Torino
Anthony, I.	University of Glasgow
Armstrong, C.	Jefferson Lab
Armstrong, D.	College of William and Mary
Arrington, J.	Argonne National Laboratory
Asaturyan, R.	Yerevan Physics Institute
Assamagan, K.	Hampton University
Averett. T.	College of William and Mary
Avery, S.	Hampton University
Bailey, K.	Jefferson Lab
Baker, O. K.	Hampton University
Barden, H.	Universitat Heidelberg
Barnes, T.	Oak Ridge National Laboratory
Battaglieri, M.	Istituto Nazionale di Fisica Nucleare, Genova
Beard, K.	James Madison University
Beck, D.	University of Illinois at Urbana-Champaign
Beedoe, S.	North Carolina A&T State University
Beise, E.	University of Maryland
Benesch, J.	Jefferson Lab
Benhar, O.	Istituto Nazionale di Fisica Nucleare Sanita
Benmerrouche, M.	University of Saskatchewan
Bennhold, C.	George Washington University
Berman, B.	George Washington University
Bernstein, A.	Massachusetts Institute of Technology
Bertin, P.	University of Clermont-Ferrand
Bertozzi, W.	Massachusetts Institute of Technology
Beuville, E.	INDIGO Systems Corp
Bianchi, N.	Istituto Nazionale di Fisica Nucleare, Frascati
Bimbot, L.	Institute de Physique Nucleare, Orsay
Bird, I.	Jefferson Lab
Black, T.	Massachusetts Institute of Technology
Blok, H.	Vrije Universiteit
Bodyagin, V.	Moscow State University

Boeglin, W.	Florida International University
Boglione, M.	Vrije Universiteit
Bossingham, R.	Lawrence Berkeley Laboratory
Bosted, P.	University of Massachusetts
Boswell, M.	Randolph-Macon Woman's College
Bowman, D.	Los Alamos National Laboratory
Boyce, J.	Jefferson Lab
Brash, E.	University of Regina
Breuer, H.	University of Maryland
Brodsky, S.	Stanford Linear Accelerator Facility
Brooks, W.	Jefferson Lab
Brown, D.	University of Maryland
Bruell, A.	Massachusetts Institute of Technology
Buck, W.	Hampton University
Burkert, V.	Jefferson Lab
Burks, M.	Lawrence Berkeley Laboratory
Burtin, E.	C.E.A. Saclay
Capstick, S.	Florida State University
Cardarelli, F.	University of Rome
Cardman, L.	Jefferson Lab
Carlini, R.	Jefferson Lab
Carlson, C.	College of William and Mary
Carman, D.	Ohio University
Cates, G	University of Virginia
Cha, J.	Jefferson Lab
Chang, C. C.	University of Maryland
Chang, T.	University of Illinois
Chant, N.	University of Maryland
Chen, J. -P.	Jefferson Lab
Christy, M.	Hampton University
Chudakov, E.	Jefferson Lab
Chung, S.	Brookhaven National Laboratory
Cisbani, E.	Istituto Nazionale di Fisica Nucleare Roma
Clark, R.	Carnegie-Mellon University
Close, F.	Rutherford Laboratory
Coffman, D.	Cornell University
Cole, P.	University of Texas at El Paso
Collins, G.	University of Maryland
Cords, D.	Jefferson Lab
Coriano, C.	Jefferson Lab
Corvisiero, P.	Istituto Nazionale di Fisica Nucleare, Genova
Cowley, A.	University Stellenbosch
Crabb, D.	University of Virginia
Crannell, H.	Catholic University of America
Cummings, J.	Rensselaer Polytechnic Institute
Cummings, W.	Argonne National Laboratory
Cwetanski, P.	Lawrence Berkeley Laboratory
Dale, D.	University of Kentucky
Danagoulian, S.	North Carolina A&T State University
Davidson, R.	Rensselaer Polytechnic Institute
Day, D.	University of Virginia
de Jager, K.	Jefferson Lab

De Leo, R.	Istituto Nazionale di Fisica Nucleare Bari
de Witt Huberts, P.	NIKHEF
Degtiarenko, P.	Jefferson Lab
Demianov, A.	Moscow State University
Denisov, S.	Institute for Higher Energy Physics
Dennis, L.	Florida State University
DeSanctis, E.	Istituto Nazionale di Fisica Nucleare, Frascati
Didelez, J.-P.	IPN ORSAY
Diehl, M.	Stanford Linear Accelerator Center
Dieterich, S.	Rutgers University
Djalali, C.	University of South Carolina
Dodge, G.	Old Dominion University
Domingo, J.	Jefferson Lab
Doughty, D.	Christopher Newport University
Dragovitsch, P.	Florida State University
Duncan, F.	Queens University
Dunne, J.	Mississippi State University
Dutta, D.	Massachusetts Institute of Technology
Dytman, S.	University of Pittsburgh
Dzierba, A.	Indiana University
Eckhardt, R.	Ruhr University-Bonn
Eden, T.	Norfolk State University
Egiyan, H.	College of William and Mary
Egiyan, K.	Yerevan Physics Institute
Elouadrhiri, L.	Christopher Newport University
Empl, A.	Rensselaer Polytechnic Institute
Ent, R.	Jefferson Lab
Epstein, M.	California State University
Ernst, D.	Vanderbilt University
Eugenio, P	Carnegie-Mellon University
Ewell, L.	University of Maryland
Eyraud, L.	Institut des Sciences Nucleaires de Grenoble
Fang, G.	Harvard University
Fantoni, S.	Interdisciplinary Laboratory
Fedyakin, N.	Institute for Higher Energy Physics
Fenker, H.	Jefferson Lab
Ficenic, J.	Virginia Polytechnic Institute
Filippone, B.	California Institute of Technology
Fivozinsky, S.	Department of Energy
Forest, J.	Jefferson Lab
Forest, T.	Old Dominion University
Fortune, T.	University of Pennsylvania
Frankfurt, L.	Tel Aviv University
Freyberger, A.	Jefferson Lab
Frois, B.	CEA Saclay
Frolov, V.	Rensselaer Polytechnic Institute
Frullani, S.	Istituto Nazionale di Fisica Nucleare, Roma
Funsten, H.	College of William and Mary
Furget, C.	Institut des Sciences Nucleaires de Grenoble
Furic, M.	University of Zagreb
Gai, M.	Yale University
Gan, L.	Hampton University

Gao, H.	Massachusetts Institute of Technology
Garo̧n, M.	C.E.A. Saclay
Garibaldi, F.	Istituto Nazionale di Fisica Nucleare, Roma
Garrow, K.	Jefferson Lab
Gaskell, D.	Oregon State University
Gasparian, A.	Hampton University
Geesaman, D.	Argonne National Laboratory
Gilad, S.	Massachusetts Institute of Technology
Gilfoyle, G.	University of Tennessee
Gilman, R.	Rutgers University
Giovanni, S.	Istituto Nazionale di Fisica Nucleare
Glamazdin, A.	Kharkov State University
Glashausser, C.	Rutgers University
Godfrey, S.	Carleton University
Goity, J.	Jefferson Lab
Gomez, J.	Jefferson Lab
Gorokhov, A.	Institute for Higher Energy Physics
Grach, I.L.	Institute of Theoretical and Experimental Physics
Gribushin, A.	Moscow State University
Griffioen, K.	College of William and Mary
Gross, F.	College of William and Mary
Gueye, P.	Hampton University
Guidal, M.	I.P.N. Orsay
Guichon, P.	C.E.A. Saclay
Gustafsson, K.	University of Maryland
Guzey, V.	Pennsylvania State University
Gyurjyan, V.	Jefferson Lab
Hadjidakis, C.	Institut de Physique Nucleaire, Orsay
Hansen, O.	Jefferson Lab
Hansper, J.	Ruhr University, Bochum
Harvey, M.	Hampton University
Hashimoto, O.	Tohoku University
Heddle, D.	Christopher Newport University
Hersman, B.	University of New Hampshire
Heyes, G.	Jefferson Lab
Hicks, K.	Ohio University
Hinton, W.	Hampton University
Holt, R.	University of Illinois
Hourany, E.	IPN-ORSAY
Huber, G.	University of Regina
Hungerford, E.	University of Houston
Huston, J.	Michigan State University
Hyde-Wright C.	Old Dominion University
Iodice, M.	Istituto Nazionale di Fisica Nucleare Roma
Ireland, D.	University of Glasgow
Isgur, N.	Jefferson Lab
Ito, M.	Jefferson Lab
Jackson, C.	Hampton University
Jackson, H.	Argonne National Laboratory
Jastrzembski, E.	Jefferson Lab
Jenning, B.	TRIUMF
Jeschonnek, S.	Jefferson Lab

Ji, C-R.	North Carolina State University
Ji, X.	University of Maryland
Jiang, X.	Massachusetts Institute of Technology
Johnson, M.	Los Alamos National Laboratory
Jones, C.	California Institute of Technology
Jones, M.	College of William and Mary
Jones, R.	University of Connecticut
Joo, K.	University of Virginia
Kaminski, R.	Henryk Niewodniczanski Institute of Nuclear Physics
Kashy, D.	Jefferson Lab
Katramatou, M.	Kent State University
Keister, B.	National Science Foundation
Keith, C.	Jefferson Lab
Kellie, J.	University of Glasgow
Keppel, C.	Hampton University
Khandaker, M.	Norfolk State University
Kharzeev, D.	RIKEN BNL
Kinney, E.	University of Colorado
Kino, K.	Tohoku University
Klabucar, D.	Zagreb University
Klein, A.	Old Dominion University
Klein, F.	Florida International University
Kodolova, O.	Moscow State University
Koltenuk, D.	University of Pennsylvania
Kornicer, M.	University of Connecticut
Korotkikh, V.	Moscow State University
Kossov, M.	Jefferson Lab
Kostin, M.	Moscow State University
Kox, S.	Institut des Sciences Nucleaires de Grenoble
Kramer, L.	Florida International University
Kruglov, N.	Moscow State University
Kuhlmann, S.	Argonne National Laboratory
Kuhn, S.	Old Dominion University
Kumar, K.	University of Massachusetts
Kumbartzki, G.	Rutgers University
Kurilov, A.	University of Connecticut
Kuss, M.	Jefferson Lab
Laget, J. M.	CEA Saclay
Landshoff, P.	DAMTP
Lassila, K.	Iowa State University
Lawrence, D.	University of Massachusetts
Leader, E.	Birkbeck College
Lebed, R.	Jefferson Lab
Leeman, C.	Jefferson Lab
Leinweber, D.	Rensselaer Polytechnic Institute
Leone, T.	Istituto Nazionale di Fisica Nucleare Torino
LeRose, J.	Jefferson Lab
Lesniak, L.	Henryk Niewodniczanski Institute of Nuclear Physics
Levelt, J.	University of Erlangen-Nuernberg
Lewis, R.	University of Regina
Liang, M.	Jefferson Lab
Lieb, J.	George Mason University

Liuti, S.	University of Virginia
Livingston, K.	University of Glasgow
Liyanage, N.	Jefferson Lab
Lolos, G.	University of Regina
Lolos, J.	University of Pittsburgh
Loman, E.	Massachusetts Institute of Technology
Londergan, T.	Indiana University
Lorenzon, W.	University of Michigan
Lourie, R.	Renaissance Tech
Lu, D.	University of Adelaide
Lung, A	Jefferson Lab
MacGregor,D.	University of Glasgow
Mack, D.	Jefferson Lab
Macleod, R.	Jefferson Lab
Madey, R.	Jefferson Lab
Magahiz, R.	Carnegie-Mellon University
Majewski, S.	Jefferson Lab
Makins, N.	University of Illinois
Manak, J.	Jefferson Lab
Marchand, C.	CEA Saclay
Margaryan, A.	Yerevan Physics Institute
Margaziotis, D.	California State University
Markowitz, P.	Florida State University
Martoff, C.	Temple University
McGeorge, C.	University of Glasgow
McIntyre, J.	College of William and Mary
McNabb, J.	Carnegie Mellon University
Meadows, B.	Indiana University
Mecking, B.	Jefferson Lab
Meekins, D.	Florida State University
Melnitchouk, W.	Jefferson Lab
Mestayer, M.	Jefferson Lab
Meyer, C.	Carnegie-Mellon University
Meziani, Z. E.	Temple University
Michaels, R.	Jefferson Lab
Mihul, A.	University of Bucharest
Milana, J.	University of Maryland
Milbrath, B.	Eastern Kentucky University
Miller, G.	University of Washington
Miller, M.	University of Illinois
Milner, R.	Massachusetts Institute of Technology
Minehart, R.	University of Virginia
Mischke, R.	Los Alamos National Laboratory
Miskimen, R.	University of Massachusetts
Mitchell, J.	Jefferson Lab
Mkrtchyan, H.	Yerevan Physics Institute
Mohring, R.	University of Maryland
Morfin, J.	Fermi National Accelerator Laboratory
Mtingwa, S.	North Carolina A&T State University
Mucifora, V.	Instituto Nazionale di Fisica Nucleare, Frascati
Mueller, A.	Columbia University
Mueller, J.	University of Pittsburgh

Mukhopadhyay, N.	Rensselaer Polytechnic Institute
Mulders, P.	National Institute for Nuclear Physics and High Energy Physics
Murgia, F.	Istituto Nazionale di Fisica Nucleare, Cagliari
Musolf, M.	Old Dominion University
Mutchler, G.	Rice University
Nanda, S.	Jefferson Lab
Napolitano, J.	Rensselaer Polytechnic Institute
Nappi, E.	Istituto Nazionale di Fisica Nucleare, Bari
Narodetskii, I.	Institute of Theoretical and Experimental Physics, Moscow
Nathan, A.	University of Illinois
Nemchik, J.	Institute of Experimental Physics
Niculescu, G.	Ohio University
Niculescu, I.	George Washington University
Niczyporuk, B.	Jefferson Lab
Nikolaev, N.	Institute of Experimental Physics
O'Brien, J.	The Catholic University of America
Olness, F.	Southern Methodist University
Owens, B.	University of Glasgow
Owens, J.	Florida State University
Pace, E.	University of Rome
Page, P.	Los Alamos National Laboratory
Palonek, A.	Los Alamos National Laboratory
Pang, A.	North Carolina State University
Peng, J.	Los Alamos National Laboratory
Perdrisat, C.	College of William and Mary
Perrino, R.	Istituto Nazionale di Fisica Nucleare, Lecce
Petratos, G.	Kent State University
Piasetzky, E.	Tel Aviv University
Pichowsky, M.	Indiana University
Piekarewicz, J.	Florida State University
Piller, G.	University of Regensburg
Polyakov, M.	Petersburg Nuclear Physics Institute
Popov, S.	Budker Institute of Nuclear Physics
Potterveld, D.	Argonne National Laboratory
Preedom, B.	University of South Carolina
Price, J.	Louisiana Technical Institute
Prout, D.	Kent State University
Puga, A.	University of Texas at El Paso
Pumplin, J.	Michigan State University
Punjabi, V.	Norfolk State University
Qiu, J.	Iowa State University
Quinn, B.	Carnegie-Mellon University
Radysushkin, A.	Old Dominion University
Ransome, R.	Rutgers University
Raue, B	Florida International University
Real, J.	Institute des Sciences Nucleaires de Grenoble
Reece, C.	Jefferson Lab
Reinhold, J.	Florida International University
Retiere, F.	Subatech Nantes Fr.
Ribeiro, E.	CENE, Portugal
Riccardi, G.	Florida State University
Ricco, G.	Istituto Nazionale di Fisica Nucleare, Genova

Ripani, M.	Istituto Nazionale di Fisica Nucleare, Genova
Roberts, W.	Old Dominion University
Roblin, Y.	Clermont-Ferrand University
Roedelbronn, M.	University of Illinois
Rondon, O.	University of Virginia
Roos, P.	University of Maryland
Rosner, G.	University of Glasgow
Rubin, P.	University of Richmond
Rutt, P.	University of Georgia
Sabatie, F.	Old Dominion University
Saha, A.	Jefferson Lab
Saito, K.	Tohoku College
Saito, T.	Tohoku University
Salgado, C.	Norfolk State University
Salme, G.	Istituto Nazionale di Fisica Nucleare
Samoilenko, V.	Institute for Higher Energy Physics
Sapunenko, V.	Istituto Nazionale di Fisica Nucleare, Genova
Sargayan, M.	Tel Aviv University
Sargsian, M.	Yerevan Physics Institute
Sarty, A.	St. Mary's University
Sarycheva, L.	Moscow State University
Savkli, C.	University of Pittsburgh
Sawafta, R.	North Carolina A&T State University
Schaefer, A.	Universitaet Frankfurt
Schoch, B.	University of Bonn
Schukin, A.	Institute for Higher Energy Physics
Schumacher, R.	Carnegie Mellon University
Scopetta, S.	European Centre for Theoretical Studies in Nuclear Physics
Scott, E.	Indiana University
Seely, M.	Jefferson Lab
Segal, J.	Jefferson Lab
Segel, R.	Northwestern University
Seth, K.	Northwestern University
Sharabian, Y.	Jefferson Lab
Sher, M.	College of William and Mary
Silvano, S.	Istituto Nazionale di Fisica Nucleare
Simula, S.	Istituto Nazionale di Fisica Nucleare, Rome
Sinclair, C.	Jefferson Lab
Smirnov, N.	Yale University
Smith, C.	University of Virginia
Smith, E.	Jefferson Lab
Smith, P.	Indiana University
Smith, Y.	Jefferson Lab
Snellings, R.	Lawrence Berkeley Laboratory
Sober, D.	Catholic University of America
Solodov, E.	Budker Institute of Nuclear Physics
Souder, P.	Syracuse University
Steffen, C.	Indiana University
Stepanyan, S.	Christopher Newport University
Stoler, P.	Rensselaer Polytechnic Institute
Strikman, M.	Pennsylvania State University
Sulanke, T.	Indiana University

Suleiman, R.	Massachusetts Institute of Technology
Swanson, E.	North Carolina State University
Szczepaniak, A.	Indiana University
Tadevosyan, V.	Yerevan Physics Institute
Taiuti, M.	Istituto Nazionale di Fisica Nucleare Genova
Takagi, F.	Tohoku University
Tang, L.	Hampton University
Taylor, M.	Jefferson Lab
Tedeschi, D.	University of South Carolina
Teige, S.	Indiana University
Templon, J.	University of Georgia
Teodorescu, L.	University of Bucharest
Terasawa, T.	Tohoku University
Thomas, A.	University of Adelaide
Timmer, C.	Jefferson Lab
Tipton, B.	California Institute of Technology
Trentalange, S.	University of California at Los Angeles
Tsubota, H.	Tohoku University
Tung, W.K.	Michigan State University
Ulmer, P.	Old Dominion University
Urciuoli, G.	Istituto Nazionale di Fisica Nucleare, Rome
Urner, D.	University of Illinois
Va'vra, J.	Stanford Linear Accelerator Center
van den Brand, J.	Vrije Universiteit
Van Orden, W.	Jefferson Lab
Vanderhaeghen, M.	University Mainz
Vlahovic, B.	Jefferson Lab
Volmer J.	Vrije Universiteit
Voutier, E.	Institut des Sciences Nucleaires de Grenoble
Vulcan, W.	Jefferson Lab
Walcher, T.	University of Mainz
Wang, K.	University of Virginia
Watson, C.	Jefferson Lab
Watts, D.	University of Glasgow
Weilhammer, P.	CERN
Weiman, H.	Lawrence Berkeley Laboratory
Weinstein, J.	University of Mississippi
Weinstein, L.	Old Dominion University
Weise, W.	Universitaet Munchen
Weisenberger, D.	Jefferson Lab
Welch, P.	Oregon State University
Welch, R.	Jefferson Lab
Weygand, D.	Jefferson Lab
Whitmore, J.	Pennsylvania State University
Whitney, R.	Jefferson Lab
Wieman, H	Lawrence Berkeley Laboratory
Williams, A.	University of Adelaide
Williams, R.	Jefferson Lab
Wilson, J.	Jefferson Lab
Winn, D.	Fairfield University
Wise, J.	Jefferson Lab
Wojtsekhowski, B.	Jefferson Lab

Wolin, E.	Jefferson Lab
Wood, S.	Jefferson Lab
Yan, C.	Jefferson Lab
Yang, J.	Chungnam University
Yegneswaran, A.	Jefferson Lab
Yershov, A.	Moscow State University
Zakharov, B.	Institute of Experimental Physics
Zeidman, B.	Argonne National Laboratory
Zhang, J.	Rensselaer Polytechnic Institute
Zorn, C.	Jefferson Lab